Application-specific Optical Tweezers.

Dissertation zur Erlangung des
akademischen Grades Doktor-Ingenieur (Dr.-Ing.)

vorgelegt der
Fakultät für Maschinenbau
der Technischen Universität Ilmenau

von

Ronald Kampmann

1. Gutachter: Univ.-Prof. Dr. rer. nat. habil. Stefan Sinzinger
2. Gutachter: Prof. Dr. Jan. G. Korvink
3. Gutachter: Prof. Dr. Oliver Kalthoff

Tag der Einreichung: 05.12.2016
Tag der wissenschaftlichen Aussprache: 05.05.2017

urn:nbn:de:gbv:ilm1-2017000200

Abstract

The objective of this thesis is to extend the classical optical design process for the development of highly efficient optical tweezers, especially adapted for optical trapping of microscopic objects. This is achieved with an optical force simulation, which is implemented in the optical design process to optimize the optical force.

Since most conventional optical tweezers are integrated in inverted light microscopes, the enhancement of the imaging function to an optical trap is often a compromise due to the possibilities allowed by the existing optical setup.

The development of optical tweezers requires the ability to optimize the optical trapping performance with respect to the boundary conditions and constrains given by the optical trapping application. Therefore, an optical force simulation tool based on the ray optics approach is developed. This tool not only allows for the calculation of optical forces but also optical aberrations can be considered and experimentally obtained data can be used as input as well.

Two optical tweezers, suited to trap particles in gaseous and liquid environment are developed in this thesis. After the design process is completed, the optical components are manufactured externally. For the characterization of the optical components, interferometric and caustic measurements are performed. Once the optical tweezer systems are assembled and aligned, the caustic of the system is measured and used as input data for the force simulation to investigate theoretically the generation of an optical trap. Finally, the optical trapping of fused silica particles with both optical tweezers is experimentally verified.

The agreement between the theoretical and experimental results demonstrates the proper function of the force simulation tool. This enables the investigation of how optical tweezers suffer from monochromatic optical aberrations. Therefore, optical trapping experiments and force simulations are performed, which reveal that aberrations without axial symmetry heavily affect the optical trapping performance, whereas aberrations leading to symmetric distortions of the focal spot and the caustic just barely influence the optical trap.

Zusammenfassung

Motiviert wird diese Arbeit durch die Entwicklung hocheffizienter optischer Systeme, welche das optische Fangen mikroskopischer Objekte ermöglichen. Dazu muss der klassische Optikdesignprozess mit einer neuen Zielfunktion, der optischen Kraft, erweitert werden.

Konventionelle optische Pinzetten sind oftmals in invertierte Lichtmikroskope integriert. Die Erweiterung der abbildenden Funktion des Mikroskops zu einer optischen Pinzette stellt häufig nur einen Kompromiss aufgrund des bereits existierenden optischen Aufbaus dar.

Speziell an die Anwendung angepasste optische Pinzetten erfordern die Optimierung der optischen Kraft im Hinblick auf die gestellten Anforderungen und die vorherrschenden Randbedingungen. Hierfür wird eine optische Kraftsimulation auf Basis der geometrischen Optik entwickelt. Diese ermöglicht das Simulieren optischer Kräfte bezüglich frei wählbarer Eingangsparameter wie der numerischen Apertur der Optik, der zu fokussierenden Intensitätsverteilung, optischer Aberrationen und anderer.

Zwei Systeme, welche das optische Fangen in gasförmigen und flüssigen Umgebungsmedien realisieren, werden mit dem erweiterten Optikdesignprozess entwickelt, wobei die Komponenten extern gefertigt werden. Nach der optischen Charakterisierung der Elemente sowie der anschließend justierten optischen Systeme wird zunächst theoretisch überprüft ob beide Systeme eine stabile optische Falle erzeugen. Anschließend wird experimentell das optische Fangen mikroskopischer Quarzglaspartikel mit beiden Systemen nachgewiesen.

Auf Grundlage der Übereinstimmung der experimentellen und theoretischen Ergebnisse wird das Verhalten optischer Pinzetten unter dem Einfluss optischer Aberrationen untersucht. Das gezielte Einbringen von Aberrationen in eine optische Pinzette sowie die entsprechende Reaktion der optischen Falle werden experimentell und theoretisch analysiert. Es stellt sich heraus das Aberrationen, welche die Symmetrie der Kaustik des optischen Systems zerstören die Stabilität und Leistungsfähigkeit der optischen Pinzette stark beeinflussen. Achssymmetrische Aberrationen hingegen beeinträchtigen die optische Falle deutlich weniger.

Acknowledgements

An dieser Stelle möchte ich mich bei Herr **Prof. Sinzinger** bedanken, daß er mir die Anfertigung dieser Dissertation am Fachgebiet Technische Optik ermöglicht hat. Seine Unterstützung nicht nur bei fachlich relevanten Themen waren mir stets eine große Hilfe die so nicht selbstverständlich ist.

Weiteren Dank schulde ich meinen Kollegen und Kolleginnen. Solch eine Arbeit ist nicht ohne ein Team möglich.

Abschließend gilt mein Dank meiner besseren Hälfte, Fränzi. Ohne Ihren Rückhalt wäre vieles deutlich schwieriger gewesen.

Contents

List of Figures

List of Tables

Abbreviations

CAD	**C**omputer **A**ided **D**esign
CCD	**C**harge-**C**oupled **D**evice
CMOS	**C**omplementary **M**etal-**O**xide **S**emiconductor
DDA	**D**iscrete **D**ipole **A**pproximation
DNA	**D**eoxyribo**N**ucleic **A**cid
eq.	**eq**uation
FDTDM	**F**inite **D**ifference **T**ime **D**omain **M**ethod
fig.	**fig**ure
FWHM	**F**ull **W**idth **H**alf **M**aximum
FEM	**F**inite **E**lement **M**ethod
GEO	**GEO**metrical Spot Radius
GLMT	**G**eneralized **L**orenz- **M**ie **T**heory
GPMM	**G**eneralized **P**oint **M**atching **M**ethod
GBE	**G**aussian image plane
GOA	**G**eometrical **O**ptics **A**pproach
μ**-HH**	**M**icro-**H**elm**h**oltz
LASER	**L**ight **A**mplification by **S**timulated **E**mission of **R**adiation
LMT	**L**orenz-**M**ie **T**heory
MOM	**M**ethod **O**f **M**oments
NA	**N**umerical **A**perture
Nd-YAG	**N**eodymium **d**oped **Y**ttrium **A**luminum **G**arnet
NIR	**N**ear **I**nfra **R**ed
NMR	**N**uclear **M**agnetic **R**esonance
NPMM	**N**ano **P**ositioning and nano **M**easuring **M**achine
OFHC	**O**xygen-**F**ree **H**igh thermal **C**onductivity
OPD	**O**ptical **P**ath **D**ifference

OT	**O**ptical **T**weezers
PMM	**P**oint **M**atching **M**ethod
PMMA	**P**oly **M**ethyl **M**eth **A**crylate
PU	**P**oly **U**rethane
PSF	**P**oint **S**pread **F**unction
RNA	**R**ibo **N**ucleic **A**cid
SLM	**S**patial **L**ight **M**odulator
SVM	**S**eparation of **V**ariables **M**ethod
tab.	**tab**le
TEM	**T**ransverse **E**lectro **M**agnetic
TIR	**T**otal **I**nternal **R**eflection
TMM	**T**-**M**atrix **M**ethod
USAF	**U**nited **S**tates **A**ir **F**orce
VSWF	**V**ector **S**pherical **W**ave **F**unctions
WA	**W**avefront **A**berration
WD	**W**orking **D**istance
WE	**W**avefront **E**rror

Symbols

a	radius	m
a	semi axis of ellipsoid	m
a	size parameter (LMT)	1
a_1	element 11 of rotation matrix R_n	1
a_2	element 21 of rotation matrix R_n	1
a_3	element 31 of rotation matrix R_n	1
a_n	scattering coefficient	1
a_n	expansion coefficient	1
ast	scaling factor for monochromatic optical aberration astigmatism	1
b	semi axis of ellipsoid	m
b_1	element 12 of rotation matrix R_n	1
b_2	element 22 of rotation matrix R_n	1
b_3	element 32 of rotation matrix R_n	1
b_n	scattering coefficient	1
c	semi axis of ellipsoid	m
c	speed of light	m s^{-1}
c_0	speed of light	m s^{-1}
c_1	element 13 of rotation matrix R_n	1
c_2	element 23 of rotation matrix R_n	1
c_3	element 33 of rotation matrix R_n	1
c_w	drag coefficient	1
$coma$	scaling factor for monochromatic optical aberration coma	1
$dist$	scaling factor for monochromatic optical aberration distortion	1
$field$	scaling factor for monochromatic optical aberration field curvature	1

$focsu$	scaling factor for monochromatic optical aberration defocus	1
g	gravity	m s^{-2}
h	height	m
i	intensity function	W m^{-2}
$\hbar$	reduced Planck constant	J s
k	numerator	1
k	wave number	m^{-1}
$\vec{k}$	wave vector	m
$\vec{k}$	direction	m
m	relative refractive index	1
n	refractive index	1
n	mode index	1
n	numerator	1
$\vec{n}$	unit vector	1
p	polarization direction parallel to the plane of incidence (index)	1
$\vec{p}$	momentum	kg m s^{-1}
p_k	expansion coefficient	1
$pist$	scaling factor for monochromatic optical aberration piston	1
r	amplitude coefficient for reflection	1
r	distance	m
r	radius	m
$\vec{r}$	vector (incident ray)	m
$\vec{r}'$	vector (refracted ray)	m
$\vec{r}''$	vector (reflected ray)	m
s	polarization direction perpendicular to the plane of incidence (index)	1
sph	scaling factor for monochromatic optical aberration spherical aberration	1
t	amplitude coefficient for transmission	1
t	time	s
t	slope (factor)	1
$tilt$	scaling factor for monochromatic optical aberration tilt	1

v	velocity	m s^{-1}
w	beam waist	m
x	Cartesian coordinate	m
x_0	field coordinate	1
y	Cartesian coordinate	m
z	Cartesian coordinate	m

$\vec{A}$	point	m
$\vec{B}$	magnetic field	T
C_{scat}	scattering cross section	m^2
D	diameter	m
$\vec{E}$	electric field	V m^{-1}
F	force	N
$\vec{F}$	force	N
GEO	geometric spot radius	m
I	intensity	W m^{-2}
L	focal length	m
$\vec{M}$	center point	m
$\vec{M}$	torque	N m
N	numerator (number of photons)	1
OPD	optical path difference	m
P	power	W (J s^{-1})
PSF	point spread function	W m^{-2}
Q_{diff}	diffraction efficiency	1
Q_{refl}	external reflection efficiency	1
Q_{scat}	scattering efficiency	1
Q_{trans}	transmission efficiency	1
R	Fresnel reflection coefficient	1
R	radius	m
R_n	rotation matrix	1
RE	Reynolds number	1

RT	ring thickness	pixel
S_i	amplitude function	$\sqrt{Wm^{-2}}$
R	Fresnel transmission coefficient	1
RMS	root mean square spot size	m
T	truncation ratio	1
T_{kn}	T-matrix element	1
U	unpolarized radiation (index)	1
U_{inc}	incident field	V m^{-1}
U_{scat}	scattered field	V m^{-1}
W_{200}	wavefront aberration: piston	wavelength
W_{111}	wavefront aberration: tilt	wavelength
W_{020}	wavefront aberration: defocus	wavelength
W_{040}	wavefront aberration: spherical aberration	wavelength
W_{131}	wavefront aberration: coma	wavelength
W_{222}	wavefront aberration: astigmatism	wavelength
W_{220}	wavefront aberration: field curvature	wavelength
W_{311}	wavefront aberration: distortion	wavelength
WA	wavefront aberration	wavelength
WE	wavefront error	m
X	Cartesian coordinate	m
Y	Cartesian coordinate	m
Z	Cartesian coordinate	m
α	angle	°
α	electric polarizability	C m^2 V^{-1}
β	angle	°
η	kinematic viscosity	Pa s
λ	wavelength	m
ω	angular frequency	rads^{-1}
ϕ	polar angle	°
ρ	density	g cm^{-3}
ρ	radial coordinate	1

Φ	angle	°
Φ	scalar field	1
Ψ_n^{inc}	discrete basis set describing the incident field	V m^{-1}
Ψ_n^{scat}	discrete basis set describing the scattered field	V m^{-1}
Θ	angle	°

Chapter 1

Introduction

1.1 Motivation

Imagine you have to pick up a microscopic object like tiny pollen or a yeast cell and precisely place it on a microscope slide for optical and chemical research. Intuitively you apply a pair of forceps to pick up the object. As soon as you try to release the pollen it sticks on the tip of the forceps. This sticking behavior is typical for micro sized objects whose gravity is small or comparable to the adhesive force coming up by bringing them in contact with a surface. To overcome the adhesive forces when releasing the object, one can either modify the surface of the gripping tool or apply a tool that allows contactless manipulation.

Since three decades an optical non-contact gripping tool is available [14] and frequently applied for the positioning and manipulation of microscopic objects. Due to its operating principle this tool is usually called optical tweezers (OT). Based on the fact that light carries momentum optical systems can be designed to tailor the light distribution in a manner that enables the generation of optical holding forces. These forces act in the opposite direction of the light propagation and provide contactless trapping of small objects with dimensions up to few 100 μm. For this purpose, usually a Gaussian laser beam is focused by use of high numerical aperture (NA) objective lenses. Thus, a steep intensity gradient is formed that has the ability to overcome gravity and hold small objects.

Up to now, optical tweezers have found their way into several applications. The majority of them relate to the investigation of cells, DNA or RNA molecules. Furthermore, OT support manufacturing processes like the two photon polymerization or are used in microfluidics as particle sorters or valves. Besides tasks taking place in liquid environments, optical tweezers are utilized for studies of Raman spectra of single airborne particles or for particle transport over large distances. Most of these applications place special demands and requirements on the optical system.

To focus on the objectives of this thesis, first, an optical tweezers has to be integrated in a high-precision positioning and measuring device to operate as a gripping tool. The second application intended is to assist a measurement method based on nuclear magnetic resonance where the optical tweezers has to trap a microscopic sample in a microfluidic channel that is integrated in the bore of a superconducting magnet. Both objectives place different requirements on the optical system and require the extension of the classical optical design process to meet the demands claimed by the applications. Therefore, a simulation tool for the computation of optical forces is developed. This tool is used in the thesis for the simulation, design and optimization of optical systems well adapted to specific application.

1.2 Objective

The aim of this work is to establish a method that allows the design and optimization of optical systems suited for specific optical trapping applications. Classical optical design procedures and software are frequently used to develop optical systems in general. Merit functions can be defined whose fulfilment leads to specific optical properties and capabilities like high on axis resolution or a tele centric imaging behavior. Thus, the design process itself has not to be reinvented, but rather it has to be extended by an additional parameter, the optical force. This new parameter has a magnitude and a direction and depends on the position of the particle relative to the optical system and of course its characteristics. Furthermore, the object itself and its surrounding have to be considered.

The optical force simulation has to link the output of the optical design software with the required feedback if the system provides optical trapping ability. This ensures the adaption of the optical system to the boundary conditions given by the application and its optimization in terms of maximum optical force per laser power.

Standard optical design software operates within the framework of ray optics. Therefore, an optical force simulation based on the geometrical optics approach (GOA) is developed first. The output intensity distribution of an optical system, its NA as well as aberrations of the system represent necessary input parameters for the force simulation. The wavefront aberrations (*WA*) are considered in terms of optical path differences (*OPD*) which enable the simulation of their impact on the trapping performance. The shape of the particles to be trapped is defined analytically by use of an ellipsoidal description. Thus, the particles can be of spherical, oblate or needle like shape in any desired orientation in space. This routine is integrated into the optical design process and allows for the optimization of systems suited for optical trapping.

The enhanced optical design process is applied for the development of two different optical tweezers. The first system is an optical tweezers capable for trapping of particles in gaseous surrounding. Motivated by a subproject in a collaborative research center [61] the task is to create and study a contactless gripping tool that should enhance the functional scope of a nano-positioning and nano-measuring machine (NPMM). The second system has to hold objects in a liquid surrounding to assist spectroscopic measurements based on nuclear magnetic resonance (NMR) [133]. The bore of a superconducting magnet filled with a specialized probe head equipped with microfluidic channels determines the optical framework. High magnetic fields lead to a system design without the use of magnetic materials.

In both applications, the final design data of the optical components is transferred to computer aided design (CAD) format. Once the optical elements are manufactured, the whole optical system is assembled and aligned. Finally, optical trapping of particles made of fused silica confirms the functionality of both systems. Furthermore, the OT and the optical force simulation are used to investigate how optical aberrations affect the trapping performance.

1.3 Thesis outline

The structure of this thesis is implemented as follows. Chapter 2 deals with the state of the art regarding theoretical aspects necessary for this work. The simulation of the scattering of light, the calculation of optical forces and monochromatic aberrations of optical systems are addressed. Initially, the scattering of light is briefly described by three approaches valid for different particle size regimes. Next, three methods for the simulation of optical forces which are based on the wave and ray optics approach are discussed. To complete the theory section, a model is presented to describe optical systems and their aberrations. Applications of optical tweezers, commonly used setups and measurement methods utilized for particle detection and force calibration are presented and discussed in the last part of this chapter.

The methods applied in this work are presented in chapter 3. The development of the optical force simulation and its implementation within a programming environment results in a tool that is used in the optical design process later on. For the realization of an interface between the optical design software and the force simulation, optical systems are approximated by use of an array of pixels describing the intensity distribution at the system output plane and a value for the focal length. Next, the consideration of wavefront aberrations in terms of optical path differences and how they are integrated in the optical force simulation is presented. Based on the simulation, simple examples are addressed which give first insights in the world of optical tweezers. The iterative design process used for the development of the optical trapping systems is explained subsequently. The last part of this chapter deals with the experimental work. Measurement methods performed for optical characterization of single optical components and the whole optical system are explained.

Chapter 4 contains the results achieved theoretically and experimentally in this thesis. Based on optical force simulations, correlations between the optical trapping performance and the parameters of the optical system like the NA, intensity distribution, refractive indices etc. are discussed. The systems developed for optical trapping are presented and studied in detail. Experimental results are compared with the predictions generated by the optical force simulation. Finally, the effect of optical aberrations on the optical trap is investigated.

The work is concluded in chapter 5. An outlook, chapter 6, gives detailed starting points for the enhancement of the optical force simulation in terms of decreasing the degree of approximation and increasing its computing speed. In view of optical system optimizations, the minimization of costs and required space are addressed. Finally, starting points for the improvement of the force measurement accuracy are given.

Chapter 2

State of the art

The main focus of this thesis is to establish a method for the development of optimized optical systems suited for optical trapping of particles in gaseous and liquid environments, as well as the investigation of optical tweezers in the presence of monochromatic optical aberrations. This chapter provides the theoretical and practical aspects, which are relevant for this thesis. To understand the fundamental relationships of the interaction of light with matter the scattering of light is described first. Next, the generation of optical forces and torque acting on microscopic particles is discussed. Since each tailored light field is shaped and focused by use of optical systems, which are usually non-ideal, monochromatic optical aberrations are discussed afterwards. The second part of this chapter covers a detailed insight in the applications of optical tweezers as well as the applied optical setups.

2.1 Theory

The first part of this chapter deals with the scattering of light, optical forces and torque, as well as optical systems affected by aberrations. Starting with the next section the interaction between light and matter is described using three models, each valid for specific particle size regimes.

2.1.1 Scattering of light

The interaction of light with matter is part of our daily life. A light source emits electromagnetic radiation, which is reflected on the surface of an object, focused by the eye lens and finally absorbed by the photoreceptor cells in our retina. In this way we are able to see objects, neglecting the post processing afterwards. If we take a closer look at what is happening with the propagation of light, the content becomes more and more complex. Besides optical non-ideal surface properties the medium between a light source and a detector is not as simple as it seems. Small objects ranging from molecules up to dust particles and small water droplets are often non-homogeneously distributed within the environment. Light which propagates through this medium is scattered by

those particles. This leads to macroscopical visible effects like the blue sky, rainbows, coronas, mirages and more.
In order to stay focused, this chapter deals with the interaction of plane waves with single dielectric and non-absorbing particles within the framework of linear optics. The scattering of light is part of mankind thinking and focus of research starting several centuries ago. First scientific relevant studies are published in the 18^{th} century [44, 151, 152, 171]. As a result of this long history several powerful theoretical models that mathematically describe the scattering of light are available. Differences in the models can be traced back to their physical origins, their assumptions and approximations which result in limited validity concerning the particles size, shape, optical properties and the properties of the light waves. This section refers to the rigorous Lorenz-Mie theory as well as commonly used approximations in special particle size-wavelength regimes. In the last part an overview will be given about the calculation of the scattering pattern of non-spherical particles.

Spherical particles of arbitrary size: Lorenz-Mie theory (LMT)

Based on the experimental studies on electromagnetic scattering performed by J. Tyndall in 1869 [264] and the theoretical investigations of Lord Rayleigh in 1871 [250], L. Lorenz in 1890 [151] and G. Mie in 1908 [170] developed the exact theory for the calculation of the scattering distribution caused by the interaction of a plane wave with a spherical object of any size, see fig. 2.1. A plane wave propagates along the optical axis in positive Z-direction and interacts with a dielectric, isotropic and spherical object. For large particles ($a \geq 10\lambda$) most of the intensity is scattered in forward direction whereas small amounts of the beam energy are scattered into discrete side lobes and backwards.

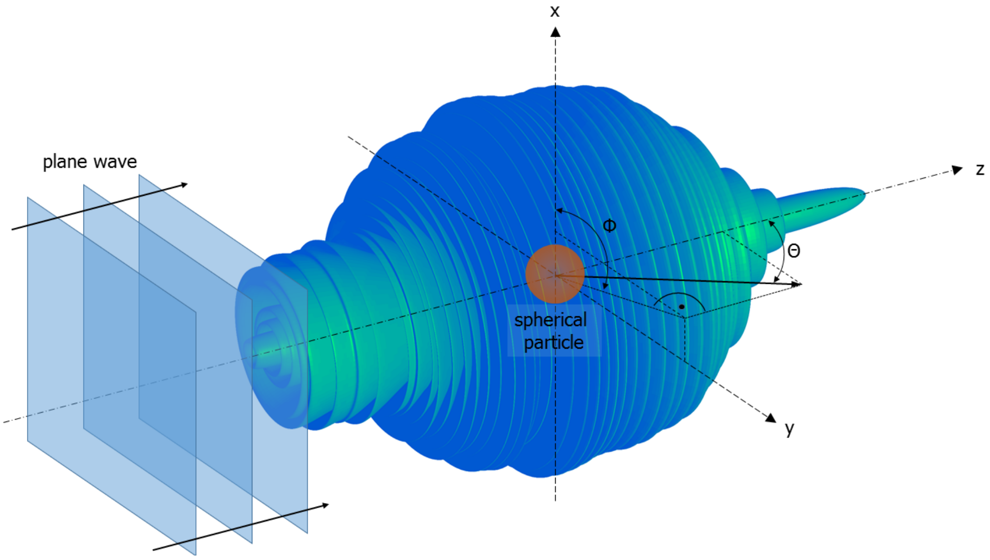

FIGURE 2.1: Logarithmic scattering distribution of an unpolarized plane wave ($\lambda = 555$ nm) which is incident on a spherical particle with radius $a = 5$ μm.

The exact derivation of the formulas is described in detail in several text books [129, 151, 170, 248]. Just the results are presented here to restrict this chapter to the essentials. The angle resolved intensity distribution as a result of scattering of a plane wave by a spherical particle is given by:

$$I_\Phi = \frac{\lambda^2}{4\pi^2 r^2}|S_1|^2(\sin\Phi)^2 = \frac{\lambda^2}{4\pi^2 r^2} i_1 (\sin\Phi)^2 \tag{2.1}$$

$$I_\Theta = \frac{\lambda^2}{4\pi^2 r^2}|S_2|^2(\cos\Theta)^2 = \frac{\lambda^2}{4\pi^2 r^2} i_2 (\cos\Theta)^2 \tag{2.2}$$

$$I_U = \frac{\lambda^2}{8\pi^2 r^2}(i_1 + i_2) \tag{2.3}$$

Indices Φ and Θ denote the polarization directions relative to the azimuthal direction and index U refers to unpolarized radiation. S_i and i_i are the amplitude and intensity functions as a result of the Lorenz-Mie theory (LMT). These values depend on the azimuth angles Φ and Θ, the particle and surrounding refractive indices n_i, the wavelength λ of the incident plane wave, the particle radius a and the distance r to the center of the particle. As indicated by the equations above, the scattering distribution is different for each polarization direction. If the incident radiation is circularly or unpolarized, the scattering distribution becomes an average of the linear polarized contributions. The rotational symmetric intensity distribution I_U is shown in fig. 2.1.

Consider the interaction of a beam with a scatterer, the amount of energy abstracted due to scattering is given by the scattering cross section C_{scat}.

$$C_{scat} = \frac{\lambda^2}{2\pi}\sum_{n=1}^{\infty}(2n-1)(|a_n|^2 + |b_n|^2) \tag{2.4}$$

a_n and b_n denote the scattering coefficients as a result of LMT [151, 170] and n is an integral value between zero and infinity. Normalizing the scattering cross section to the circular area of the particle, one obtains the scattering efficiency Q_{scat}.

$$Q_{scat} = \frac{C_{scat}}{\pi a^2} = \frac{\lambda^2}{2\pi^2 a^2}\sum_{n=1}^{\infty}(2n-1)(|a_n|^2 + |b_n|^2) \tag{2.5}$$

The scattering efficiency or in other words the area of the beam scattered by a small sphere is approximately twice as large as its geometrical cross section. It appears surprising that energy is scattered within a larger area compared to its geometrical cross section. For a simple explanation large particles can be used. One part of the incident beam directly interacts with the obstacle. The other parts of the beam, which propagate in the entire region nearby the obstacle are diffracted at its edges. Thus, the efficient interacting area of the beam is larger than the particles geometrical cross section.

Eq. 2.1 to 2.3 above represent the rigorous solutions to calculate the scattering pattern in the far field region [129]. They are valid for all particle sizes with the restriction of a dielectric, isotropic, non-absorbing material and particles of spherical shape.

Spherical particles small compared to the wavelength: Rayleigh approximation

Consider particles, which are small compared to the wavelength the Rayleigh approximation is suitable [250]. The particle is described by an oscillating dipole and the equations for the intensity pattern can be simplified to:

$$I_\Phi = \frac{16\pi^4 a^6}{r^2\lambda^4}(\frac{n^2-1}{n^2+2})^2, \tag{2.6}$$

$$I_\Theta = \frac{16\pi^4 a^6}{r^2\lambda^4}(\frac{n^2-1}{n^2+2})^2(\cos\Theta)^2. \tag{2.7}$$

In the case of unpolarized radiation the equation can be written as:

$$I_U = I_\Theta = \frac{8\pi^4 a^6}{r^2\lambda^4}(\frac{n^2-1}{n^2+2})^2(1+(\cos\Theta)^2). \tag{2.8}$$

The application of eq. 2.8 yields for an unpolarized plane wave with $\lambda = 555$ nm interacting with a particle ($a = 0.1\mu$m) to the typical oscillating dipole emission distribution shown in fig. 2.2.

The equations above depend directly on the particle size, refractive indices and the wavelength of the incident light. The calculation of scattering coefficients is not necessary. The scattered intensity represented by the rigorous solution developed by Lorenz and Mie increases with the square of the wavelength. In Rayleigh's solution the wavelength dependency changes to a reciprocal relationship to the power of 4. This means that light with decreasing wavelength will be scattered mainly in back and forward direction instead sideways. This behavior is illustrated in fig 2.2, which shows the scattering distribution of a dipole oscillating in the X-Y-plane. The amount of radiation scattered into

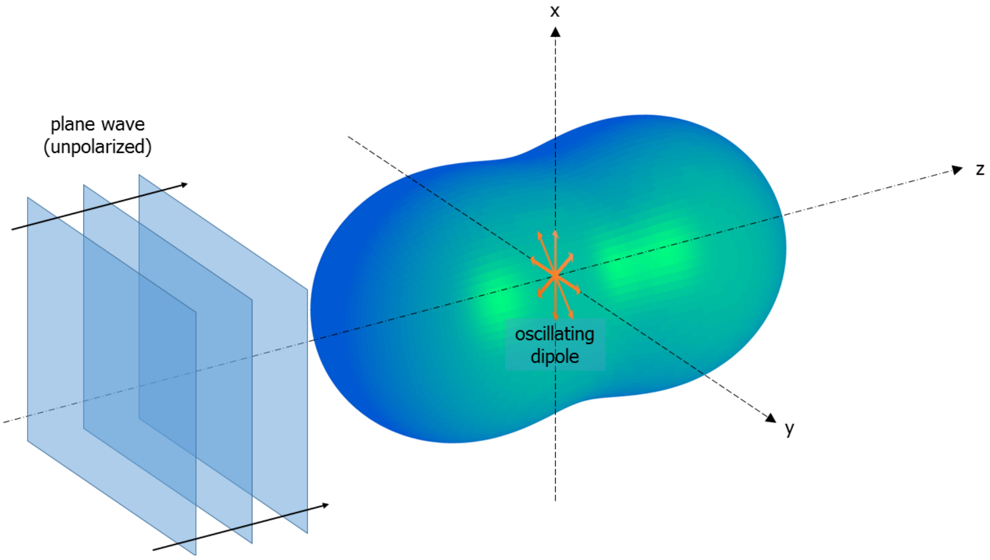

FIGURE 2.2: Scattering distribution of an unpolarized plane wave ($\lambda = 555$ nm) with a spherical particle ($a = 0.1$ μm).

the forward and backward region is the same. The scattering efficiency can be simplified to:

$$Q_{scat} = \frac{C_{scat}}{\pi a^2} = \frac{128\pi^4 a^4}{3\lambda^4}(\frac{n^2-1}{n^2+2})^2. \tag{2.9}$$

If particles are small compared to the wavelength, Rayleigh's approach used for the calculation of the scattering efficiency agrees well with the rigorous results found by Lorenz and Mie [50]. Both efficiencies increase with increasing particle size whereas the rigorous solution converges for large particles. The Rayleigh approach is frequently applied for the calculation of scattering patterns for large molecules and nano particles up to small water droplets.

Spherical particles large compared to the wavelength: Geometrical optics approach (GOA)

If the particle size is significantly larger than the wavelength of the incident light, the geometrical optics approach (GOA) is suitable for the description of the scattering pattern [10, 149]. In this model the incoming plane wave is expressed as a fan of rays. The interaction of a ray with the particle surface is described by use of the vectorial laws of refraction (eq. 2.10) and reflection (eq. 2.11), see fig. 2.3 [96].

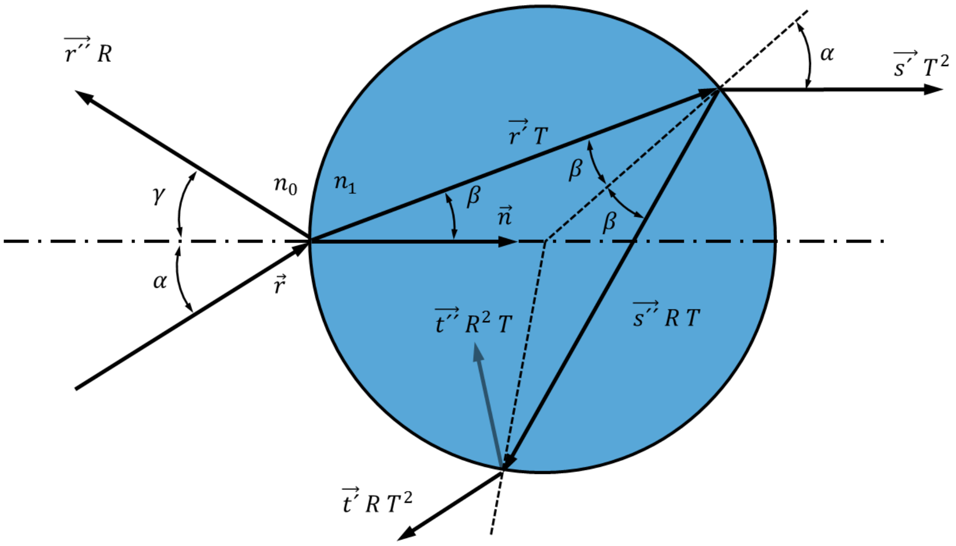

FIGURE 2.3: Reflection and refraction of a ray $\vec{r}$ which is incident on the surface of a spherical particle.

Ray $\vec{r}$ is incident onto a surface at an angle α to the surface normal $\vec{n}$. The surface represents the physical interface formed by the particle and the surrounding medium with the refractive indices n_0 and n_1, respectively. One portion of the incoming ray $\vec{r}$ is refracted into the particle ($\vec{r}'$) whereas another portion is reflected ($\vec{r}''$). Both resulting rays can be described using eq. 2.10 and 2.11.

$$\vec{r}' = \frac{n_0}{n_1}\vec{r} - \vec{n}(\frac{n_0}{n_1}\vec{r}\vec{n} - \sqrt{1 - (\frac{n_0}{n_1})^2(1 - (\vec{n}\vec{r})^2)}) \tag{2.10}$$

$$\vec{r}'' = \vec{r} - 2(\vec{n}\vec{r})\vec{n} \tag{2.11}$$

In compliance with energy conservation, Fresnel's equations [96] are taken into account for each ray-surface interaction. The values R and T in fig. 2.3 are the reflection and transmission coefficients. They result from the amplitude coefficients r and t squared, respectively, see eq. 2.12 to 2.15. The Fresnel coefficients depend on the angle of incidence, the polarization direction of the incoming ray and the refractive indices of both media. The indices s and p denote the polarization direction oriented perpendicular and parallel relative to the plane of incidence.

$$R_s = (r_s)^2 = (\frac{\cos\alpha - \sqrt{(\frac{n_1}{n_0})^2 - (\sin\alpha)^2}}{\cos\alpha + \sqrt{(\frac{n_1}{n_0})^2 - (\sin\alpha)^2}})^2 \tag{2.12}$$

$$R_p = (r_p)^2 = (\frac{(\frac{n_1}{n_0})^2\cos\alpha - \sqrt{(\frac{n_1}{n_0})^2 - (\sin\alpha)^2}}{\cos\alpha + \sqrt{(\frac{n_1}{n_0})^2 - (\sin\alpha)^2}})^2 \tag{2.13}$$

$$T_s = \frac{n_1\cos\beta}{n_0\cos\alpha}(t_s)^2 = \frac{n_1\cos\beta}{n_0 cos\alpha}(\frac{2\cos\alpha}{\cos\alpha + \sqrt{(\frac{n_1}{n_0})^2 - (\sin\alpha)^2}})^2 = 1 - R_s \tag{2.14}$$

$$T_p = \frac{n_1\cos\beta}{n_0\cos\alpha}(t_p)^2 = \frac{n_1\cos\beta}{n_0\cos\alpha}(\frac{2\frac{n_1}{n_0}\cos\alpha}{(\frac{n_1}{n_0})^2\cos\alpha + \sqrt{(\frac{n_1}{n_0})^2 - (\sin\alpha)^2}})^2 = 1 - R_p \tag{2.15}$$

The solid curves for the reflection and transmission coefficients are opposed to each other as can be seen from eq. 2.12 to 2.15. Since surface and bulk scattering are neglected the maximum value of the sum of R and T is equal to one. The dotted curves show the Fresnel coefficients for an interface between optical dense material ($n_1 = 1.5$) and air. Total internal reflection (TIR) occurs at an angle of incidence of 42°.

As indicated in fig. 2.3, the refracted part of the incident ray may experience multiple internal reflections. This can be expressed as an infinite series. The first reflected ray has the intensity of the incoming ray I_0 multiplied by the factor R. All other outgoing ray intensities can be derived from the eq.:

$$I_k = I_0 \sum_{k=1}^{m} T^2 R^{k-1}, \tag{2.16}$$

with k denoting the number of internal ray-surface interactions. For angles of incidence up to 45° the amount of reflected intensity is usually less than 10% of the incident beam, see fig. 2.4. Due to the drop of ray intensities after multiple internal reflections only a finite number of reflected rays (typically 4 to 5 interactions) need to be taken into account in the series.

The scattering efficiency Q_{scat} consists of three parts, the efficiency for diffraction Q_{diff},

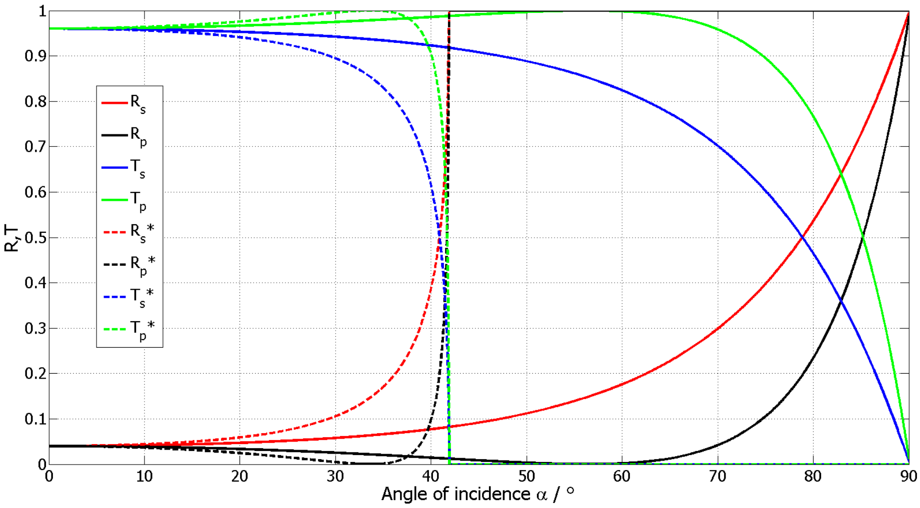

FIGURE 2.4: Fresnel coefficients for reflection and transmission for a physical interface between two media with relative refractive index $m = \frac{n_1}{n_0}$ of 1.5 for solid curves and m = 0.67 for dotted curves plotted against the angle of incidence. Note: at an angle of incidence of 56° (Brewster angle) the parallel polarized component of the reflected ray becomes zero.

external reflection Q_{refl} and transmission Q_{trans} [29].

$$Q_{scat} = Q_{diff} + Q_{refl} + Q_{trans} \tag{2.17}$$

Eq. 2.16 indicates that the efficiency Q_{trans} can be calculated by an infinite series too. To obtain Q_{refl} all incident rays and their first reflected part have to be added up. In all size regimes discussed here, the diffraction efficiency increases the effective cross section of the particle beyond its geometrical borders. That means more energy is scattered by the particle than the light incident on it. This fact is known as the extinction paradox and is discussed in detail in [29, 137, 239]. In sum, the total scattering efficiency has a value of around two. One part of the incident intensity is reflected and transmitted and the other part, same size than the first part, is diffracted at the borders of the particle [137].

In order to obtain the far field scattering pattern, it is necessary to sum up all rays with respect to their direction of propagation, polarization state and intensity whether they are diffracted, refracted or transmitted. The more rays are traced through the particle the higher is the resolution of the scattering distribution. This is the difference to the approaches described above. The non-analytical approach of GOA implies high numerical effort for quantitative results.

However, the great advantage of GOA is the expandability of the model to complex particle shapes and beam geometries which enables the consideration of optical systems and non-analytical beam profiles.

Scattering at non-spherical particles

Light scattering at non-spherical particles has been studied extensively during the past three decades. Detailed insights and overviews are given in [30, 174, 226]. In this subsection a brief overview on the methods and approaches, which can be applied in this context, is given.

In principle, the starting point for the development of a rigorous model is to analytically or numerically solve Maxwell's equations [165]. Even the GOA is connected to a wave optical approach and can be traced back to electro dynamics.

The separation of variables method (SVM) was developed by Oguchi [195] and Yamamoto [8]. The incident, internal and scattered field is expressed as new vector spherical wave function (VSWF) with specific expansion coefficients. These coefficients are calculated analytically by use of boundary conditions for the electromagnetic field at the particles surface. This method enables the simulation of the interaction of light with small particles of spheroidal shape.

The finite element method (FEM) was evolved in the late 70s [177]. The vectorial Helmholtz equation is solved numerically by use of boundary conditions at well-known positions. By discretizing the particle in small volume cells the electromagnetic filed is specified at the nodes and can be calculated for various particle shapes.

Another approach is to describe the particle by use of a sufficient fine grid stretched over its surface. This is called the point matching method (PMM) [195]. Due to limited validity of the PMM, its unknown expansion coefficients are described by additional equations, which finally lead to the generalized PMM [2, 179, 196]. The GPMM is applicable to rotational symmetric anisotropic scatterers of large size.

Yee [286] has chosen another approach. Instead of describing the spatial structure of matter and radiation, he transferred the problem to the time domain. This leads to the finite difference time domain method (FDTDM). Further development [135, 253] has made this method to a powerful and common used simulation, which is freely available [229]. To calculate the electromagnetic field absorbing boundary conditions are applied. By solving the time dependent Maxwell curl equations in discrete time steps the evolution of the electromagnetic field can be described.

If the material of the particle is non-homogeneous, anisotropic or optically active the method of moments (MOM) developed by Harrington [99] is used for the simulation of the external field. The field inside the scatterer is determined by discretizing the particles volume into small cubic cells. Shortly thereafter, the commonly used discrete dipole approximation (DDA) [213] was derived from the MOM. The scatterer is discretized by coupled electromagnetic dipoles. As mentioned in the Rayleigh-scattering approach, the response of a dipole to an excitation is well known. Summing up all dipole contributions the scattered field of a particle can be simulated.

Waterman [273] developed the T-matrix method (TMM) in 1971. Again VSWFs are used to describe the incident and scattered field. The T-matrix itself contains all necessary information about the scatterer, such as its size, shape, orientation and optical properties. Fortunately, the T-matrix has to be calculated once only. That way a known incident field is transformed by a matrix multiplication to the scattered field distribution.

The method of choice strongly depends on the particle characteristics, the required accuracy as well as the available computing power whereas the FDTDM, FEM and TMM are the most commonly used models in stray light calculations. Fig. 2.5 shows the validity of the methods described in this chapter. It becomes clear that some methods are only limited applicable. The advantage of these methods is that they are usually fast and resource friendly. On the other side, several methods exist, which are valid for a broad range of sizes and shapes. The computational effort of these methods is comparatively high.

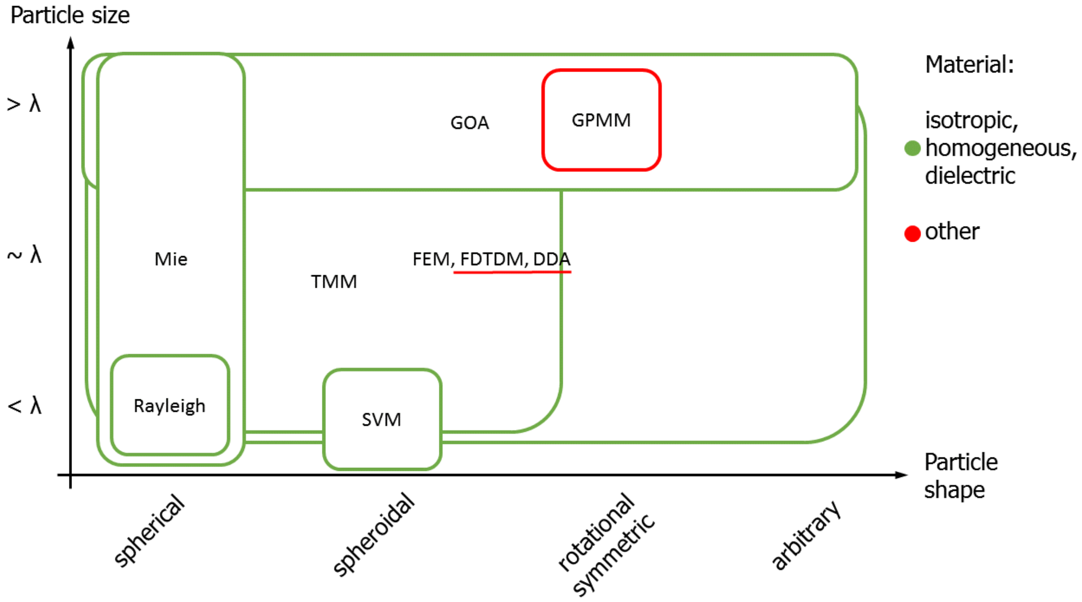

FIGURE 2.5: Validity of methods used for the calculation of the scattering of light.

2.1.2 Optical forces

For the mathematical description of radiation forces one intuitively may use the ray optics model, which describes the interaction of a ray or even a photon with a surface of an object. As shown in fig. 2.5, it becomes clear that this approach is valid for particles large compared to the wavelength. However, the change of a physical value, in this case the change of the direction of propagation of the incident ray is the reason for the momentum transfer. Consider the rigorous description of the light-matter interaction by solving Maxwell's equations, the optical force is introduced by changes of the incident electromagnetic field. Since the electromagnetic field is linked directly to the momentum, the theory of light scattering can be adapted to calculate optical forces [204].

For the rigorous description of optical forces the methods described above are required. Only few approaches, e.g. the TMM or GOA have emerged and are commonly used to simulate optical forces and torque.

The size of the particle and its shape are important factors for choosing a suitable model to calculate optical forces. In the following, two methods are described briefly for the case if the particle size is small or comparable to the wavelength of the incident light. For particles large compared to the wavelength, GOA is discussed in greater extant. This is the method of choice for the optical force simulation used in this thesis.

Particles small compared to the wavelength: Rayleigh approximation

If the particle size is smaller than the wavelength the Rayleigh approximation [14, 98] can be applied. In this model the particle is approximated as an infinitely small dipole induced by the incident electromagnetic field. The forces acting on the particle result from the scattering of the electromagnetic wave and the movement of a point charge due to an electromagnetic field [98].

$$\vec{F}_{scat}(\vec{r}) = \frac{8\pi n_1}{3c_0} k^4 a^6 (\frac{(\frac{n_1}{n_0})^2 - 1}{(\frac{n_1}{n_0})^2 + 2})^2 \tag{2.18}$$

The scattering force $\vec{F}_{scat}$ (eq. 2.18) acts in the direction of the incident electromagnetic wave. The direction is defined by the wave vector $\vec{k}$ and the associated wave number $k = \frac{2\pi}{\lambda}$.

$$\vec{F}_{dipole} = \alpha(\frac{1}{2}\nabla\vec{E}^2 + \frac{d}{dt}(\vec{E} \times \vec{B})) \tag{2.19}$$

Eq. 2.19 represents the Lorenz force $\vec{F}_{dipole}$. α denotes the electric polarizability, which describes the introduction of a dipole moment of an atom or molecule by the electric field $\vec{E}$. $\nabla = \vec{e}_x\frac{d}{dx} + \vec{e}_y\frac{d}{dy} + \vec{e}_z\frac{d}{dz}$ represents the Nabla operator in Cartesian coordinates which is a vector differential operator applied on the electric vector field in eq. 2.19. In the second term the cross × means the vector product of the electric $\vec{E}$ and magnetic field $\vec{B}$. This force acts in the direction of the largest intensity gradient and is oriented perpendicular to the optical axis. Both forces act simultaneously and have to be added vectorially to obtain the net optical force.

Particle sizes similar compared to the wavelength: T-Matrix method

The rigorous solution of Maxwell's equations is required for the simulation of optical forces in this size regime. For arbitrarily shaped particles with non-homogeneous material properties the FEM [275, 276], FDTDM [46, 82] and DDA [238] are commonly used methods to simulate optical tweezers. All of them have large computational requirements but provide accurate results [238]. In contrast, the TMM is quite resource friendly but not applicable to all particle geometries and matter compositions [215]. This method is freely available [185], well documented [173, 187] and briefly discussed in the following.

The TMM has its origin in the Lorenz-Mie theory [151, 170] used for the scattering of plane waves at dielectric spherical particles, as discussed in section 2.1.1. In the late 1970s a rising demand arose for a theoretical description of the interaction of small particles with an incident laser beam [39, 178, 256, 261]. As a result, the LMT was extended to simulate generally shaped beams at arbitrary positions. This is known as the generalized Lorenz-Mie theory (GLMT) [89, 97, 157]. The incident electromagnetic field is analytically approximated as an infinite series of new vector spherical wave functions (VSWF) weighted with expansion coefficients [8, 173, 195, 273]. The VSWFs have to be solutions of the Helmholtz equation [86]. Nieminen et al. published a method in 2003 [187], where they used a least square fit to find a solution, which complies with the Helmholtz equation and has the far field pattern of a highly focused laser beam. The details of this approach are described in [187, 189] and the results are shown below. The incident field U_{inc} can be formulated as:

$$U_{inc} = \sum_{n}^{\infty} a_n \Psi_n^{inc}, \tag{2.20}$$

with a_n as the expansion coefficients of the incident field, Ψ_{inc} is the discrete basis set of functions describing the incident field with their mode index n. The scattered field U_{scat} looks quite similar and can be written as:

$$U_{scat} = \sum_{k}^{\infty} p_k \Psi_k^{scat}, \tag{2.21}$$

with p_k as the expansion coefficients for the field scattered by an optically trapped particle. Finally, the relationship of the expansion coefficients can be described using the T-Matrix T:

$$p_k = \sum_{k}^{\infty} T_{kn} a_n. \tag{2.22}$$

The T-Matrix with its elements T_{kn} characterizes the particle to be optically trapped. Fortunately, the T-Matrix only depends on the size of the particle, its shape, orientation and optical properties and is independent of the the electromagnetic field [186]. For all following calculation steps the T-Matrix can be used in a repetitive manner, which is the advantage of this method. A detailed review of the TMM is given in [188]. Optical forces and torque acting on particles of different shapes are simulated and discussed using the TMM-toolbox [185]. The toolbox is implemented within the programming environment Matlab [163] and is freely available at [185].

Particles large compared to the wavelength: Geometrical optics approach (GOA)

If the particle size is large compared to the wavelength of the incident radiation GOA provides accurate results [10, 18, 35, 40, 81, 109]. This approach is the method of choice used in this thesis.

Beside the simple structure of GOA in terms of handling the propagation of light, the approach is directly compatible to ray optics based system and lens design. In this work the GOA is used in an iterative optical design process for the design and optimization of optical trapping systems. Thus, the fundamentals of this approach are described in detail in this section and the implementation can be found in chapter 3.

A propagating plane wave can be simplified to a ray orientated perpendicular to its wavefront. The ray is defined by its direction. The intensity can be associated with its length and the polarization direction with an additional value. In order to calculate optical forces, the radiation pressure or even better the momentum of the ray has to be considered.

Consider a ray hits the surface of a perfect mirror. The intensity of the ray remains unchanged but the ray direction, denoted by the indices in and out changes. Due to its new direction of propagation, defined by the wave vector $\vec{k}_{out}$, the ray momentum $\vec{p}$ has changed and can be written as:

$$\vec{p}_{out} = N\hbar\vec{k}_{out}. \tag{2.23}$$

N represents the number of photons carried by the ray and $\hbar$ is the reduced Planck constant. In order to keep the conservation of momentum, which is described in Newton's second and third law, the interaction partner of the ray needs to react with an equivalent change of its momentum $\vec{p}_{mirror}$.

$$\vec{p}_{mirror} = \Delta\vec{p} = N\hbar\vec{k}_{in} - N\hbar\vec{k}_{out} = N\hbar(\vec{k}_{in} - \vec{k}_{out}) = N\hbar\vec{k}_{\Delta} \tag{2.24}$$

The magnitude of this momentum can be written as:

$$\Delta p = N\hbar\vec{k}_{\Delta} = N\frac{n_0\hbar\omega}{c} = N\frac{n_0 E}{c}, \tag{2.25}$$

with n_0 for the refractive index of the medium, c is the speed of light, ω is the angular frequency and E defines the photon energy. For the sake of completeness, the momentum associated with the ray is formulated according to Minkowski's definition [172] see eq. 2.25 and not as Abraham [1] did. The eq. of the momentum can be differently defined, which is called the Abraham-Minkowski-controversy and is discussed in detail in [16, 19, 20, 208, 289]. Following Abrahams definition, the refractive index of the medium is written in the denominator of eq. 2.25. Minkowski postulated that the momentum of the ray is transferred to the medium. This means, if the refractive index of the medium increases the transferred momentum of the incident ray raises. Therefore, the refractive index has to be written in the numerator as done in eq. 2.25, which is the most common definition used in the theory of optical tweezers [10, 12, 38, 208]. However, the optical force exerted by the ray on the mirror surface is

$$\vec{F}_{ray} = \frac{n_0}{c}\frac{dE_{ray}}{dt} = \frac{n_0 P_{ray}}{c}\vec{r}. \tag{2.26}$$

P is the power of the ray, which is equivalent to the energy amount of the ray transferred to the surface per unit time and the unit vector $\vec{r}$ defines the direction [10, 40, 221]. In order to calculate the total force, the ray-surface interactions of all rays have to be considered.

Let us assume that a focused laser beam is expressed by three rays 1_a, 2_a and 3_a of equal intensity, as shown in fig. 2.6. The focal point of the beam is located in front of a spherical particle. Behind the focal point the diverging rays interact with the particle surface. For simplification, the number of ray-surface interactions is limited to two. This means a ray hits the particle, interacts with its surface and the refracted part interacts with the particle surface on its back. Furthermore, the reflected parts of the rays 1_a and 3_a are neglected. Hence, just the incoming and outgoing contributions of each ray are considered. The second ray hits the surface perpendicularly. The major part (approximately 90%) of this ray (2_a) is transmitted through the particle in Z-direction without a change of its direction of propagation. On the other hand, the transmitted parts (1_b and 3_b) of ray 1_a and 3_a contain about 80% of the input intensity each. Both rays change their direction of propagation. This is visualized by the two momentum triangles shown in fig. 2.6, which show the momentum of the incident (black) and outgoing (light grey) ray, as well as its changes (dark grey). Finally, applying eq. 2.24 and 2.26 and the interaction of a ray with a particle, shown in fig. 2.3 the net optical

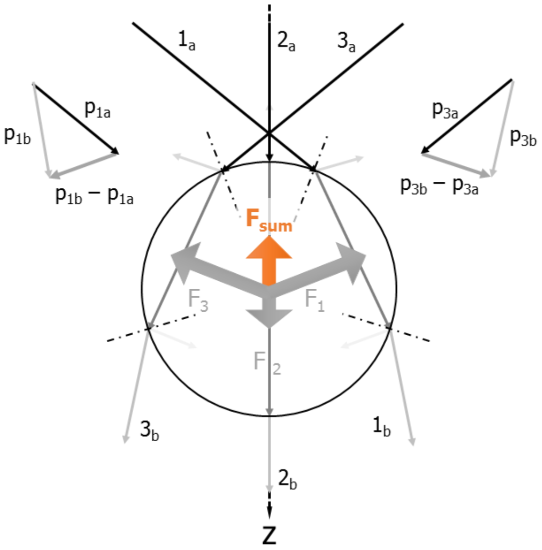

FIGURE 2.6: Interaction of three rays with a spherical particle of refractive index n_1 within the environment characterized by the refractive index $n_0 < n_1$.

force can be written as:

$$\vec{F}_{sum} = \frac{p_{beam}}{3}((\vec{p}_{1a} - T_1^2\vec{p}_{1b}) + (\vec{p}_{3a} - T_3^2\vec{p}_{3b}) + (\vec{p}_{2a} - T_2^2\vec{p}_{2b})). \tag{2.27}$$

The values $\vec{p}_i$ are the unit vectors of the rays and T_i the Fresnel coefficients for transmission. The last element of the sum contributes to a force in Z-direction whereas the other portions of the sum, resulting from ray 1 and 3, contain force components in X-, Y- and negative Z-direction. Due to the axial symmetry of ray 1 and 3 the X- and Y-components cancel each other and just the negative Z-components remain. The sum of all three rays results in a net optical force $\vec{F}_{sum}$ acting on the spherical particle in negative Z-direction. This force accelerates the particle in the backwards direction of the incident beam, as visualized by the orange arrow in fig. 2.6.
Eq. 2.27 as well as fig. 2.3 and fig. 2.6 illustrate the procedure applied in the GOA. Each ray interacting with the particle contributes an associated force. The net optical force is obtained by the summation of all force contributions of each ray-surface interaction. If the particle shape is non-spherical, the equations become more complex since the Fresnel coefficients have to be calculated separately for each ray-surface interaction. Furthermore, if the profile of the incident beam is non-rotationally symmetric or if the beam is affected by aberrations, the number of rays required for a sufficient precise approximation of the beam increases dramatically. These aspects are the key topics of the implementation of GOA and are discussed in detail in chapter 3.

2.1.3 Optical systems and their monochromatic aberrations

Optical elements and systems, no matter what kind suffer from diffraction and optical aberrations, which result in a spread focal area (point spread function - *PSF*) instead of a single geometrical focal point [274]. The origin of these aberrations can be traced back to various sources. Manufacturing related errors of the optical elements cause shape tolerances, surface roughness and microscopic tool marks. They result in deviations of the elements optical function from the designed one [21, 243]. Geometric tolerances of the optical elements mounted in optic holders cause additional deviations. Furthermore, the characteristics of a real beam compared to its theoretical prediction, as well as its propagation through the optical system leads to various additional effects. This list could be easily continued.

In this work the implementation of defects is focused on monochromatic wavefront aberrations [130, 274, 283]. The origin of monochromatic aberrations is due to the nonlinearity of the refraction of rays between two media with refractive indices n_0 and n_1 as described in Snell's law, see eq. 2.28.

$$n_0 \sin(\alpha) = n_1 \sin(\beta) \tag{2.28}$$

The refraction angle β of a ray, which is incident on the surface at the angle α is linked with the refraction indices of the interface and the sine function. This causes a nonlinearity in the relation of both angles to each other. For simplicity, optical systems are often described applying the paraxial model. This model replaces Snell's law with a small-angle approximation, which is valid for rays close to the optical axis. If the angles or the distance from the optical axis increase the errors due to this linear approximation rise [180].

Neglecting diffraction effects, an ideal optical system images all rays originating from an object point to an associated point in the Gaussian image plane (GBE). In order to mathematically describe this fact, each point in the GBE can be considered as the center of a spherical wavefront. Following this model, the optical system ideally converts the spherical wavefront originating from the object point into a spherical wavefront converging to the image point. Optical aberrations will cause deviations of the wavefront curvature leading to non-spherical distorted wavefronts. These deformations can be mathematically described by series expansions, which are well known as Seidel aberrations [49, 130].

To link Seidel aberrations with GOA, as discussed in detail in chapter 3, the optical path difference (*OPD*) and the geometric spot radius (*GEO*) can be utilized. The *OPD* indicates the size of the lead or residue of an aberrated wavefront compared to its ideal. Following Wyant's [283] definition, which is consistent with the results obtained by interferometric measurement techniques, fig. 2.7 illustrates the *OPD* and its sign convention. If the radius of curvature of the aberrated wavefront is small compared to the ideal, the *OPD* is positive (OPD^+). The center of curvature is located in front of the focal point. Consider a wavefront with small curvature (large radius of curvature) compared to the ideal, the *OPD* is negative (OPD^-). The *OPD* can be computed directly using wavefront aberration theory [274]. First, assume rotational symmetric optical systems, as it is the case in conventional optical tweezer setups [74, 183, 267]. This allows the following definition of the wavefront aberration (*WA*) in polar coordinates [274, 283].

$$\begin{aligned} WA(x_0, \rho, \theta) = W_{200} x_0^2 + W_{111} x_0 \rho \cos\theta + W_{020} \rho^2 + W_{040} \rho^2 + W_{131} x_0 \rho^3 \cos\theta \\ + W_{222} x_0^2 \rho^2 \cos^2\theta + W_{220} x_0^2 \rho^2 + W_{311} x_0^3 \rho \cos\theta \end{aligned} \tag{2.29}$$

The value x_0 is the field coordinate normalized to the maximum field position in the image plane. ρ is the radial coordinate normalized to the systems exit pupil. θ is the

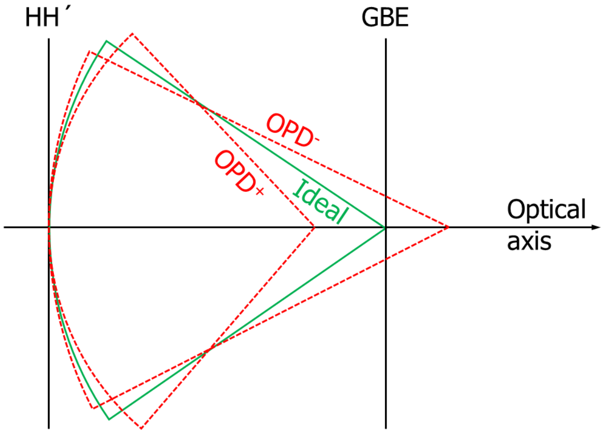

FIGURE 2.7: Definition of the optical path differences (OPD^{+} and OPD^{-}) between the principle planes HH' and GBE.

polar angle. The indices at the wavefront aberrations show the dependency on the power of the coordinates x_0, ρ and the angle θ. The eight elements of the sum are related to *WA*s of unique symmetry and are called piston (W_{200}), tilt (W_{111}), defocus (W_{020}), spherical aberration (W_{040}), coma (W_{131}), astigmatism (W_{222}), field curvature (W_{220}) and distortion (W_{311}).

If the image height is zero, as is the case for on-axis focusing applications, eq. 2.29 can be simplified to field independent *WA*s [283].

$$WA(\rho,\theta) = W_{11}\rho\cos\theta + W_{20}\rho^2 + W_{40}\rho^4 + W_{31}\rho^3\cos\theta + W_{22}\rho^2\cos^2\theta \tag{2.30}$$

Consider a single lens, the outgoing wavefront can be of complex shape depending on design, manufacturing and alignment errors. Apart from the huge number of possible reasons for non-ideal imaging behavior, commonly used lenses and optical systems show well defined aberration patterns. By use of interferometric measurements, these patterns can be identified and used to mathematically describe the optical aberrations and how they affect the optical functionality [274] and the performance of an optical tweezers as well. Equations 2.29 and 2.30 describe the *WA*, which can be directly transferred to the *OPD*. The coefficients W_i are used to scale the *OPD* in wavelength units.

The *OPD* of each ray causes a broadening of the lateral spot size in the image plane. This generates a unique spot pattern for each type of aberration. To achieve a mathematical framework for the spot calculation one has to substitute eq. 2.30 in the natural exponential function. A new value, the wavefront error (*WE*) is obtained.

$$WE(x_0,\rho,\theta) = e^{-i2\pi WA(x_0,\rho,\theta)} \tag{2.31}$$

This eq. transfers the wavefront aberration (*WA*) to a frequency representation oscillating between zero and two π. If the *WA* increases the frequency of the *WE* oscillation rises. To visualize how *WA*s affect the shape and size of the focal point, the point spread function (*PSF*) is convenient to use [243]. The *PSF* can be computed by the Fourier transform of the *WE*.

$$PSF(x,y) = \mathfrak{F}\{WE(\omega)\} = \int WE(\omega)e^{-i2\pi W(x_0,\rho,\theta)}d\omega \tag{2.32}$$

As indicated by its name, the *PSF* describes the response of a signal transferring system to a point like input. Figures 2.8 and 2.9 show single optical aberrations and a combination of them visualized as the *PSF*, *OPD* and the *WE*. All aberrations are computed for on-axis positions, i.e. without the field dependency given by the value x_0 in eq. 2.29. The aberrations, shown in fig. 2.8 are piston, tilt and distortion. All of them cause a linear phase term added to the ideal wavefront. The shape of the wavefront and thus the *PSF* remains unchanged [283]. Due to the field independence of the aberrations discussed here, tilt and distortion seem identical, see eq. 2.29 and fig. 2.8. Apart from the aberrations presented in fig. 2.8, which can be classified to 1^{st} order optical aberrations, higher order aberrations often occur in optical imaging and trapping systems as well. These aberrations are shown in fig. 2.9 and are known as Seidel aberrations [231]. According to their exponential dependencies on the field and radial coordinate x_0 and ρ, as well as the polar angle θ, the higher order aberrations are: astigmatism, defocus, field curvature, spherical aberration and coma. All of them add a non-linear phase term, as visualized by the wavefront error and the associated optical path difference. These aberrations result in a broadening of the focal spot with characteristic patterns.

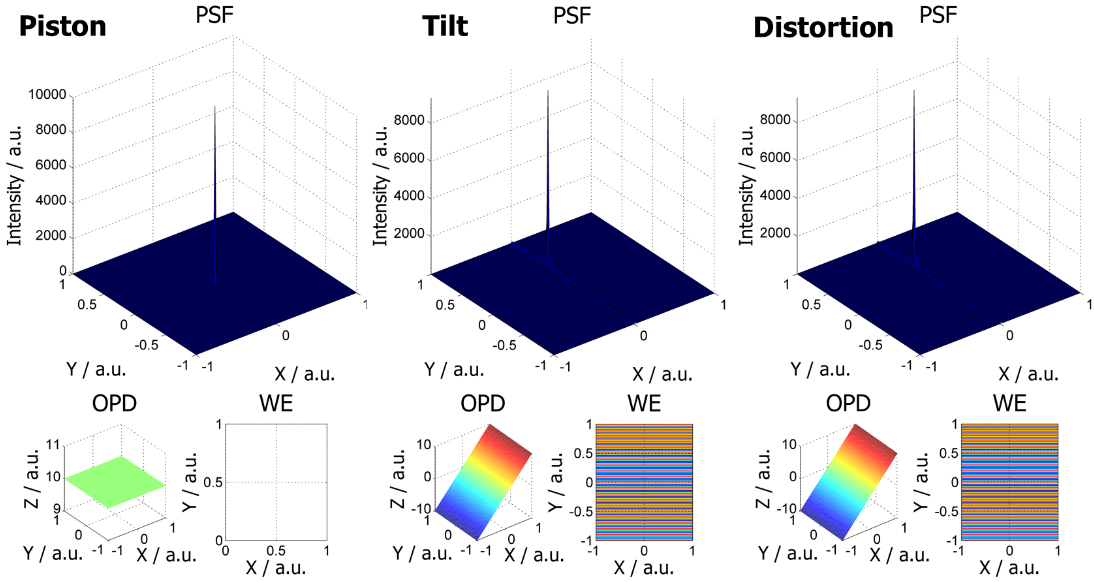

FIGURE 2.8: Optical aberrations, which add a linear phase values to an ideal wavefront.

Astigmatism, for instance, is due to non-perfect axis symmetric optics causing a slightly cylindrical optical phase. This results in wavefronts of different curvatures leaving the optics.

Defocus and field curvature add the same phase term for on-axis points. Defocus can be traced back to an image plane which is axially shifted relative to the focal point. Field curvature has its origin in the nature of curved optical surfaces as most lenses and mirrors have. Assuming a plano-convex lens, the focal length for rays leaving the lens

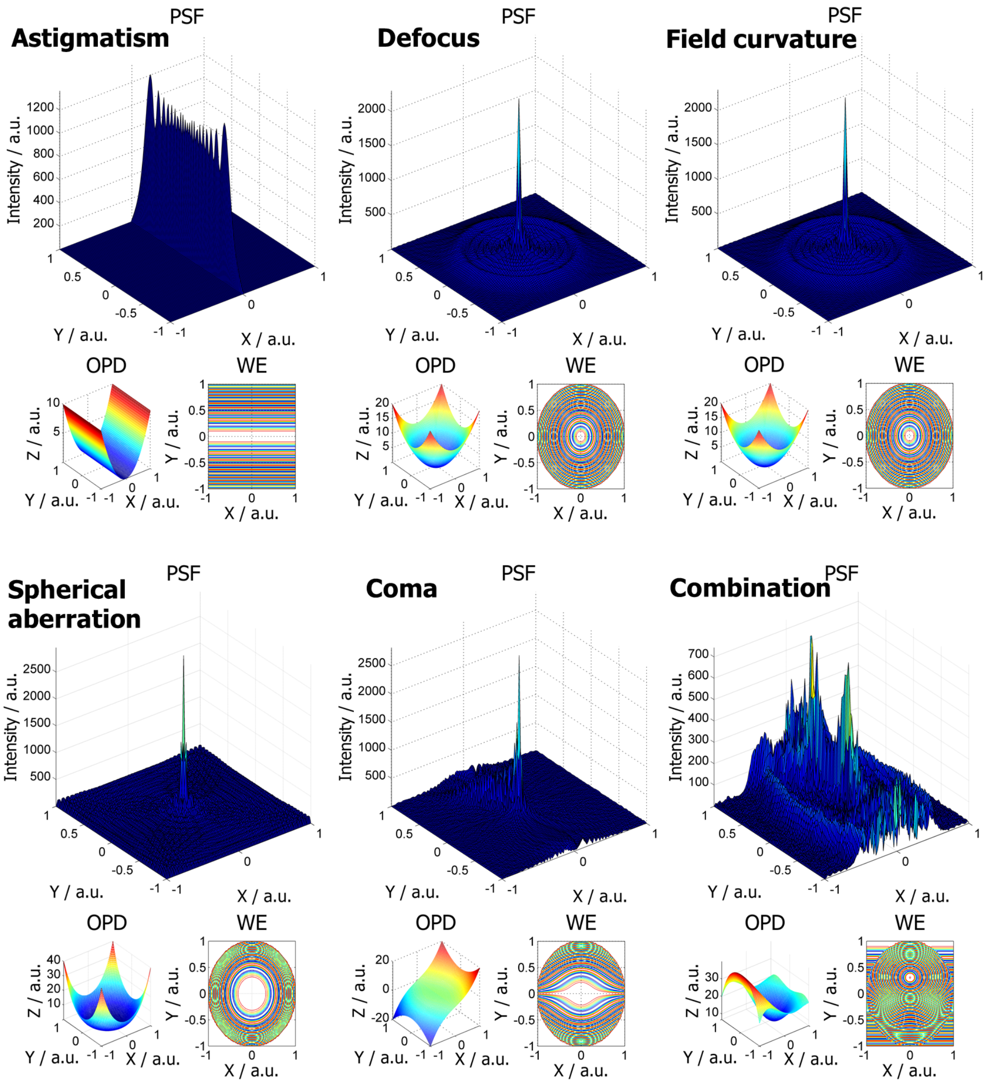

FIGURE 2.9: Optical aberrations (Seidel aberrations), which add a non-linear phase values to an ideal wavefront.

is equal and independent of their field position. To fulfill this relationship, the focal points of all rays need to be positioned on a curved image plane, which is known as the Petzval sphere [93]. The fourth power dependency on the radial coordinate characterizes the spherical aberration. Due to the higher refraction angle of rays exiting a lens at its edges, their intersection points with the optical axis are different. Marginal rays are focused in front of and paraxial rays behind the focal point, which can be determined as the point of least confusion.

The Seidel aberration coma, shown in fig 2.9, has a unique spot pattern. This wavefront error is typical for adjustment related errors caused by tilted or decentered optical elements. The *PSF* looks non-symmetrically and off-axis rays are focused away from the optical axis and form a comets tail like pattern. The last example, given in fig. 2.9, is a combination of aberrations. The *PSF* looks quite chaotic but the *OPD* and the *WE* show symmetric patterns. The *WE* can be experimentally obtained using wavefront sensors like interferometers [23, 167] or other phase measurement setups [210]. The methods available for directly measuring wavefronts and the mathematical description presented in this section enable the investigation of how optical aberrations affect the performance of optical tweezers.

2.2 Optical tweezers

This section gives an overview about the different types of optical tweezers and the optical components necessary for the optical setup. Furthermore, techniques for monitoring particles and cells, as well as methods utilized for force calibration of the optical trap are introduced. The applications optical tweezers are used for are presented afterwards. The last part of this section focuses on the research performed regarding how optical aberrations affect the performance of optical tweezers.

2.2.1 Overview: Setup and types of optical tweezers

The operating principle of optical tweezers is based on the generation of a potential well by meticulously tailoring and focusing a laser beam. If a particle is located close to this well, radiation forces accelerate the particle in the direction of its center. Furthermore, diverse non-optical forces act on the particle ranging from friction, gravity up to forces introduced by Brownian motion. They all form an equilibrium point at a specific position inside the well. In this case one can speak of a stable optical trap since additional forces are required to remove the particle.

Starting with the first experimental investigation of optical forces in 1970 [9] A. Ashkin developed a single beam gradient trap, which was able to hold latex particles in two dimensions inside a test chamber made of glass. Two dimensional trapping means, that the latex spheres are stably trapped in lateral direction (X-Y-plane) but pushed against the glass cell wall to fix them in Z-direction. Due to the small focusing angle no potential well was generated in Z-direction to form a three dimensional trap. Thus, the particles were accelerated in beam direction by radiation pressure. 16 years later [14] Ashkin published the first results of real three dimensional optical trapping using a high NA objective lens (NA=1.25). Up to now, this configuration is commonly used in standard optical tweezer setups [83, 138, 183, 267], see fig. 2.10. Starting with the light source, optical tweezer applications require high energy densities. By the development of the first laser source [159] in the early 1960s this requirement was satisfied. Usually, for optical tweezing applications lasers beams with a Gaussian transverse electromagnetic (TEM_{00}) mode are used [14, 28, 242]. If the object to be optically trapped is a biological specimen the right choice of the wavelength is important. Due to the high transparency of biological cells the near infrared (NIR) spectral range is well suited. For non-biologic applications laser sources of any other emission wavelength (strongly depending on the optical properties of the particle) which provide enough output power are applicable [204]. In general, lasers with an output power in the range of few tens of milliwatts are required to trap and hold a particle [183]. Beside the mostly used TEM_{00}

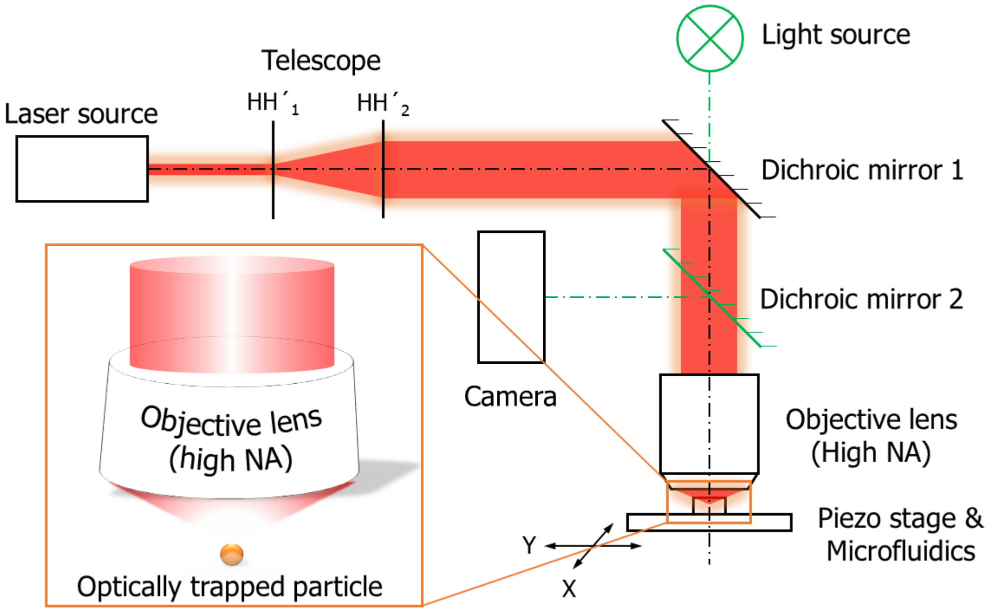

FIGURE 2.10: Sketch of a standard optical tweezers setup with trapping laser source, beam expander and objective lens for high NA focusing to create the optical trap (enlarged view bottom side) and the observation (green) of the trapping volume.

mode higher Laguerre-Gaussian modes, especially the so called Donut mode (TEM_{01}^{*}) are applied in optical tweezer setups [10, 288]. These modes provide higher axial trapping forces [79, 80, 94, 183] compared to laser modes carrying intensity on the optical axis. Furthermore, Laguerre-Gaussian laser beams carry orbital angular momentum [101, 102, 204, 206]. Thus, it is possible to generate torque to an optically trapped particle [101, 204, 228].

Without additional modifications the second device necessary for optical manipulation is a high NA focusing lens, usually an objective lens [14, 183]. Due to the majority of optical trapping applications established in biologic fields [116, 267], the specimen is surrounded by a liquid or suspension. Therefore, immersion objective lenses with NA >1 are commonly used. The high NA is required due to the interplay of scattering and gradient forces. The higher the NA the lower the scattering force. These lenses are commercially available and can be used for both, imaging the specimen and highly focusing the trapping laser beam.

To adapt the diameter of the trapping laser to the input aperture of the objective lens additional optics and devices like beam expanders are integrated into the beam path. Steering optics is used to tune the position of the focus and thus to move an optically trapped object within the sample chamber. If no imaging of the specimen is required, photodiode quadrant detectors are utilized to verify if an object is trapped. In order to characterize the optical trap, see section 2.2.3, this kind of detector is often used to detect oscillations of the particle caused by Brownian motion [5, 183].

The main functions required for optical trapping applications are provided by inverted light microscopes [5, 242, 267]. Minor modifications like the integration of a dichroic mirror for coupling the trapping laser beam into the microscope beam path (see fig. 2.10) or the insertion of optical filters are necessary. Due to the common platform of optical tweezers and light microscopes, as well as the variety of modifications and extensions done in the last three decades, optical tweezers have become a powerful tool with unique properties. One of the most innovative approache used to enhance the functionality of optical tweezers is the application of a spatial light modulator (SLM) [111]. Motivated by the new possibilities (multiple trapping of particles, particle movement and rotation), the phase of the trapping beam can be manipulated in a controlled manner by the integration of SLMs in the optical tweezers setup which was done by several research groups starting in the late 90s [63, 71, 100, 176, 218]. The intensive research on SLM based optical tweezers, known as holographic optical tweezers, enables fascinating opportunities in a wide variety of applications. This is discussed later on in this chapter.

If the application allows a free beam path in one direction another approach can be used. A second focused beam is incident from the opposite direction and compensates the scattering forces introduced by the first optical tweezers. Setups combining two objective lenses to form a stable optical trap are called counter propagating optical tweezers [90, 116, 222]. The idea again can be traced back to A. Ashkin [9]. Two counter-propagating focused laser beams form an equilibrium of optical forces at their interaction point. Instead of using two objective lenses [31, 222] a fiber based tweezers [48, 95] or other setups [209, 279, 292] are possible. Optical trapping setups using counter-propagating beams allow the application of low NA lenses, i.e. for beams converging at relatively small angles. This result in large working distances compared to single beam gradient traps.

Another common approach for the generation of stable optical traps is the application of fibers. The advantages of fiber optical traps are the small size compared to conventional tweezers, the high degree of integration due to the flexible beam guiding and the comparatively low cost. Unfortunately, the realization of sufficiently high focusing angles is challenging [203]. Thus, often counter propagating beams [48, 56, 240] or crossed [47] fiber setups are applied to improve the stability of the trap.

Two dimensional optical manipulation (trapping and movement) is achieved for particles positioned on surfaces [107, 254] or waveguides [148, 291]. In order to overcome the need for more than one optical fiber the geometry of the fiber core and tip is optimized. The aim is to redistribute the intensity away from the optical axis to outer regions of the beam [144, 192, 257].

Optimizing the trapping efficiency in terms of decreasing the size of the focal spot produced by objective lenses, fibers or other optical components is theoretical limited by diffraction effects [86]. This limit can be circumvented with the transition to near-field optical tweezers. First optical manipulation was demonstrated with small particles on a high refractive index surface using total internal reflection (TIR) [124]. In scanning near field optical microscopy the interaction of the fiber tip with the substrate was investigated with regard to optical forces [59, 161, 191]. Further research on evanescent fields and optical forces was realized with waveguides [125, 148] and nanometer sized apertures [197]. Since techniques for micro- and nano- structuring are available nowadays, the specific structuring of surfaces suited for trapping applications is in the focus of intense research [117, 181, 290]. For deeper insight and detailed explanations following review articles are recommended [108, 118, 216, 233].

2.2.2 Measurement techniques for particle detection

Different techniques and methods for the detection and imaging of small particles in the frame work of optical tweezers are presented here. Furthermore, the calibration of optical tweezers by measuring indirectly the optical force is discussed. In general, the detection of the object to be optically trapped with sufficient spatial and temporal resolution is a necessary condition for its analysis and investigations to be performed [183, 267].

For the determination of the lateral position of a micro-sized object coherent and incoherent radiation sources are applied. This leads to different approaches for the signal detection. Consider incoherent illumination, a commonly used method is to image the particle on a quadrant photo diode [76, 175, 237]. Small movements of the particle are transferred to current changes of the photo diodes associated quadrant. This method is able to detect movements in the nanometer range with a high sampling rate (few 100 kHz).

Due to the integration of optical tweezers in light microscopes the imaging of particles is realized with the microscopes objective lens and a CMOS or CCD based imaging sensor. In comparison to photo diodes, standard imaging sensors have low image recording rates (20 to 100 frames per second) depending on the imaging sensor, the kind of connection to the computer as well as the computer itself. High speed cameras are really fast (up to 10000s of frames per second) but quite expensive. The application of digital image processing routines enables subpixel resolution [17] and real time object tracking [41, 52, 88, 128].

An overview about the history of position measurement techniques using coherent light sources is given in [267]. Polarization based interferometry [252] is based on the same principle as differential interference contrast used in microscopy. The circularly polarized trapping beam is subdivided into two parts of orthogonal polarization. Due to the phase function of the trapped object, the polarization of both beams has changed relative to each other. By combining the beams an elliptical polarization state result which contains information about the trapped object.

In the late 90s, the back focal plane interferometry was developed as a result of already utilized methods such as the polarization based interferometry and the quadrant photo diode based particle detection [3, 84, 269]. This technique is based on the detection of the interference pattern caused by the trapping laser and the stray light scattered by the trapped particle. The relative position of the particle to the trapping laser beam can be obtained by this method. Thus, optical forces can be computed directly from these measurements and the knowledge of the particle surrounding.

Finally, three dimensional position detection is obtained by applying the back focal plane interferometry [212, 223] and considering the Gouy phase shift [86]. This phase shift of value π occurs if a Gaussian beam propagates through its waist. The knowledge of the phase difference between the scattered light and the trapping beam can be used to determine the axial position of the particle [223]. Beside this method, several other approaches based on two photon fluorescence [77], evanescent wave fluorescence [43] and others [183, 267] are applied for axial particle position measurements.

2.2.3 Force calibration

Each precision tool has to be characterized and calibrated to provide accurate results. Due to the non-contact working principle of optical tweezers, novel methods were developed and optimized in terms of increasing the accuracy of the position and force measurement [183].

Usually the position and movement of an optically trapped particle contain information about the force and stiffness of the optical trap [267]. The techniques used for force measurements and thus for the calibration can be classified into active or passive working principles. Within a region of a few hundred nanometers the behavior of an optical trap can be approximated by Hooke's law. It states that the force exerted by a spring to an attached weight depends linearly on the distance. This linear dependency is described by the spring constant, which has to be determined in order to characterize the stiffness of the optical trap.

The Brownian motion of small particles in a gaseous or liquid surrounding depends on the size, mass and shape of an object. Furthermore, the characteristics of the entire medium like the viscosity, density and temperature has to be known. If these values are available both, the spring constant and the position of the optical trap can be directly obtained from the particle oscillation (amplitude and frequency) and its power spectrum [24, 37, 58, 85, 267].

The following methods are based on actively influencing the particle position. The determination of the optical trap stiffness can be realized by placing the trapped particle in a laminar flow. Alternatively, the particle can also be pulled slowly through the surrounding medium. Once the particle leaves the trap, the maximum holding force can be calculated from the relative speed of movement and the Stokes' law of friction. Simultaneously, the shift of the particle position due to changes of the relative flow velocity, allows the calculation of the trap stiffness [37, 136, 237].

The information about the optical force exerted on a particle, is also contained in the amount and the angular distribution of the scattered light. The scattering pattern directly results from the momentum transferred to the particle [91, 241, 258]. Deviations from the theoretical assumptions made in this method like the non-ideal Gaussian beam profile, the shape of the particle and non-perfect homogeneous surrounding medium affect the scattering pattern and represent inaccuracies [267]. Another approach to directly measure optical forces and calibrate the trap is to use an additional already calibrated optical trap [220]. Stretching objects with known spring constants like two tethered particles or DNA molecules can be applied as well [220, 272].

Factors, which affect the calibration accuracy, are focus of scientific work up to now. The influence of the distance between the specimen and the cover slip is intensively studied and results in a hydrodynamic correction [78]. Thermal drifts of the mechanical assembly of optical tweezers are studied and compensated [36]. The effect of manufacturing related errors or optical aberrations on the trapping performance is also focus of current research [68, 69, 122].

2.2.4 Applications of optical tweezers

This section gives a brief overview about optical trapping applications. Biology is one of the most important fields for the utilization of optical tweezers. In 1987 [13, 15] A. Ashkin's work was motivated by studies on biological specimen like organelles, viruses and bacteria. The aim was to study the specimen without destroying them. This was made possible by the invention of optical tweezers [9, 14].

Due to the similar components required for optical tweezing and microscopic studies, the merge of both techniques allows the simultaneous manipulation and observation of biological objects. As mentioned earlier, a wavelength in the range of 800 to 1100 nm (NIR) where most biological matter is transparent [251] is suited for optical manipulation. Optical forces can be tuned between few tens of femtonewtons up to hundreds of piconewtons. Together with the principle of contactless force transmission intense research in biological fields was promoted [251, 267].

For instance, the function of the movement mechanism used by cells which is called the molecular motor (Dynein arm: few tens of nanometers in length) was investigated [232]. The possibility to combine optical tweezers with spectroscopic measurement techniques enables the identification of optically trapped cells (2 to 3 μm in diameter) with Raman [285] or fluorescence spectroscopy [34]. As discussed in section 2.1.2, the ability to exert torque on small objects was used to distinguish healthy red blood cells (flat disc with 7 μm in diameter) from those infected with the Malaria virus [62] or to study the cellular invasion with malaria parasite [51]. Also the investigation of the function, structure and genetic code of proteins, nucleic acids and enzymes like the DNA and RNA are focus of intense research [74]. Optical tweezers can also be used for the indirect micromanipulation in terms of moving mechanical micro grippers to trap cells and prevent those from damage caused by laser radiation [6]. More insights in biological applications are given in detailed review papers [183, 246, 251, 267] and text books [11, 116, 204].

In assembly and manufacturing technologies growing demands for contactless positioning of small objects force the utilization of optical tweezers as a tool. The processing of carbon nano-tubes [211], the integration in the assembly procedure of the two photon polymerization processes [112, 132, 200], the support of manufacturing of nano-mechanical systems and structures [106, 262] and the utilization for parallel assembling processes [162] are just few examples. The simultaneously trapping and individual manipulation of several objects in parallel, realized by holographic optical tweezers is used in a variety of applications [53, 65, 100, 140, 145]. Applying this technique, microscopic objects can be positioned precisely within complex and three dimensional structures [166]. Thus, axial positioning without steering optics is possible. Furthermore, the integration of SLMs in the optical tweezers setup enables the introduction of torque to an object. That way, a Gaussian laser beam with TEM_{00} mode can be transferred to a beam carrying torque [92, 204].

Optical trapping in air is quite challenging compared to a liquid environment and was achieved first by Omori and co-workers in 1997 [198]. Due to the low viscosity of gases and the lack of its stabilizing effect on the particle, stable optical trapping is difficult [156, 198]. In addition, the missing buoyancy force results in almost full gravitational forces acting on the particle [198] and the high relative refractive index of the particle and its surrounding increases the scattering force and destabilizes the optical trap [278]. Moreover, the non-homogeneous heating of the particle by the highly focused trapping

laser beam induces photophoretic forces [55, 70], which are significantly larger than the optical forces [234]. Finally, the particle supply is a non-trivial task since the adhesive forces between the particle and another interface are usually in the range of hundreds of nanonewtons [103, 169]. This force value can hardly be overcome with optical tweezers. Great effort is spent on the modification of the surfaces in order to reduce the adhesive forces [169] or on the application of high frequency oscillations e.g. by use of an ultra-sonic transducer [143]. Inspite of these challenges several applications emerged. Successfully optical trapping [120, 168, 169, 198, 217], rotation [147] and transport of particles [234] over long distances (0.5 m) [235] underline the usability of optical tweezers in gaseous surroundings. In addition, the optical trapping of airborne particles enables Raman spectroscopic investigations [205, 271, 278] for single aerosol characterizations.
The demands in the growing field of applications optical tweezers are used for require more customized solutions for the implementation in optical systems. A. Ashkin started in 1986 with standard high NA objective lenses [14] for trapping of particles. In 1999 SLMs were implemented in optical tweezers setups to increase its functionality and efficiency [100, 218]. Up to now, the setup of optical tweezers remains unaffected: The optimization of the system in terms of efficiency enhancement is just done barely. This improvement and the adaption of optical systems to specific optical trapping tasks implies the extension of standard optical design procedures. New merit functions with their scope on optical forces and torque have to be implemented [121]. Thus, integrated design procedures can overcome specific hurdles and may open new fields of applications optical tweezers can be used for.

2.2.5 Effect of optical aberrations on the performance of optical tweezers

Each optical component integrated in the optical trapping system introduces aberrations. The sum of all these non-ideal contributions may result in noticeable negative effects, which made the optical trapping complicated or impossible.
One of the most frequently appearing aberration is due to the refractive index mismatch of the specimen environment and its boundary, a coverslip for instance. The non-linearity of the law for refraction (eq. 2.28) causes spherical aberration [49, 93] as illustrated in fig. 2.11. The green rays represent the ideal wavefront focused in one focal point. Due to the refraction at the glass-water interface (see the inset in fig. 2.11), the rays are refracted and propagate with higher angles (red line) relative to the optical axis. Thus, the focal point is distorted and the steepness of the potential well necessary for optical trapping decreases tremendously. The example, shown in fig. 2.11, is overstated but clearly visualizes the effect of refraction due to the refractive index mismatch.
In 1995 Felgner and coworkers found out that forces introduced by an optical tweezers strongly depend on the distance between the trapping position and the coverslip. If the distance increases the axial trapping efficiency decreases exponentially [75]. Rohrbach and Stelzer [224] developed a wave optics based theoretical model for the simulation of how optical trapping forces, the trap stiffness and the steepness of the potential well are affected by spherical aberrations. The simulation results predict what Fällman [72] found out in experiments performed short time later. By optically trapping using a high NA objective lens and the comparison to trapping realized with low NA lenses, he showed that with increasing distance from the cover slip the influence of spherical

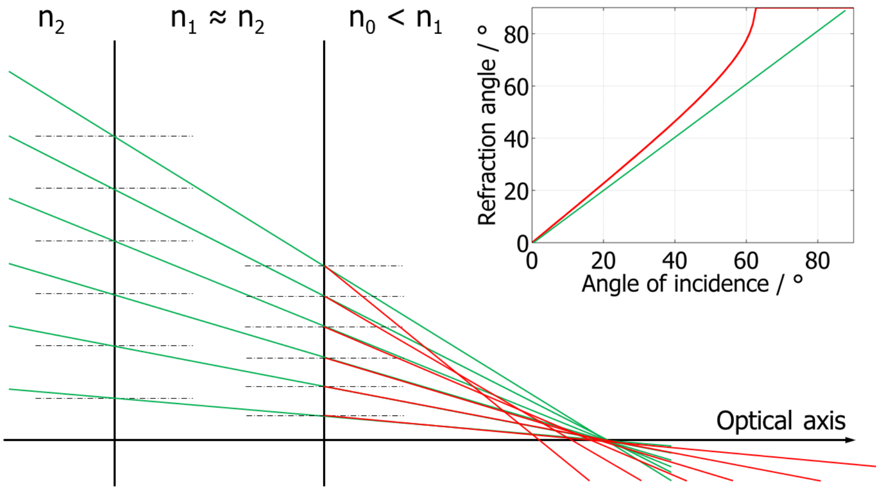

FIGURE 2.11: Spherical aberration due to refraction at the interface between two media glass (n_1=1.5) and water (n_0=1.33), as usual for optical tweezers.

aberrations increase and optical trapping becomes difficult. Due to their optimization low NA lenses are more suited if the trapping depth increases.

The degree of overfilling the aperture of the objective lens with the trapping laser beam is a useful approach to optimize the trapping performance. But the position of the optical trap inside the environment has to be considered for this optimization. Furthermore, if the position of the coverslip changes the axial position of the trap shifts and depends again on the degree of overfilling the aperture, as wells as the kind of the objective lens [72].

Continuing the studies on spherical aberrations, few years later, the trap stiffness was investigated with respect to the applied objective lens for water- and oil-immersion lenses [268]. The optical trap realized with the oil immersion objective lens suffers from spherical aberrations whereas the water-immersion objective lens maintains the trap stiffness, even for larger distances.

Another approach to decrease the effect of spherical aberrations and increase the trapping efficiency is to optimize the refractive index of the immersion medium [219]. A change of the refractive index by 0.01 shifts the axial position of the optical trap by few micrometers. Optical traps, which operate in gaseous surrounding also suffer from spherical aberrations. The reason for this kind of aberration is the jump of the refractive index at the wall of the sample chamber, as well as its distance to the focal point [158, 255]. By tuning the refractive index of the immersion oil, which optically matches the objective lens with the test chamber wall, the optical trap can be stabilized. In addition, the change of the mechanical tube length was used to decrease spherical aberrations, as already done for optical trapping in liquid surroundings [126].

Optical tweezers are also affected by other aberrations, which are common in most optical systems. The aberrations coma, astigmatism and spherical aberration were added to an experimental setup by visualizing the aberrations typical phase function on a SLM display [225]. It was found out that the lateral trapping stiffness is hardly influenced by moderate amounts of aberrations. The compensation of optical aberrations can be

performed either by applying an SLM or, as was done before, by a deformable mirror [202]. This is done by modifying the phase of the trapping laser beam. In addition, the deformable mirror was used to change the axial position of the particle [201].
The frequent application of SLMs in optical tweezer setups allows for the improvement of the trapping efficiency by aberration correction [281]. Using Shack-Hartmann sensors to measure the phase of a distorted wavefront, aberrations can be iteratively minimized by adding the conjugate phase of the distortion on the SLM [150]. This method was enhanced further whereas the software developed to optimize the SLM in combination with a wave front sensor is freely available [32]. Due to the steady improvements of SLMs [134] and other active optical elements, the correction of aberrations, not only in optical tweezing applications [7, 104, 154, 182] achieves even better results [42, 64, 280].
Another approach to optimize the trapping performance is to consider optical aberrations as early as possible, which means in the optical design process. That way the origin of aberrations can be taken into account and considered in the optical design before the systems components are fabricated and assembled [120, 122, 194].

Chapter 3

Methods

This chapter is divided into a theoretical and an experimental part. The simulation of optical forces and its combination with ray based optical design is presented and discussed in the first part. The measurement methods for characterizing the optical components and the whole optical system are introduced in the second part.

3.1 Optical force simulation: Implementation

A focused laser beam can be approximated by a fan of rays. In order to theoretically investigate optical forces and torque introduced by a ray which is incident onto a small object its intersection point has to be known. Tracing the rays through the object and considering each interaction leads to individual momentum transfers between the rays and the object. Summing up over all ray contributions the net optical force and torque acting on the particle results, see section 2.1.2.

3.1.1 Raytracing and general description of an ellipsoid

A ray can be mathematically described by use of a 1^{st} order tensor. The parametric form of a linear equation defines a ray with its starting point $\vec{A}$ and direction $\vec{k}$:

$$\begin{pmatrix} X_x \\ X_y \\ X_z \end{pmatrix} = \begin{pmatrix} A_x \\ A_y \\ A_z \end{pmatrix} + t \begin{pmatrix} k_x \\ k_y \\ k_z \end{pmatrix} \tag{3.1}$$

In order to trace a ray through a defined volume, its environment has to be known and objects acting as possible interaction partners have to be described numerically or analytically. In this work the general description of an ellipsoid is used to define the object, see fig. 3.1. Using this mathematical definition of a closed quadratic surface, different shapes, which are common in nature can be analytically described in an approximated fashion. Starting with a sphere, also oblate, prolate and needle like object shapes can be addressed.

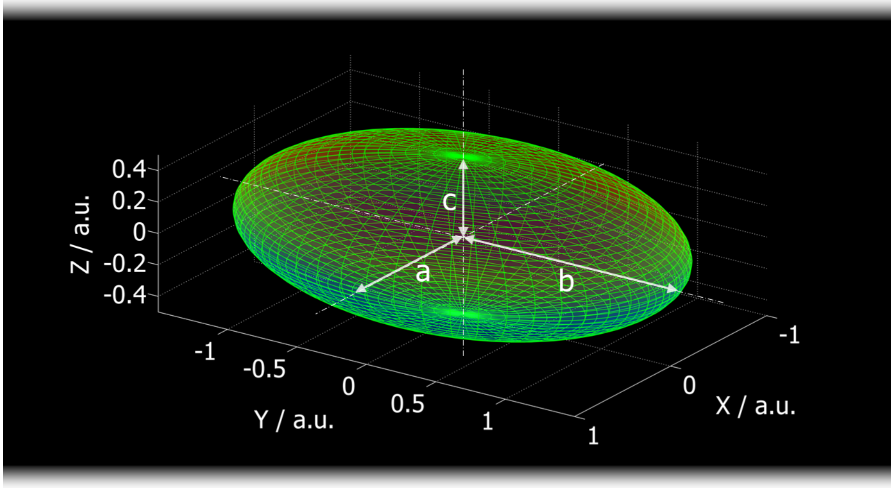

FIGURE 3.1: Ellipsoidally shaped body defined by its semi axes a, b, c in Cartesian coordinates.

The standard equation of an ellipsoidally shaped body in Cartesian coordinates is given by:

$$1 = \frac{(x - M_x)^2}{a^2} + \frac{(y - M_y)^2}{b^2} + \frac{(z - M_z)^2}{c^2} \tag{3.2}$$

with a, b, c as the semi axis of the ellipsoid and M_i as its center. To rotate a geometrically described object its scalar field (Φ) has to be multiplied with the rotation matrix $(R_n(\alpha))$. The scalar field of an ellipsoid can be written as:

$$\Phi = \begin{pmatrix} \frac{(x-M_x)^2}{a^2} \\ \frac{(y-M_y)^2}{b^2} \\ \frac{(z-M_z)^2}{c^2} \end{pmatrix} \tag{3.3}$$

The rotation matrix for a rotation by the angle α around an axis defined with the unit vector $\vec{n} = (n_x, n_y, n_z)^T$ is:

$$R_n(\alpha) = \begin{pmatrix} n_x^2(1-\cos\alpha)+\cos\alpha & n_x n_y(1-\cos\alpha)-n_z\sin\alpha & n_x n_z(1-\cos\alpha)+n_y\sin\alpha \\ n_y n_x(1-\cos\alpha)+n_z\sin\alpha & n_y^2(1-\cos\alpha)+\cos\alpha & n_y n_z(1-\cos\alpha)-n_x\sin\alpha \\ n_z n_x(1-\cos\alpha)-n_y\sin\alpha & n_z n_y(1-\cos\alpha)+n_x\sin\alpha & n_z^2(1-\cos\alpha)+\cos\alpha \end{pmatrix} \tag{3.4}$$

and abbreviated for clarity:

$$R_n(\alpha) = \begin{pmatrix} a_1 & b_1 & c_1 \\ a_2 & b_2 & c_2 \\ a_3 & b_3 & c_3 \end{pmatrix} \tag{3.5}$$

By the multiplication of the ellipsoids scalar field (eq. 3.3) with the rotation matrix (eq. 3.5) the following eq. can be obtained:

$$1 = \begin{pmatrix} \frac{(xa_1+ya_2+za_3)^2}{a^2} \\ \frac{(xb_1+yb_2+zb_3)^2}{b^2} \\ \frac{(xc_1+yc_2+zc_3)^2}{c^2} \end{pmatrix} \tag{3.6}$$

This eq. allows one to analytically describe a two dimensional ellipsoidally shaped surface by selecting the semi axes a, b and c according to the desired shape. The position relative to the origin of the coordinate system can be defined with the values M_x, M_y and M_z defining its center. The orientation of the ellipsoid can be determined with the rotation angle α and the definition of the unit vector $\vec{n}$.

In order to find the intersection points of a ray with the ellipsoid surface the linear equation of a ray (eq. 3.1) has to be substituted in the scalar field of the ellipsoid (eq. 3.6). By applying the solution for quadratic equations the factor t in eq. 3.1 can be calculated. Solving the quadratic equation, the following three cases for the value t can occur. No solution means that the ray does not hit the object, one solution for t stands for one intersection point at the outer limits of the ellipsoid (grazing incidence) and two solutions for t represent two intersection points (entry and exit) of the ray with the ellipsoid. A case discrimination shows which of both intersection points is the first and the second.

If a ray hits the surface it is divided in two parts, a reflected and a refracted component. To calculate the direction of these rays the laws for refraction (eq. 2.10) and reflection (eq. 2.11) have to be applied. In addition, information about the surface of interaction is required. The normal of the surface gives its orientation. Therefore, the gradient of the ellipsoids scalar field has to be calculated. Using three dimensional Cartesian coordinates the gradients components are the partial derivatives of the scalar field Φ, which results in:

$$\nabla\Phi = \begin{pmatrix} \frac{\partial\Phi}{\partial x} \\ \frac{\partial\Phi}{\partial y} \\ \frac{\partial\Phi}{\partial z} \end{pmatrix} = \begin{pmatrix} \frac{2a_1(a_1x+a_2y+a_3z)}{a^2} & \frac{2b_1(b_1x+b_2y+b_3z)}{b^2} & \frac{2c_1(c_1x+c_2y+c_3z)}{c^2} \\ \frac{2a_2(a_1x+a_2y+a_3z)}{a^2} & \frac{2b_2(b_1x+b_2y+b_3z)}{b^2} & \frac{2c_2(c_1x+c_2y+c_3z)}{c^2} \\ \frac{2a_3(a_1x+a_2y+a_3z)}{a^2} & \frac{2b_3(b_1x+b_2y+b_3z)}{b^2} & \frac{2c_3(c_1x+c_2y+c_3z)}{c^2} \end{pmatrix} \tag{3.7}$$

This vector is oriented perpendicular to the ellipsoids surface at the point of intersection. For an incident ray (eq. 3.1) and by substituting the gradient (eq. 3.7) in the vectorial law of refraction (eq. 2.10) and reflection (eq. 2.11) both rays can be calculated. For each ray and its divided parts, the routine has to be repeated.

3.1.2 Calculation of optical forces

In this section the connection of the ray-surface interaction and the transfer of momentum is described. Following the previous sections, the intersection points of a ray with an object, the surface normal at these positions and the refracted and reflected rays are known. Using Fresnel's equations the power associated with each ray can be computed. The optical force caused by an incident ray can now be calculated using eq. 2.26.

Due to multiple interactions of an incident ray with the particle surface, the force calculation has to be developed within an infinite series, as indicated in eq. 2.16 for the ray intensities of the refracted and reflected parts. The contribution of a ray-surface interaction to an optical force acting on the particle can be described step by step. An incident ray carries a force:

$$\vec{F}_{ray} = \frac{n_0 P_{ray}}{c} \frac{\vec{r}}{|\vec{r}|}. \tag{3.8}$$

The reflected part of the incident ray can contribute a force given by:

$$\vec{F}_{refl} = \frac{n_0 R P_{ray}}{c} \frac{\vec{r}''}{|\vec{r}''|}. \tag{3.9}$$

The power of the reflected ray is obtained by weighting the power of the incident ray P_{ray} with the Fresnel coefficient for reflection R. All other optical force contributions belong to the refracted ray, which is divided into an infinite number of internally reflected rays. Those exit the particle again by refraction at the surface. The outgoing rays can be computed by the following series, compare eq. 2.16, with k as the counter for the internal ray-surface interactions.

$$\vec{F}_{trans} = \frac{n_0 P_{ray}}{c} \sum_{k=1}^{m} T^2 R^{k-1} \frac{\vec{r}'_k}{|\vec{r}'_k|} \tag{3.10}$$

Due to the symmetry of the ray paths within a spherical object, the Fresnel coefficients R and T for each ray-surface interaction have to be computed just for the first time and remain the same for all other interactions. In case of non-spherical objects like ellipsoids the coefficients have to be computed for each interaction. Furthermore, if the incident ray is polarized, specific attention must be paid, especially for non-spherical particles. If a ray hits a spherical particle, due to the symmetry given by a sphere the reflected and refracted rays remain in the same plane, as shown in fig. 3.2 a). In this case the polarization direction of the incident ray and its refracted and reflected parts remain the same. If no common plane of the rays exists, see fig 3.2 b), the degree of polarization will change for each ray. The Fresnel coefficients for transmission and reflection depend on the polarization and in consequence on the plane of incidence. Thus, they have to be computed for each interaction. On the other hand, due to the change of the rays local coordinate system for each ray surface interaction, the allocation of the polarization direction with respect to the incident beam has to be considered.
In case of an unpolarized incident ray the total optical force can be computed by:

$$\vec{F}_{tot} = \vec{F}_{ray} - \vec{F}_{refl} - \vec{F}_{trans} = \frac{n_0 P_{ray}}{c} \left(\frac{\vec{r}}{|\vec{r}|} - R_0 \frac{\vec{r}''}{|\vec{r}''|} - \sum_{k=1}^{m} T^2 R^{k-1} \frac{\vec{r}'_k}{|\vec{r}'_k|} \right) \tag{3.11}$$

Consider a polarized ray, two additional terms, one for each polarization direction emerge in equations 3.8 to 3.11. Furthermore, the Fresnel coefficients are now specific for each ray-surface interaction, as indicated by the counter k for internal ray surface interactions.

$$\vec{F}_{tot,s} = \frac{n_0 P_{ray}}{c} \left(\frac{s\vec{r}}{|\vec{r}|} - R_0 \frac{s''\vec{r}''}{|\vec{r}''|} - \sum_{k=1}^{m} T_1 T_{k-1} \frac{s'_k \vec{r}'_k}{|\vec{r}'_k|} \prod R_k^{k-1} \right) \tag{3.12}$$

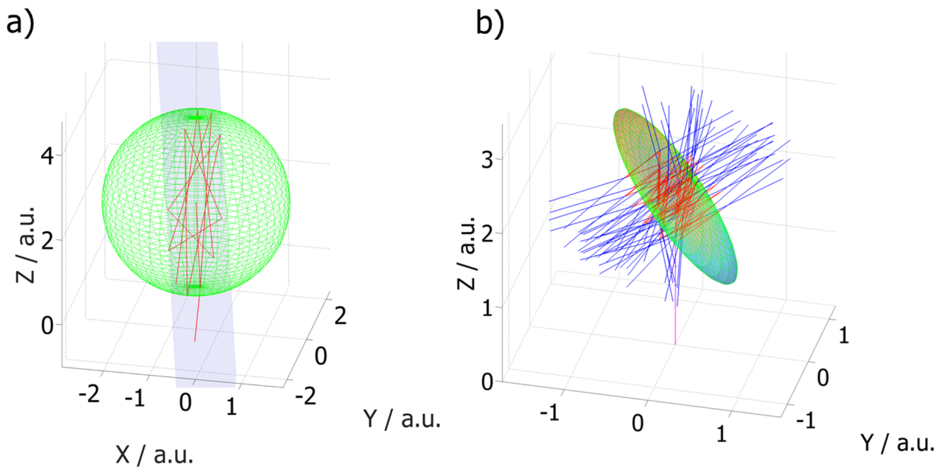

FIGURE 3.2: Multiple internal reflection of a ray that is incident on a spherical particle, all rays stay in the same plane (blue area) a); Multiple interaction of a ray with an ellipsoidally shaped particle without a common plane b).

$$\vec{F}_{tot,p} = \frac{n_0 P_{ray}}{c}\left(\frac{p\vec{r}}{|\vec{r}|} - R_0\frac{p''\vec{r}''}{|\vec{r}''|} - \sum_{k=1}^{m} T_1 T_{k-1}\frac{p'_k\vec{r}'_k}{|\vec{r}'_k|}\prod R_k^{k-1}\right) \tag{3.13}$$

$$\vec{F}_{tot} = \frac{\vec{F}_{tot,s} + \vec{F}_{tot,p}}{2} \tag{3.14}$$

Eq. 3.12 and 3.13 describe the total optical force acting on a particle caused by the s- and p-polarized component of the incident ray. The additional factors s and p compared to eq. 3.11 are due to the change of the polarization direction for each additional part of the incident ray. The Fresnel coefficients depend now on the interaction and are indicated with the counter k. In addition, the coefficient for reflection R has to be multiplied (k-1)-times with its predecessors. Finally, to obtain the overall optical force introduced by the ray fan, one has to sum up over all rays and their interactions with the object surface.

3.1.3 Calculation of optical torque

In order to calculate the total torque acting on a particle the procedure is quite similar to the optical force calculation. In general, torque is introduced to an object if a force acts on it at a point away from its center of mass. The value of the torque $\vec{M}$ can be calculated by the cross product of the external force $\vec{F}$ and the point of action $\vec{r}$.

$$\vec{M} = \vec{r} \times \vec{F} \tag{3.15}$$

Applying eq. 3.15 by substituting eq. 3.12 to 3.14 results in:

$$\begin{aligned}\vec{M}_{tot,s} = \frac{n_0 P_{ray}}{c}((\vec{X}_0 - \vec{X}_M) \times \frac{s\vec{r}}{|\vec{r}|} - (\vec{X}_0 - \vec{X}_M) \times R_0 \frac{s''\vec{r}''}{|\vec{r}''|} - \\ \sum_{k=1}^{m}(\vec{X}_k - \vec{X}_M) \times T_1 T_{k-1} \frac{s'_k \vec{r}'_k}{|\vec{r}'_k|} \prod R_k^{k-1})\end{aligned} \tag{3.16}$$

for rays polarized perpendicular and

$$\begin{aligned}\vec{M}_{tot,p} = \frac{n_0 P_{ray}}{c}((\vec{X}_0 - \vec{X}_M) \times \frac{p\vec{r}}{|\vec{r}|} - (\vec{X}_0 - \vec{X}_M) \times R_0 \frac{p''\vec{r}''}{|\vec{r}''|} - \\ \sum_{k=1}^{m}(\vec{X}_k - \vec{X}_M) \times T_1 T_{k-1} \frac{p'_k \vec{r}'_k}{|\vec{r}'_k|} \prod R_k^{k-1})\end{aligned} \tag{3.17}$$

for rays polarized parallel to the plane of incidence. The values X_k represent the interaction points on the particles surface and X_M is the particle center. The total torque acting on a particle is obtained by:

$$\vec{M}_{tot} = \frac{\vec{M}_{tot,s} + \vec{M}_{tot,p}}{2}. \tag{3.18}$$

Due to the axial symmetry of ellipsoidally shaped objects each point on the surface has the same center of mass whether the shape is spherical, oblate or needle like.

In order to be able to simulate motion dynamics of an optically trapped or manipulated particle its moment of inertia has to be calculated, as well as the contributions of external factors like friction, Brownian motion and other microscopic or macroscopic effects. This is not done in this thesis but the used routine can be extended to this case within the framework of a time resolved kinematic simulation, as done in [35].

3.1.4 Model for the description of optical systems

In this thesis, the model developed for the description of optical systems operates as an interface between the optical design and the optical forces simulation. That way, the effect of changes and modifications of the optical system on the optical trapping capabilities can be simulated directly. Therefore, it is not necessary to describe each optical element or surface of the optical system. This is done by use of commercially available optical design software [146, 287]. Indeed, the wavefront leaving the output aperture of the optical system is the input value for the force simulation and has to be approximated by the model. In terms of GOA the wavefront is represented by a fan of rays. They leave the system and are defined by their intensity, polarization, starting position and direction of propagation.

The intensity distribution and the position of the rays exiting the optical system are described by use of a two dimensional array of pixels. Each pixel contains the information about the intensity of the ray using double precision with 64 bits. The number and size of the pixels determine the position or, more accurately, the starting point of the ray. The polarization of the whole ray fan is described by two numbers, one for each polarization direction. Thus, each ray has its own intensity and starting position but the same polarization state as its neighbours. This approximation is done to reduce the computational effort but if necessary the model can be easily extended to consider e.g. radially polarized beams. Assuming ideal focusing properties, each ray is focused in one global focal point as shown in fig. 3.3. This model allows the approximation

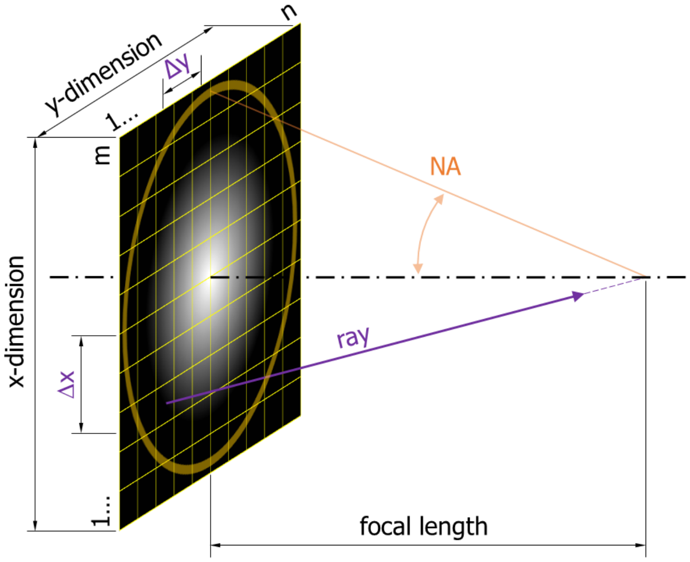

FIGURE 3.3: Approximation of an ideal optical system focusing a Gaussian intensity distribution.

of an arbitrary intensity distribution with sufficiently high sampling resolution. In the present case, all rays are focused ideally in one focal point located on the optical axis. The direction of the optical axis is oriented perpendicularly to the array of pixels. Its lateral position is set to the coordinates $x = \frac{m}{2}$ and $y = \frac{n}{2}$. For specific applications the direction and position of the optical axis with respect to the array of pixels can be varied within the simulation. The direction of propagation of each ray is defined by the coordinates of its associated pixel and the focal length. Similar to eq. 3.1, the mathematical description of the rays can be written as a first order tensor.

$$\begin{pmatrix} Ray_x \\ Ray_y \\ Ray_z \end{pmatrix} = \begin{pmatrix} Pixel_x \\ Pixel_y \\ Pixel_z \end{pmatrix} + t \begin{pmatrix} \frac{m}{2} - Pixel_x \\ \frac{n}{2} - Pixel_y \\ focal\ length \end{pmatrix} \tag{3.19}$$

The maximum NA of the system is determined by the half of the smallest array size, as visualized by the yellow colored circle in fig. 3.3. Rotational symmetry is maintained by choosing the center of the $m \times n$ array as the position of the optical axis. Besides the approximation of arbitrary theoretically calculated intensity distributions the great advantage of this model is the straight forward integration of experimentally obtained measurement data. The pixel size and pitch of the used detector (e.g. CCD or CMOS monochrome/RGB chip) defines the sampling of the array of pixels. The grey/RGB value of each pixel represents the intensity of the corresponding ray. During the measurement the lateral position of the camera chip has to be precisely aligned so that the optical axis is located at the center of the chip. The distance between the camera chip and the focal point is equal to the focal length used as an input value for the optical force simulation.

3.1.5 Implementation of optical aberrations

Optical systems approximated by the model described in the last section are assumed to be ideal. This means, all rays exiting the system are focused in one point located on the optical axis. By the implementation of an additional mathematical quantity, which considers the effect of monochromatic optical aberrations non-ideal optical systems can be approximated in a more detailed manner.
The realistic performance of optical systems can be described by use of aberrated wavefronts. The value and sign of the optical path difference (OPD) determines the curvature of the aberrated wavefront compared to its ideal. The OPD can be written as [284]:

$$\begin{aligned} OPD = coma(\rho^3 \cos\theta) + sph(\rho^2)^2 + focus(\rho^2) + ast(\rho^2(\cos^2\theta)) + \\ tilt(\rho\cos\theta) + pist + field(\rho^2) + dist(\rho\cos\theta). \end{aligned} \tag{3.20}$$

The values *coma*, *sph*, *focus*, *ast*, *tilt*, *pist*, *field* and *dist* represent scaling factors for the strength of the monochromatic optical aberrations coma, spherical aberration, defocus, astigmatism, tilt, piston, field curvature and distortion, respectively. The value ρ is the radial coordinate in the exit pupil and θ is the polar angle.
Consider two points positioned in the exit aperture of the optical system at different heights. If the optical system is assumed to be ideal, both points are focused in one infinitesimal spot located on the optical axis, as visualized in fig. 3.4 with the green rays. Aberrations introduce an *OPD* and as a result the intersection points of the rays with the optical axis are located within an extended area. This area can be defined laterally by the geometrical spot radius (*GEO*) and axially by a focal region, denoted as $\pm\Delta L$. If the height h of the ray starting point located in the exit pupil is large compared to the *GEO* the model works well. As highlighted by the dashed red line, if the height (Δh) is small compared to the *GEO* a negative *OPD* may result in a diverging ray, which never intersects with the optical axis. This has to be considered in the implementation of the optical force simulation. Following ray based optical design software, the quality of an optical system can be defined by spot radii in the image plane (GBE). For instance, a small on-axis spot radius is obtained by an optical system with small aberrations. Monochromatic aberrations like coma, astigmatism, spherical aberration can cause a broadening of the spot area, whereas tilt and distortion lead to a shift of the spot position. The maximum value for the spot size follows from the intersection point of an aberrated ray with the GBE located at the laterally largest distance with respect to the optical axis. Since the *GEO* is determined just by one ray the root mean square (*RMS*) spot size is often used to evaluate the quality of an optical system. The *RMS* represents an averaged value of all intersection point distances in the GBE. Its value can be significantly smaller than *GEO*, but care has to be taken since the *RMS* strongly depends on the ray density and the sampling grid (statistically, hexapolar, Cartesian, etc.) chosen for the pupil plane. The *RMS* is exact for an infinite number of rays traced through the system and gives physical information about the energy density in the focal region. Fig. 3.5 shows the dependency of the *RMS* radius on the ray density using an axial symmetric optical system designed in Zemax [287].

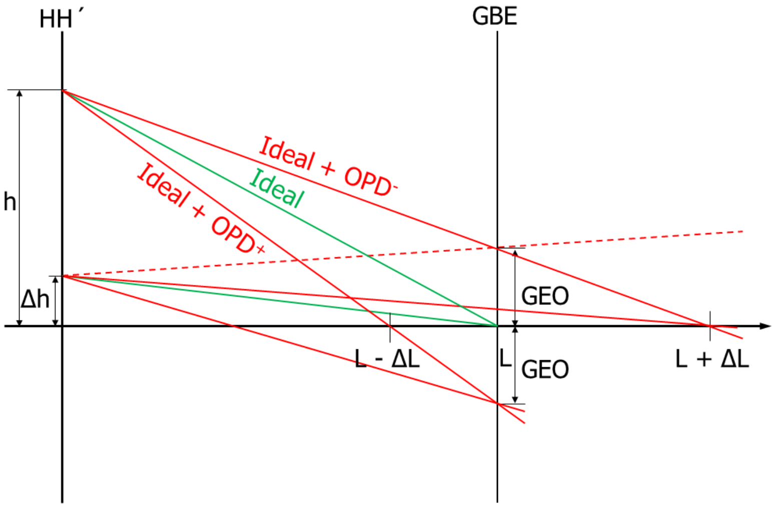

FIGURE 3.4: Consequences of optical aberrations on the optical path difference (*OPD*) and the geometrical spot radius (*GEO*) for two points located in the exit pupil.

All spot diagrams, shown in fig. 3.5, represent the same optical system. The number of the considered rings of the hexapolar pupil raster increases from 3 (fig. 3.5 left) to 30 (fig. 3.5 right). Since the value for the *GEO* remains the same, the *RMS* deviation decreases significantly. The maximum ray density is limited within the optical design software [287] to the value of 200 which results in a value for the *RMS* of 8.4 μm. As a consequence, the computing time also increases with rising ray densities. This has to be considered in the optical force simulation routine as well.

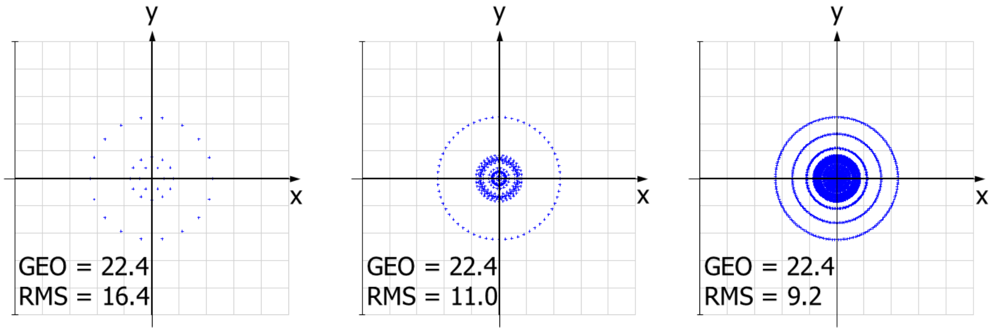

FIGURE 3.5: Decreasing averaged spot size (*RMS*) with increasing ray density (number of rings: 3, 10, 30) using a hexapolar raster in the pupil plane [287]; the units are micrometers.

Due to the strong dependency of the *RMS* error on the ray density, which is directly linked to the sampling of the intensity distribution exiting the optical system, see fig. 3.3, the value of the *GEO* is applied in this work to scale optical aberrations. Furthermore, the Cartesian raster applied for the sampling grid is iso-energetic but may cause a non-symmetrical weighting of the system edges. This would also distort the *RMS* value for off-axis intensity distributions, like the Gaussian TEM_{01}^{*} mode.

For the implementation of optical aberrations to the model described above, the *OPD* is calculated by applying eq. 3.20 to each pixel of the exit pupil. This result in an array of *OPD* values, which is normalized to its maximum value. It has the same dimension and size as the intensity distribution of the system. Thus the *OPD*-matrix contains information on the aberration for each ray or pixel.

Fig. 3.6 shows the geometric and angular relationships for the transformation of the *OPD* to the focal shift $\pm\Delta L$. *GEO* is used as a scaling factor. The focal shift causes a change in the propagation angle of the ray relative to the optical axis and has finally consequences for the momentum transfer. Since the values for the *OPD* are normalized both focal shifts, $\Delta L'$ and ΔL are now scaled with the user-defined maximum spot size *GEO*. Thus, the chosen aberrations, which will affect the ideal optical system result in the typical spot diagram with the specified spot size (*GEO*). The pixel specific value of

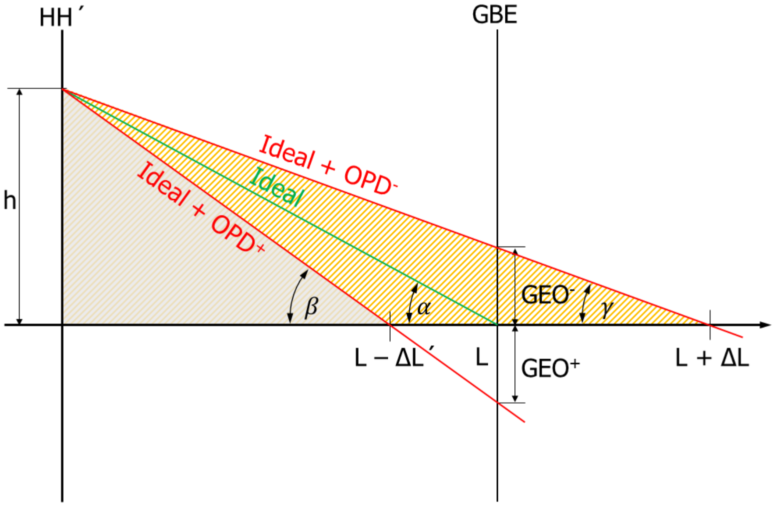

FIGURE 3.6: Geometric and angular relationships used for the integration of optical aberrations to model non-ideal optical systems.

the spot height ($GEO^{\pm}_{pixel}$) in the GBE is obtained by applying the intercept theorem to the geometric relationships, shown in fig. 3.6.

$$GEO_{+}(pixel) = \sqrt{(L - \frac{L}{\frac{\rho_{pixel}}{GEO} - 1})^2 + \rho^2} - \sqrt{\rho_{pixel}^2 + L^2} \tag{3.21}$$

$$GEO_{-}(pixel) = \sqrt{(L + \frac{L}{\frac{\rho_{pixel}}{GEO} - 1})^2 + \rho^2} - \sqrt{\rho_{pixel}^2 + L^2} \tag{3.22}$$

Now the starting point of a ray associated to a pixel in the exit pupil with height h is known. The value $GEO^{\pm}_{pixel}$ determines the intersection point of the ray with the GBE. The unknown negative focal shift $-\Delta L'$ can be obtained using the grey triangle, shown in fig. 3.6. It forms the geometric relationship between the pixel height h, the positive OPD^{+} and the resulting focal shift $-\Delta L'$. Applying the Pythagorean theorem and the solution for quadratic equations the negative focal shift can be expressed as:

$$-\Delta L'_{pixel,1/2} = L \pm \sqrt{L^2 + GEO_+(pixel)(2\sqrt{\rho^2 + L^2} + GEO_+(pixel))} \tag{3.23}$$

$$\Delta L'_{pixel,1/2} = -L \pm \sqrt{L^2 + GEO_-(pixel)(2\sqrt{\rho^2 + L^2} + GEO_-(pixel))}. \tag{3.24}$$

Eq. 3.23 and 3.24 are used to add pixel specific focal shifts to the focusing properties of the optical system. Those cause in sum a spot diagram with characteristic spot pattern and the desired maximum spot size *GEO*.

It might be confusing to choose the kind of the optical aberration as input variables and *GEO* to scale them. In general, the coefficients W_{ijk} used in eq. 2.29 and 2.30 scale the optical aberrations and have the unit of the wavelength [284]. This makes sense in wavefront measurement techniques using interferometers [87] since the results are encoded modulo two π. In this work the focal spot is measured using a CMOS camera positioned in the focal plane. In this case the value *GEO* follows directly from the measurement and the shape of the spot gives information about the kind of aberrations.

3.1.6 Optical force simulation

To summarize the last sections, for ray optics based force simulation a ray tracing routine propagates rays through the object to be trapped. The optical system is described with a two dimensional array of pixels placed at its exit pupil. Since the optical axis is positioned in the center of the array the NA is defined by the array edge and the focal length. To approximate optical aberrations, the focal length is modified with a focal shift scaled by the spot size *GEO*. By using the general description of an ellipsoidal body the particle is positioned initially at the focal point. Applying the vectorial law for refraction (2.10) and reflection (2.11) as well as Fresnel's equations (eq. 2.12 to 2.15) at the interaction points, the momentum transfer between the rays and the particle can be calculated. Finally, using eq. 3.14 and 3.18 optical forces and torque acting on the particle can be computed.

In order to simulate optical tweezers, detailed knowledge about the forces acting in the immediate surrounding of the focal area is required. To this end the particle is virtually placed at several positions distributed on a sufficiently tight grid around the focal area. For each position optical forces and torques are simulated by tracing all rays of the optical system through the focal region. That way a three dimensional array of optical forces and torques around the central trapping position is obtained. For particle positions located far from the focal region the number of ray-particle interactions usually decrease. This means less computational effort to create large force maps compared to those simulated with higher sampling rate and smaller size. If the intensity distribution exiting the optical system is rotationally symmetric to the optical axis it is convenient to reduce the optical force matrix dimension to a two dimensional description. This significantly reduces the computational effort. To give a rough estimation; if the intensity distribution is sampled by an array of 100 times 100 pixels and if the raytracing routine considers four internal ray-surface interactions 110000 rays have to be calculated. To describe the neighborhood of the focal point with a three dimensional grid applying 40 points for each dimension 7.04 billion rays have to be traced in total. This huge number requires high computational power to be solved within a short time span. This

can be reduced by a massive parallelization of the routine that allows the computation of single rays on multicore graphics processing units (GPUs) as done in many optics simulations [73, 119, 164, 227, 249]. This is not done in this work but should be noted as a starting point for further optimizations. The reduction of the problem to a two dimensional description reduces the number of rays to a maximum value of 176 million which is easily manageable by use of current computer technology.
Consider a standard optical tweezers application, a spherical particle placed in a liquid environment has to be optically trapped. The parameters for such an optical force simulation are given in tab. 3.1.

Table 3.1: Parameters used for the optical force simulation.

Shape	Diameter	Material	Medium	Int. dist.	Laser power	NA	GEO
spherical	10 μm	PMMA	H_2O	TEM_{00}	50 mW	1.3	1 μm

Using these input parameters, the routine calculates optical forces for each desired particle position. The output is given as a two dimensional force map in Z- and X-direction, see fig. 3.7. Each black cross is linked with a red line representing the result of the optical force simulation at this position. The direction of the red line shows the direction of the force acting on the particle (green object) that is placed with its center of mass on the black cross. The length of the line indicates the amount of the optical force.

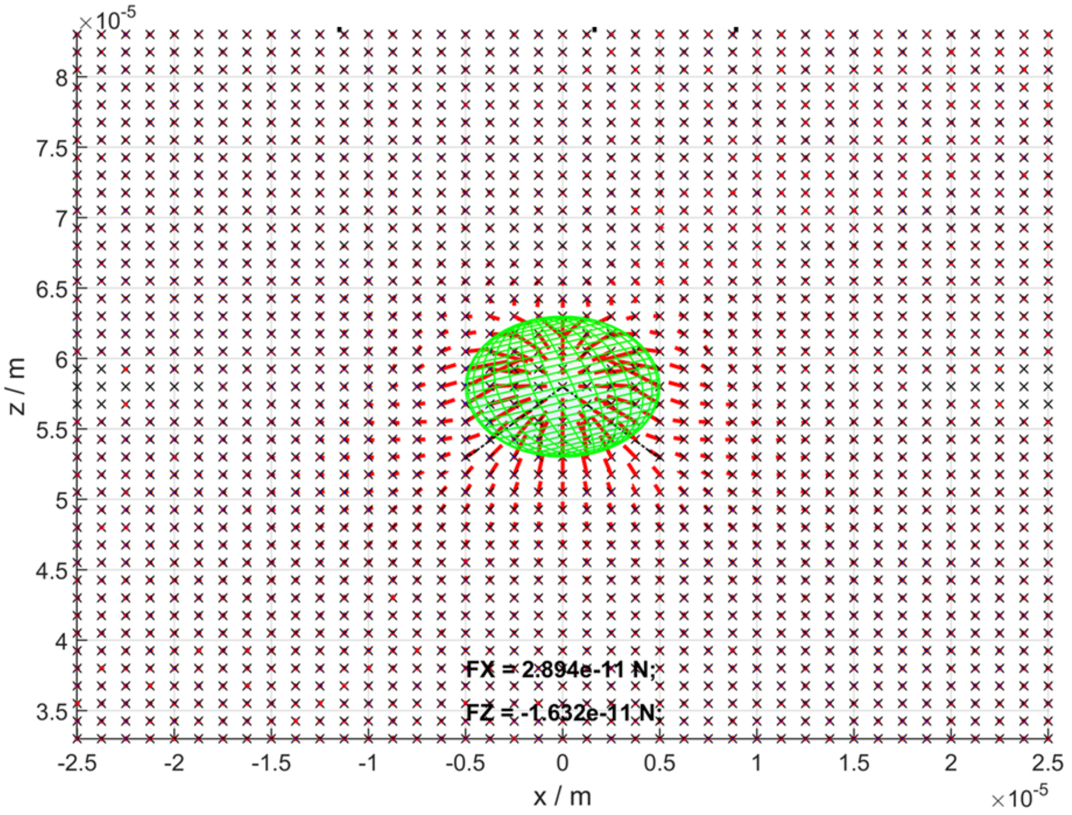

Figure 3.7: Two dimensional map showing optical forces for 40 times 40 particle positions using a resolution of 1.25 μm.

As suggested from the pattern formed by the red lines, the optical forces are concentrated to the focal point marked with the two black lines. They visualize the focal point with a focusing angle of 77.8° for a NA of 1.3. The maximum optical force acting on the particle in negative Z-direction is $F_{-z} = 16$ pN and in X-direction $F_x = 29$ pN. Since the particle is placed in a liquid environment its buoyancy leads to a net gravity force of less than one pinconewton. Thus, the particle can be optically trapped and held stably from any direction. This is visualized in fig. 3.8, showing cross sections along the optical and the X-axis of the force map presented in fig. 3.7. Both diagrams show optical forces acting on the particle positioned on a grid in the direct neighborhood of the focal point. If the particle is placed on the optical axis in front of the focal spot (positive forces in fig. 3.8 left), the particle is pushed in positive Z-direction until it reaches the close proximity of the focal point. Due to the forces acting in negative Z-direction the particle is pulled backwards (negative forces in fig. 3.8 left) if it is placed further back. Neglecting gravity, the particle is held stably at the equilibrium point between positive and negative optical force components. The same principle can be applied for the optical forces acting in lateral (F_x) direction, see the force diagram right in fig. 3.8. Within a range of ±5 μm around the optical axis, the particle is pushed to the equilibrium point. If the particle is located within this the region it will be accelerated in the direction of the focal point and thereby to the position of the optical trap. On the other hand, if the particle is placed outside this region it will be pushed away from the optical trap.

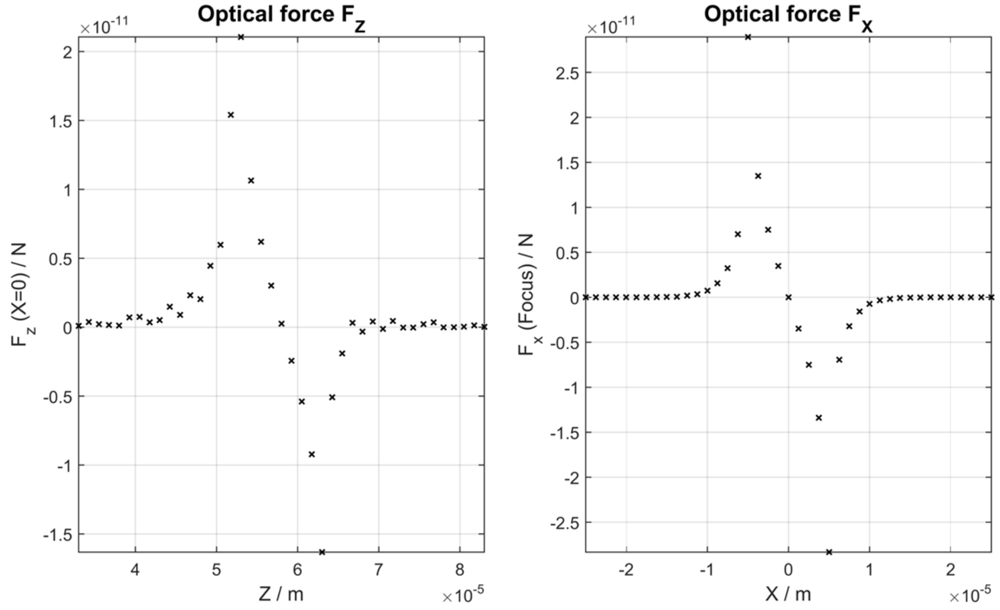

FIGURE 3.8: Sections along the optical axis at $X = 0$ (left) and along the X-axis at $Z = 58$ μm (right) showing optical forces acting in Z- and X-direction, respectively (liquid surrounding medium).

A stable optical trap should always show a force curve shape as visualized in fig. 3.8. Consider all three dimensions, the point of zero crossing optical forces has to be enclosed by high force peaks with positive and negative sign. Furthermore, the attracting force,

optical tweezers are known for, is achieved with optical force components acting in negative Z-direction, that means in the opposite direction of the incident light.
In the previous example the PMMA particle is suspended in a liquid surrounding. This leads to a comparatively small relative refractive index of $n_{rel}=\frac{n_{particle}}{n_{medium}}=1.11$. If the particle is placed in air, the relative index of refraction increases. Keeping the focusing angle the same, leads to an increase of the refraction angles and thus the amount of momentum transferred from the light to the particle raise. Accordingly, the optical forces achieved with the same input parameters as given in tab. 3.1 (except the surrounding medium) are noticeably larger, see fig. 3.9. The optical force achieved in X-direction is

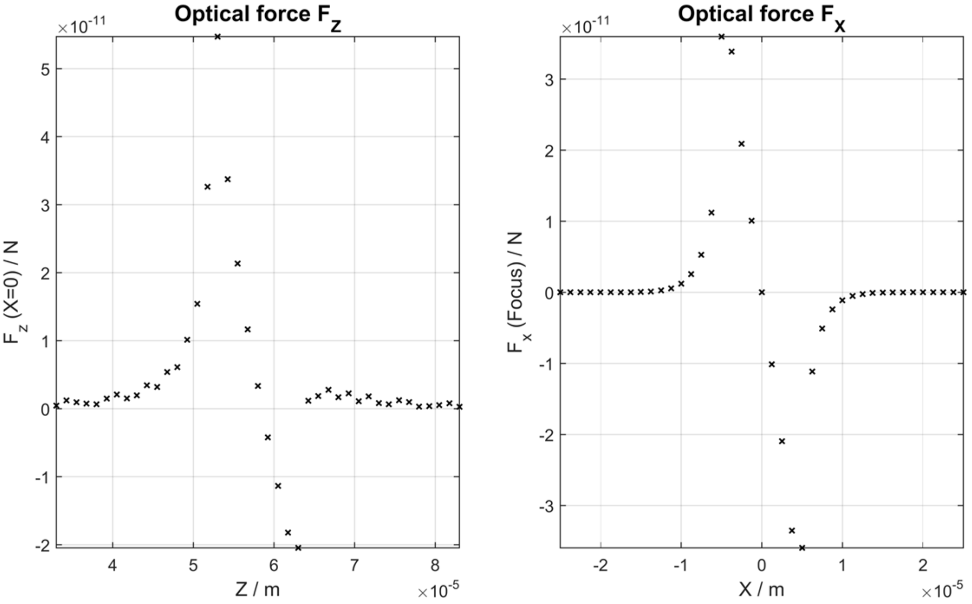

FIGURE 3.9: Optical forces acting in Z-(left) and X-(right) direction using similar input parameters as given in tab. 3.1, (gaseous surrounding medium).

increased to $F_x = 35$ pN ($F_{x,H_2O} = 29$ pN) and in negative Z-direction to $F_{-z} = 20$ pN ($F_{-z,H_2O} = 16$ pN). Furthermore, the forces acting in positive Z-direction are twice as high compared to a liquid surrounding. This makes optical trapping more challenging because the particle is accelerated towards the focal point and may have too much kinetic energy to be stopped by the retro driving optical force. Furthermore, the photophoretic force contributes an additional force component in positive Z-direction (section 2.2.4) which affects the trapping curve shape but is not considered by the applied optical force simulation. In contrast, the optical forces acting in X-direction, see fig. 3.9 right, are symmetrically distributed around the optical axis and generate again a stable optical trap. This illustrates, the orientation of the optical trap relative to the gravity or other external forces has to be taken into account as well.
In both scenarios discussed above, the object to be trapped is assumed to be of spherical shape. If the material of the particle is not birefringent the net torque generated by an optical tweezers using a laser beam of TEM_{00} mode is zero [155, 270]. Suppose that the particle to be trapped is not spherical and is placed in the surrounding of the optical trap slightly tilted. The axes of symmetry of the particle do not coincide with the global

coordinate system of the optical trap. Hence torque is introduced to the particle and it starts to rotate until a symmetric orientation is reached.

In the following example the object is ellipsoidally shaped and again made of PMMA. Two of its semi axes are 5 μm and the third has a length of 12.5 μm. In addition, the long axis is orientated along the optical axis but rotated around the X-axis by 30°. All other parameters are the same as given in tab. 3.1. The relative position in space is visualized in fig. 3.10. The red lines represent once again the optical force acting on the object placed with its center of mass at the position of the cross. Despite its ellipsoidal shape the object is pushed to the focal point and will be stably held. However, the blue lines visualize the axis of rotation and their length indicates the strength of the optical torque. The majority of them show in positive X-direction whereas the object is oriented with its tip diagonally down, see the three dimensional inset in fig. 3.10. Applying the right-hand-rule to the blue lines one could imagine that the ellipsoid experiences a torque which rotates it back in the X-Z-plane. As soon as the particle is oriented along the optical axis the net optical torque becomes zero and it is stably held in this orientation and at this position.

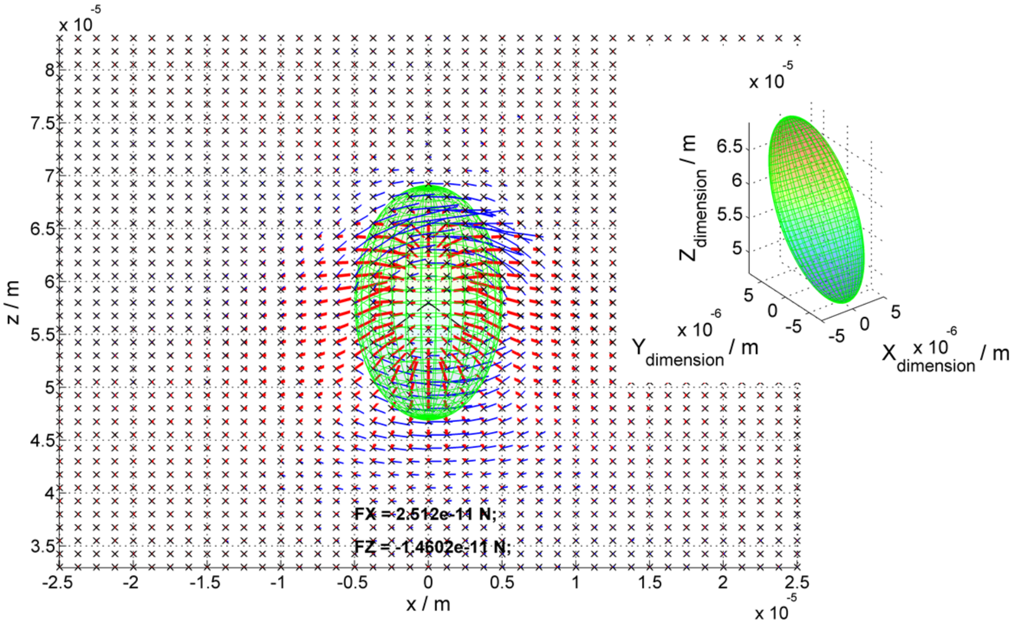

Figure 3.10: Optical forces and torque introduced to an ellipsoidal object with semi axes $a = b = 5$ μm and $c = 12.5$ μm rotated by 30° around the X-axis.

The simulation routine presented in this section is used later on in chapter 4 to discuss the influence of several input parameters like the intensity distribution in the exit pupil, the NA, optical aberrations, etc. to the optical forces. Finally, the simulation is used as a tool in the optical design process.

3.2 Iterative optical design process

In this section the process of the development of an optical tweezers is described. Starting from the application and its goal concepts are derived and transferred to optical start systems used for the design process. Optimizing both optical systems in order to maximize the ratio of force per laser power, the final optical tweezer systems are developed to be highly efficient and adapted to the application.

3.2.1 Building the start system

At the beginning of each optical design process stands the application and the demand the optics has to fulfil. In optical trapping applications usually the goal is to optically trap and hold microscopic objects. To generate first concepts, essential boundary conditions and requirements are deduced from the intended application. Defined specifications are useful in order to not start the development from scratch but rather relate to an existing solution and optimize it. Furthermore, the reduction of the optical functionality to the essentials necessary for optical trapping may result in a highly adapted and efficient optical tweezers. Tab. 3.2 lists important parameters, which have to be known to find suitable concepts for getting started with the optical development process. Once the concepts are assessed they can be transferred to the optical design process. Assume that the optical trapping application is similar to the example considered for optical force simulation in section 3.1.6. This example is selected due to its similarity with conventional optical tweezers applications [183, 267]. It can be summarized by the following specifications according to tab. 3.2. The surrounding medium is liquid assuming a refractive index of 1.33. The environment the particle is embedded is a microfluidic channel with a wall thickness of less than 170 μm. Optical trapping is planned to be close to the wall-liquid interface. The object to be trapped has a spherical shape with 10 μm in diameter. It is made of PMMA or fused silica, assuming isotropic and dielectric material conditions. The 2D/3D movement of the object should be possible within a two dimensional field of 500 μm side length. The number of objects to be optically

Table 3.2: Specifications of optical trapping systems.

Surrounding medium	Environment	Object to be trapped	2D/3D Movement of object	Number of objects to be trapped	Rotation of object
Gaseous	Trapping chamber	Size	No	Single (on axis trapping)	No (symmetric beam
Liquid	Wall thickness	Shape	Yes (time multiplexing, spatial multiplexing)	Several (time multiplexing, spatial multiplexing)	Yes (polarization, angular optical momentum)
Vacuum	Working distance	Material	-	-	-

trapped is one. According to the last column of tab. 3.2 the rotation of the object is not intended. Finally, the particle has to be observable within the full field as claimed for optical manipulation.

Based on these specifications one can start with a simple concept, containing all important components like the trapping laser source, beam preparation, steering and shaping optics, high NA focusing and observation optics [183, 242].

But in the end, optical trapping is realized by highly focusing an incident laser beam. Due to the liquid surrounding a trapping chamber is required. This is planned to have walls of thickness less than 170 μm, which allows the application of standard high NA immersion objective lenses. Since the working distance is close to the interface, oil immersion objective lenses can be used [22]. They are corrected for microscopic imaging in liquid media within a large field of view and they provide high focusing angles. As laser source a Nd-YAG (neodymium doped yttrium aluminum garnet) solid state laser with an emission wavelength of 1064 nm and Gaussian intensity profile can be used [25, 236, 260]. Thus biological specimen can be optically manipulated as well [138, 183, 184, 207]. For the movement of the particle within the microfluidic channel, the whole sample chamber can be precisely moved utilizing a piezoelectric stage [131, 183, 266]. Finally, for the observation task the same objective lens as applied for the generation of the optical trap can be used. By introducing an additional illumination source coupled into the beam path with a dichroic mirror the observation can be performed with a camera positioned in the image plane of the objective lens. The concept shown in fig. 3.11, illustrates an optical setup suited for optical trapping and observation of the specimen in parallel. Due to the demand of imaging the same field in the image plane as used for optical trapping a standard objective lens is chosen. If the simultaneous observation is not important, the focusing optics can be designed itself with respect to an optimization in terms of high optical trapping efficiency neglecting the imaging function. In the present case other options for optimizing the trapping efficiency have to be found. For instance, a beam shaping element can be introduced behind the telescope optics. This could be a diffractive optical element used for optimizing the intensity distribution of the beam.

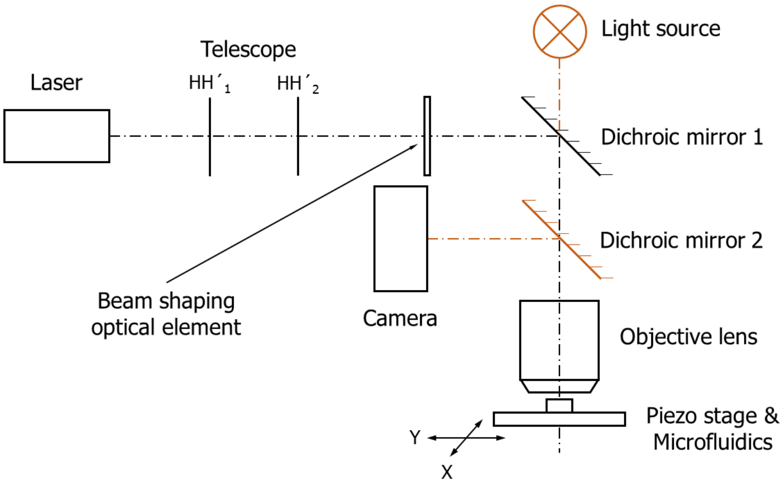

FIGURE 3.11: First concept deduced from the specification of an optical tweezers for trapping inside a microfluidic channel.

In the next step the system can be modeled in the optical design software. In this work Zemax [287] is used for optical design. By applying standard optical components for the assembly of the optical system low costs are maintained. Optimizing the system in terms of small spot sizes within a field of one times one millimeter provides sufficient trapping forces in the desired trapping region.

For the verification of the optical forces theoretically achievable with this system, the intensity distribution in the exit pupil is exported as a two dimensional array of pixels, see section 3.1.4. This array, the focal length and the value for the maximum spot size (GEO), as well as estimations regarding the kind of optical aberration are applied as input for the optical force simulation. By optimizing these parameters in terms of a maximum ratio of force per photon, the optical design software and the force simulation are used in an iterative manner. That way the merit function used in the optical design software is extended to achieve maximum optical forces per used laser output power.

3.2.2 Expanding the merit function

The development of optical tweezers is initially close to optical lens and system design. The maximum (GEO) and averaged (RMS) spot size has to be minimal all over the image plane. This assures the generation of steep potential wells visible as high intensity gradients. Furthermore, optical aberrations have to be minimized in order to achieve symmetric and stable optical traps all over the field of interest. Consider that these goals are achieved within the optical design process using commercial software [287].

As mentioned earlier, the intensity distribution inside the focused beam plays a crucial role in the achievement of high optical forces. This fact is clarified in fig. 3.12, showing diagrams of optical forces for three different intensity distributions (TEM_{00}, plane wave, ring shaped beam) using the input parameters given in tab. 3.1. The close correlation between the optical forces and the intensity distribution in the systems exit pupil becomes obvious. All distributions form a stable optical trap with a positive force peak followed by zero crossing and the concluding negative force peak. The lateral forces F_x of all considered distributions show quite similar curve shapes whereas the Gaussian input results in the highest lateral forces. Regarding the axial forces, see fig. 3.12 left, differences occur referring to the peak amplitudes, the shape and size of the force curve. The Gaussian intensity distribution forms the weakest optical trap whereas both, the uniform and ring shaped intensity patterns, result in a very steep force gradient around the focal point. The steep curve shapes are tantamount with a high trapping stiffness and thus beneficial for optical trapping applications. This behavior is discussed in detail in chapter 4 and can be summarized with an important statement for the merit function of optical trapping systems. The redistribution of the intensity of the beam from its center to the edges seems to be a key parameter to optimize an optical system in terms of high optical forces. This means that an ideal system with a high NA is not optimized simultaneously for the generation of an efficient optical trap. Focusing high intensities with high angles is rather beneficial for stable optical traps.

At this point the iterative nature of the design process becomes clear. The optical system and its components have to be optimized in terms of good imaging properties first. Within the optical force simulation, the intensity distribution at the exit pupil of the system can be optimized to achieve a steep optical force gradient. Back to optical lens design optimizing the off-axis imaging quality of the system will increase the trapping

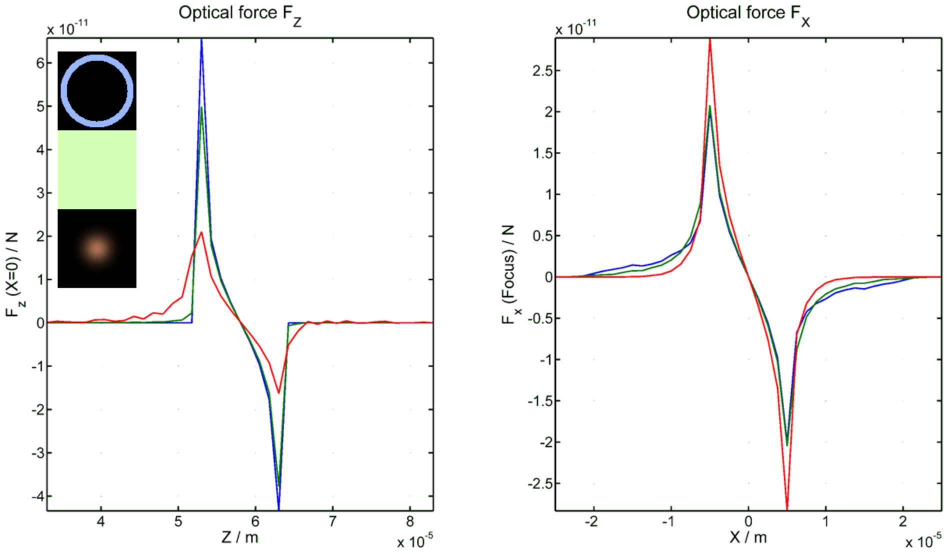

FIGURE 3.12: Axial (F_z) and lateral (F_x) optical forces achieved with the same system as described in tab. 3.1 and fig. 3.7 but with three different intensity distributions: Gaussian (red), uniform (green) and ring shaped (blue).

efficiency further. Since the optimization of optical systems is always a tradeoff between different objectives, one cannot give a general rule for an optimizing strategy valid for all optical trapping systems. However, it is obvious that optical systems with high numerical aperture and good imaging quality for outer field points should be well suited also for optical trapping applications.

3.3 Optical characterization

This section deals with the experimental measurement methods applied to characterize the quality and optical functionality of the optical systems and components used in this thesis. The characterization of the surface quality is done by interferometric measurements. Caustic and spot measurements are applied to determine the optical function of the optics.

3.3.1 Optical measurements of the surface quality

For the determination of shape tolerances and surface roughness of the optical components, a white light interferometric setup is used. Its working principle is based on the interference of light waves. The beam exiting the light source is divided in two parts. One part, the measurement beam, is reflected on the surface of the measurement object and interferes with the second part of the beam, which works as a reference. Thus the information about the curvature, as well as the micro and macro roughness of the optical surface is coded in the interference pattern. To obtain a three dimensional representation the relative distance between the surface and the measurement system is varied within a range equal to the height of the surface profile. Since the coherence length of the light source is short compared to the scanning range, interference occurs just at specific surface heights. By scanning along Z-direction the interference pattern shifts over the surface profile and information about the whole surface can be collected. The shorter the coherence length, the higher is the axial measurement resolution. A detailed description of the fundamentals describing white light interferometry is given in [57, 141, 282].

To briefly discuss the method and its performance, a spherical concave mirror manufactured inside a copper substrate by ultrahigh-precision micro-milling process [247] is investigated. The region of interest is set to the center of the curved mirror surface. Further parameters are an axial scanning range of 2 μm in combination with a field of view of 1.2 mm^2 around the center of the curved mirror. In fig. 3.13 the surface data is visualized in a color coded two dimensional plot. The curvature of the concave mirror surface (radius of curvature 0.2 m) is clearly visible in all plots shown in fig. 3.13. Furthermore, the tool marks of the milling process become visible in the surface plot. This micro roughness can be measured and recognized more clearly if the tilt and the ideal curvature is subtracted from the measurement. This finally leads to the three dimensional plot of the mirror surface, shown in fig. 3.14. The line shaped traces show the three dimensional trajectories of the milling tool which are typical for the chosen manufacturing strategy. The average surface roughness inside the field of view is $R_a =$ 53.8 nm. This measurement method is quite powerful for the determination of micro and macro surface roughness. In addition, the curvature of the surface can be determined by applying a stitching algorithm, which allows for the piecewise measurement of larger elements with high lateral resolution. Using the raw-data of the measurement in technical computing software [163] more complex mathematical operations can be applied to investigate the surface profile. Finally, the measured optical surface can be directly compared with the design data of the optical component.

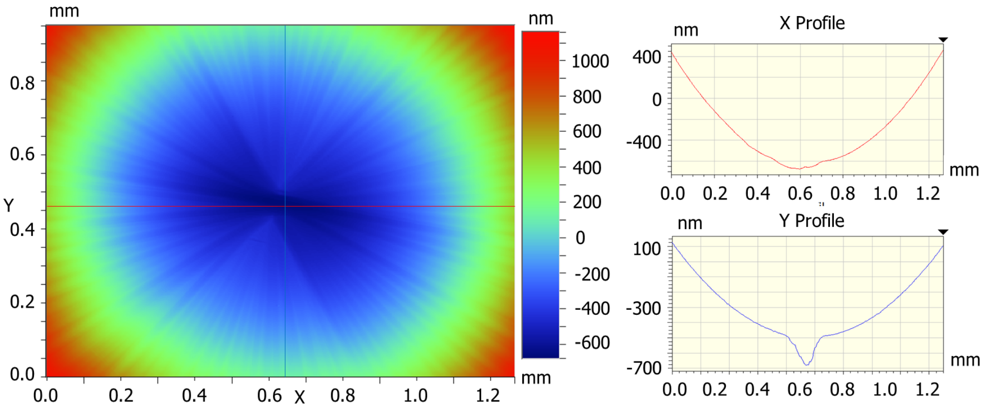

FIGURE 3.13: Surface plot and two cross sections of a concave mirror.

This method is applicable to optical surfaces, which have a sufficient reflectivity. Even the Fresnel reflections at the surface of transparent optical elements like lenses contain

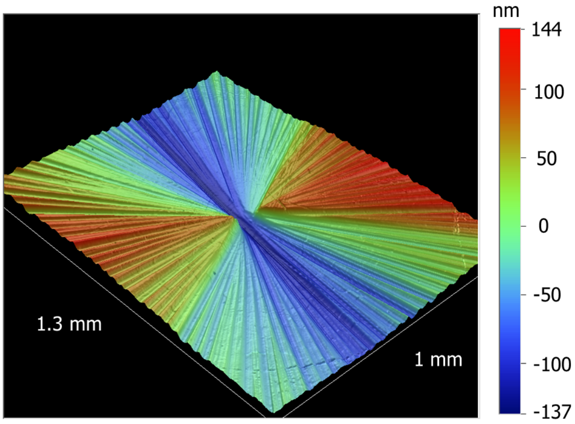

Figure 3.14: Three dimensional surface plot of the concave mirror adapted by removing a tilt between the mirror and the white light interferometer, as well as the mirrors curvature.

enough signal intensity for this kind of measurement. One important restriction is the optical quality of the surface in terms of low surface roughness. To achieve a closed surface of data points representing the measured surface, a high NA objective lens helps for the collection of sideward reflected light with higher spatial frequencies compared to the specular reflected light. Since the spatial angle is also limited for high NA lenses the slope of the surface should be as flat as possible and the average surface roughness R_a should be below 1 μm. Thus, highly diffuse surfaces and steep edges reflect the light within a broad angular spectrum which cannot be covered by the objective lens and its limited NA. In this case, the intensity collected is too small to generate a signal response. In addition, a high surface curvature results in the same effect. Rays reflected on the measurement surface with high angles miss the NA of the objective lens and cannot be detected.

3.3.2 Characterization of the optical functionality

If a Gaussian beam interacts with an optical element its phase function and intensity distribution will be influenced. Each optical element is designed to fulfill a well-defined optical function in terms of modifying e.g. the input beam with respect to its phase or intensity distribution, polarization state and direction, the spectral properties, etc. in a desired fashion. In this work the intensity distribution and phase function of an incident Gaussian beam is changed by use of refractive beam shaping optics. Its functionality can be verified by measuring and comparing the input and output intensity distribution. Furthermore, a parabolic focusing mirror is applied to generate the optical trap.
To be well prepared for this kind of measurements, the characteristics of the used laser beam have to be known. For the determination of the properties of a laser beam (beam quality factor M^2, beam width, divergence and profile, etc.) an international standard ISO 11146 [114] is used for the experimental setup and measurement procedure. The Gaussian beam produced by the laser source is focused with a lens of a precisely defined

focal length. The intensity distribution of the beam is measured at several axial positions within and outside the Rayleigh length according to the standard [114]. For the measurement a camera with sufficiently high resolution and small pixel size has to be used. In the present setup a CMOS camera (model: UI-1240SE, by IDS [110]) with a resolution of 1280 times 1024 pixels is applied. The pixel size is 5.3 μm with a dynamic range of 8 bit. The camera is mounted on a manually driven linear stage to precisely adjust the axial measurement positions. With this equipment, shown schematically in fig. 3.15 the quality factor M^2, the beam waist and the Rayleigh length can be calculated. The precise knowledge of the beam parameters is the starting point for further steps like the design process of the optical elements, the optical characterization of the manufactured optics and the alignment of the optical system.

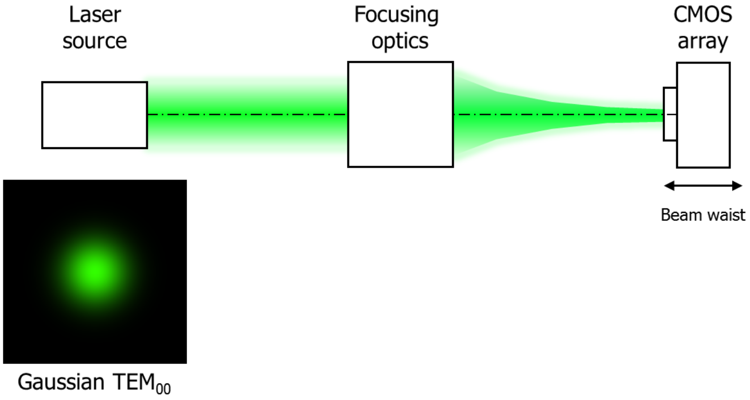

FIGURE 3.15: Schematic of the setup used for intensity measurement, applying a laser source with Gaussian output beam (TEM$_{00}$) and a CMOS array for detection mounted on a manually driven linear stage.

Assume a beam shaping device, which transforms a collimated Gaussian input beam into a collimated ring shaped intensity distribution. In order to verify the optical functionality of the beam shaper the measurement setup shown in fig. 3.16 can be utilized. Since the phase of the incident beam is expected to be a plane wave with Gaussian intensity distribution, the first surface of the beam shaping element has to be located precisely at the beam waist of the incident laser beam. In order to ease the alignment, the Rayleigh length of the incident beam should be selected as long as possible. In the present example the beam is transformed to an annularly shaped intensity distribution with zero intensity on the optical axis. The axial position of the camera is selected to be in the far field region. This means that the distance is large compared to the aperture of the beam shaping optics [86]. In addition, by changing the axial position of the camera and constantly measure the intensity distribution, the degree of the beam collimation can be observed and adjusted.

This leads directly to the caustic measurement, which is applied to investigate the phase function of a beam. The setup is similar to that described for the characterization of laser beams [114], see fig. 3.15. By incrementally moving the camera in axial direction through the focal region the focusing power of a lens or a mirror can be characterized. In order to demonstrate the function of the setup, fig. 3.17 shows the measurement of

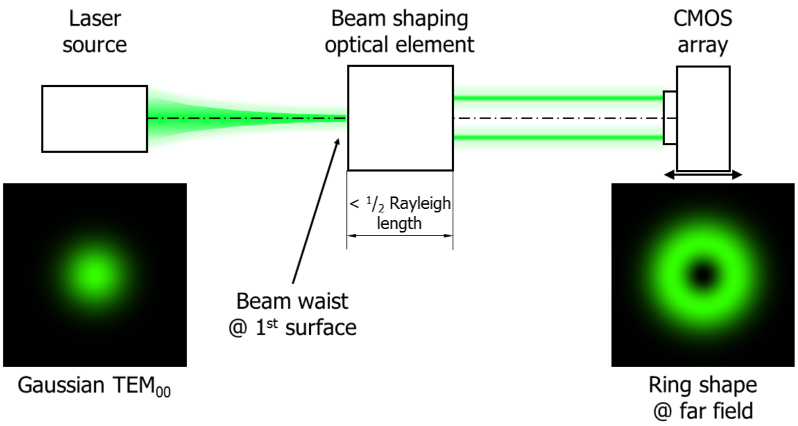

FIGURE 3.16: Schematic of the setup used for beam shaping, applying a laser source with Gaussian output beam (TEM_{00}), a beam shaping optical element and a CMOS array for detection mounted on a manually driven linear stage.

the caustic of a real optical system. A Gaussian beam is shaped by a refractive double axicon. Due to fabrication inaccuracies, the resulting collimated ring illumination is not ideal, i.e. the ring is not closed. The manufacturing errors can be directly observed. The second axicon surface is divided in several triangular shaped segemnts instead of a closed conical surface. The aberrated intensity distribution propagates along the optical axis and is focused by use of a high NA focusing lens. Several intensity measurements were made within the focal region with an increment of 50 μm. Fig. 3.17 shows the caustic in the focal region. In addition, the intensity distributions measured at the focal

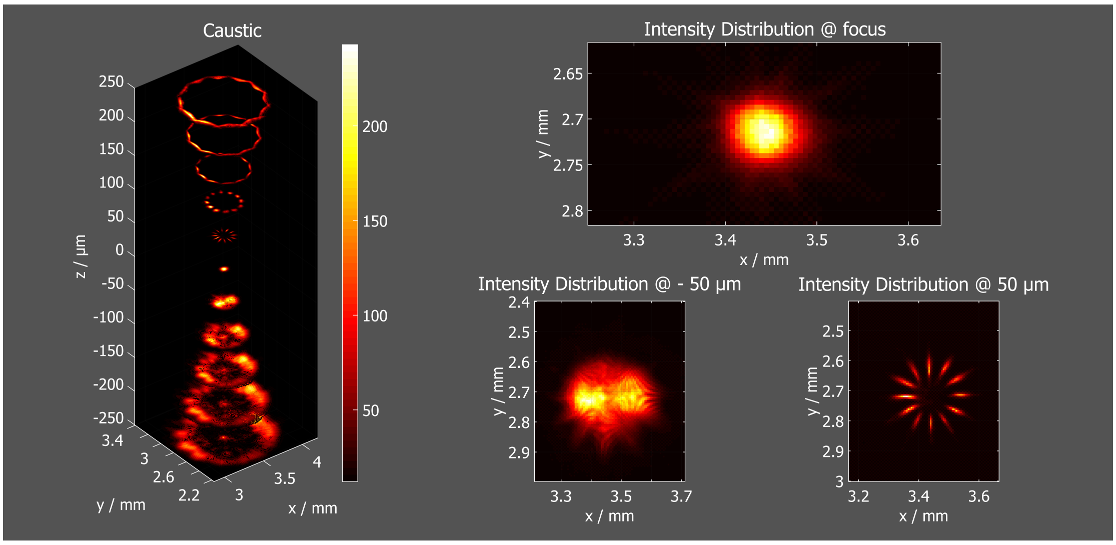

FIGURE 3.17: Caustic measurement of an optical system affected by manufacturing related errors.

point, as well as immediately in front of and behind the focus position are shown right in fig. 3.17. Intensity measurements performed at 11 positions form the caustic shown left in fig. 3.17. The element is illuminated from the bottom and the beam propagates upwards along the optical axis in positive Z-direction. The high focusing of the annularly shaped intensity distribution to a focal spot and the subsequently diverging propagation of the beam is clearly visible. As highlighted by the intensity measurements on the right side of fig. 3.17, the system suffers from manufacturing related aberrations. They lead to a broad non-symmetric spot and an inhomogeneous segmented ring shaped intensity distribution.

These intensity and caustic measurements are used to characterize the optical systems and their components. Furthermore, they can be applied to verify the correct alignment of the optical elements within the tweezers setup. Tilted or decentered optical elements e.g. can be easily aligned since tilt result in a coma-shaped spot pattern and decentered elements cause a non-symmetric intensity distribution.

Chapter 4

Experimental and numerical results

In this chapter the development of two different optical tweezers suited for optical trapping in gaseous and liquid environments, as well as the influence of optical aberrations on the optical trapping performance are discussed.
By applying the optical force simulation, the behavior of optical tweezers is investigated in view of several parameter variations (NA, intensity distribution, refractive indices). Based on these considerations two optical tweezers are designed, characterized and the optical trapping is experimentally verified. These results are compared with optical force simulation. The reasonable agreement of the theoretical predictions and experimental results verifies the correct function of the optical force simulation routine. This enables the investigation of the behavior of optical tweezers in the presence of optical aberrations, which is discussed in the final section 4.4 of this chapter.

4.1 Optical force simulations

In this section the results of optical force simulations are presented and discussed. The focus of the investigations is the influence of fundamental parameters like the refractive indices of the particle and the surrounding medium, the shape of the particle, the NA of the focusing lens and the intensity distribution.

4.1.1 Influence of the refractive index

If a ray is incident on a surface between two optically different media, the ray is divided into a refracted and a reflected part. The angles of refraction and reflection, as well as the intensities of the beams determine directly the amount of momentum transferred from the incident beam to the surface. The angle of the refracted part depends on the relative refractive index of both media and the angle of incidence, see eq. 2.10.

(vectorial law of refraction). Due to Fresnel's equations (eq. 2.12 to 2.15) the amount of the intensity of both rays is a function of the refractive indices and the angle of incidence as well, visualized in fig. 2.4.
Since the majority of optical tweezer applications is the trapping of particles within a liquid environment ($n_0 \approx 1.33$), the dependency of the refraction angle from the angle of incidence and the refractive index of the particle (n_1) is visualized in fig. 4.1. Consider a physical interface between two media with low and comparatively high relative refractive index. In the first case the angle of refraction is almost identical to the angle of incidence, which is illustrated with the linear relationship between both angles at the backside of the surface plotted in fig. 4.1. This case is exploited in oil immersion based microscopy where a physical interface between two media with almost identical optical properties is formed. For an increase of the relative refractive index the relationship between the angle of incidence and the refraction angle becomes non-linear, visualized with the curved shape of the surface plotted in fig 4.1. This behavior is described by Snell's law (eq. 2.28), [86]. The general statement of fig. 4.1 is that for an increasing relative refractive index between the object and its environment the refraction angle rises. Therefore, the direction of propagation of the incident ray and hence its momentum changes.

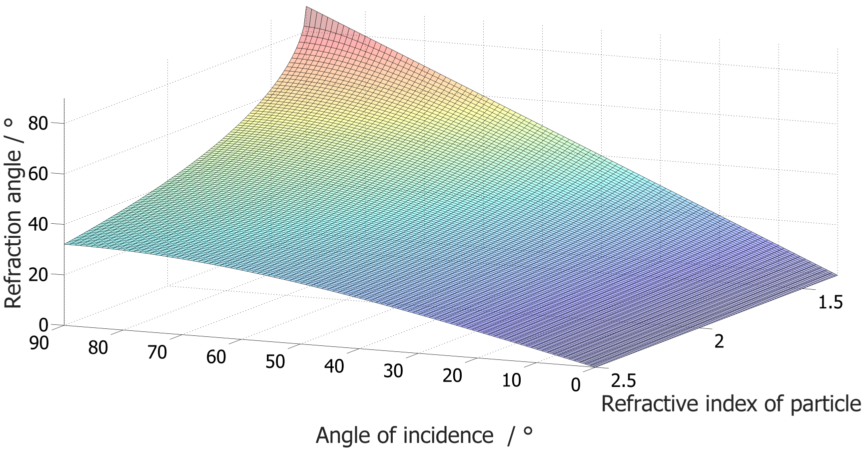

FIGURE 4.1: Refraction angle as a function of the angle of incidence and the refractive index of the particle (surrounding medium $n_0 = 1.33$).

Consider a physical interface between two media oriented in the X-Y-plane and a ray that propagates in the X-Z-plane. The power of the ray is $P_{ray} = 10$ mW and it is unpolarized. The direction of propagation of the refracted ray changes for an increasing angle of incidence relative to the X-Z-plane. Applying eq. 2.26, the optical force that is introduced by a ray on the surface can be written as:

$$\vec{F}_{ray} = \frac{n_0 P_{ray}}{c}\vec{r} - \frac{n_0 T P_{ray}}{c}\vec{r}' - \frac{n_1 R P_{ray}}{c}\vec{r}'', \tag{4.1}$$

$\vec{r}$ is the unit vector for the incident ray, $\vec{r}'$ and $\vec{r}''$ are the unit vectors for its refracted and reflected components, respectively. Applying this equation for a parameter run of the refractive index of the second medium n_1 and the angle of incidence, the optical force acting on the interface in Z-direction can be visualized by a surface, plotted in fig. 4.2.

For an angle of incidence of 90° the optical force is zero since the ray does not interact with the surface. A ray which hits the surface perpendicularly (angle of incidence of 0°) is partly reflected such that a part of its momentum is transferred to the surface and cause radiation pressure. This can be experimentally measured [12, 38, 289]. For an increasing refractive index of the second medium the optical force rises. This behavior can be traced back to the increase of the reflection coefficient (eq. 2.12 and 2.13) and thus an increase of the momentum transfer from the ray to the medium [172]. On the other hand, if the angle of incidence increases, the transmitted part of the ray is refracted and its direction of propagation changes. This deflection results in an additional momentum transferred to the surface. If the refractive index of the medium increases the angle of refraction increases as well and hence the contributions to the optical forces rise, see fig. 4.2. The Fresnel coefficients determine the value of how much the reflected and transmitted part of the incident ray contribute to the momentum transfer. In sum, the momentum transfer contributions given by the Fresnel coefficients and the change of the ray direction of the refracted and reflected ray cause the non-linear curve shape of the optical force.

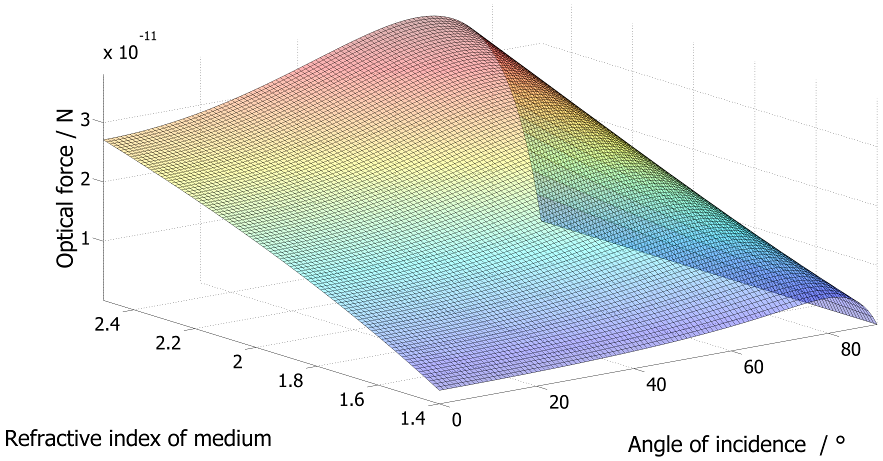

FIGURE 4.2: Optical forces acting on a plane interface (positive Z-direction) between two different optical media ($n_0 = 1.33$) for incident plane wave ($P = 10$ mW) as a function of the angle of incidence and the second medium (n_1).

The significant influence of the particles refractive index (n_1) on the optical forces is clearly visible, see the steady increase of the optical forces plotted in fig. 4.2. Furthermore, the surrounding medium (n_0) also affects the optical forces as already pointed out in section 3.1.6.

In the case of a spherical particle instead of a single planar surface follows that for lower refractive indices of the surrounding medium the optical forces acting along the optical axis increase. In contrast, the retro driving forces decrease which makes optical trapping in gaseous surroundings more challenging compared to trapping in liquids.

Since optical forces depend on the refractive index of the particle medium (n_0) and its surrounding (n_1) this fact is studied in detail by use of the optical force simulation. Ashkin already published in 1992 [10] that the gradient and scattering force strongly depend on the relative refractive index. Further work is spent in studying this effect for negative refractive indices [4, 115]. In this work the investigations are confined to materials of the particle and its surrounding usually applied in optical tweezers applications. The Parameters used for the simulation are given in tab. 3.1 section 3.1.6. The laser power is assumed to be 50 mW distributed over the whole beam according to the used intensity distribution. The beam is unpolarized and has a Gaussian profile sampled with 101 times 101 pixels. The focusing angle is 77.8°, which gives a numerical aperture of NA = 1.3 for a liquid environment and NA = 0.98 for gaseous surrounding. In terms of optical aberrations, the optical system is assumed to be nearly ideal with a geometric spot radius of $GEO = 1\ \mu$m caused by spherical aberrations. The particle is of spherical shape with a diameter of 10 μm. The waist of the Gaussian beam $\frac{w_1}{e^2}$ is defined by the decrease of the maximum intensity I_0 to a value of $\frac{I_0}{e^2}$. As frequently applied in the literature, the truncation ratio T is given by the ratio of the beam waist to the radius $R = \frac{D}{2}$ of the system input aperture.

$$T = \frac{\frac{w_1}{e^2}}{\frac{D}{2}} \tag{4.2}$$

For the optical force simulations the waist of the Gaussian beam is half of the radius of the input aperture which leads to a value of $T = 0.5$. Tab. 4.1 lists the material combinations used for the optical force simulation in the liquid and gaseous environment. The results are shown in fig. 4.3.

TABLE 4.1: Relative refractive indices used for optical force simulations regarding liquid and gaseous surrounding ($n_0 = 1.33$; $n_0 = 1$) of typical, as well as fictive applied particle materials (n_1).

$n_{rel,fluid}$	1.09	1.11	1.18	1.25	1.3	1.4
n_1 / medium	1.45 / SiO_2	1.48 / PMMA	1.57 / PS	1.66 / SF1	1.73 / LaF	1.86 / LASF9
$n_{rel,fluid}$	1.5	1.6	1.8	2.0	2.5	-
n_1 / medium	2.0 / fictive	2.13 / fictive	2.39 / fictive	2.66 / fictive	3.33 / fictive	-
$n_{rel,gas}$	1.1	1.2	1.33	1.4	1.45	1.48
n_1 / *medium*	1.1 / fictive	1.2 / fictive	1.33 / H_2O	1.4 / Silico. oil	1.45 / SiO_2	1.48 / PMMA
$n_{rel,gas}$	1.57	1.7	2.0	2.5	-	-
n_1 / *medium*	1.57 / PS	1.7 / LaF	2.0 / fictive	2.50 / fictive	-	-

It is obvious that for both environments the curve shapes look quite similar except the magnitudes of the optical forces. The forces acting on the particle in X- and positive Z-direction (red and blue curve) non-linearly increase for rising refractive index of the particle. Large forces in X-direction laterally stabilize the optical trap whereas the increase of forces acting in positive Z-direction (green curve) cause a non-symmetric trapping curve shape see fig. 3.8 and 3.9, which destabilizes the trap. All forces are zero at a relative refractive index of $n_{rel} = 1$ since no optical interface between the environment and particle exists.

In contrary to the increasing trend of F_x and F_{+z} the back driving forces (F_{-z}) reach a

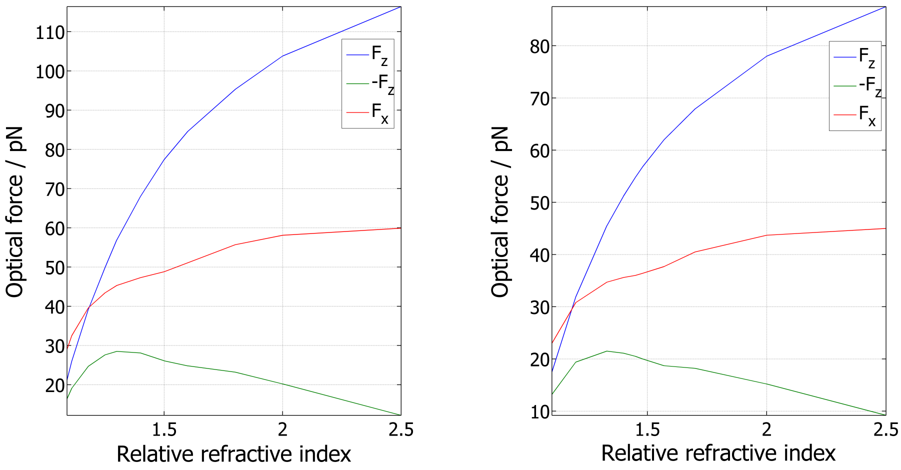

FIGURE 4.3: Maximum optical forces acting along ($+F_z$) and contrary (F_{-z}) to the optical axis as well as perpendicular (F_x) to it, simulated for liquid (left) and gaseous (right) environment.

maximum at a relative refractive index of roughly 1.33. That means for optical tweezing applications in a liquid environment (fig. 4.3 left) using the parameters mentioned above, beads made out of flint glasses or other materials with refractive index of approximately $n_1 = 1.7$ are supposed to achieve a highly stable optical trap. If the refractive index of the particle is less than 1.7, the trap is still stable just the ratio of the forces acting in X- and Z-direction varies but not within a crucial range. However, caution is advised if the refractive index becomes larger than values of two, although the variety of optically transparent and homogeneous materials with this specification is quite small. Particles of high refractive index are strongly pushed forward to the equilibrium position of the optical trap and may achieve such high amount of kinetic energy that their movement cannot be stopped by the back driving force.

The dependency of the optical forces on the refractive indices presented in fig. 4.3 right is similar for gaseous surroundings at the first glance. In this case the refractive index of the surrounding is nearly one and thus the relative refractive index is the same as the refractive index of the particle to be trapped. That way keeping all simulation parameters constant the maximum optical trapping force (F_{-z}) is achieved for particles with a refractive index of 1.33. Hence the trapping of liquid aerosols like water droplets results in a beneficial ratio of forward pushing and back driving optical forces. As the focusing angle is kept constant for all simulation it should be mentioned that the NA of the system increases for media with larger refractive indices. This will be addressed in the next section.

4.1.2 Influence of the numerical aperture

Most optical tweezer setups utilize high NA objective lenses [183, 267] to create the steep intensity gradient required for optical trapping. To overcome limitations of the working distance or to expand the lateral field of optical manipulation, low NA focusing optics are studied to apply them for optical tweezers [54, 245]. In order to get an impression of how the optical trapping force (F_{-z}) suffer from rays incident with low angles a variety of numerical apertures are simulated. Focusing optics applied in liquid and gaseous environment are theoretically investigated and the results are visualized in fig. 4.4. and tab. 4.2 lists the corresponding focusing angles. The same input parameters are used for the simulations as performed previously, see tab. 3.1. The light travels along the optical axis, which is equivalent to positive Z-direction. Once again, a Gaussian input intensity distribution with truncation ratio $T = 0.5$ is selected. First we consider optical tweezers, which use immersion objective lenses, see fig. 4.4 left. By increasing the NA of the system and hence the focusing angle, optical forces acting in positive (blue curve) and negative (green curve) Z-direction rise. This behavior starts from a value of NA = 0.6 which corresponds to a focusing angle of 26.8° in a liquid environment

TABLE 4.2: Numerical apertures (NA) and associated focusing angels (α) for liquid and gaseous surrounding ($n_0 = 1.33$; $n_0 = 1$).

NA (n_0=1.33)	0.6	0.7	0.8	0.9	1.0	1.1
α / ○	26.8	31.8	37.0	42.6	48.8	55.8
NA (n_0=1.33)	1.2	1.25	1.3	1.33	-	-
α / ○	64.5	70.0	77.8	83.0	-	-
NA (n_0=1.0)	0.6	0.65	0.7	0.75	0.8	0.85
α / ○	36.9	40.5	44.4	48.6	53.1	58.2
NA (n_0=1.0)	0.9	0.95	0.99	-	-	-
α / ○	64.2	71.8	81.9	-	-	-

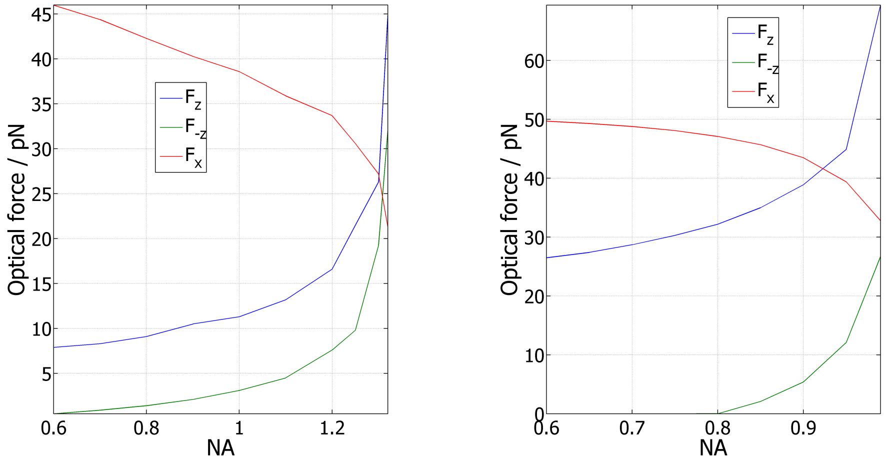

FIGURE 4.4: Lateral and axial optical forces as a function of the NA for liquid (left) and gaseous (right) environment.

(n=1.33). Focusing lenses with values of less than NA = 0.6 are not able to create a three dimensional optical trap for the applied simulation parameters. Nonetheless, due to the optical forces which act in positive Z-direction it is possible to realize optical manipulation in two dimensions as Ashkin did in 1970 [9]. Thereby the particle is optically pressed against the wall of the test chamber.

The red curves represent the forces acting in lateral direction. In both cases lateral forces decrease for an increasing NA of the focusing optics. This means, for optical trapping using a low NA objective it is favorable to laterally trap the particle. In this case gravity acts perpendicular to the optical axis.

Optical trapping in gaseous surrounding is more challenging compared to more dense (optically and volumetric mass) environment as already discussed in section 2.2.4 and mentioned in section 3.1.6. Again, the optical forces acting in positive and negative axial direction rise with larger focusing angles, see fig. 4.4 right. Interestingly, the trapping force (F_{-z}) reaches nearly the same values for angles larger than 70° (NA = 0.94) compared to the liquid environment. In contrast to this, the threshold for the generation of a three dimensional optical trap would be achieved only with focusing angles larger than 53° (NA $>$ 0.8). This focusing angle is twice as high compared to optical trapping in fluidic media.

In conclusion, the ratio of the axial optical forces (F_{-z} and F_z), shown in fig. 4.4 favors more stable trapping conditions in optically dense media if the same NA for the focusing optics is applied. Thus, the requirements on the focusing angle for optical tweezing applications in gaseous environments are significantly higher in contrast to fluid based optical traps. As mentioned earlier, a powerful parameter for increasing the trapping forces is to optimize the intensity distribution of the focused beam which is the topic of the next section.

4.1.3 Influence of intensity distribution

The intensity distribution used for optical tweezers, defines the angle resolved amount of intensity focused by the focusing optics. That means, expressed in parameters used for the optical force simulation, intensity values located at the edge of the array of pixels are focused with angles large compared to those pixels positioned near the center. Based on the simulation results presented in fig. 4.4 high trapping forces can be achieved by increasing the system NA. In other words, increasing the focusing angle of high intensity values can lead to the same result. Thus, a redistribution of the beam input intensity could be a beneficial approach to increase the trapping performance without applying expensive high NA objective lenses [26, 79, 120, 199, 228].

The easiest way to increase the intensity at the edge of the beam is to expand the trapping laser beam and overfill the limiting system aperture [183]. As defined with eq. 4.2 in section 4.1.1 the ratio of the beam diameter to the system aperture can be expressed with the truncation ratio T. To simulate its influence on the optical forces, the truncation ratio is incrementally increased starting from a Gaussian beam with a waist one third of the aperture (T = 1/3) up to a plane wave (T = infinity). The same input parameters as specified by tab. 3.1 are used. By choosing a gaseous surrounding and a minimum NA of 0.8 in combination with a Gaussian beam profile of truncation ratio T = 0.5, the optical tweezers should not be able to create a stable optical trap, see fig. 4.4 right. By increasing T higher intensity values are moved to the outer regions of the beam.

This can be experimentally realized using a beam expander positioned in the beam path right in front of the objective lens. The results are represented by optical forces acting in X-direction, as well as in positive and negative Z-direction (red, blue and green curve) and are visualized in fig. 4.5. By increasing T above values of 0.5 optical forces acting in negative Z-direction (green curve) rise and form an optical trap. Simultaneously, optical forces that push the particle in light direction (blue curve) increase as well, whereas optical forces acting in lateral direction slightly fall off. Obviously, the redistribution of the intensity to the edge of the beam is a powerful parameter to optimize the trapping performance of optical tweezers. Without replacing the focusing optics with a higher NA objective lens the optical system could be optimized to form a stable optical trap.

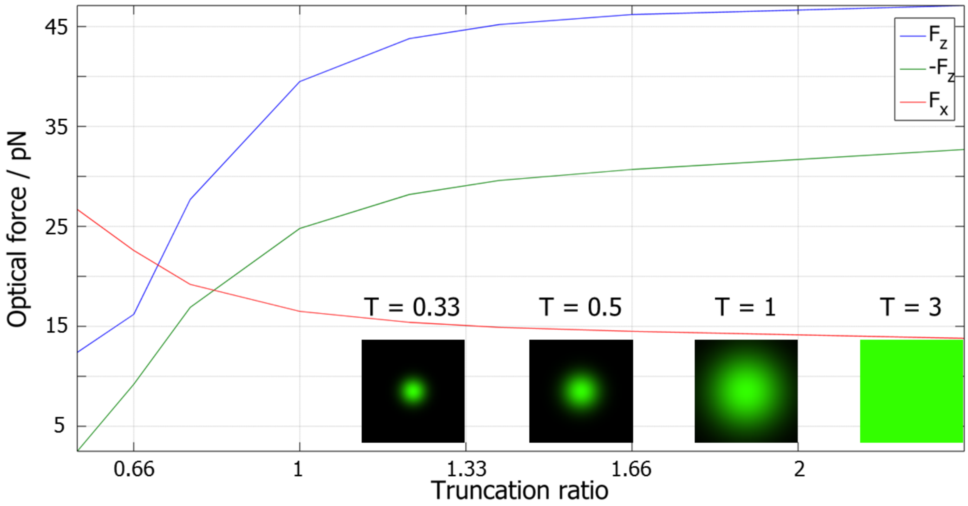

FIGURE 4.5: Optical forces as a function of the truncation ratio T of a Gaussian beam (TEM_{00}) in gaseous environment using NA = 0.8.

Since that strategy seems to work, the next logical step is to investigate how the optical trap reacts if the intensity on the optical axis is minimized while keeping the total intensity constant. By applying a beam shaping optical element like a diffractive optical element, axicon lens or SLM the intensity redistribution can be realized. The Gaussian intensity gradient, shown in fig. 4.5, represents a smooth decrease of the intensity at the center to the edge. It might be useful for this simulation to realize a ring shaped intensity distribution. Thus, the maximum value of the whole beam intensity can be transferred to its edge, see fig. 4.6. The thickness of the rings is varied between one and 20 pixels with a maximum outer ring diameter of 101 pixels. Again, the same input parameters for the force simulation are applied as given in tab. 3.1. The redistribution of high intensity values from the optical axis to the edge of the beam leads to a significant increase of optical trapping forces as indicated by the green and blue force curves in fig. 4.6. The highest optical trapping force is achieved with the ring distribution of smallest thickness. In this case the total power of the beam is carried by its outer border. Increasing the thickness of the ring leads to a rising number of rays carrying high intensities which are focused at lower angles. Simultaneously the intensity at the edge decreases, since the total power of the beam is distributed over the whole array of pixels. As a result, the trapping forces become smaller. The optical force acting in

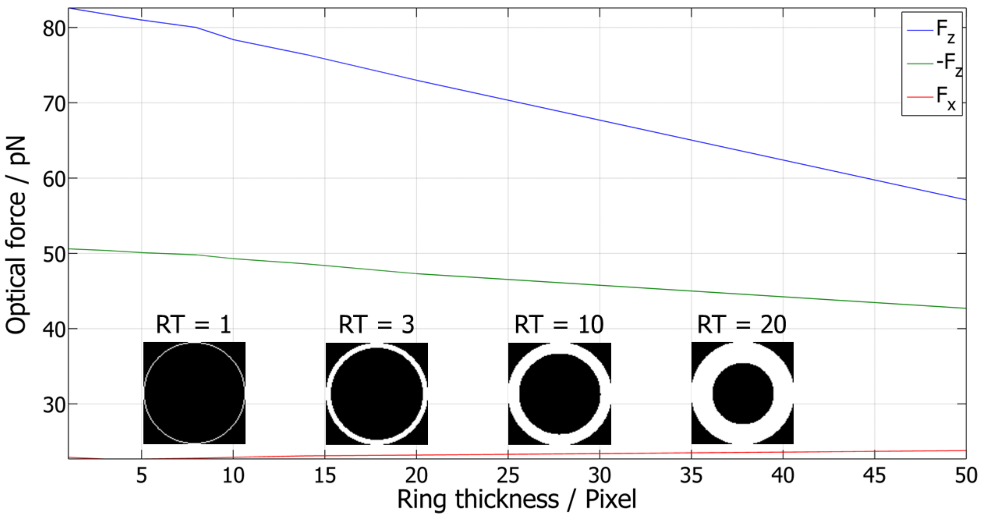

FIGURE 4.6: Optical forces as a function of the ring thickness in gaseous environment using NA = 0.8.

positive Z-direction (F_z) follows the same trend and decrease for larger ring diameters but noticeably steeper. Therefore, the ratio of positive and negative axial forces becomes smaller which means the shape of the axial trapping profile becomes more symmetric. Thus, by the redistribution of the intensity to the outer regions of the beam limited by the systems aperture higher trapping forces can be achieved but the optical force curve shape in general becomes slightly non-symmetric.

The lateral optical forces (red curve) remain nearly the same since all rays are focused within an area of 1 μm. Consider a cross sectional area oriented perpendicularly to the optical axis and located at the focal point each focused intensity distribution would nearly look identical.

To conclude, a ring shaped beam profile with zero intensity on the axis and maximum intensity at the edge (limiting system aperture) leads to the highest optical forces acting in negative Z-direction. But simultaneously, the stability of the trap is slightly decreased. This behavior has to be considered especially for optical trapping application in gaseous surroundings.

4.1.4 Particles of different size and non-spherical shape

The ray optics based model applied in this work is valid for particles large compared to the wavelength. Large means that the value a, see eq. 4.3, has to be greater than 10 to 20 [10, 109].

$$a = \frac{2\pi r}{\lambda} \tag{4.3}$$

r is the radius of the particle and λ the wavelength of the incident light. Using a laser source with an emission wavelength of 1 μm GOA should provide accurate results for a spherical particle with a radius down to 3 μm.

Due to the ray optics based approach of GOA the optical forces are independent of the size of the object to be trapped. If a spherical particle is placed in the focal point the angle of incidence of the rays is independent of the size of the particle. To prove that fact simulations are performed with the input parameters as described above (tab. 3.1; liquid surrounding, NA = 1.3, Gaussian beam with $T = 0.5$, geometric spot radius $GEO = 1$ μm) for a variety of particle diameters starting from 3 up to 100 μm. The optical forces acting on the particle in lateral and axial direction remain the same for all considered particle sizes.

This result represents the contrary to the increasing cross sectional area of a particle with growing diameter interacting with an ideal plane wave, see section 2.1.1. In the case of focused light fields a beam is focused within an area usually smaller than the particles diameter. Thus, the extension of the beam is small compared to its size and the whole ray fan interacts with the particle, which explains the independence of the particle size and the optical forces.

During the previous investigations we considered spherical particles. If the particle becomes non-spherical like an oblate or needle, its orientation has to be taken into account as well. The first shape studied is an oblate shaped object placed in the X-Z-plane oriented with its large cross sectional area perpendicular to the incident beam which propagates along positive Z-direction. Another shape to be considered is a needle shaped object oriented along the optical axis. The orientation of both objects is varied incrementally by tilting them around the Y-axis between angles of 0° and 100°. Since the objects have rotational symmetry and are tilted around their center, which corresponds to the optical axis the result for the tilt angles 80° and 100° should be the same. Optical forces are plotted in fig. 4.7 as a function of the tilt angle for an oblate (left) and needle (right) shaped object. Optical forces acting on both objects show a similar behavior

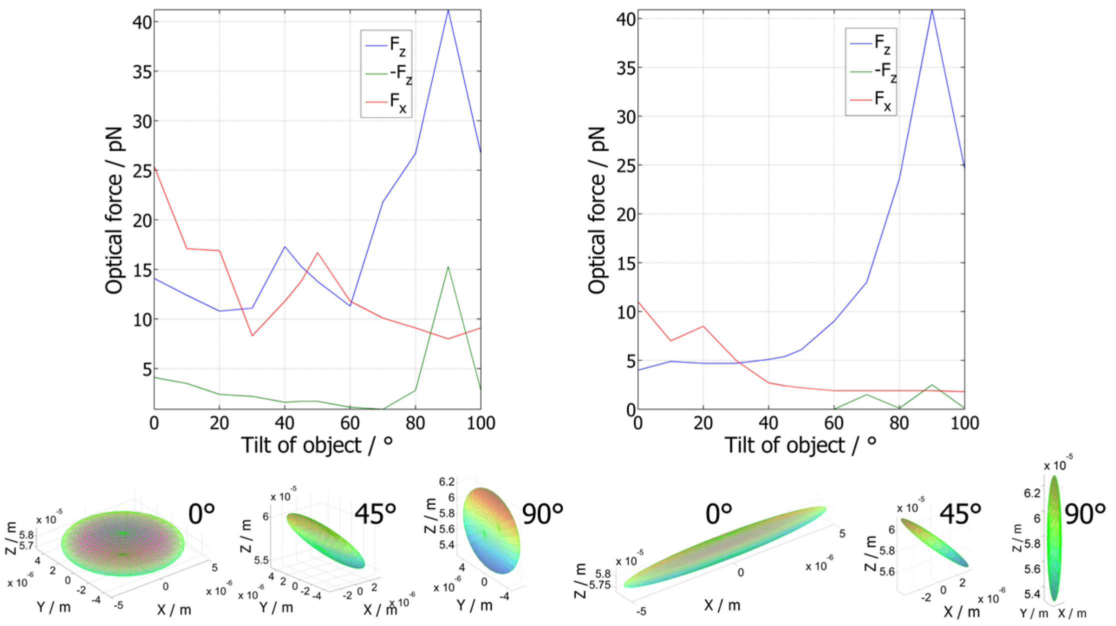

FIGURE 4.7: Optical forces acting on an oblate (left) and needle (right) shaped object made of PMMA suspended in liquid surrounding for tilt angles around the Y-axis.

while changing the object orientation relative to the trapping beam. At a rotation angle of 90° (long semi axis equal to optical axis) the highest trapping forces are achieved for both object shapes. If the orientation of the object is perpendicular (0°) to the optical axis optical trapping becomes challenging for oblate and impossible for needle shaped objects. For increasing rotation angles between 0° and 90° optical forces acting in lateral direction (red curve) roughly decrease while axial forces rise. Due to the strong dependency of the optical forces on the shape and orientation of non-spherical objects, optical trapping has to be theoretically investigated before an optical trapping system is started to be developed.

4.2 Optical system for trapping of particles in air

The motivation for the development of an optical tweezers suited to trap particles in a gaseous surrounding originates from the functional enhancement of a nano-positioning and nano-measuring machine (NPMM) [160]. This machine was engineered within the framework of a collaborate research center [61]. Since the position accuracy of this machine is in the sub-nanometer range, a precise tool is required for the positioning of microscopic particles on a glass wafer or other substrates. If small objects are picked up by a micro gripper they stick on its surface due to adhesive forces and cannot be released. Optical tweezers do not suffer from this effect and are well suited to be utilized as a micro tool to trap, hold, transport or manipulate and finally release microscopic objects.

In this section the process of the development of an optical system highly adapted to this application is described. Starting with the application, necessary requirements, boundary conditions and constraints are derived to create the optical concept. Based on the experiences that have been gained from the optical force simulation a starting system is developed and optimized using the iterative optical design process. After the systems components were designed, optimized and fabricated their quality and optical function is verified using interferometric and caustic measurements. Once the whole optical system is adjusted, optical trapping of spherical fused silica particles is performed. Note, in the previous simulations particles made of PMMA are considered as well. The refractive index of PMMA (n=1.4816 @ 1070 nm) is slightly higher compared to fused silica (n = 1.4496 @ 1070 nm). Furthermore, the density of fused silica ($\rho = 2.201 \frac{g}{cm^3}$) is large compared to PMMA ($1.18 \frac{g}{cm^3}$). This means if an optical tweezers is able to stably hold a particle made of fused silica, it should be able to easily trap PMMA particles of the same size and shape. The experimental results achieved with the developed optical system are compared with the theoretical predictions obtained with the optical force simulation.

4.2.1 Development of the optical system: Concept

Starting from the application the tool should be used for optical manipulation of single particles within gaseous surrounding. For the experimental work initially two kinds of particles are used, one kind is made of fused silica and the other of PMMA. In both cases the shape is spherical with a minimum diameter of 3 μm. The working distance (WD), which means the space between the tool and the object to be optically trapped, has to be sufficiently large (i.e. > 1 mm). That way collision between the optical micro gripping tool and the surface the particle has to be placed on should be avoided. The volume of the optics itself should be comparable to standard objective lens and it has to provide the possibility for observation. In addition to minimize the heat input into the NPMM, the optical trapping system has to be energy efficient in terms of a high ratio of optical force per incident laser power. These requirements and further details can be summarized with respect to tab. 3.2 to the following specification sheet.

- Optical trapping of single particles in gaseous surrounding.
- Working distance: WD > 1 mm.
- Particles: transparent material (fused silica, PMMA), diameter in the range of several micrometers, spherical shape.
- No movement or rotation of the particle planned.
- Numerical aperture: NA > 0.8 (minimum focusing angle of 53°).
- Size of trapping system: comparable to an objective lens, which means a cylindrical volume with a maximum diameter of 30 mm and length of 60 mm.
- Energy efficient optical system (maximum trapping force per incident laser power).
- Observation optics: verification if object is trapped.

As pointed out by the simulation of optical forces acting on a spherical object placed in gaseous surrounding for different numerical apertures, see fig. 4.4 right, three dimensional optical trapping is only possible for values of NA ≥ 0.8 using a Gaussian beam with truncation ratio $T = 0.5$. A value of NA $= 0.8$ for a gaseous environment corresponds to a focusing angle of 53°. Consider the transition of rays from the focusing lens material to air the critical angle to avoid total internal reflection (TIR) is about 41° for glasses with refractive indices of 1.5. For an optical interface between media with high (glass) and low (air) refractive index, the refraction angle of 53° is achieved with an angle off incidence of 32°, which is significantly less than the critical angle, see the dotted black line visualizing the Fresnel coefficients for transmission illustrated in fig. 2.4. Note, the surface normal is assumed to coincide with the optical axis which may change for the final lens design. In addition, the Fresnel losses increase for angles of incidence larger than 10°, see fig. 2.4.

To achieve an energy efficient optical trapping system, the investigation of the influence of different intensity distributions on the optical forces, see section 4.1.3, leads to a concept realizing a non-Gaussian i.e. ring-shaped beam profile. Within this research project [61] a previous optical system suited for trapping of particles in liquid surrounding was already developed [193, 194]. Thereby the incident light beam is transformed by an axicon into a divergent annularly shaped intensity distribution propagating along the optical axis. This ring is focused by use of an aspheric surface 650 μm behind the optics. Both optical functions are combined within a monolithic optical element made of PMMA. By directly linking the optics to a microfluidic channel using deionized water as index matching material no TIR occurs on the back of the optics. The system provides a maximum NA of 1.25 which corresponds to a focusing angle of 70°. Since this system is suited to optically trap only in liquid surrounding and does not offer the possibility for simultaneous observation, a new system has to be designed. Based on the requirements, findings and preliminary investigations the following concept has been developed (fig. 4.8). Since the laser source to be used for optical trapping has Gaussian profile (TEM_{00}), a suitable optical element for the redistribution of the intensity from the optical axis to the edge of the beam is required. This can be done with an optical function implemented either in a reflective or refractive optical surface. A further possibility for the implementation of a beam shaping function is the use of a diffractive optical element. In contrast to the trapping system developed previously [193], the system presented in fig. 4.8 suggests a collimated ring shaped distribution generated by the beam shaping element. In the center of the system space is left for the integration of imaging optics. However, due to the interface between the optics and the gaseous surrounding, care has to be taken to prevent the optical performance from losses caused by TIR. Since the focusing optics has to enable the observation of the trapped particle as well, the orange beam path visualized in fig. 4.8 can be utilized.

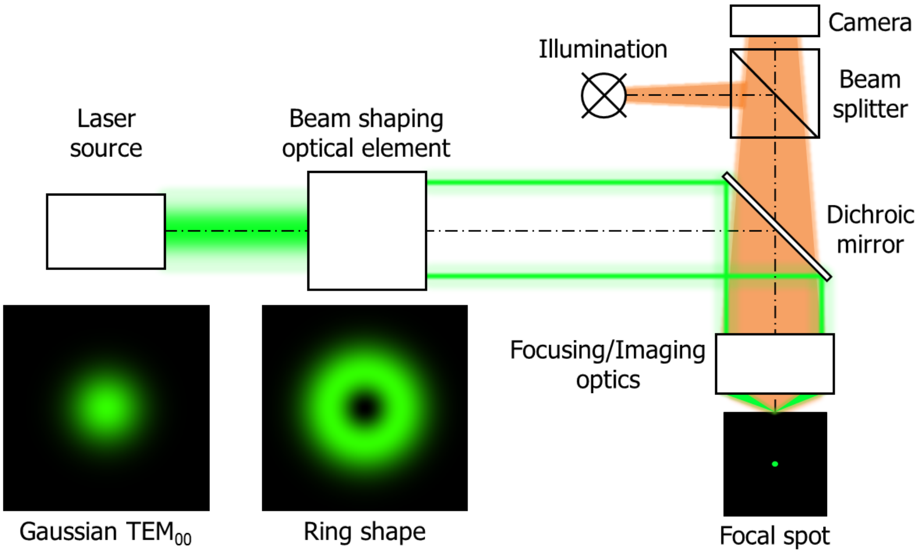

FIGURE 4.8: First concept of the optical system for trapping (green ray path) particles in gaseous environment and observation (orange ray path) in parallel.

Based on detailed studies of diffractive optical elements to shape the ring profile it turns out that the efficiency of the lithographically manufactured elements is not sufficient. Thus, the Gaussian to ring beam shaping task is realized using a refractive axicon. By adjusting the center of such optical elements to the optical axis an incident Gaussian beam is initially shaped to an interference phenomenon called Bessel beam [66, 67, 139]. If the tip of the axicon is oriented towards the light source, the Bessel beam is formed inside the optical element. Further propagation of the beam beyond the region of interference results in a ring profile with increasing diameter. To achieve a collimated ring a second axicon with inverted slopes can be applied.

Since the homogeneity and the collimation of the annular intensity distribution depends strongly on the alignment of both axicons relative to each other, as well as to the incident laser beam a monolithic optical element is beneficial. The alignment in this case is transferred to the manufacturing process and only the precisely fabricated double-axicon has to be aligned relatively to the incoming laser beam. Often the geometric tolerances feasible in the manufacturing process are significantly higher compared to the adjustment process afterwards. Especially angular errors of the axicon slopes and the tilt of the axicons relative to each other strongly affect the quality of the ring illumination [122]. These considerations lead to the monolithic design shown in fig. 4.9. If a collimated ray fan is incident on the first axicon surface each ray is refracted with the same angle relative to the surface normal. The second axicon surface is located at the back of the element and has the same slope angle. The incident ray is refracted by the same angle just with different sign. Therefore, the axicon material, the slope angle and the length of the double axicon define the diameter of the ring shaped intensity distribution leaving the component.

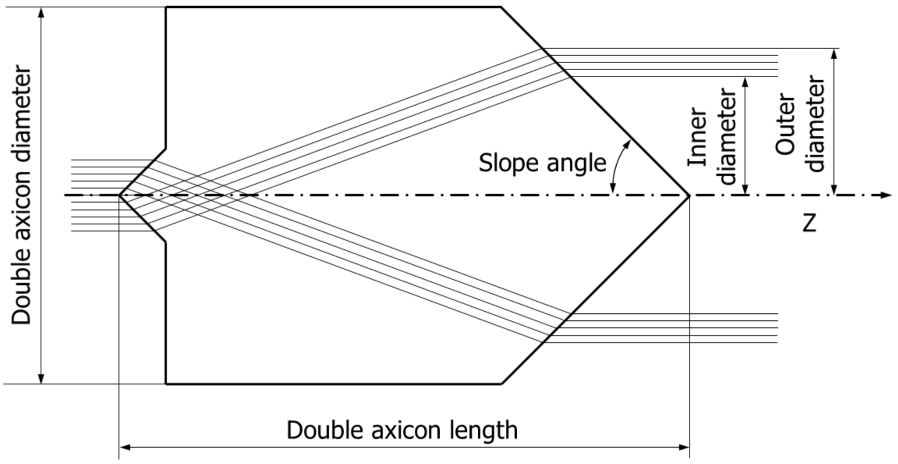

Figure 4.9: Double axicon used for Gaussian to ring beam shaping.

The collimated annularly shaped beam can be focused ideally (without spherical aberration) using ellipsoidal surfaces (refractive index sequence: glass, air). In contrast, the focusing of off-axis field points may be difficult using such an aspherical surface. As indicated in fig. 4.8, the intensity of the laser beam used for optical trapping is concentrated on its edges. Consequently, the center area of the ring-shaped beam is open for the integration of a second optical function.

The required focusing angle for optical trapping in gaseous surrounding cannot be achieved using single plano-convex lenses made of standard optical materials (refractive index below 1.7). Realizing the focusing angle either with two or more optical surfaces leads to an increased system complexity and higher costs. If materials with high refractive index are applied, the Fresnel losses increase resulting in the demand for anti-reflection coatings. These considerations lead to the application of a reflective surface for focusing the collimated ring allowing focusing angles up to 90°.

A parabolic mirror surface is well suited to ideally focus an incoming collimated ray fan. Since only the outer region of the incident beam has to be focused just a section of the parabolic mirror is required, as shown in fig. 4.10. The central area is not needed

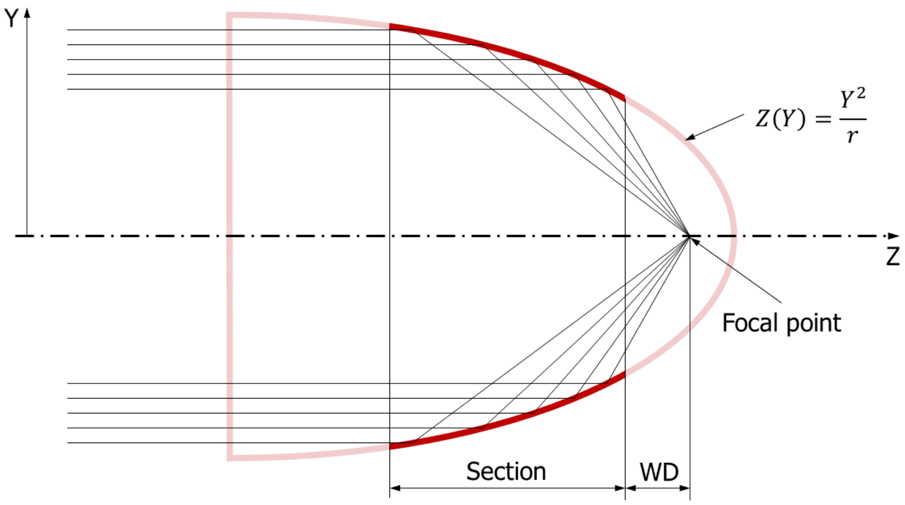

FIGURE 4.10: Required section of the parabolic mirror with the radius r for ideally focusing the ring distribution at a focal point with the working distance WD.

for focusing a ring shaped beam and can be used for the implementation of an imaging system. The slope at the inner aperture of the parabolic mirror defines the maximum focusing angle, i.e. the NA of the focusing system. Higher NAs result in the need for larger curvature of the parabolic mirror with the consequence that the working distance is reduced and the free range in its center shrinks. On the other hand, if the radius of curvature of the paraboloid raises the WD again decreases but the inner aperture remains constant. This is important since the inner aperture of the parabolic mirror limits the diameter (and thus the NA) of the observation optics. For the observation of the radial area nearby the focal point of the parabolic mirror the imaging optics must not block the trapping beam path. In response to the condition of limited space available inside the NPMM the optical concept is adapted accordingly, see fig. 4.11. The trapping optics consists of two optical elements used for beam shaping and beam focusing. Due to the same but inverted slope of the second axicon surface a collimated annularly shaped beam leaves the element. This ring propagates in free space until it is focused ideally without aberrations by a segmented parabolic mirror.

For observation, an additional illumination beam is incident on the particle sideways. The trapped particle acts like a point source and the scattered light, is deflected to the observation optics located outside the trapping system. The outer dimension of the 45° plane mirror and its distance to the trapped particle determine the maximum NA of the imaging system. As indicated with the orange beam path in fig. 4.11, the 90°-beam deflection leads to a distortion of the image. The reason can be traced back to geometric relationships regarding the vicinity of the trapped particle relative to the plane mirror. The distortion can be optimized by adapting the angle of the mirror so that the beam is axially symmetric after the 90° beam deflection. Unfortunately, this optimization is just valid for exact one distance of the particle to the center of the mirror. Since the main task of the observation optics is to verify if a particle is optically trapped, the imaging quality has not to be as good as achieved with a highly optimized microscope

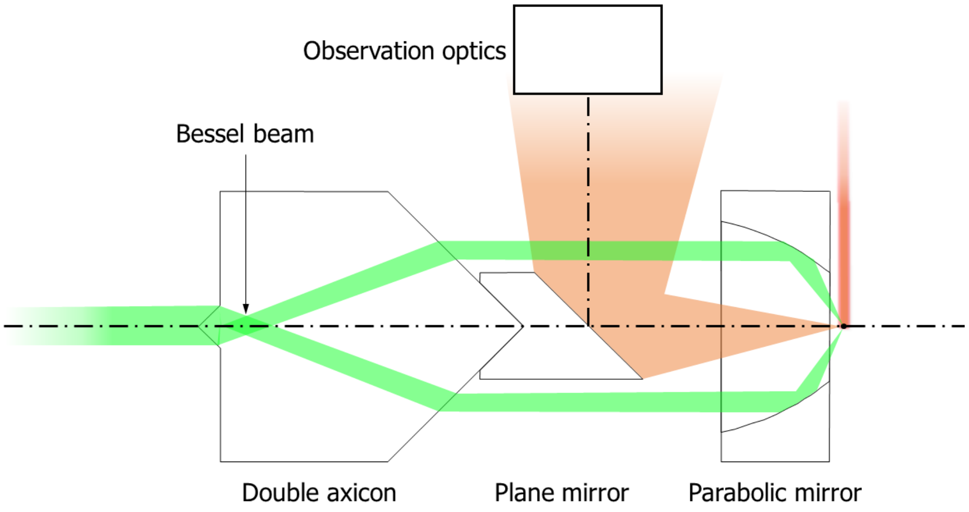

Figure 4.11: Final concept of the optical system for trapping (green ray path) of particles in gaseous environment and integrated plane mirror for observation (orange ray path).

imaging system. Thus, an image distortion can be accepted since it can be partially compensated afterwards using image processing techniques.

In principle, it is possible to exploit the scattered light of the trapping laser for observation. The separate illumination laser source, shown in fig. 4.11 is necessary to make the observation independent of the trapping laser and the changes of its intensity. If e.g. an optically held particle should be released, the trapping laser will be switched off and observation immediately is impossible, which has to be avoided.

The optical components conceptually presented in fig. 4.11 are the starting point for the iterative optical design process which is discussed in the following section.

4.2.2 Development of the optical system: Iterative optical design process

The development of systems suited for optical tweezing applications requires new merit functions implemented in the optical design process. This is different to conventional lens design, since a new value, the optical force has to be considered and optimized. The classical design process is extended by the optical force simulation based on GOA [123]. In order to start with the design process, the concept derived from the specifications given in the previous section has to be optimized. The crucial design parameters are the sufficiently large WD and the NA of the parabolic mirror. Since the size, especially the outer radius of the trapping system is limited a compromise between the WD and the NA needs to be found. This tradeoff leads to parameters, which have to be optimized for a sufficient trapping performance of the system.

- Inner and outer diameter of the ring shaped intensity distribution: 10 to 25 mm (free space for observation optics restricts inner diameter; size of the trapping system and mounting limits outer diameter).

Since the annular intensity distribution is realized with a double axicon, its slope angles, the material and the length of the component directly define the ring diameter. Furthermore, the waist of the Gaussian beam has to positioned at the first axicon surface and determines the thickness of the annular intensity distribution, see fig. 4.9.

- Focusing angle and distance between last surface of the parabolic mirror and the object to be trapped.

The parabolic mirror, which focuses the collimated ring is specified by the radius of curvature and the segment radii. It is obvious, see fig. 4.10, that outer rays are focused with lower angles compared to rays located closer to the optical axis. As a consequence, high NA focusing can be achieved by ring distributions with smaller diameters. In addition, larger radii of curvature of the parabolic mirror are required which is advantageous for the manufacturing process.

For the material of the axicon PMMA is chosen since it is well suited for the milling processes and provides high transparency within a broad spectral range. The slope angle of both axicons is set to 45°. In order to mount the components with standard optic holders, the outer diameter of both components is set to 25 mm. Due to the handling of the components during the manufacturing process and the mounting later on, the optically active area is limited to a maximum diameter of 20 mm. The length of the double axicon and the parabolic mirror is initially set to 35 mm and 10 mm, respectively. Enough space is left between both elements to integrate the observation optics. The focusing mirror has a parabolic shape defined by a conic constant of -1. Its radius of curvature is -4 mm. The section of the paraboloid starts at 3.15 mm from its center which yields an inner aperture radius of 5 mm. These parameters lead to a free working distance of 1.1 mm. Fig. 4.12 shows the conceptual drawing of the system start design. The green area marks a cylindrical volume with a diameter of 20 mm within the trapping laser beam will propagate. Surfaces within this area which interact with the beam are planned to be of optical quality. The system presented in fig. 4.12 has a clear aperture with a radius of 5 mm available for the integration of additional observation optics and provides a maximum NA of 0.9 for the trapping beam. Consider a Gaussian beam is incident on the first axicon tip. Due to the relocation of the high intensities at the center of the Gaussian profile to the outer regions of the ring shaped distribution, they are focused with comparatively low NA. If an inverted axicon is applied for the ring generation, higher intensities propagate at the inner edges of the ring. This will result in higher trapping forces but the manufacturing of an accurate inverted tip is difficult. Thus, the double axicon, as illustrated in fig. 4.12 is preferred. Consequently, the NA of the system is not a sufficient information to describe the trapping potential generated by the system. Instead the intensity values of the annular distribution have to be linked to the focusing angles in order to calculate the trapping forces.

This is achieved using the optical force simulation tool where the intensity distribution is expressed as an array of pixels, each linked with an associated focusing angle, see fig. 3.3. The intensity distribution generated behind the parabolic mirror at 100 μm in front

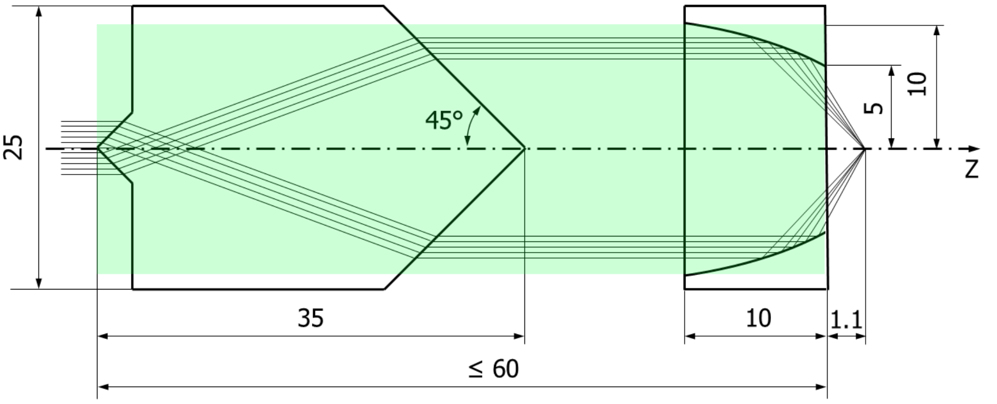

Figure 4.12: Start design of the optical system for trapping particles in gaseous surrounding.

of the focal point is computed by the optical design software [287] and used as input for the force simulation. Further input parameters applied for the force simulation are a laser power of P = 50 mW, a refractive index of n= 1.4496 @ 1070 nm (fused silica) of the spherical particle with a diameter of 10 μm and as given by the optical design software a value for the spot radius of GEO = 1 μm. Optical forces acting on the particle in axial and lateral direction are visualized in fig. 4.13. The maximum optical trapping force (acting in negative Z-direction) achieved with this system design is 29.5 pN. Optical forces acting in Z-direction (fig. 4.13 left) form a stable optical trap with steep force walls. Neglecting external forces like gravity, the particle will be trapped optically on the optical axis (X = 0) at the position Z = 100 μm. As indicated with both optical force curves (gravitational force acting on particle 11.31 pN, optical force F_{-z} = 29.5 pN), there is still potential left to optimize the system in terms of increasing the working distance. Based on the considerations concerning the relation of the WD with the parameters of the parabolic mirror, shown in fig. 4.10, the WD can be increased by decreasing the radius of curvature. In parallel, the section of the parabolic mirror has to be adapted such that the inner aperture radius is kept constantly at 5 mm. The results are visualized in fig. 4.14.

The variation of the radius of curvature from 4 to 3 mm leads to an increase of the working distance from 1.1 to 2.7 mm. In contrast, the trapping force drops from 29.5 to 17.1 pN using an input laser power of 50 mW. Furthermore, the ratio of optical forces acting in positive and negative Z-direction significantly rise. Thus, a highly non-symmetric axial optical trap occurs. Further optimizations using the iterative optical design process finally lead to a radius of curvature of 3.5 mm, which means a good compromise between a sufficiently large working distance and a stable optical trap. Applying this value a working distance of more than 1.8 mm can be achieved. Moreover, the ratio of the axial optical forces responsible for trapping the particle compared to the scattering forces pushing the particle away is also favorable, see green the curve in fig. 4.14 left. To summarize the optimal parameters of the parabolic mirror, a suitable working distance

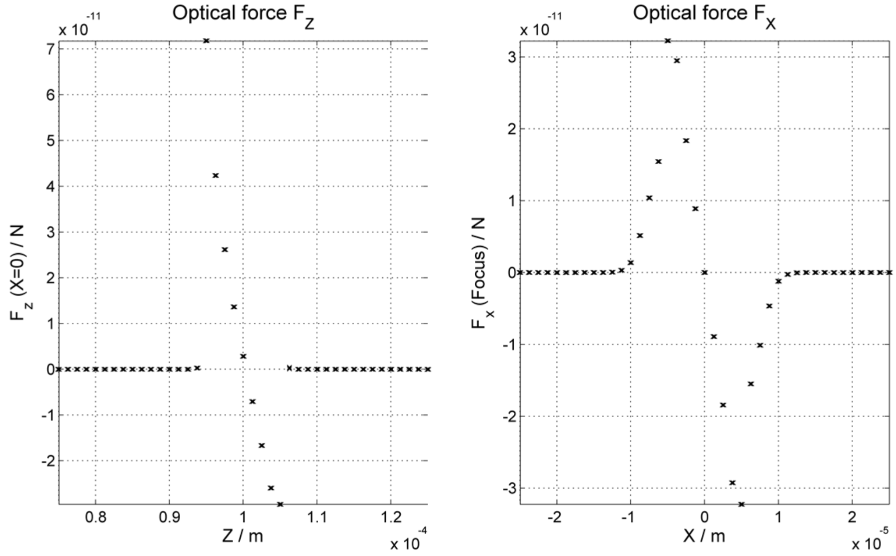

FIGURE 4.13: Optical force simulation (gaseous surrounding) of the first system design. Optical forces acting in axial (left) and in lateral direction (right).

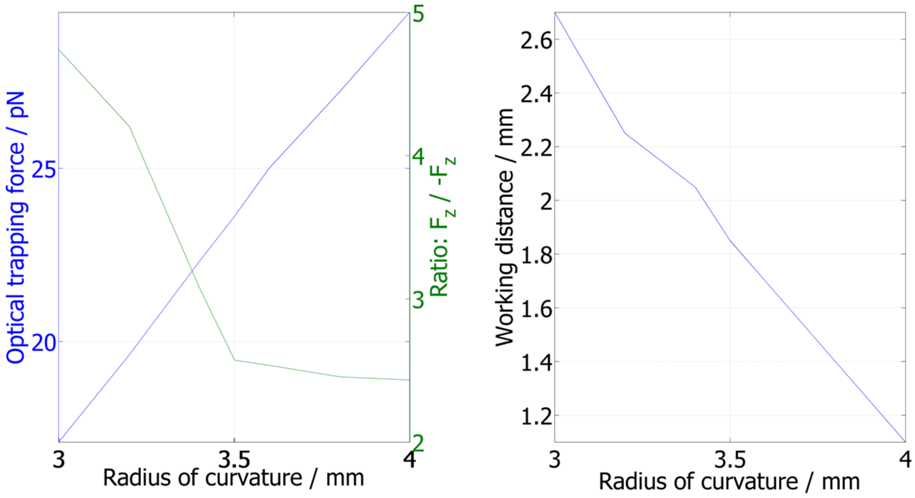

FIGURE 4.14: Optical forces and working distance as a function of the paraboloid radius of curvature.

with a stable optical trap is maintained with a radius of curvature of 3.5 mm and by using a section of the parabolic surface starting at 3.75 mm from its center. This leads to an inner aperture of 5 mm (free space for the observation optics) and an entrance aperture for the collimated ring distribution of 10 mm.

Since the maximum length of the system should not exceed 60 mm (length of standard objective lenses [259]), the space for the integration of additional optics is limited. The current length of the double axicon is 35 mm and 10 mm for the parabolic mirror. This results in a length of 15 mm available for the observation optics. Remembering the

concept shown in fig. 4.11, the imaging beam path leaves the trapping system sideways. In order to leave enough space to not block the observation beam path, the trapping system has to be optimized in that way too.
One approach to increase the space left for the observation optics, is to decrease the length of the double axicon. Considering the current setup, if the cross-sectional area of the first axicon is equivalent to the size of a Gaussian beam, the inner diameter of the collimated ring leaving the second axicon is 6.1 mm. In addition, the inner part of the ring contains less intensities than the outer area. The focusing angle generated by the parabolic mirror rises if the distance between the ray to be focused and the optical axis decrease. Consequently, by reducing the length of the double axicon to 30.9 mm the inner diameter of the annular intensity distribution is adapted to the inner aperture of the parabolic mirror. These modifications finally lead to a maximum optical trapping force of 29.7 pN and an axial optical force ratio of 2.4 as shown in fig. 4.15. The diagrams presented in fig. 4.15 look quite similar to those shown in fig. 4.13, representing optical force simulations of the first system design. But in contrast to the first design the working distance is increased from 1.1 to 1.9 mm. Furthermore, the length available for additional observation optics is extended from 15 to 19 mm which represents almost one third of the whole system length.

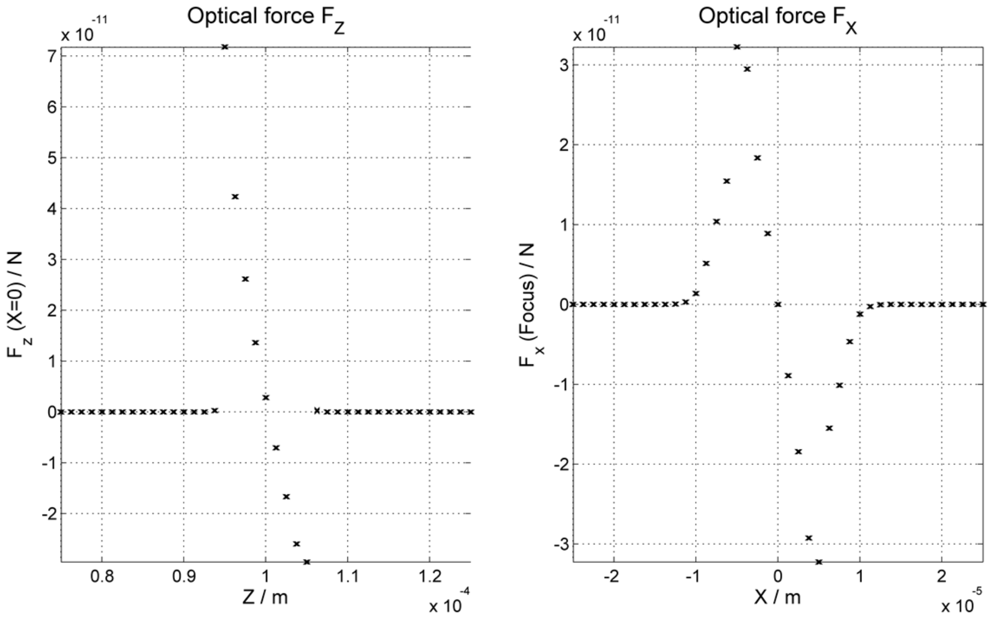

FIGURE 4.15: Optical force simulation of the final system design. Optical forces acting in axial (left) and in lateral direction (right).

The conceptual drawing of the optical trapping systems final design is shown in fig. 4.16. By arranging both components directly next to each other, the total system length is 40.9 mm. A cylindrical volume of 19.1 mm in length is left for the integration of a mirror to deflect the imaging beam path by 90°. The slope angles of both axicons are set to 45° and the material between these surfaces is supposed to be PMMA. Variations of the slope to higher angles lead to increasing Fresnel losses as shown in fig. 2.4. Decreasing the slope angle requires a larger double axicon length to achieve the same ring dimensions at its exit. The diameter of the first axicon is set to 4 mm providing enough cross

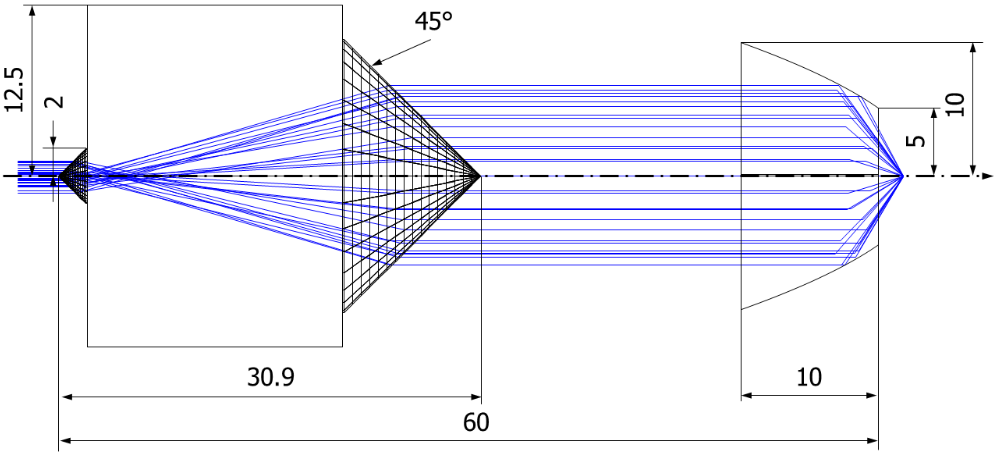

FIGURE 4.16: Final design of the optical system for trapping particles in gaseous surrounding.

sectional area to efficiently shape Gaussian beams with diameters up to 2 mm ($\frac{1}{e^2}$). The parabolic mirror has a radius of curvature of 3.5 mm. For the mirror a section starting at 3.75 mm from its origin is applied. This yields to an inner aperture of 5 mm. With an outer aperture of 10 mm the thickness of the parabolic mirror follows with 10 mm. These parameters completely describe the geometry of the trapping system.

As indicated with the conceptual drawing of the optical system presented in fig. 4.11, the observation of the object to be optically trapped is realized outside the trapping system. An integrated mirror deflects the imaging beam laterally out of the system. Due to the inner diameter of the collimated ring shaped intensity distribution leaving the double axicon, free space with a cylindrical volume of 10 mm in diameter and 20 mm length is available. The geometry of the mirror is adapted accordingly. The diameter of the mirror is set to 10 mm and the total length is 15 mm. To realize a 90° beam deflection, the mirror surface has an angle of 45°. For the mounting of the component a conical hole is designed on its back. This hole is the counterpart to the second axicon surface resulting in a self-alignment, see fig. 4.17. The distance between the mirror and the double axicon is not drawn to scale. In order to easily mount the mirror on the second surface of the double axicon, a threaded blind hole is introduced at the center of the conical shaped cavity.

Due to the non-symmetric shape of the mirror the farthest distance between the object to be trapped and the mirror edge is applied to determine the maximum NA. Assuming a total system length of 60 mm and a working distance of the parabolic mirror of 1.9 mm, the maximum NA for the observation optics is 0.17. Applying the Abbe diffraction limit, this value is sufficient to image particles with 10 μm in diameter. For the externally placed imaging system a standard two lens setup with a CMOS camera is used.

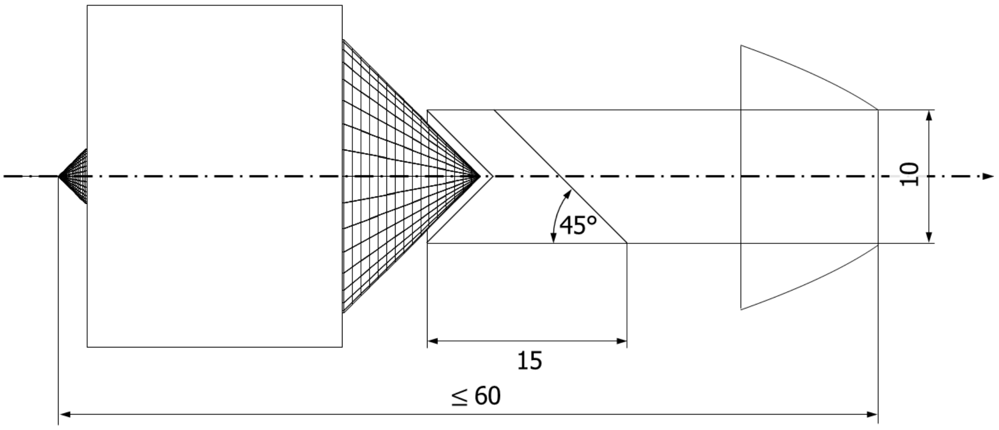

FIGURE 4.17: Mirror for the 90° deflection of the imaging beam path.

4.2.3 Characterization of the optical components: Surface measurements using white light interferometry

All optical elements, the double axicon, the parabolic mirror and the 45° plane mirror were fabricated by the company LT-Ultra [153]. The double axicon is made of PMMA with a diamond turning process. For the parabolic mirror the same process is used. Its material is OFHC (Oxygen-free high thermal conductivity) copper with an additional gold coating as protection layer and for higher reflectivity. The 45° plane mirror is made of an aluminum alloy (AlMgSi1) that is highly resistant and with high reflectivity. Thus, no additional coating is required. For optical mounting the double axicon, shown in fig. 4.18 a), it is assembled with an optical adhesive [190] on a lens adapter. Since most energy of the incident Gaussian beam is concentrated on the optical axis and hence

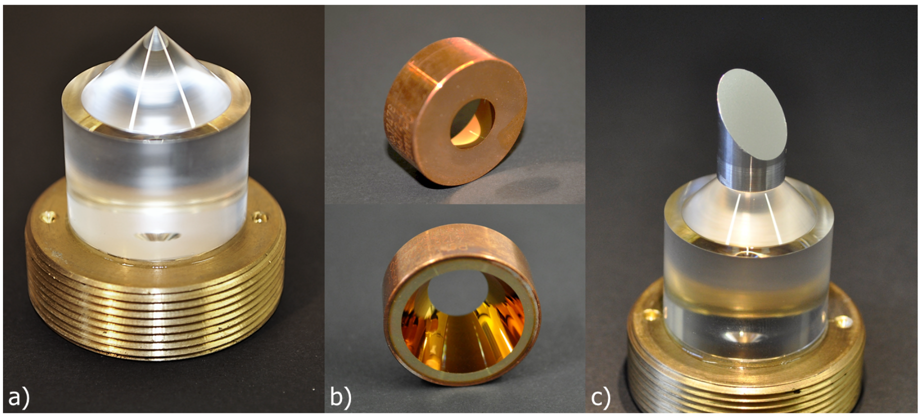

FIGURE 4.18: Optical components: double axicon a), parabolic mirror b) and 45° plane mirror c) mounted on the double axicon.

distributed by a comparatively small region of the first axicon, the quality of the tip has to be as high as possible. Therefore, the first axicon surface is located inside the adapter to prevent damages of the tip.

Fig. 4.18 b) shows the unmounted parabolic mirror from its back (upper image) and front (lower image). The gold coating added to the parabolic surface increases the reflectivity approximately by 5 % in the visible and by 0.3 % in the near infrared spectral range. These reflectivity enhancements have minor importance since the main purpose of the gold coating is to minimize the corrosion of the copper surface. The 45° plane mirror is shown in fig. 4.18 c). It is mounted on the tip of the second axicon surface by applying an optical adhesive [190]. Due to the self-aligning connection of the 45° plane mirror and the double axicon just the orientation of the mirror relative to the optical setup has to be adjusted later on.

In order to verify the shape accuracy and roughness of the optical surfaces, each component is optically characterized using white light interferometry. Starting with the double axicon, a roughness of $R_a \leq 20$ nm is verified for both conical surfaces. To obtain this value the measurement data is post-processed by subtracting the curvature of the cone and a measurement tilt error as well. The tilt error is due to misalignment of the optical component relative to the objective lens of the white light interferometer. After these post processing steps a plane surface results and its average depth variations can be used to compute the surface roughness, see fig. 4.19. The false color image presented in fig. 4.19 left, shows the data for the plane surface of the second axicon. The traces of the diamond turning process are clearly visible and are oriented perpendicularly to the axis of symmetry for both axicon surfaces. Consider the tilt of the traces relative to the X- and Y-profiles (fig. 4.19 right) a tool mark period of 10.8 μm ± 1.7 μm follows from the peak to peak distances. This potentially results in a Fresnel lens like diffraction pattern which has to be clarified with caustic measurements.

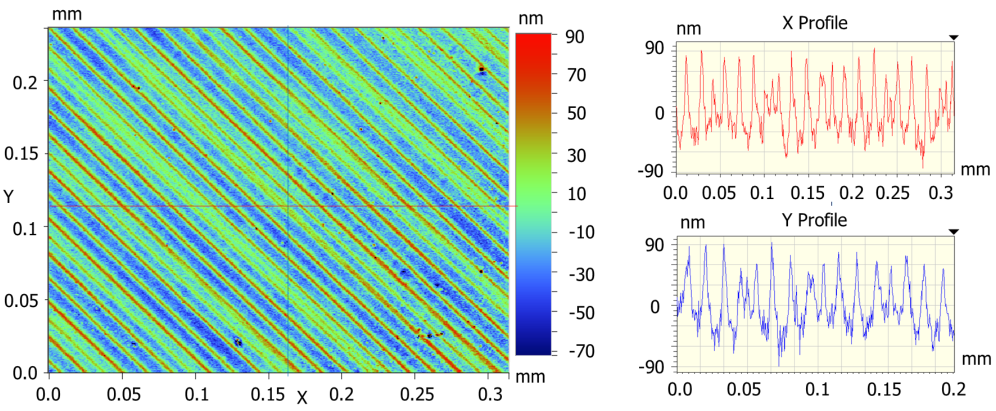

Figure 4.19: White light interferometric measurement of the second conical surface of the double axicon.

For the investigation of the axicon tips, the component is placed inside the white light interferometer oriented along the direction of the objective lens and its depth scan movement. Due to the small radius of curvature of both tips and the limited NA of the objective lens, the reflected light is just collected within a comparatively small region. Nonetheless, the curvature of both tips is apparent and visualized in a three dimensional graphic, shown in fig. 4.20. The blue areas represent regions where no data is available. The extraction of several cross sections result in a radius of curvature of 70,3 μm ± 14.2 μm for the first and 0.53 mm ± 0.05 mm for the second axicon tip. The region of data points available for the inspection of the first axicon (fig. 4.20 left) is more than 10 times smaller compared to the second one (fig. 4.20 right). This fact results from the higher radius of curvature of the first tip. Since the measurement beam is incident vertically, the major part of the beam is reflected and propagates nearly horizontally. These rays can not be collected by the objective lens. Just the rays which are incident directly on the axicon tips contribute to the measurement data.

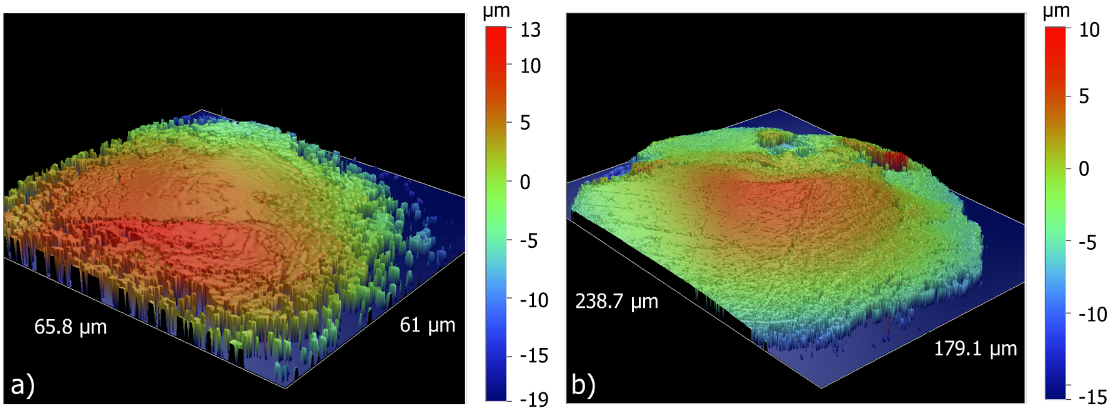

FIGURE 4.20: White light interferometric measurement data of the first a) and second b) axicon tip visualized in three dimensions.

For the 45° plane mirror a surface roughness of $R_a < 6$ nm is verified experimentally. Due to the steep slope of the parabolic mirror and the limited working distance of the white light interferometer no measurement data could be achieved. Because of the good agreement between the measurement results of the double axicon and the plane mirror with the values specified by the manufacturer [153], the surface quality of the parabolic mirror is assumed to be within its specifications.

4.2.4 Optical setup for trapping and observation of particles in gaseous surrounding

The laser source used for the optical trapping experiment is an Ytterbium doped fiber laser with an emission wavelength of 1070 nm [113]. The beam quality factor is verified to be better than $M^2 = 1.1$ and the laser radiation is linearly polarized with a contrast of 92% between both polarization directions. Fig. 4.21 visualizes the optical setup schematically. The diameter of the beam leaving the collimation optics is 5.87 mm ± 0.11 mm ($\frac{1}{e^2}$) at its waist. In order to match the beam with the first axicon, its diameter is reduced to 1.96 mm by use of a 3:1 telescope. For beam quality improvement a spatial filtering is implemented at the Fourier plane of the telescope applying an aperture of 200 μm in diameter. After leaving the telescope the beam is refracted at the first surface of the double axicon and is transformed to a divergent ring. The second axicon surface collimates the divergent beam and results in a collimated ring shaped distribution with an inner and outer diameter of 12.84 mm ± 0.18 mm and 14.93 mm ± 0.1 mm, respectively which matches well with the values obtained for the final optical design. The ring propagates around the 45° plane mirror and hits the parabolic surface of the focusing mirror. Finally, the beam is focused at a distance of 2.05 mm behind the parabolic mirror. These components represent the optical tweezers with a telescope used for beam preparation. Between both elements a 45° plane mirror is integrated to realize simultaneous observation. The observation laser beam ($\lambda = 532$ nm) hits the trapped particle at a particular angle of incidence relative to the optical axes. This angle is optimized for maximum scattered intensity available for both observation directions. The side observation is realized with an objective lens providing super long working distance and a magnification of 8. Hence the particle is imaged through an IR filter onto a CMOS array. Axial observation is realized by a 90° beam deflection via the 45° mirror. By applying a two lens imaging setup with an IR filtering the object to be trapped is imaged onto another CMOS sensor. To determine the optical resolutions achieved in both observation directions a USAF test chart [265] is applied as imaging target. In lateral direction (objective lens) line pairs of the group 7 element 3 can be resolved which corresponds to a maximum resolution of 3.1 μm. For observation in axial direction (45° plane mirror), the target lines of the group 6 element 5 are imaged as separate objects onto the CMOS sensor. This yields to a maximum resolution of 4.92 μm. Both resolutions achieved with the optical systems presented in fig 4.21 are sufficient to resolve a particle with a diameter of 10 μm. It should be noted that single particles, which scatter light act as point sources and thus, the position of significantly smaller objects can be determined as well.

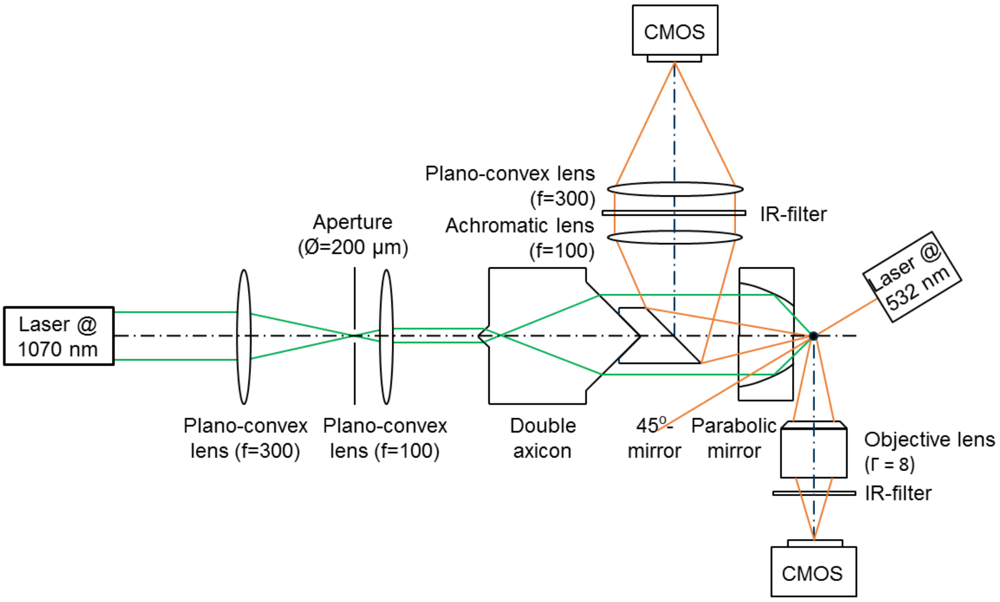

FIGURE 4.21: Optical setup for the optical trapping (green) and observation (orange) of particles in gaseous environment.

To avoid that the laser beam used for observation directly hits the CMOS sensors it has to be oriented in between. As mentioned before, the angle of illumination can be optimized in terms of maximum scattering intensity for both observation directions. Using Lorenz-Mie theory, as described in section 2.1.1 the scattering pattern of a plane wave (λ = 532 nm) scattered by a spherical fused silica particle of 10 μm in diameter is computed and visualized in fig. 4.22 right. The angle of incidence of the observation laser source is selected such that both observation directions match the side slopes of the scattering pattern. For an angle of incidence of $\alpha = 20.9°$ at least three scattering lobes contribute to the intensity available for the observation in both directions. In addition, the ratio of forward to sideward scattering is optimized to provide maximum stray light intensity. The influence of the angle of incidence on the particle brightness can be observed directly in the trapping experiments for both directions. The optical setup used for optical trapping and observation in parallel is presented in fig. 4.23. The collimated trapping laser beam leaves the fiber collimator and propagates downwards through the telescope and the double axicon until it is focused by the parabolic mirror. Fig. 4.23 b) shows the side observation applying an objective lens and a CMOS camera. The axial observation is presented in the upper section of fig. 4.23 b). The laser source hits the trapped particle and the stray light propagates through the output aperture of the parabolic mirror and is deflected by the 45° plane mirror. This beam is finally imaged onto the CMOS camera.

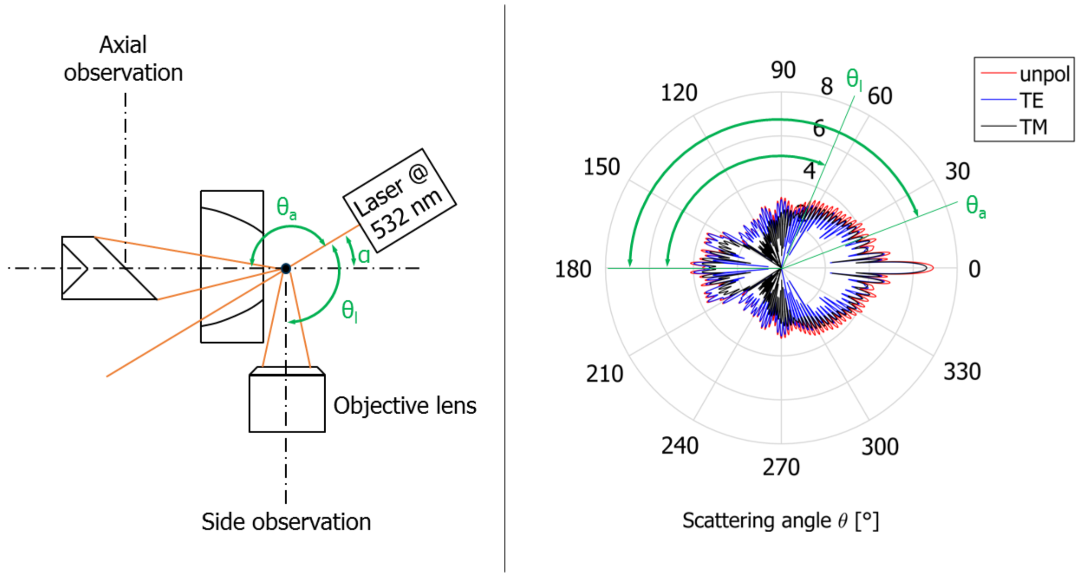

FIGURE 4.22: Schematic drawing of the optical setup applied for the observation (left) and the scattering pattern (right) based on Lorenz-Mie theory for unpolarized (unpol) radiation and for the polarization directions oriented perpendicular (TE) and parallel (TM) to the plane of incidence.

In order to reduce the impact of externally introduced turbulences an enclosed air volume is maintained by a customized test chamber. The stability is provided by transparent glass walls (microscope cover slides) with a height of 76 mm, a width of 26 mm and a thickness of 1 mm. The walls are assembled at the edges with double-sided tape. For the front wall, cover slides with smaller lateral dimensions and a thickness of 170 μm are applied. Thus, the spherical aberrations are minimized. The particle supply is realized

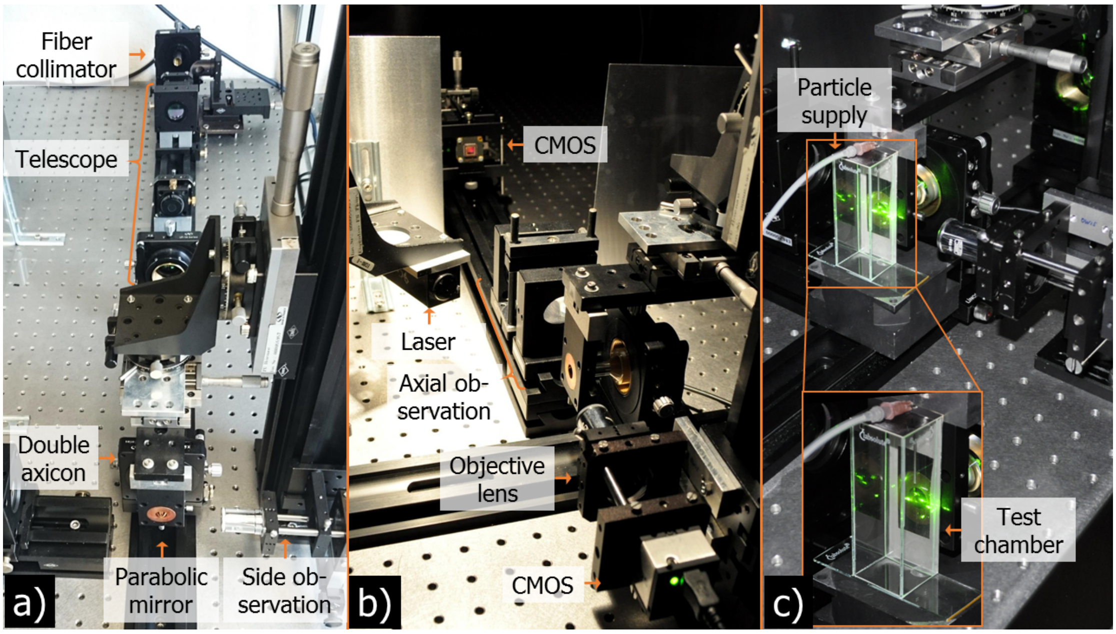

FIGURE 4.23: Optical setup for optical trapping a) and observation b), as well as the test chamber c) with particle supply on the top.

using a small tube connected with a hose and a syringe filled with air and the particles as powder. By compressing the syringe, the particles are accelerated through the hose and leave the tube directly above the position of the optical trap.

4.2.5 Characterization of the optical system: Intensity measurements

According to the procedure described in section 3.3.2, the focal spot and the caustic of the system is measured by a CMOS based sensor. For the well aligned optical trapping system the caustic is recorded step by step within an axial range of 2.5 mm around the focal point. Intensity measurements were performed incrementally each 50 μm. Fig. 4.24 presents the caustic within an axial range of 500 μm measured around the focal point. The focal spot of the system is presented enlarged top right. One pixel located at the center of the sensor (5.3 μm) is illuminated perfectly. Investigations of several spot measurements lead to a full width half maximum (FWHM) focal spot size of 27 μm ± 3 μm.

Interestingly, the annularly shaped intensity distributions recorded in front of and behind the focal point show different widths and shapes, see the intensity distributions measured at a distance of the focal point of ± 200 μm, shown in fig. 4.24 right. To investigate the relationship of the ring width and its position on the optical axis further intensity measurements were performed at larger distances. The thinnest ring width is achieved at a position located 200 μm behind the focal point. For positions larger than 200 μm the ring width increases and is comparable to those measured in front of the focal point. This behavior can be traced back to manufacturing errors and the physical nature of Gaussian beams. The assumption made, that the trapping laser beam leaves

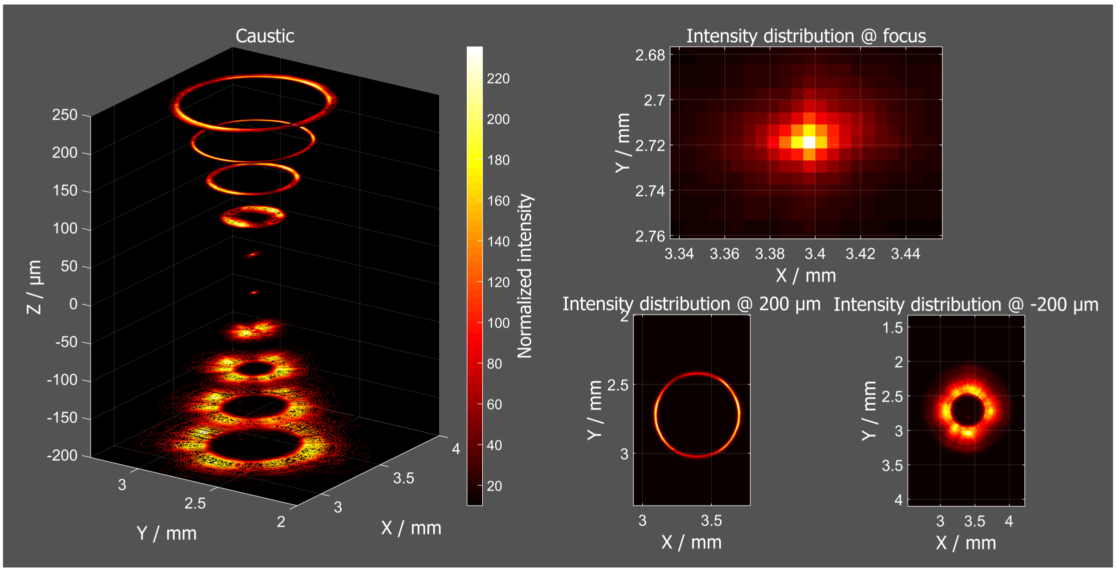

FIGURE 4.24: Caustic measurement of the optical trapping system and intensity distributions recorded at the focal region.

the collimation optics as a plane wave is just an approximation. In fact, the beam always propagates as a convergent or divergent wavefront which causes the differences of the ring shape especially around the focal region.

For the experimental determination of the working distance, the intensity is measured directly behind the parabolic mirror and at the position of the smallest spot size. The displacement of the CMOS sensor between both positions is used to calculate the working distance. The internal setup of the CMOS camera model UI-1240SE contains a cover glass in front of the CMOS chip. Between this cover glass and the CMOS chip a volume filled with air of approximately 500 μm thickness is left free. This arrangement leads to a parallel beam offset, which has to be considered. Finally, a working distance of 2.05 mm is achieved. This value is 150 μm larger compared to the designed working distance of 1.9 mm. Due to measurement tolerances, as well as missing geometries and tolerances of the internal camera setup, which is not specified by the manufacturer [110] an error of 10 % should be estimated for distant measurements of strong diverging beams. This finally yields to a working distance of 2.05 mm $\pm$ 205 μm.

4.2.6 Optical trapping in gaseous surrounding

For optical trapping experiments spherical fused silica particles with a diameter of 10 μm were used [277]. The gravity is 9.81 $\frac{m}{s^2}$ and for a volumetric mass density of 2.201 $\frac{g}{cm^3}$ a gravitational force of 11.31 pN acting on the particle results, neglecting friction and buoyancy. This force has to be overcome in order to optically hold a particle. Furthermore, since the particle falls into the optical trap, its momentum has to be compensated as well. The experimental setup shown in fig. 4.23 indicates that gravity acts on the particle perpendicularly to the optical axis. This orientation has two advantages: the particle supply can be realized easier compared to an optical setup oriented vertically.

Secondly, the optical holding force, which has to act towards gravity is realized with the lateral optical forces, see fig. 4.15 right. This force is 10% higher compared to the optical forces acing in negative axial direction.
Using this configuration without the additional laser source applied for illumination, the side observation shows the caustic of the trapping optics, see fig. 4.25. The trapping beam propagates from left to right. Due to the reflection of the laser beam on the entrance wall of the sample chamber the bright area left occurs. The caustic becomes visible by particles falling downwards through the focused trapping beam. Fig. 4.25 is generated from a video of 50 min recording time and 20 frames per second. If a particle falls through the beam it scatters the light and causes a visible trajectory of grey values on the image recorded with the CMOS sensor. By use of image processing afterwards, all frames are copied into matrices. If the matrix elements have values above a defined threshold they are copied in another matrix, which is shown in fig. 4.25. This matrix has only the values one representing an occupied element or zero for empty elements. The parabolic mirror is located at the position $Z = 0$. By highlighting the shape of the caustic with the red colored lines, the circle positioned at their intersection point qualitatively marks the location of the optical trap. Once a particle is trapped optically, a bright spot will occur inside this region.

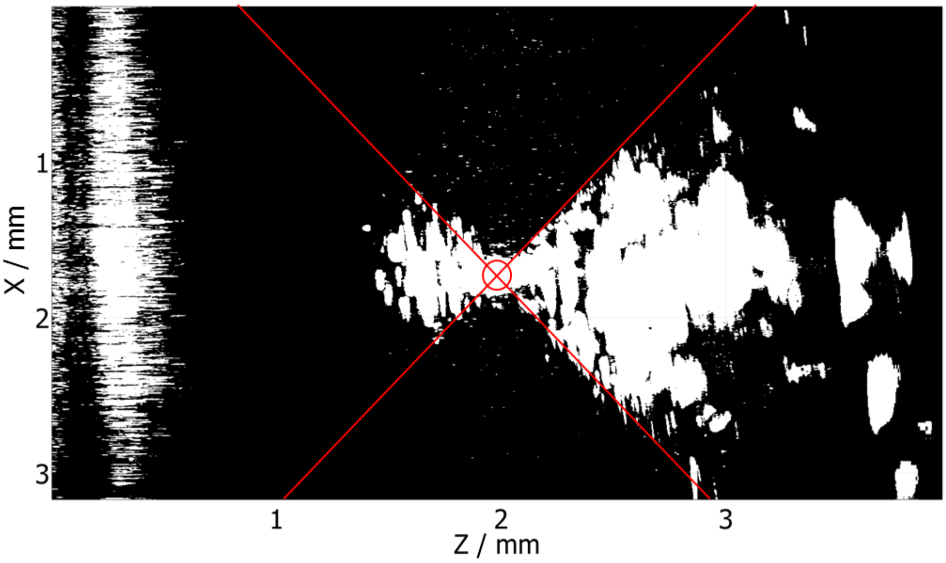

FIGURE 4.25: Side observation showing the caustic of the optical trapping system (oriented from left to right) by particles which become visible while falling downwards through the focused beam.

To visualize optical trapping, the videos recorded with the camera are processed again. Now, the length of stay is visualized by adding up all frames of the video to a new matrix of gray values, see fig. 4.26. Comparing the gray values of the particle qualitatively with the bright areas caused by stray light on the left hand side of fig. 4.26 its high brightness becomes clear. For the observation of the particle without an additional light source it is definitely noticed by the CMOS imaging sensor if a particle is optically trapped. As mentioned before, it is advantageous to use a separate illumination source for the observation. The image recording procedure is the same as applied for fig. 4.25 and 4.26, but

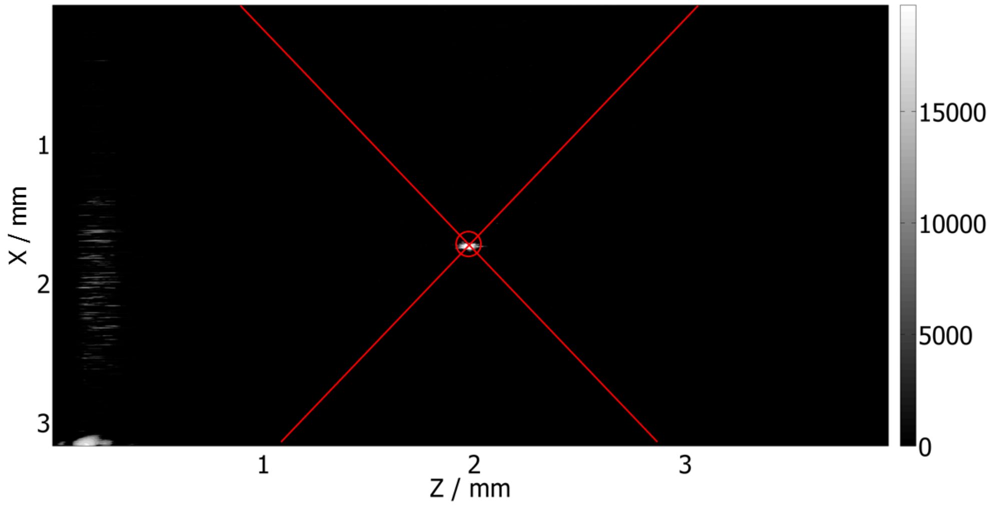

FIGURE 4.26: Optical trapping of a spherical fused silica particle with 10 μm in diameter in gaseous surrounding; the gray values represent intensities above a certain threshold depending on their length of stay in arbitrary units.

the intensity provided by the illumination laser source is much less. The trapping laser power is varied within a range of few mW up to 2 W. Thus, even the scattered light for such high intensities by far exceeds the dynamic range of the CMOS chip. Especially the higher laser power can cause damage to the sensor. NIR-filters are implemented in front of each sensor and the additional laser source provides the illumination of the particle. The NIR trapping laser source has an analogue knob to tune the laser power. A display shows the pump-diode current. To link the diode current to the output laser power several measurements were performed using a silicon-photodiode based sensor [45]. The sensor is placed at several positions within the beam path and directly behind the parabolic mirror. As a result, the relation between the diode current and the laser power at the focal position is obtained. It has been found that one third of the laser beam power is lost by propagating through the system starting from the fiber collimator to the exit aperture of the parabolic mirror. The laser power values given in this section represent always the power at the position of the optical trap.

Optical trapping of single particles is observed in axial and lateral direction presented with the 6 frames shown in fig. 4.27. First, the particle is optically trapped with a laser power of 1 W. By incrementally reducing the laser power, stable optical holding is verified down to values of 29.8 mW ± 1 mW. The frames shown in fig. 4.27 are recorded while the trapping region is illuminated with the additional observation laser (frequency doubled Nd:YAG laser source, $\lambda = 532$ nm) whereas its beam center is adjusted to the trapped particle such that it shines as bright as possible. By varying the angle of incidence of the illumination laser while maintaining the overlap of the beam center with the particle to be trapped fluctuations of the particle brightness due to scattering can be observed. As discussed in the previous section, according to the scattering pattern the angle of incidence is optimized, see fig. 4.22. Specific attention has to be paid to avoid reflections of the illumination laser beam at the optical elements or its mountings. Both frame series show a bright spot on the center left which is caused by the entrance of the

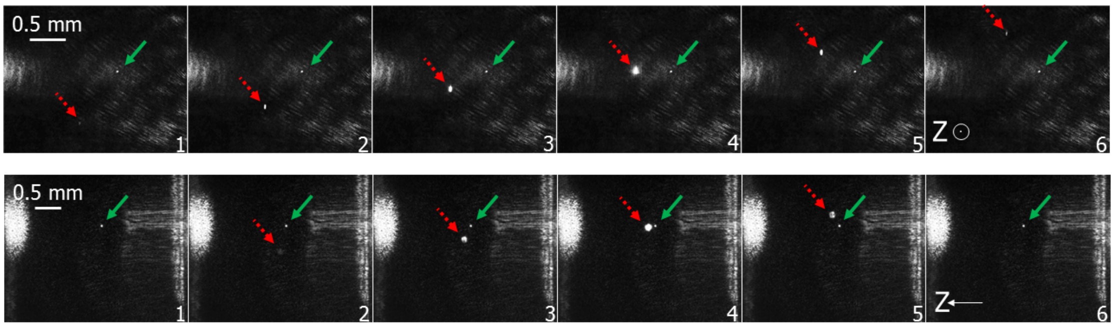

FIGURE 4.27: Optical trapping (green arrow) of a spherical fused silica particle with a diameter of 10 μm in gaseous surrounding and a free particle passing by (red arrow) observed in axial (top) and lateral (bottom) direction.

illumination laser beam in the test chamber. While optically holding a particle (green arrow in fig. 4.27) a free particle (red arrow in fig. 4.27) passes by in upward direction. This means that turbulences inside the trapping chamber cause a drag and accelerate free particles upwards. As observed frequently, if the particles reach the upper region of the chamber they turn around along a loop shaped trajectory and fall down at the edges of the sample chamber. The same process happens at the bottom of the test chamber until the particles rise again at the center of the chamber.

The movement speed of free particles at the focal region is measured and has a value of 0.6 $\frac{mm}{s}$ for a laser power of 50 mW. This behavior supports the particle supply since particles pass the region of the optical trap in repetitive manner. Furthermore, the speed and the trajectories of the particles strongly depend on the dimension of the test chamber and the trapping laser power. The movement of particles only starts by turning on the trapping laser and gets faster by increasing the laser power. However, the most crucial factor is the depth of the chamber. A value of 4 mm is determined to be optimal. If the depth is increased, the volume of the chamber rises so that the particle density decreases and particles are traveling through the trapping region rarely. In contrast, if the distance between the front and rear wall is chosen to be less than 3 mm, the particle speed rises until optical trapping becomes nearly impossible.

Due to the regular occurrence of optical trapping of multiple particles in parallel, this fact is discussed in the following. Since the particle supply is realized by use of a syringe filled with air and fused silica spheres, the compression of the syringes volume leads to a particle flux through a hose that ends in a needle. The exit of the needle is located above the optical trap but despite precise alignment, optical trapping is realized in statistical terms. Hundreds of particles leave the syringe needle and fall through the focal region of the optical trap until the flow conditions start to distribute them. In some cases, it happens that more than one particle is trapped at the same time and at slightly different positions. Fig. 4.28 shows three large bright spots located in the focal region. This area is visualized enlarged in the inset at the top right. Again the grey value gives information about the length of the stay. Obviously all three particles are not held at the same position and none of the particle is trapped at the position of the main trap shown in fig. 4.26. Multiple optical trapping is mostly observed within an area of 200 times 200 μm but sometimes even further out. In addition, the existence of local traps is underpinned during the experiments. Particles that are trapped at these

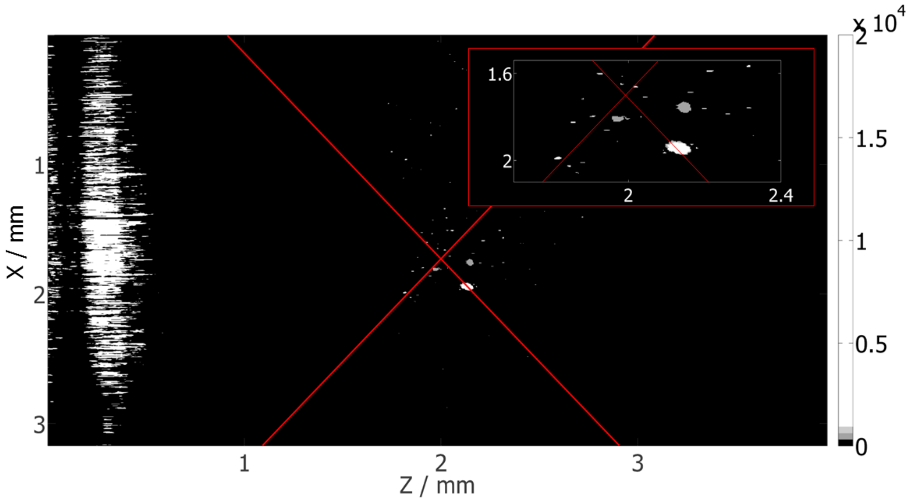

FIGURE 4.28: Multiple optical trapping of fused silica particles with 10 μm in diameter in gaseous surrounding; the gray values represent the length of stay of the trapped particles.

positions execute oscillating movements. The laser output power required to optically hold particles with the local traps is higher compared to trapping particles with the main trap. Once the laser power is set to values below 50 mW the locally trapped particles leave their positions along the particle stream in the chamber. This behavior triggers the interest in further investigations of non-ideal optical trapping conditions caused by tolerances in the alignment process and of the optical elements itself, as well as trapping as an interaction of optical and non-optical forces, see section 4.4.

Therefore, the optical force simulation is applied using the intensity distribution measured 300 μm in front of the focal point. The simulation result shows channel like structures of optical force vectors acting in positive X-direction, see fig. 4.42 in section 4.4. These optical force components and the non-optical forces generate a force equilibrium where particles can be trapped [120, 122]. The optical tweezers presented in this section is applied in section 4.4 to clarify these observations and to study how optical aberrations affect the trapping performance.

Based on the knowledge earned with this system, a second optical tweezers which enables the trapping of particles in liquid environment is discussed next.

4.3 Optical system for trapping of particles in liquid environment

The application this optical tweezers has to be used for is to assist a measurement method which requires high magnetic fields. Nuclear magnetic resonance (NMR) spectroscopy serves as a method to analyze the structure and dynamics of molecules and atoms [27, 214]. This method is very briefly explained in this work, more detailed information is given in several text books [105, 142]. Just the fundamental principle is described.

An atomic nucleus has a spin and can absorb and transmit electromagnetic energy. By applying a constant magnetic field B_0, the nuclei located in the field are aligned accordingly. If an additional magnetic field B_1 with a different orientation is applied in pulsed mode (MHz or radio frequency range) the orientation of the nuclei spins are perturbed relative to the original applied constant magnetic field B_0. Once the B_1 field is turned off each nucleus starts a precession [142] movement back to its initial orientation given by the B_0 field. Due to the fact, that each accelerated charge emits radiation [165], the precession of the nuclei causes a specific response, which depends on the nuclei, its surrounding and the applied magnetic fields [142]. If the properties of the nucleus and the fields are known, its molecular surrounding can be determined. The samples investigated with this method usually are of microscopic size and often located in liquid solvents. Optical tweezers can serve as a tool to manipulate the object of interest in terms of adapting its position, rotation and orientation.

For this purpose, an optical system has to be developed, which must consist of non-magnetic materials like glass, PMMA or copper. Furthermore, the system has to enable optical trapping in liquid surroundings embedded in a sample chamber with a wall thickness of almost 1 mm. This wall consists of several optically transparent layers having slightly different refractive indices [244]. The sample chamber serves as an NMR probe and is optimized for high resolution and high sensitivity NMR measurements as well as sufficient transparency for optical applications.

4.3.1 Development of the optical system: Concept

The optical boundary conditions and constraints for the development of the optical tweezers are very strict since the system has to be integrated within an existing setup made for non-optical purposes. According to table 3.2 the specifications to be met can be listed as follows.

- Optical trapping (and spinning) of single particles in liquid surrounding.
- Working distance: WD ≈ 1 mm through a stack of optically transparent layers.
- Solvent located inside sample chamber accessible from two sides, see fig. 4.29.
- Numerical aperture: limited by Helmholtz (HH) coil, NA ≈ 1.09 (focusing angle of 55°).
- Trapping of single particles made of optically transparent material (fused silica, PMMA, birefringent, etc.), diameter in the range of one to few 10 μm, spherical and ellipsoidal shape.
- Rotation of particles planned in the final stages of the project.
- Size of trapping system: semi cylindrical volume (radius 35 mm, length 70 mm).
- Optics and mounting made of material suited for high magnetic fields and with minor effect on magnetic environment (field homogeneity).

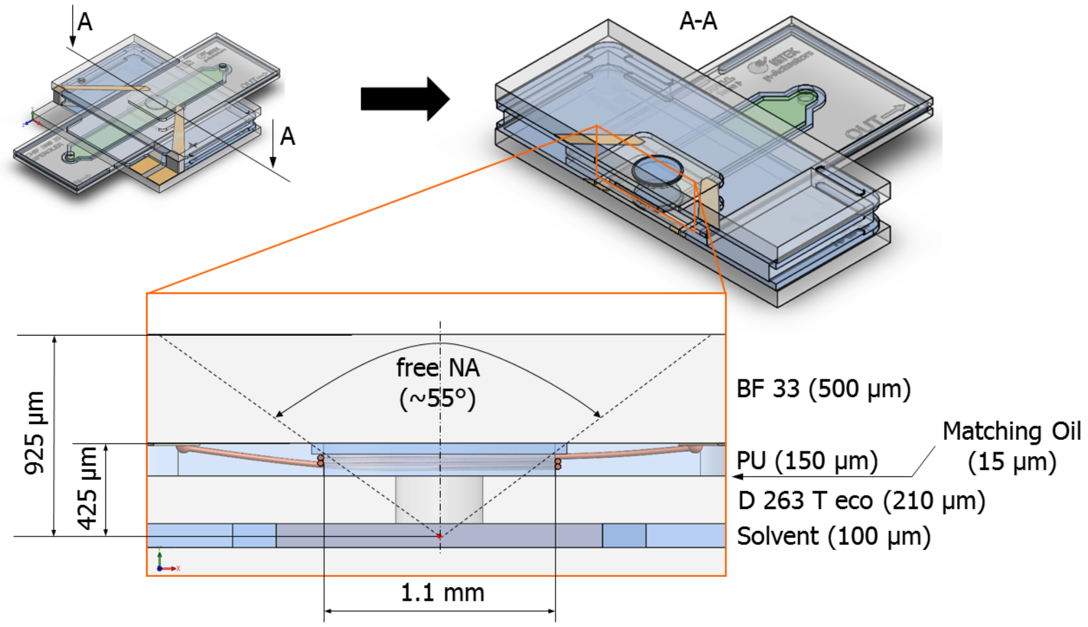

FIGURE 4.29: Optical environment, μ-HH coil probe [244].

First, the microfluidic environment formed by the coil chip is discussed in view of its optical properties. The wall of the sample chambers top chip consists of 4 layers starting from the top: 500 μm borosilicate glass BF33 [230], 150 μm polyurethane (PU), a matching liquid ($\approx$ 15 μm) which adapts the refractive indices of PU and BF33. The last layer has a thickness of 210 μm and consists of borosilicate glass D 263 T eco [230] which belongs to the sample insert that finally contains the solvent and the particle (50 μm distance to D 263 layer) to be optically trapped. Hence, the shortest distance from the top of the probe to the object has a length of 925 μm. The maximum NA is limited by a coil made of copper with an inner diameter of 1.1 mm. This leads to a maximum focusing angle of 55°. The bottom chip has an optically equivalent setup. These are the inner constraints.

The outer limitations the optical system must meet are due to its integration in the bore of a superconducting magnet providing a magnetic field of 11.74 T [33]. A cross section of the magnet is shown in fig. 4.30. The scheme shows the outer environment of the optical system. This superconducting magnet has a bore of 70 mm in diameter. Within this bore the μ-Helmholtz (HH) coil probe mounted on a standard probe head has to be precisely aligned to the center of the magnet marked with the arrow in fig. 4.30 denoting the trapping position. Since the probe is mounted on a printed circuit board made of opaque material the trapping volume is accessible just from one side which is a further restriction compared to the list given before. This and the geometry of the circuit board lead to a semi cylindrical shaped volume with 70 mm in length and 35 mm radius which determines the maximum outer dimensions of the optical system and its mounting.

The particle to be trapped is of spherical or ellipsoidal shape made of optical transparent media. Due to the buoyance force that has recognizable values in a liquid compared to a gaseous environment, objects with sizes of few 10 μm can be optically trapped. Considering a spherical particle with 30 μm in diameter made of PMMA, the net gravity

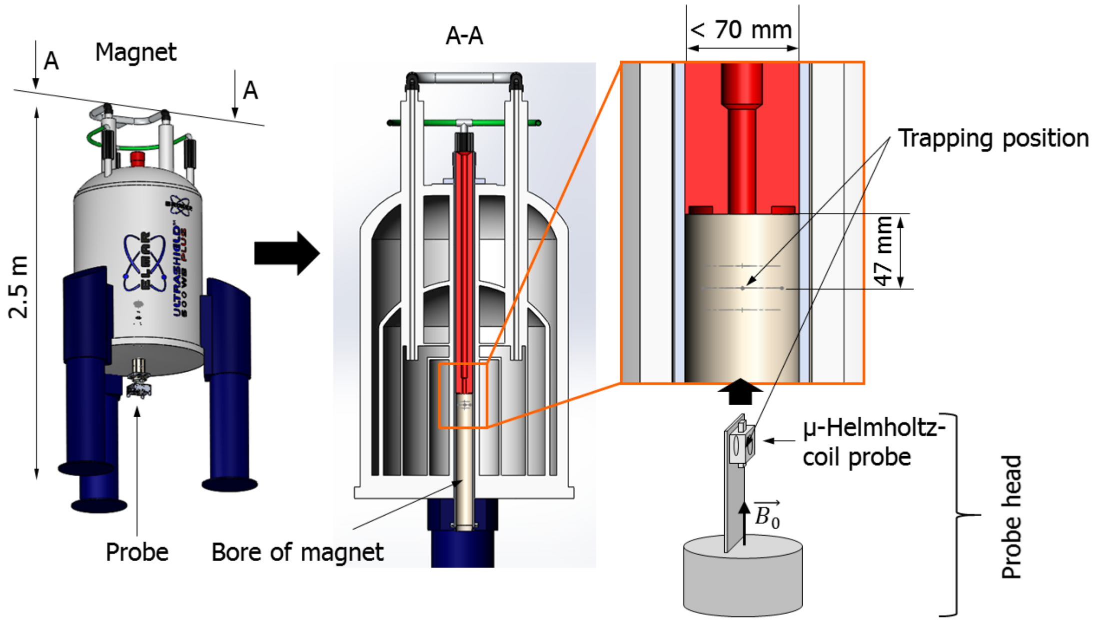

FIGURE 4.30: From left to right: sketch of the superconducting magnet (Bruker Avance III) and its cross section A-A with enlarged center region and probe head with mounted μ-HH coil probe.

force that acts on it in a liquid surrounding is 25 pN, which is still in the order of optical forces.

Once a particle is trapped no position changes or the trapping of multiple particles in parallel is intended. However, the possibility to introduce torque on the particle should be provided. As mentioned in tab. 3.2, torque can be generated with a circularly polarized trapping beam for particles with birefringent properties. Since the volume available for the optical system is comparable small this polarization state is planned to be introduced externally by use of a quarter wave plate.

It is obvious that the trapping laser source also has to be located outside the magnet, which requires a beam supply and preparation. This can be done via free space propagation using mirrors and lenses or with a fiber based optics that is suited to work in high magnetic fields. The fiber based solution will be preferred in this work since the alignment effort is small compared to large distance free space propagation. Furthermore, the particle is planned to be optically trapped outside the magnet. Once a particle is optically held, the whole probe head along with the optical system will be inserted in the bore.

To focus on the optical tweezers, the beam supply is not discussed in this work, rather a laboratory setup is used to achieve the experimental verification of the optical tweezers. The optical system developed to trap in gaseous surrounding is optimized in terms of high trapping efficiency. By the redistribution of the on-axis intensity of a TEM_{00} beam to its edges, the scattering force decreases and the stability of the optical trap rises. This approach is used again. The optical trapping has to be realized perpendicular to the magnet bore and the laser source should be placed outside the magnet. Thus, a 90° beam deflection has to be implemented in the optical system. Finally, the laser beam has to be focused inside the μ-HH coil probe. Therefore, the optical system has to provide three optical functions: 1. beam shaping, 2. beam deflection and 3. focusing. In contrary to the system discussed in the previous section, the observation of the object to be trapped is not planned. Thus, the optical components marked with the green beam path shown in fig. 4.8 are used as a starting system for the iterative design process. Taking into account the external environment of the magnet bore, the concept shown in fig. 4.8 can be adapted to the scheme shown in fig. 4.31. Consider the concept up right in fig. 4.31, the laser beam propagates upwards from below and is shaped by a double axicon (green component) to a collimated ring distribution. A right angle prism (blue component) deflects the beam by 90° into a parabolic ring mirror (orange component). Finally, the ring distribution is focused at the position of the parabolic mirrors focal point. The μ-HH coil probe has to be precisely positioned (see fig. 4.31 top and bottom right) so that the focal point of the parabolic mirror and the position of the particle in the microchannel nicely match.

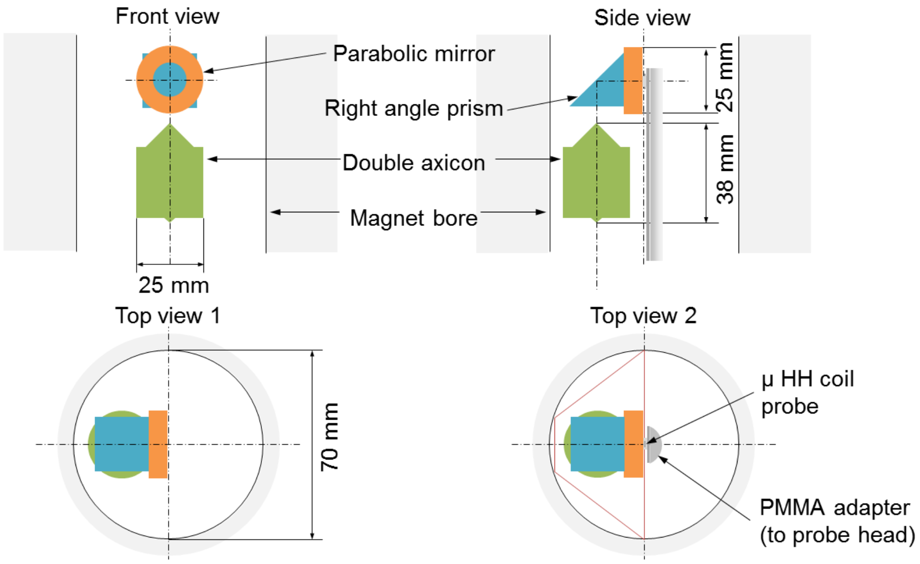

FIGURE 4.31: Concept of the optical system (green: double axicon, blue: prism, orange: parabolic mirror) for trapping of particles inside the μ-HH coil probe mounted on a PMMA adapter (grey).

4.3.2 Development of the optical system: Iterative optical design process

As the concept of the optical system has similarities to the system discussed in previous section 4.2, the new design has not to be developed from the scratch. The trapping beam has to be focused through the wall of a microfluidic channel. Since the concept shown in fig. 4.31, suggests an optical transition between a gaseous surrounding (inside parabolic mirror) and the micro channel wall, the focused beam will be refracted. This interface will introduce spherical aberrations which prevent perfectly focusing as provided by parabolic mirrors. Fig. 4.32 illustrates the introduction of aberrations for three cases applying an focusing angle of 55°. The first example, illustrated in fig. 4.32 left, shows

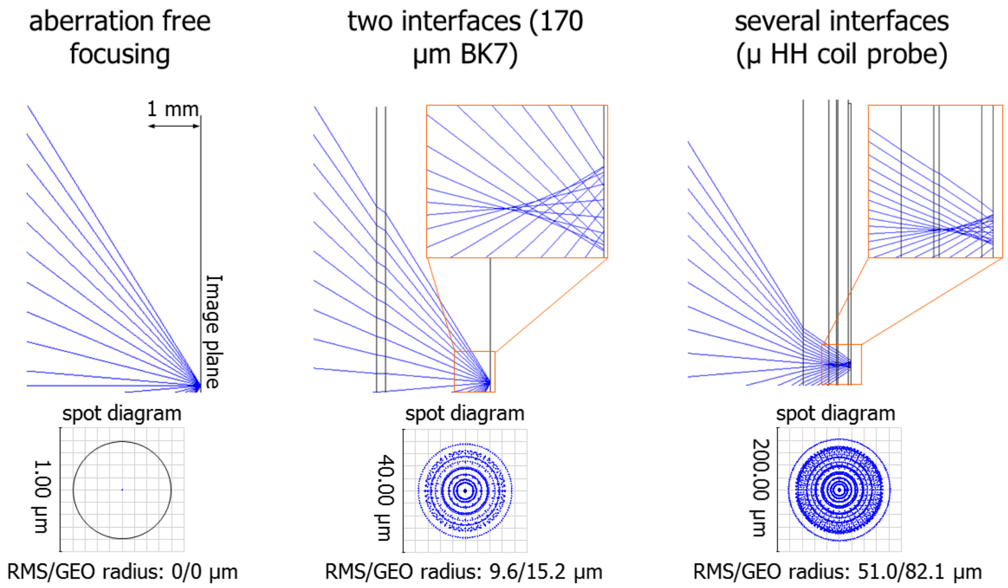

FIGURE 4.32: Rise of spherical aberrations by introducing a cover slip (central example) and the μ-HH coil probe (right).

ideal focusing in free space. The rays (blue) propagate from left to right and are perfectly focused in one point, see the spot diagram below. A geometrical spot radius of $GEO = 0\ \mu$m occurs. If a cover slip (thickness of 170 μm) is placed 2 mm in front of the focal point, spherical aberrations are introduced which is shown in the spot diagram in the middle of fig. 4.32. Finally, fig. 4.32 right, shows spherical aberrations if the μ-HH coil probe is introduced. The spot radius significantly increases to a value of $GEO = 82.1$ μm. In order to theoretically verify if this value allows optical trapping an optical force simulation is performed. Using a spot radius of $GEO = 82.1\ \mu$m spherical aberration as the kind of the optical aberration, the measured intensity distribution to be focused taken from the previous setup (see fig. 4.24 bottom right) and the parameters for this optical system, optical forces are calculated for the three cases presented in fig. 4.33. It is obvious, the introduction of spherical aberrations leads to a strong decrease of optical forces acting in positive and negative direction. Furthermore, a local second force maximum rises beside the main optical trap, which makes the optical trapping even at higher laser powers challenging. These simulation results imply the modification of the optical tweezers concept to avoid this huge amount of spherical aberrations.

As suggested in fig. 4.32, the introduction of a planar optical interfaces to the focused ray fan results in a broadening of the spot due to the non-linearity of Snell's law. This can be circumvented by means of two different approaches.

First, the planar surface can be replaced by a spherical shaped interface. This can be realized with a droplet lens placed on the top of the μ-HH coil probe. To maintain perpendicular incidence its radius of curvature must be the sum of the wall thickness plus the droplet lens sag. If this condition is violated the position of the focal spot will axially change and spherical aberrations will be introduced. Since the total optical path

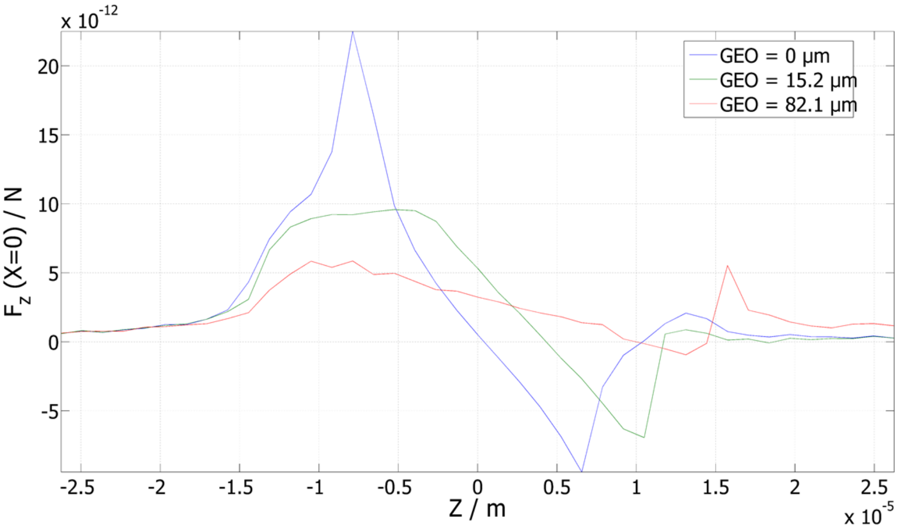

Figure 4.33: Axial optical forces for aberration free (blue curve) and spherical aberration affected (green and red curve) focusing properties.

length starting from the probe surface to the trapping position amounts 925 μm and the lens sag is limited due to tight space restrictions, the droplet lens radius of curvature will end up at few mm. This lens size means a non-standard optical component and thus it has to be manufactured. Furthermore, if such a lens is available, its position has to be perfectly aligned with respect to the focused ray fan and the probe. Both efforts, the manufacturing of the droplet lens and its alignment, can be avoided with another approach, which will be treated in this thesis.

The high jump of the refractive index of the optical interface between the μ-HH coil probe glass wall and the gaseous surrounding can be significantly reduced by linking the focusing optics and the microfluidic channel as done by Oeder [194]. This trapping optics has a monolithic design with a total length of 59 mm and provides beam shaping and focusing. Since the system exceeds the internal space left for the optics inside the magnet and the function of 90° beam deflection is not available, the design has to be modified accordingly.

Fig. 4.34 shows the final system design of the optical tweezers. The total system length is 55 mm and its width is 26.2 mm. Due to the manufacturability, the optical system is divided in three components instead of one monolithic optical element. First, a Gaussian beam is incident on the first axicon surface (slope angle 45°) and is shaped to a divergent ring profile. This ring distribution is collimated at the flank of the double axicon (angle 8.243°) by total internal reflection (TIR). The 90° beam deflection is realized with a right angle prism, which is a standard optical component. Finally, the collimated and ring shaped beam is focused into the μ-HH coil probe by a segmented parabolic lens with a radius of curvature of 3.4 mm. All optical components are assembled using optical adhesive [190]. Thus, the alignment effort is transferred to the manufacturing process, which is the same strategy as applied for the optical tweezers suited to trap in gaseous environments. After the alignment of the optical tweezers to the incoming beam, it has to be linked to the μ-HH coil probe using deionized water as index matching fluid.

The design of the whole system (see fig. 4.29 and fig. 4.34) is performed with the optical

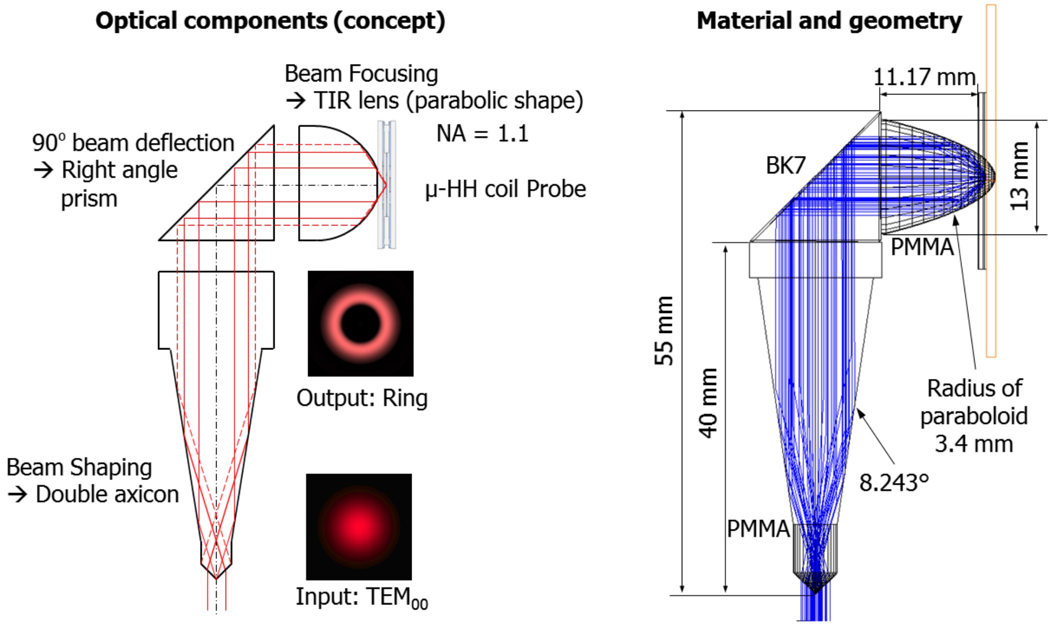

FIGURE 4.34: Design of optical tweezers showing optical components (left) and the applied materials and geometries (right).

design software [287] and the optical force simulation as applied in the previous section 4.2.2. A spot size of GEO = 5.5 μm for the system shown in fig. 4.34 is obtained. Due to refractive index mismatches between the layers of the μ-HH coil probe the aberrated focal spot is mainly caused by spherical aberrations.

The spot size and the simulated intensity distribution 100 μm in front of the focal point are used as the input parameters for the optical force simulation, see fig. 4.35. To keep comparability with the optical tweezers discussed in chapter 4.2, the particle to be trapped is of spherical shape, with 10 μm in diameter and made of fused silica. A laser power of 50 mW is applied. Both optical force curves show stable optical trapping conditions in axial (fig. 4.35 left) and lateral (fig. 4.35 right) direction. Compared to fig. 4.33, the axial trapping force has a steep force gradient and no local maxima. The maximum trapping force theoretical achievable with this design is 15.7 pN, which represents almost the half of the force achieved with the tweezers optimized for gaseous surrounding (29.7 pN). However, considering the lower relative refractive index between the particle and its surrounding medium (see section 4.1.1) this result predicts stable optical trapping. Once the design data is transferred to CAD data, the components are planned to be manufactured externally.

The double axicon and the TIR lens are manufactured by the company LT-Ultra [153] whereas the right angle prism is purchased from Thorlabs [259].

4.3.3 Characterization of the optical components

The right angle prism is purchased with standard optical quality which means a surface roughness of $R_a < 10$ nm. All optical surfaces are polished and uncoated. The plane surface and the cone, as well as the tip of the double axicon were measured using white

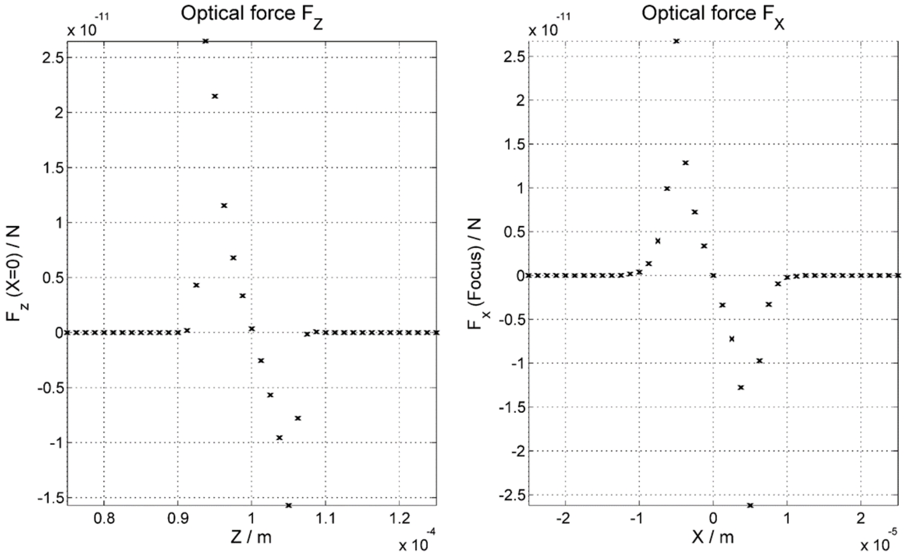

FIGURE 4.35: Optical force simulation (liquid surrounding) of the final system design. Optical forces acting in axial (left) and in lateral direction (right).

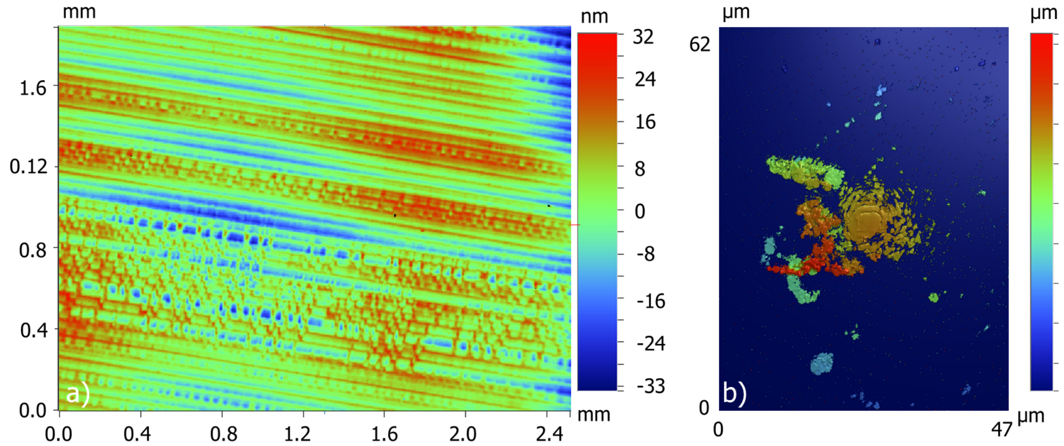

FIGURE 4.36: White light interferometric measurement data of the plane surface a) and the tip b) of the double axicon.

light interferometry. For the plane surface, shown in fig. 4.36 a) a roughness of R_a = 5.86 nm is obtained. Due to the steep flank of the tip, this measurement method is not suited for the verification of the geometry. The false color image shown in fig. 4.36 b), illustrates the few data points achieved with the white light interferometer. Since the optical function of the second axicon surface is based on TIR, each surface defect cause decoupling of light. For the determination of the surface roughness several measurements were performed at different positions. By mathematically subtracting the axicon curvature a plane surface is obtained. This leads to a surface roughness between 13 nm $\leq R_a \leq$ 31 nm. Both surface profiles illustrated in fig. 4.37, show the curvature of the conical shaped second axicon overlaid with the tool marks (orientation: upper left to bottom right). These marks will cause a decoupling of a certain amount of the

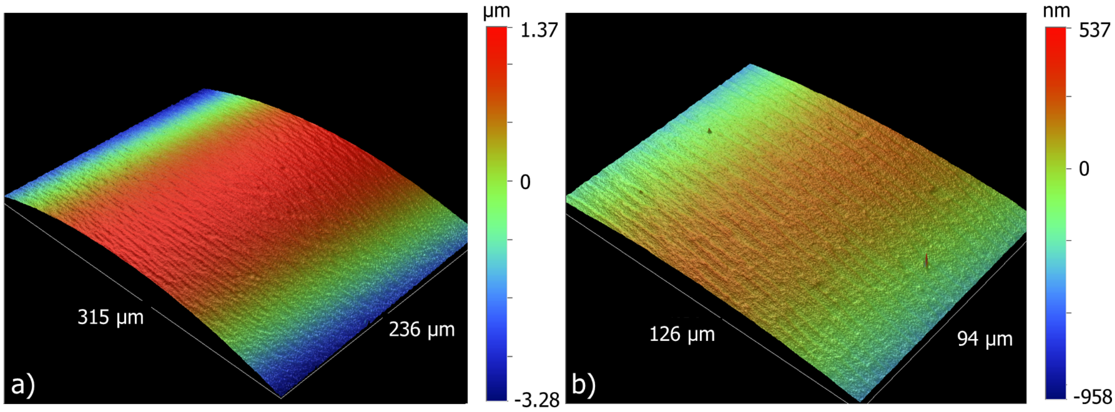

FIGURE 4.37: White light interferometric measurement data of second axicon surface using magnification of 20x a) and 50x b) visualized in three dimensions.

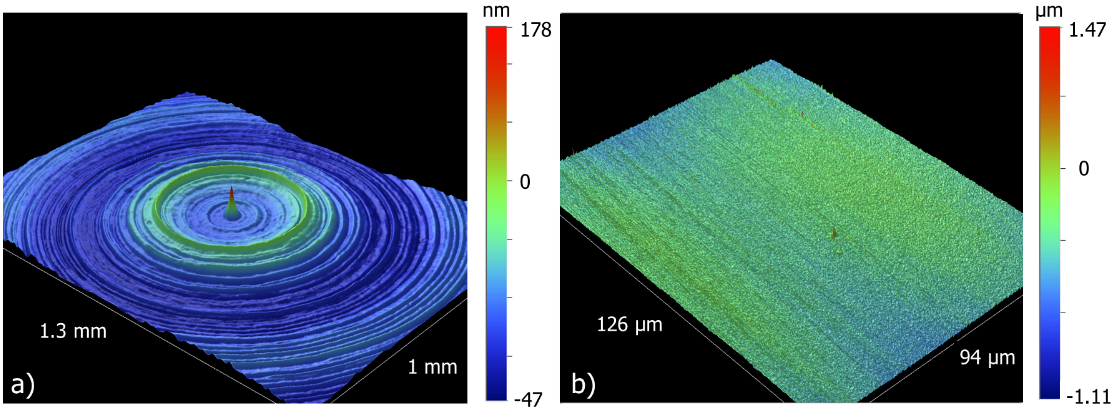

FIGURE 4.38: White light interferometric measurement data of the TIR lens planar output surface a) and the parabolic shaped surface b) visualized in three dimensions.

intensity of the internal propagating beam.

The TIR lens is measured at both planar surfaces and at the parabolic profile as well. Whereas the roughness measured at the planar surfaces has values of $R_a < 9$ nm, the parabolic surface once again shows tool marks with ripples of the same scale. One exception is the center region of the planar output surface. The final stage of the lathing process becomes visible, see fig. 4.38 a) with a peak of 200 nm in height.

Unfortunately, high fitting tolerances occur during the subtraction of a parabolic surface from the measurement data. Thus, the value of the surface roughness will be falsified. Since the tool marks are similar to those measured at the conical surface of the double axicon, the roughness R_a of the TIR lens parabolic surface is expected to be in the same scale, which means values below $R_a = 31$ nm.

4.3.4 Optical setup for trapping and observation of particles in liquid surrounding

The main components of the optical tweezers system were assembled by applying an optical adhesive [190]. Due to the natural perception of symmetries of the human eye [263], the alignment of the components to each other is done using a stereo microscope. First, the circularly shaped plane surface of the double axicon is aligned and glued on the square shaped prism leg surface. The optical adhesive is hardened using UV exposure. Since the outer diameter of the double axicon equals to the legs of the prism the alignment can be precisely realized. Next, the TIR lens is assembled to the second leg surface of the prism. The alignment is comparable to the central positioning of a circle within a slightly larger square shaped area. Fig. 4.39 shows the assembled optical tweezers. The optical system is mounted afterwards on a multi axis platform providing six degrees of freedom: three for translation and three for rotation. The orientation of the optical tweezers can be adjusted using the axes of the stage in such a way that the double axicon axis of symmetry is identical to the optical axis of the laser beam. Therefore, the leg surface of the right angle prism can be used for the first alignment step. The incoming laser beam has to be reflected in itself. Then, the system is shifted laterally so that the incoming laser beam is incident on the tip of the double axicon, see the red beam paths in fig. 4.40. Due to TIR on the optical tweezers output surface, the caustic, as well as the focal intensity distribution cannot be determined. Thus, the optical trapping experiment itself will verify the proper alignment of the optical system. The whole optical setup is shown schematically in fig. 4.40 left. The trapping laser beam propagates from the top downwards. Its diameter is reduced to 1.96 mm by use of a telescope, as described in section 4.2.4. The beam hits the tip of the double axicon and a Bessel beam is formed inside. The divergent ring beam propagates inside the double axicon until it is collimated at the second conical axicon surface. Since the slope of the second axicon is designed for a collimated incident beam, its waist must be located at

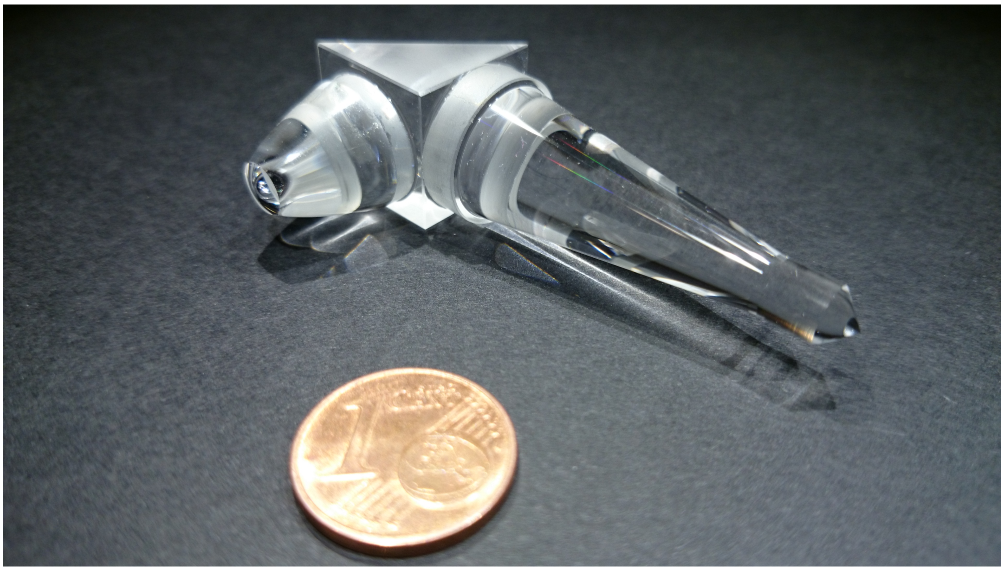

Figure 4.39: Photograph of the optical tweezers.

the tip of the first axicon. The collimated ring shaped beam is then reflected by 90° at the glass-air interface of the prism hypotenuse. Finally, the beam is focused by the parabolic surface of the lens.

In order to simplify the optical trapping experiment for the verification of the functionality of the optical tweezers an optical equivalent microfluidic channel is used to emulate the layer stack of the μ-HH coil probe. Ray tracing simulations have shown that the different layers do just barely affect the spot size. Mainly, the aberrations are introduced by the refraction of the beam on the interface between the output surface of the TIR lens and the first layer of the probe. By assembling a 500 μm thick cover slip with two 150 μm thick cover slips using optical adhesive, the wall of the μ-HH coil probe is approximated. The microfluidic channel is realized with a halved spectrometer cuvette glued on the assembled wall. This sample chamber is shown in fig. 4.40 within the enlarged view. It is optically linked to the output surface of the TIR lens by using an index matching fluid. Due to its high purity, which result in a natural evaporation without any residues, deionized water is preferred for the matching fluid and for the surrounding medium of the particle. As illustrated with the green beam path in fig. 4.40, an additional laser source is applied to illuminate the sample volume. The same setup as described in section 4.2.4 is used to observe the particle but this time the observation direction is perpendicular to the illumination and not optimized for high scattering intensities. For the particle supply the same strategy is applied as used for the optical trapping in gaseous surrounding. Particles are added to the liquid surrounding again by applying them with a syringe but this time suspended in deionized water. Thus, optical forces acting in lateral dimension are exploited once again to trap the particle, see fig. 4.35 right. These forces ($F_X = 26.5$ pN) are clearly larger compared to the optical forces acting in axial direction ($F_{-Z} = 15.7$ pN).

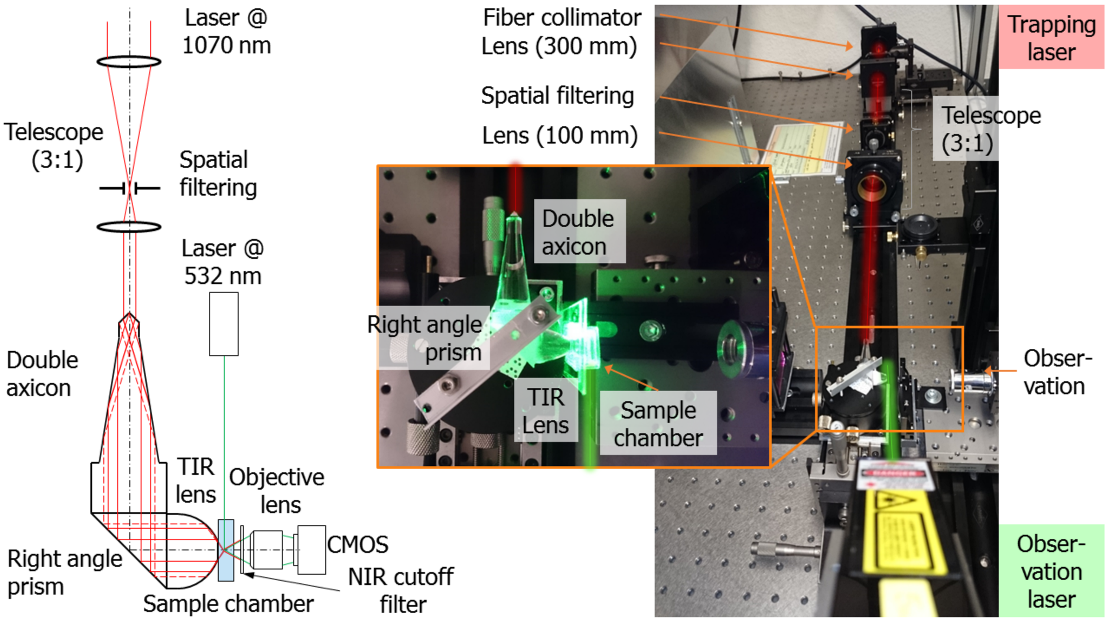

FIGURE 4.40: Schematic drawing (left) and photograph (right) of the optical setup.

4.3.5 Optical trapping in liquid surrounding

Spherical fused silica particles with a diameter of 10 μm [277] are applied for optical trapping. Due to the buoyancy of water a net gravitational force of 6.16 pN acts on the particles. Since the optical trapping is realized side wards, the optical forces acting in lateral direction have to overcome this value for stable optical holding, see fig. 4.35. Compared to the optical trapping in gaseous surrounding, the kinetic energy of the particle should be smaller since the friction between the particle and the water molecules will damp the movement.

The trapping laser source is set to an output power of 1 W. Particles are supplied to the liquid environment by use of a solution of deionized water. Once a particle is optically trapped, the laser power is incrementally reduced to find the minimum value required for optical trapping. Due to the liquid environment the laser power available at the trapping position cannot be determined. The almost similar setup of this system compared to the tweezers described in section 4.2 gives an indication how the power loss can be estimated. The main loss of the incident beam will happen at the tip of the double axicon due to Fresnel reflections. For the other optical interfaces of the optical tweezers and the sample chamber, the refractive index mismatch is comparably small and the Fresnel losses can be neglected. Another appreciable source for intensity losses are the optical surfaces which have to provide TIR. The surface roughness will partially violate the condition of TIR and light can couple out. However, this effect can not be observed in such a scale that it has to be considered. Finally, an intensity loss of 33% is assumed for the determination of the laser power at the focal region.

As indicated with the optical setup shown in fig. 4.40, the optical trapping is observed in axial direction. Once the particles are supplied to the medium they fall slowly to the ground. If they reach the focal position of the optical tweezers they will be trapped. Fig. 4.41 shows a sequence of 10 frames while a particle is optically held (indicated with the green arrow) and a free particle (red arrow) passes by. The same fact happens compared to the optical trapping in gaseous surrounding. Due to the heating of the surrounding medium with the focused laser beam, a convection process starts and the particles move upwards. Compared to the previous setup, the particle speed is slower. This is indicated by the frame numbers in fig. 4.41. Each second frame is shown. The

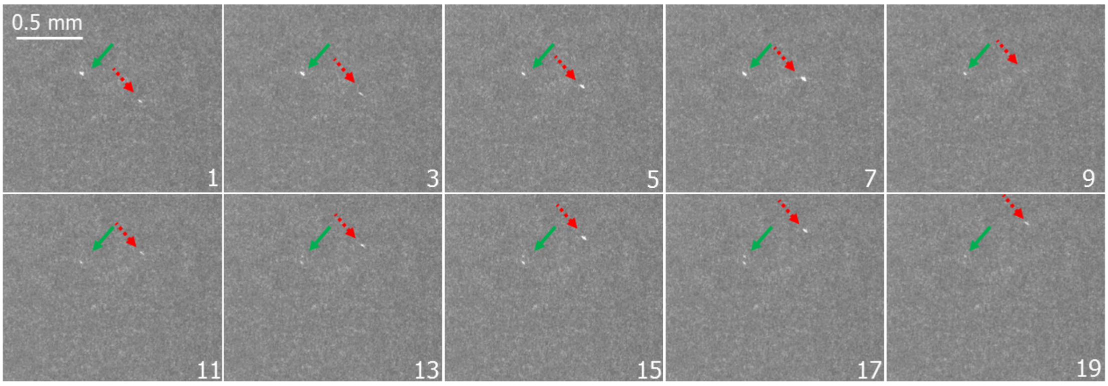

Figure 4.41: Optical trapping (green arrow) of fused silica particle with 10 μm in diameter in liquid surrounding and free particle (red arrow) passing by observed in axial direction.

framerate is 15.5 frames per second. Within 20 frames the free particle moves over a distance of 500 μm. This results in a particle speed of 0.4 $\frac{mm}{s}$, which is one third less compared to the speed in gaseous surrounding (0.6 $\frac{mm}{s}$). Probably the speed will rise for particles made of PMMA due to their lower weight.
The optical trapping is achieved in a reproducible manner several times. During the experiments a laser power of 170 mW necessary for optical holding is determined. As mentioned earlier, this value has to be decreased by 33% to achieve the expected laser power at the focal point. This result in 112 mW, which is the minimum laser output power required to trap a spherical fused silica particle with 10 μm in diameter using this optical setup. The optical force simulation predicts a lower laser power which indicates the presence of non-ideal system properties like optical aberrations potentially introduced by alignment errors of the optical tweezers or manufacturing related issues. This topic is discussed in detail in the following section. However, the correct function of the optical system is demonstrated. The next step would be the replacement of the sample chamber with the μ-HH coil probe and further optical trapping experiments to investigate the reasons for the high laser power required for optical trapping.

4.4 Investigation of the impact of optical aberrations

During the optical trapping experiments performed with both optical tweezers, deviations to the theoretical predictions frequently appear. The laser power required for optical holding, especially for the optical trapping in liquid surrounding is significantly larger than the theoretical value. Furthermore, multiple optical trapping of particles in gaseous surrounding at positions beside the main optical trap indicate differences between the experiment and the theory. To clarify these deviations or at least to give potential indications why discrepancies appear, the effect of optical aberrations specifically introduced to the system designed for optical trapping in air is investigated.

4.4.1 Well-aligned optical tweezers

The first situation to be investigated is an optical system suited to trap particles in gaseous surrounding. The intensity distribution is measured 300 μm in front of the focal point by use of a CMOS sensor. The recorded intensity distribution, its distance to the focal point and a geometrical spot size equal to the experimentally determined FWHM spot size are the main input values for the optical force simulation. The measured intensity distribution used for the optical force simulation shows an annular but inhomogeneous and non-rotational symmetric shape. Since the system components are well adjusted and a Gaussian beam of good quality ($M^2 = 1.1$) has been used for illumination, the non-ideal distribution can be traced back to errors of the optical components applied in the trapping system. The original image recorded with the CMOS camera has a resolution of 1280 times 1024 pixels. The selection located at its center, see fig. 4.42 top right, is extracted since no intensity values, except noise are present outside. To keep the computational effort reasonable, the resolution of this selection is reduced by a factor of 3 using a cubic interpolation algorithm to achieve an image with a resolution of 101 times 101 pixels.

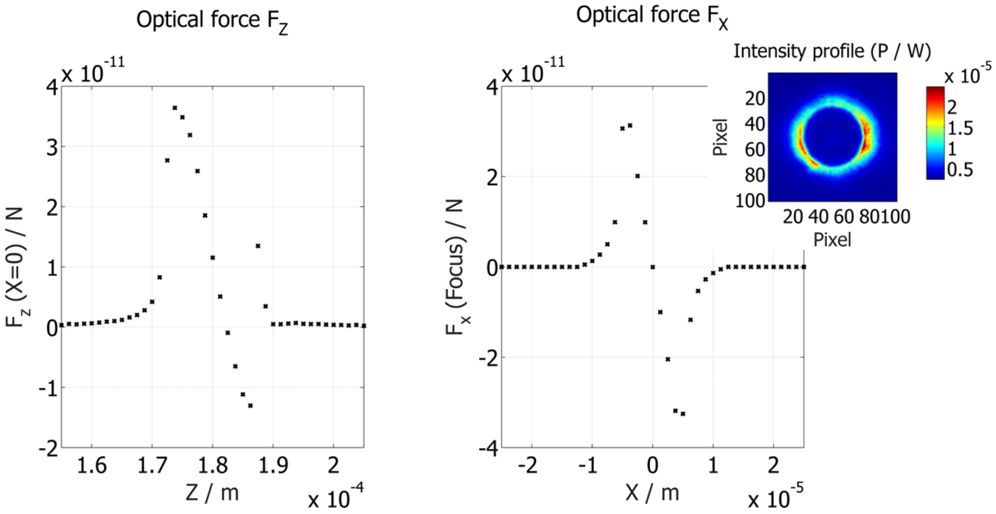

FIGURE 4.42: Optical forces acting in axial and lateral direction on spherical fused silica particles with 10 μm in diameter using an intensity distribution measured 300 μm in front of the focal point for laser power of 50 mW and a gaseous surrounding.

Obviously, the graphical illustration of optical forces acting in axial direction, see fig. 4.42 left, shows apart from the small local force maximum an almost perfect optical force profile. The shape of the curve around the equilibrium point located at Z = 182 μm is very steep and beneficial for optical tweezing applications. Due to the orientation of the optical tweezers, optical trapping is achieved perpendicularly to gravity. Hence, the optical forces acting in lateral direction, shown in fig. 4.42 right, have to overcome the gravitational force. The shape of the simulated function has almost ideal properties. It has to be mentioned, that diffraction effects and real beam profiles (Gaussian beams) are not considered in this geometrical optics approach. In addition, both diagrams shown in fig. 4.42 represent the cross section of the optical forces through the focal point and along the optical axis. They do not show all the information necessary to describe off-axis optical trapping. A two dimensional map (area of 50 times 50 μm) that shows optical forces acting on a spherical particle, see fig 4.43 gives more information in this respect. Since the optical trap is orientated horizontally and realized inside a test chamber made of glass additional non-optical forces occur. The optical axis is oriented along the Z-direction whereby the focused beam propagates form the bottom upwards. The gravity acts along positive X-direction but is small compared to the drag that acts on the particle in the opposite direction. Thus, a net (non-optical) force acts on the particle in negative X-direction. Consider the areas located left below and right above the point X = 0 and Z = 100 μm, optical forces act in opposite direction to the net external forces and have values of the same scale. Taking the net external force into account, several positions arise where the forces which act on the particle create a balance of powers. Thus, particles can be trapped at these positions. This observation is supported by experimental observations. As mentioned before, if a particle is held optically in a local trap its position is not stable. Furthermore, by varying the laser output power the particle moves along a trajectory with the same slope compared to the silhouette formed by the red force vectors shown in fig. 4.43. This helps to explain the

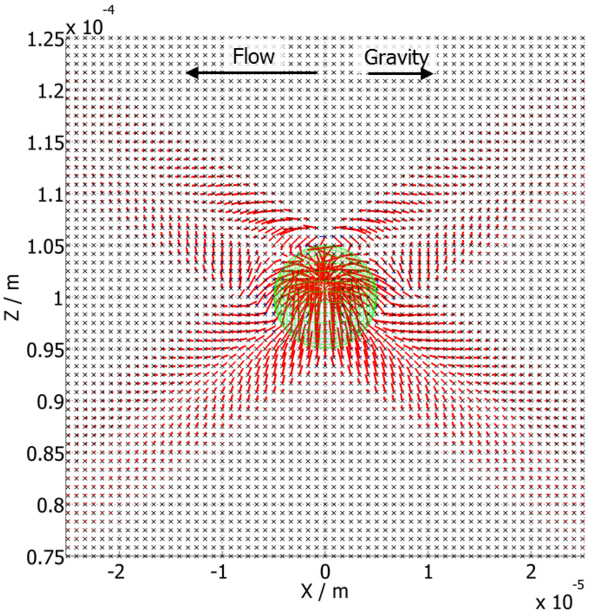

FIGURE 4.43: 2D map of the optical forces acting on spherical fused silica particle with 10 μm in diameter.

existence of multiple optical traps with the orientation of the optical axis perpendicular to gravity.

4.4.2 Positioning and orientation tolerances

The optical system can be divided into three groups, the beam delivery, the trapping system and the observation optics. The beam delivery system consists of the fiber collimator connected to the NIR laser source via an optical fiber and the 3:1 telescope with the spatial filtering located at its Fourier plane. Precise alignment of the beam delivery optics, as well as of the whole system is necessary. Deviations can lead to a wrong beam height and position, a non-collimated beam leaving the telescope as well as to an oblique beam path. The wrong positioning of the aperture used for spatial filtering can introduce a (non-)symmetric airy pattern distributed around the trapping beam and significant intensity losses. In this section the beam delivery system is assumed to be well adjusted. Because of the independence of the observations optics this part can also be excluded from the considerations of the trapping forces.

The alignment of the system developed to trap particles in gaseous surrounding consists of a double axicon and a parabolic mirror. Since the alignment of the two axicons relative to each other is fixed due to the monolythic design, the alignment effort is significantly reduced [122]. Thus, the position and orientation of the double axicon and the parabolic mirror have to be verified. Fig. 4.44 shows combinations of tilt and position tolerances of both components. The first case presented in fig. 4.44, represents the ideal alignment of the trapping system. The incident beam hits the center of the first axicon and is shaped to a symmetric ring. This divergent ring is collimated by the second axicon and ideally focused with the parabolic mirror.

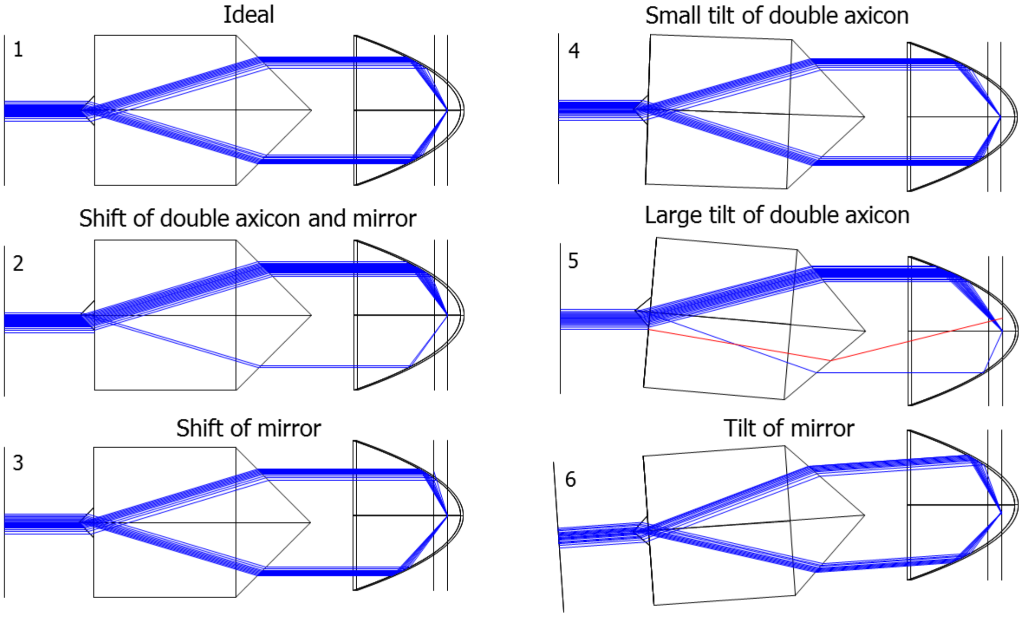

FIGURE 4.44: Ideal setup (1), positioning (2, 3) and tilt (4, 5, and 6) tolerances of the double axicon and the parabolic mirror.

Due to the monolithic design of the double axicon, the collimated output is maintained if a shift error occurs (see sub image 2 in fig. 4.44). The same behavior follows for small lateral positioning errors of the parabolic mirror (see sub image 3 in fig. 4.44). These errors do not result in a broadening of the focal spot compared to the correctly aligned system. However, the ring shaped intensity distribution is not symmetric anymore and the focusing angles show a non-symmetric behavior as well. This directly affects the trapping performance.

To investigate this effect, a particle is trapped and held by use of the ideally aligned optical system. Next, by slightly shifting the double axicon relative to the beam center the collimated intensity distribution becomes non-symmetric. During this process the particle remains trapped but changes its position along a trajectory similar to the caustic shown in fig. 4.25. It should be noticed that, due to the reduction of trapping performance by specific mis-alignment of the system, the laser power required for stable optical trapping increases. Thus, the laser power applied for this experiment is 77 mW, which is more than twice as high as required for optically holding particles in the well-aligned optical trap. Fig. 4.45 shows the position of the particle and its movement during the mis-alignment. For the well aligned system the particle is trapped at X $\approx$ Z $\approx$ 2 mm. Mis-alignment of the system by stepwise shifting the double axicon below the optical axis, results in the particle movement highlighted with the red arrow in fig. 4.45. This movement is reversible within a range of few 100 μm. As the particle reaches the position Z $\approx$ 1.5 mm it leaves the trap along the flow direction (negative X-direction). The intensity distribution of the system is measured 300 μm in front of the focal point. Immediately after the trapping experiment the intensity distribution is measured while aligning the double axicon back to the center of the beam. These data is used as input for the optical force simulation. Fig. 4.46 shows the intensity distribution used as input (bottom) and two force maps, one for the aligned system (up left) and the other

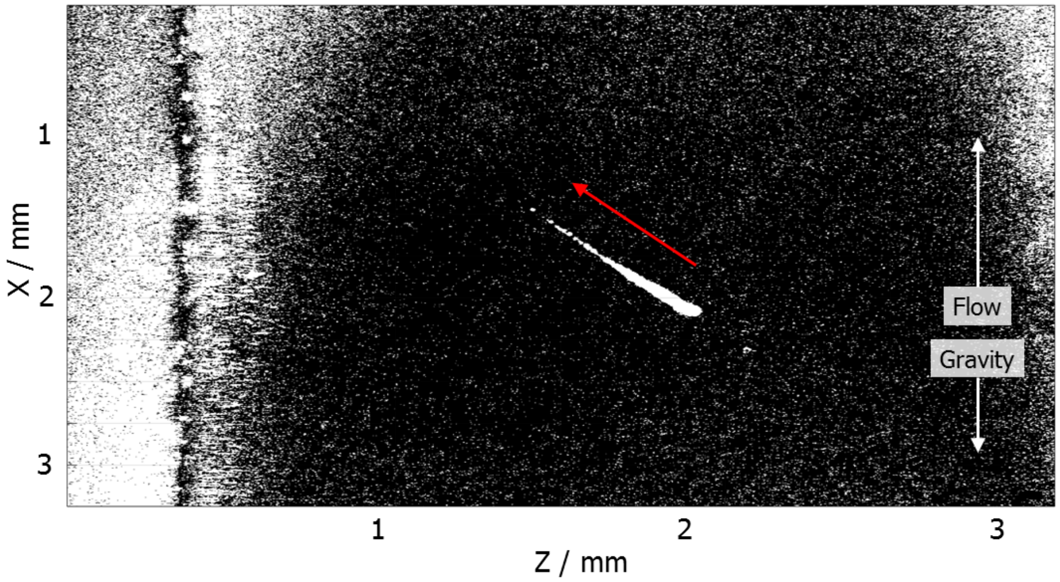

FIGURE 4.45: Movement of the trapped particle (red arrow) to smaller values of X and Z during a vertical shift (X-direction) of the double axicon introducing non-symmetric intensity distribution.

for the mis-aligned system (up right). The left map shows the optical forces which are

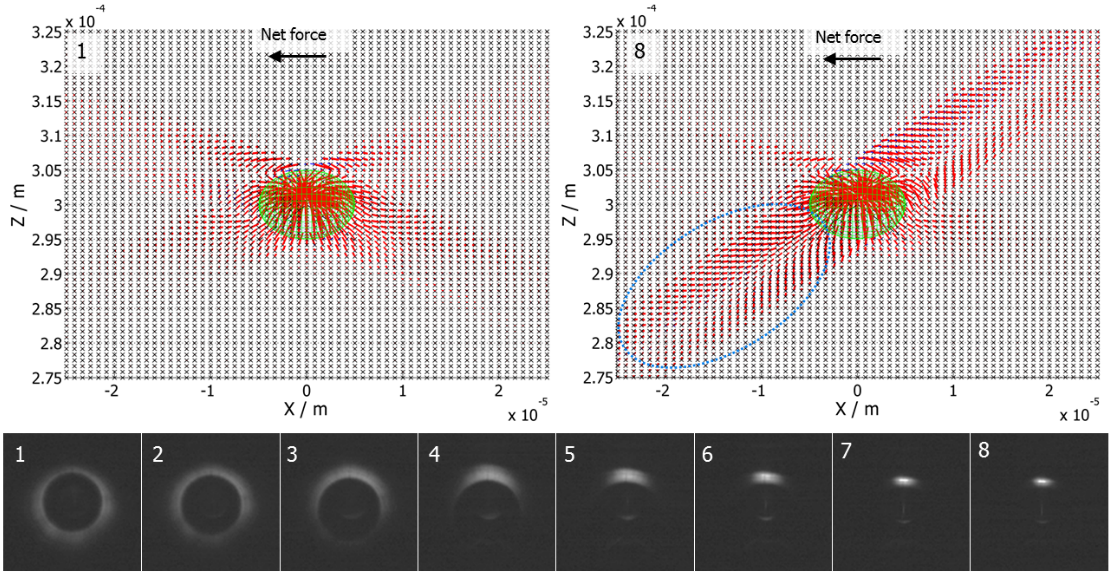

FIGURE 4.46: Optical forces acting on a spherical fused silica particle with 10 μm in diameter for two input intensity distributions (aligned system left, sub image 1; mis-aligned system right, sub image 8) and the associated intensity distributions (bottom) measured 300 μm in front of the focal point.

symmetrically distributed as a result of the focused symmetric ring profile. The particle is trapped at the center. As indicated by the force map shown right in fig. 4.46, the movement of the particle is probably due to a combination of the net external (non-optical) force and the optical force generated by the trap. The area highlighted with the blue ellipse marks optical force vectors that act in opposite direction to the net force. Imagine, this grid represents a potential that describes a force gradient, the direction of the particle movement in negative X- and Z-direction agrees well to the direction given by the blue ellipse. Inside the elliptically shaped region the optical force and the net external force build a balance of powers where a particle can be trapped.

In contrast to the lateral mis-alignment of system components, the tilt of the double axicon or the parabolic mirror leads to an increase of the spot size. Small tilt errors (sub image 4 in fig. 4.44) of the double axicon lead to a non-collimated ring distribution leaving the second axicon surface. As a consequence rays propagate not parallel to the optical axis are not ideally focused by the parabolic mirror. In addition, larger tilt errors result in more complex aberrations. Some rays propagating at the edge of the beam miss the first axicon and are refracted at the front shell surface of the double axicon (red ray in sub image 5 in fig. 4.44). These rays partially do not hit the focusing mirror. The worst case scenario represents sub image 6 in fig. 4.44. In this case the parabolic mirror is tilted relative to the incident beam. Thus, the direction of propagation of each ray is not consistent with the axis of the parabolic mirror. This error results in a non-homogeneous broadening of the spot size with coma like shape. It should be noted that coma is an inherent aberration of parabolic mirrors. The increase of the spot size leads to a flattening of the intensity gradient and thus, to decreasing optical forces. In addition, a non-symmetric spot shape results in a corresponding shift of the optical trap position.

To experimentally study this case, a fused silica sphere is optically trapped and held by use of the aligned optical tweezers. By tilting the double axicon around the Y-axis, rays that do not exactly propagate in the X-Z-plane leave the second axicon in a direction oriented non-parallel to the optical axis. These rays cause a coma like aberration in the focal plane of the parabolic mirror, see fig. 4.47. For illustration of the non-collimated ring distribution leaving the double axicon it is tilted around the Y-axis by 3°. The oblique rays propagating inside the ring are difficult to see for smaller tilt angles, e.g. for 1° as used for the ray optics based simulation and for the experiment.

During the experiment the particle is optically held with a laser power of 31 mW. While tilting the double axicon the position of the particle varies along negative X-direction as visualized in fig. 4.48. In addition, the trapped particle starts with small oscillations until it leaves the optical trap. This indicates once again the existence of local traps formed by optical and non-optical forces. The movement of the particle and the associated force map simulated by using the intensity distribution recorded at the focal point and by considering an *OPD* due to coma-aberrations is shown in fig. 4.48. The distance of the particle movement until it leaves the trap is approximately 100 μm in negative X-direction. Once again, the movement seems to be due to the formation of a balance of powers between the optical force, the flow force and gravity, which is highlighted by the blue ellipse in fig. 4.48.

The coma aberration introduced by tilting the double axicon, cause a non-symmetric ring profile which leads to a distorted focal spot, see fig. 4.47. This in turn affects the optical forces acting in axial and lateral direction. The symmetric curve shape of

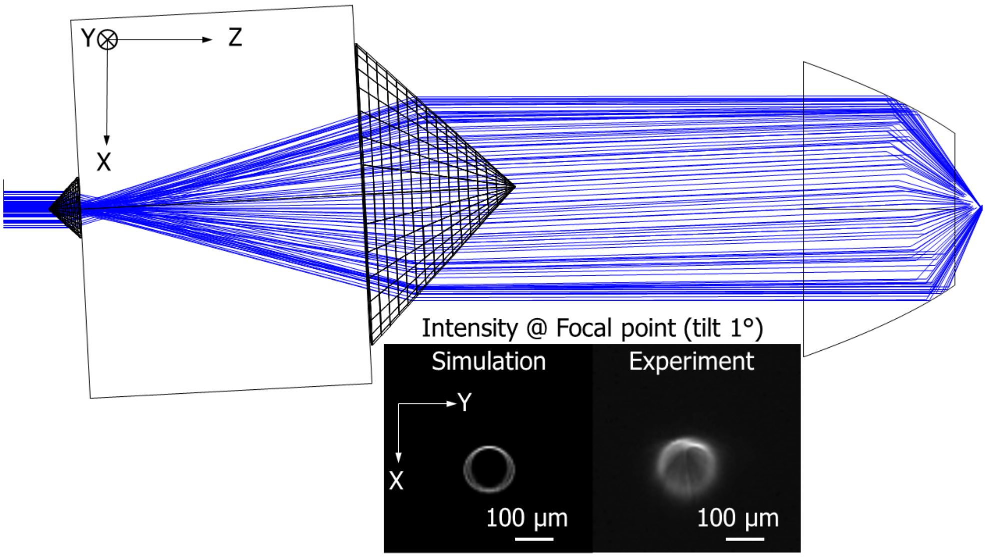

FIGURE 4.47: Tilt of the double axicon by 3° (for illustration) relative to the incident ray. Intensity distribution at the focal point for a tilt of the double axicon by 1° measured and simulated using raytracing software.

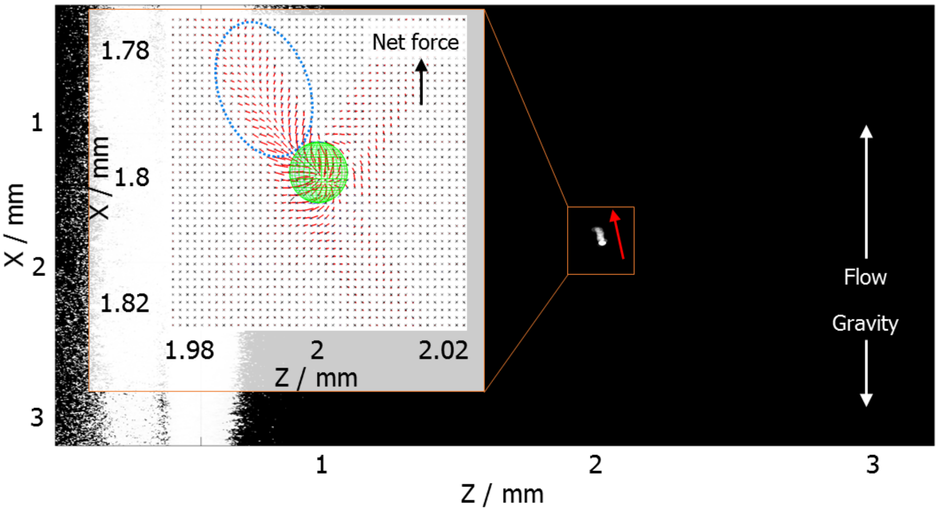

FIGURE 4.48: Movement of the trapped particle (along the red arrow) to smaller values of X and Z during tilt (around Y-axis) of the double axicon to introduce coma aberration. The inset shows the force map obtained by optical force simulation using experimental data as input.

the lateral optical forces becomes non-symmetric and the value of the optical forces decreases, compare fig. 4.42 and 4.49. The trapping forces acting in negative Z-direction, visualized left in fig. 4.49 are significantly lower compared to the well aligned optical tweezers, see fig. 4.42. The curve shape of the optical forces acting in lateral direction (fig. 4.49 right) turned to a non-symmetric profile for the introduced coma like aberration. Especially the values of forces acting in positive X-direction decrease. These forces

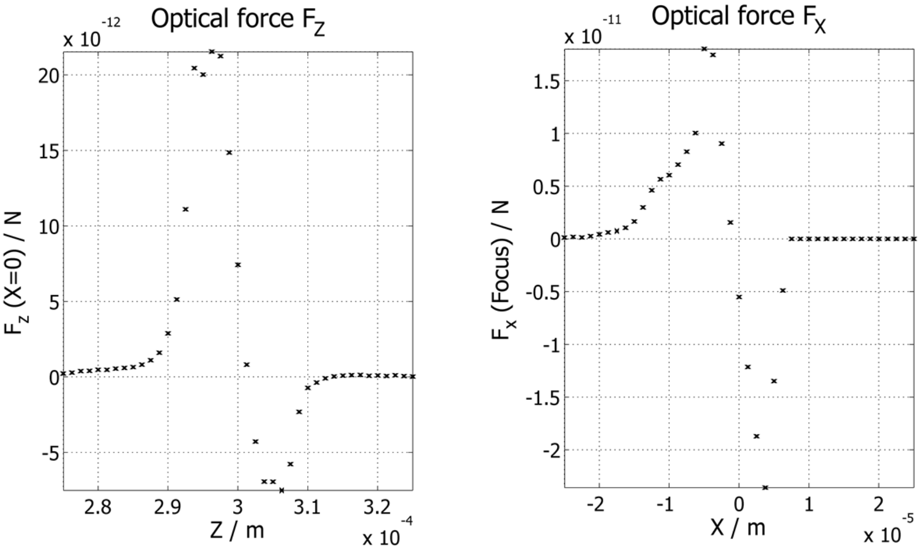

FIGURE 4.49: Optical forces acting in axial and lateral direction on spherical fused silica particles with 10 μm in diameter using an intensity distribution measured 300 μm in front of the focal point of coma-aberrated optical tweezers for laser power of 50 mW.

have to overcome the non-optical net force present in the trapping chamber. Their decrease directly affects the performance of the current optical trap realized in horizontal direction.

4.4.3 Spherical aberrations

Each optical system or component, which introduces spherical or even planar refractive optical surfaces suffers from spherical aberrations, see section 2.2.5. Consider a perfect parabolically shaped focusing mirror and an ideally collimated incident beam no spherical aberrations occur. As indicated with fig. 2.11, spherical aberrations are also caused by the introduction of a thin glass plate inside a focused ray fan. This happens for both optical tweezers setups since trapping is realized inside a test chamber with walls made of optically thicker media compared to the surrounding medium of the particle. Due to free optical parameters of the sample chambers, which allow the adaption of the channel to the final application the systems are not optimized with respect to this source of aberration. The thickness of the entrance glass wall to the focal point determines the amount of spherical aberration introduced. In both optical tweezer systems, the position of the entrance glass wall is fixed, since it is in direct contact to the focusing optics. Note, for the optical trapping in liquid surrounding, the distance between the glass and the focal point influence the spot size due to spherical aberrations as well.
The optical tweezers developed in this work are planned to be applied for different test chambers and hence, the thickness of the entrance glass or its layer composition may change. Thus, for the optical trapping in gaseous surrounding the relationship of the geometrical spot size *GEO* to the glass thickness is investigated using ray tracing simulation [287]. For a focused ray fan with a NA of 0.85 various glass walls are inserted in

front of the focal point. Their thickness is varied from zero to 2.51 mm. The geometrical spot radius linearly increases with the rise of the wall thickness, see fig. 4.50 left. Using a ray density of 20 [287] the *RMS* value of the spot is almost 1.6 times smaller compared to *GEO*. These values and the intensity distribution measured at 300 μm in front of the focal point without a glass plate are used as input for the optical force simulation. Three dimensional optical trapping is theoretically ensured up to a wall thickness of 1.5 mm using borosilicate glass (N-BK7), see fig. 4.50. A wall thickness of 1.5 mm corresponds to a GEO of 120 μm. For this spot size the optical force acting in negative Z-direction drops below a value of 0.01 pN. Since the force is directly proportional to the laser power an increase by the factor 20, which is equal to a laser power of 1 W results only in 0.2 pN. Note that the optical trapping is achieved with the optical forces acting in the lateral direction but the Z-force component is necessary for axially stabilizing the particle. This value is still too small for stable optical trapping in gaseous surrounding. On the other hand, two dimensional optical trapping [9] should still be possible also for a larger wall thickness. As visualized in the force diagram, shown in fig. 4.50 right, optical forces decrease with increasing spot size (GEO). This has to be expected since a broad focal spot means a comparatively flat intensity gradient whereas for optical trapping steep gradients are required.

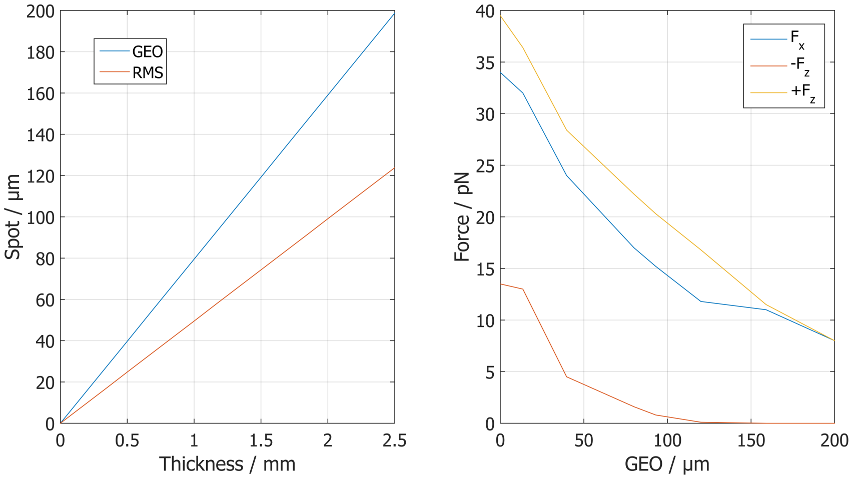

FIGURE 4.50: Relationship between the spot radius to the thickness of the wall made of N-BK7 for NA of 0.85 in gaseous surrounding (left) and associated optical forces for laser power of 50 mW (right).

In order to experimentally verify these simulation results, a test chamber is developed which offers the possibility for changing the front glass. Six walls of different thicknesses were investigated. The maximum wall thickness to be considered in the simulation is set to 2.5 mm since for higher values the focal point would be located inside the wall. For the experiment the maximum wall thickness is 2 mm, since the simulation predicts that three dimensional optical trapping becomes impossible for wall thickness greater than 1.5 mm.

Fused silica spheres with 10 μm in diameter were trapped at the position of the main optical trap by applying a laser power of 1 W. By incrementally reducing the laser power the minimum value for optical trapping is found for each wall thickness.

Since particles passing by in upwards direction with an average speed of 0.6 $\frac{mm}{s}$, the drag and the gravitational force have to be considered. The particle velocity can be twice as high as for a laser power of 1 W, but for the laser powers applied for the experiment the value can be assumed to be constant. While a particle is trapped the following forces form a balance. Gravity acts downwards whereas the buoyant force and drag acting upwards. Thus, the optical force has to act downwards to reach a force equilibrium. To find out which kind of drag is present the Reynolds number has to be calculated. This number predicts if the flow is laminar or turbulent. As only the movement speed of not trapped particles is known, the flow speed of the air must be calculated first. In order to take both cases, i.e. laminar and turbulent flow into account the balance of forces is derived twice. The absolute values of forces acting on the particle are as follows, (the sign gives the direction of action):

$$F_g = -\frac{4}{3}\pi r^3 \rho_{particle} g, \tag{4.4}$$

$$F_b = \frac{4}{3}\pi r^3 \rho_{air} g, \tag{4.5}$$

$$F_{d,laminar} = 6\pi\eta r(v_{flow} - v_{particle}), \tag{4.6}$$

$$F_{d,turbulent} = \frac{1}{2}\rho_{air} c_w \pi r(v_{flow} - v_{particle})^2. \tag{4.7}$$

Eq. 4.4 describes the gravitational force and 4.5 the buoyancy force. Forces for laminar and turbulent flow are given by eq. 4.6 and 4.7. The value r is the particle radius (5 μm), g stands for the gravity (9.81 $\frac{m}{s^2}$) and ρ is the density (ρ_{air} =1.2041 $\frac{kg}{m^3}$; $\rho_{particle}$ =2201 $\frac{kg}{m^3}$). The velocity is given by v ($v_{particle}$=0.6 $\frac{mm}{s}$), η (17.1 μPa s) is the kinematic viscosity and c_w (0.09 to 0.45) is the drag coefficient, which depends on the kind of flow. The Reynolds number is given by:

$$Re = \frac{\rho_{air} v_{flow} 2r}{\eta}. \tag{4.8}$$

In each case (eq. 4.6 or 4.7), the flow velocity leads to a Reynolds number that indicates laminar flow. Thus, eq. 4.4 to 4.6 are used to describe the balance of forces. Applying these equations, the flow velocity of air inside the test chamber at the position of the optical trap is 13 $\frac{mm}{s}$. This yields a net force acting on the particle in upwards direction of F_{net} = 9.66 pN. Therefore, the minimum optical force required for optical trapping must be equal or greater than 9.66 pN.

For each wall thickness the corresponding value for *GEO* is calculated using optical design software [287]. These values, the minimum laser power experimentally applied for optical trapping and the intensity distribution of the non-aberrated system measured 300 μm in front of the focal point were used as input data for the optical force simulation. Since optical trapping is realized horizontally the optical forces (F_x) that act perpendicular to the optical axis, have to be at least as high as 9.66 pN. The values for *GEO*, the optical forces and experimental results are presented in tab. 4.3. Up to a wall thickness of 1 mm stable optical trapping is realized. The value of the simulated optical forces (F_x) required for optical trapping is always higher than the net force. In addition, optical forces (F_{-z}) acting towards the light direction have to be greater than zero, to provide three dimensional optical trapping. These conditions are fulfilled for all

Table 4.3: Comparison of the experiment and the optical force simulation for front glass walls of different thickness.

Thickness / μm	170	500	1000	1170	1500	2000
GEO / μm	13.5	39.7	79.5	93	120	159
Power / mW	29.8 ± 1	31.8 ± 1.2	46.8 ± 1.1	184.3	530.3 ± 28	-
F_x / pN	19.39	15.8	17.2	59.75	142.63	-
-F_x / pN	7.76	2.87	1.51	2.77	0.62	0
$\frac{F_z}{F_{-z}}$	2.8	6.3	13.8	27	287.9	-
Remarks	Stable trapping	Stable trapping	Stable trapping	Non-stable trapping	Non-stable trapping	No trapping

successful trapping experiments. Furthermore, it should be noted that the position of the optical trap shifts in axial direction for an increase of the wall thickness.

For wall thicknesses above 1 mm the particle strongly oscillates while it is trapped. Changes in the flow direction and speed may cause the oscillations of the trapped particle around its point of equilibrium. Thus, the stability of the optical trap can also be linked to the ratio ($\frac{F_z}{-F_z}$) of optical forces acting in positive and negative Z-direction. If the ratio has values significantly greater than one, the probability rise that the scattering force (F_z) pushes the particle out of the optical trap.

During the trapping experiments the laser power is reduced to find the minimum value required for optical trapping. This procedure leads to a particle movement along trajectories from time to time, as shown in fig. 4.45 and 4.48. This behavior can be traced back to the formation of possible trapping positions along the caustic of the focused trapping laser beam as discussed previously. The interplay of optical forces and the net external forces can result in temporary stable trapping conditions.

For trapping experiments performed with a wall thickness of 2 mm, no optical trapping has been achieved which is predicted by the optical force simulation. In the end, the consistency between the values of the laser power experimentally applied for optical trapping and the values predicted by the optical forces simulation verifies the correct function of the developed force simulation routine and the given assumptions for the explanation of the optical trap behaviour in the presence of spherical aberrations.

4.4.4 Optical force simulations of further aberrations

In the previous sections, the correct function of the optical force simulation tool has been verified using experimental results. The effects of spherical aberration and coma, as well as non-symmetric intensity distribution are investigated. Another often seen effect in optical systems is astigmatism which can be traced back to small tilt errors of optical components. This leads to different values of the refractive powers for different axial planes of a lens which finally cause a non-symmetric broadening of the focal spot depending on its axial position.

For geometric spot radii up to 100 μm caused by astigmatism, optical forces are simulated for the optical tweezers suited to trap particles in gaseous surrounding. Once again the position of the optical trap shifts along the optical axis in positive Z-direction. Simultaneously, the optical forces acting in lateral and axial direction decrease and become non-symmetric. Fig. 4.51 shows optical forces for an astigmatism aberrated optical tweezers ($GEO = 100$ μm) plotted on a map and two cross sections along Z- and X-direction. Unfortunately, for increasing astigmatism the ratio of forces acting in axial direction becomes unfavorable for optical tweezing. The optical force acting in negative Z-direction decreases until only scattering forces remain. Also the forces that act in lateral direction become non-symmetrically distributed. This has to be taken into account for the determination of the behaviour of the optical trap concerning its orientation. However, compared to the focal spot pattern and the spot radii caused by spherical aberration, astigmatism will affect the performance of an optical tweezers in the same order of magnitude.

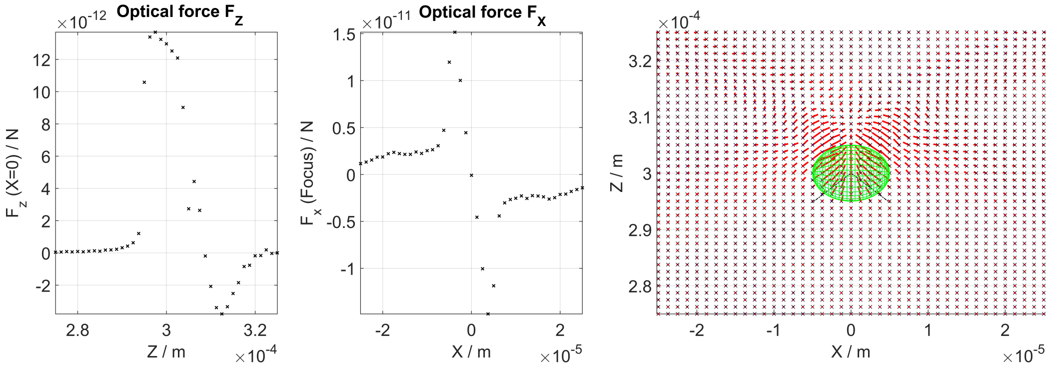

FIGURE 4.51: Optical forces acting in axial (left diagram) and lateral (center diagram) direction on a spherical fused silica particle with 10 μm in diameter for optical tweezers aberrated by astigmatism ($GEO = 100$ μm). The associated force map (right) shows optical forces nearby the optical trap.

Although tilt is not a real wavefront aberration since it does not lead to a deformation, it is briefly discussed in the following. Assuming that the optical system is aberrated by tilt only. As a result the focal point shifts and induces a non-symmetric focusing cone. If the focal spot is shifted in positive X-direction, rays that leave the exit pupil at opposite positions have to be focused with higher angles compared to rays leaving the exit pupil on the other side. This dramatically distorts the symmetry of the optical trap, as shown in fig. 4.52. Compared to the non-aberrated system presented in fig. 4.42, the optical force curve becomes less steep, see fig. 4.52 left. In addition, the maximum optical force achieved decreases by roughly 30% compared to the ideal case. This has to be considered if the integration of steering optics or a particle movement in general is planned, as done in most standard optical tweezers setups.

Optical aberrations usually occur as combinations of single aberrations with different contributions. A combination of monochromatic aberrations consisting of tilt, defocus, astigmatism, coma and spherical aberration is discussed next. The two examples show how different aberrations affect optical tweezers. The first combination of optical aberrations (defocus, coma and astigmatism with equal contributions) leads to a geometrical spot size of 100 μm, see fig. 4.53 left. Despite this comparatively high value the shape

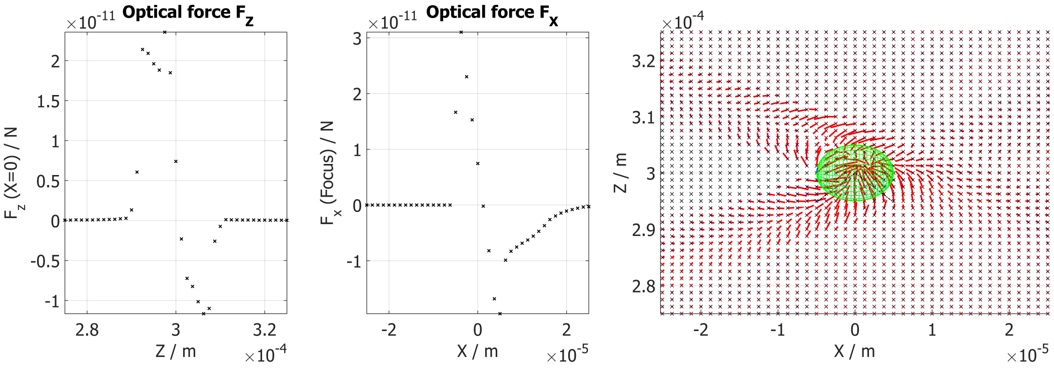

FIGURE 4.52: Optical forces acting in axial (left diagram) and lateral (center diagram) direction on a spherical fused silica particle with 10 μm in diameter for optical tweezers with tilt error of 20 μm. The associated force map (right) showing optical forces nearby the optical trap.

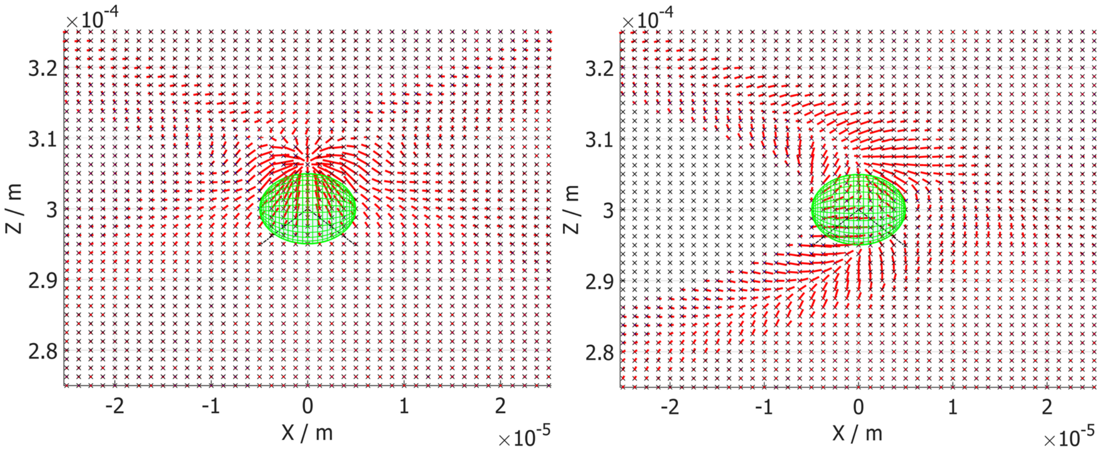

FIGURE 4.53: Map showing optical forces acting on a spherical fused silica particle with 10 μm in diameter. Left: $GEO = 100$ μm for defocus, coma and astigmatism; Right: $GEO = 50$ μm for tilt, coma, astigmatism and spherical aberration.

of the optical trap is almost symmetrical. The location of the trap is clearly visible and the optical forces that act in negative Z-direction are large enough to provide stable optical trapping conditions. In contrast, the force map shown right in fig. 4.53, is the result of a combination of tilt, coma, astigmatism and spherical aberration with equal contributions. In this case a geometrical spot size of 50 μm is assumed. The shape of the optical trap is strongly distorted and three dimensional optical trapping is nearly impossible. Optical forces acting towards light direction do not exist and particles will be pushed in forward and side directions.

These two examples demonstrate that optical aberrations, which lead to a laterally shifted trapping position and a distorted trap shape affect the optical trapping performance most severely. Aberrations which lead to symmetric distortions like spherical aberration or defocus have only minor impact on the trapping performance.

Chapter 5

Conclusion

This thesis is focused on the design, optimization and experimental verification of optical tweezers. The main aspects studied can be concluded in three parts, which are linked with each other. To calculate optical forces a simulation tool based on the geometrical optics approach is developed first. This tool is used together with classical optical design software to design and optimize two optical systems suited to optically trap particles in either gaseous or liquid environment. Both systems were studied experimentally. Finally, the behaviour of optical tweezers in the presence of optical aberrations is investigated theoretically and experimentally which forms the third part of the thesis.

Optical force simulation

Based on the GOA a simulation tool was developed, which enables the theoretical investigation of optical forces and torque acting on microscopic objects. The objects to be considered are mathematically described as generalized ellipsoidally shaped bodies like needles or oblate objects arbitrarily oriented. Thus, the behavior of various objects like cells, beads and droplets in an optical trap can be theoretically studied.

For modelling of the optical system, its intensity distribution is expressed by an array of pixels with associated dimension parameters to maintain optical parameters and geometries. This array represents the starting point of the rays. The distance to an initially ideal focus point serves as a reference value for the ray directions which directly leads to the NA of the system. Using this simulation tool the influence of various parameters (NA, intensity distribution, refractive index of the particle and the surrounding, etc.) on the optical forces was studied.

By the implementation of wavefront aberrations to the optical force simulation non-ideal system properties can be considered. This enables the investigation of how optical aberrations affect the optical trapping performance. Typical alignment errors, which are critical for the stability and function of the optical trap were pointed out and are avoided or minimized within the optical design process.

Design of optical trapping systems

For the development of an optical system specifically adapted to trap particles in gaseous or liquid environment the classical design process was enhanced by the integration of an optical force simulation. This approach leads to an additional merit function in the optical design process, which allows for the optimization of the ratio of optical forces per laser power.

The first step of each design process is to determine the boundary conditions and requirements to be fulfilled by the optical system. Derived from the best suited concepts the start system for the iterative optical design process was selected. The optical tweezers for trapping of particles in gaseous environment was the first system developed in this thesis. By optimizing the system in terms of a sufficiently large working distance and a high ratio of optical force to incident laser power, the beam shaping and focusing modules, as well as the final system properties and specifications were determined. Crucial positioning tolerances of the beam shaping device that consist of two axicons were transferred to the manufacturing process which leads to a component of monolithical shape. For the realization of a high focusing power a parabolic ring mirror was designed, combining ideal focusing properties and large focusing angles. These components represent the major parts of the first optical trapping system. Due to the ring shaped laser beam, which propagates between the double axicon and the parabolic mirror enough space is left to integrate a 45° mirror. This allows for the observation of the trapping volume with external placed imaging optics. The size of the optical tweezers is comparable to standard objective lens.

The second optical tweezers developed in this thesis enables optical trapping in liquid environment through the wall of a microfluidic channel. Furthermore, the system allows for the operation in high magnetic fields which require non-magnetic materials. Based on the first design the beam shaping approach, which enables high optical forces at lower NA was applied on this system too. Due to excellent focusing properties of parabolic mirrors, this principle was adapted for this system as well, which finally leads to a parabolic focusing lens based on total internal reflection. To further reduce the alignment effort all components were assembled using optical adhesive and form a monolithic optical element.

In both systems, the approach of intensity redistribution from the center of a laser beam to its edges was aimed. Compared to conventional optical tweezers that focus Gaussian TEM_{00} beams this beam profile provides higher optical forces and allows for higher working distances.

Experimental work

The optical tweezers system suited to trap in gaseous environment consists of three optical elements, each fabricated externally with an ultra-precision diamond turning or flycutting process. The beam shaping optics is realized as a monolithic double axicon made of PMMA, whereas copper is used for the parabolic mirror. Applying an additional gold coating the copper surface is protected from corrosion. Finally, for imaging optics a 45° plane mirror is made of aluminum. White light interferometric and caustic measurements were performed to characterize the optical elements. The components were mounted in a multi-axis lens positioner to provide comprehensive alignment.

For optical trapping a laser source that emits in the near infrared spectral region is used. This enables the manipulation of biological specimen due to their transparency in the near infrared. An additional laser source with an emission wavelength in the visible range is applied for observation. To observe the optical trapping of particles along the axis and from the side, two CMOS sensors with imaging optics were used. For the separation of the optical trap from the environment, a cubic test chamber with side and front walls made of glass was positioned directly behind the parabolic mirror. Using this setup, the optical trapping of spherical fused silica particles with a diameter of 10 μm was demonstrated. The minimum laser power required to hold such a particle is 30 mW.

Using the same laser sources and beam supply the second optical tweezers for trapping in liquid environment is implemented in the same laboratory setup. Due to the high optical quality of the former externally fabricated elements, the same supplier was chosen for the manufacturing of the optical components applied in this system. Since the function of the system is based on total internal reflection, all components are again characterized using white light interferometric measurements. To significantly reduce the alignment effort, the components were assembled using optical adhesive. The optical trapping of spherical fused silica particles with a diameter of 10 μm was verified experimentally. For this system the laser power necessary to hold a particle is 112 mW. This value is almost 4 times larger than for the first optical tweezers, which is not predicted by the optical force simulation. This result implies the presence of aberrations due to misalignment errors.

The optical trapping performed with both optical tweezers verifies the correct function of the developed optical force simulation tool. Based on this results the optical tweezers for trapping in gaseous environment and the optical force simulation were applied to study the influence of monochromatic optical aberrations on the performance and stability of optical tweezers. It was found that aberrations, which lead to axially symmetrical distortions (spherical aberration, defocus) affect the optical trapping functionality less compared to those which introduce non-symmetric beam profiles and caustics (tilt errors, coma, astigmatism, etc.).

Chapter 6

Outlook

As usual this work has come to its end with still a lot of additional research to be performed. The most interesting aspects are briefly addressed here.

Optical force simulation

The correct performance of the force simulation tool has been verified experimentally but it can be optimized in various aspects. First, the simulation, especially the computation of the force map is non-deterministic and highly parallelizable. Up to now the implementation takes no advantage of parallel computing. The speedup achievable by efficiently [119] transferring the code to parallel processing on graphics processing units would be tremendous. Just to give an impression, instead of two hours one minute or less should be possible for the computing time of an optical force simulation as done frequently during the optical design process. This would make the simulation tool much more comfortable to use.

To increase the accuracy of the simulation, Gaussian beams can be approximated as complex rays [60, 127] using the GOA. That way the simulation of the intensity distribution at the focal point and the exact position of the optical trap can be modelled with higher precision. Furthermore, the implementation of higher order monochromatic aberrations can be easily achieved since just the equation of the *OPD* has to be extended.

Finally, to optimize the iterative optical design process, the interface between the optical design software Zemax [287] and the programming environment [163] can be automated. The current version of the optical design software [287] provides the full control of its routines via the programming environment Matlab [163]. This can be exploited to enhance the communication of both software packages since both are required for the design of optimized optical tweezers.

Experimental setups

The first optical tweezers setup has been developed in accordance to the optimal parameter combination given by the application of trapping particles in a gaseous environment and the requirements and constraints to be fulfilled. Also the axial observation via the 45° plane mirror forms a solid basis for the externally placed imaging optics. By applying a non-planar mirror with a functionalized surface profile one could improve the image quality in terms of decreasing the degree of distortion and increasing the resolution, as well as the contrast. Furthermore, the mounting of the double axicon and the parabolic mirror in a well designed optics holder will reduce the influence of alignment related errors.

Regarding the system developed for optical trapping in liquids, the alignment accuracy during the assembly of the components to each other can be improved by fixed stops or holders specially designed for the assembly process.

Also the characterization (trap stiffness, trapping efficiency and geometry of the optical trap) and the calibration of the optical trap could be improved with photodiodes instead of applying comparatively slow CMOS based cameras. This enables the use of the power spectrum method (see section 2.2.3) to investigate the properties of the trap. In addition, the replacement of the CMOS array with quadrant photodiodes or positioning sensitive detectors could also ensure the verification if an object is optically trapped. This would significantly reduce the costs, the required space and weight at the same time.

General

Optical tweezers have been an integral part of science for many years now. Their application becomes more and more regular and versatile compared to the fancy method it used to be. The developed force simulation tool allows for the estimation and consideration of the behaviour of optical tweezers in the presence of non-ideal conditions as usual for industrial and scientific optical environments. The possibility to firmly integrate the developed force simulation into the optical design process should push the frequent application of optical tweezers further to become a standard tool compared to its mechanical alternatives. Both optical systems build in this thesis demonstrate the unique and advantageous properties of optical tweezers.

Bibliography

[1] M. Abraham. Zur elektrodynamik bewegter körper. *Rendiconti del Circolo Matematico di Palermo (1884-1940)*, 28(1):1–28, 1909.

[2] H. Al-Rizzo and J. Tranquilla. Electromagnetic scattering from dielectrically coated axisymmetric objects using the generalized point-matching technique (gpmt). *Journal of computational physics*, 119(2):356–373, 1995.

[3] M. W. Allersma, F. Gittes, R. J. Stewart, C. F. Schmidt, et al. Two-dimensional tracking of ncd motility by back focal plane interferometry. *Biophysical Journal*, 74(2):1074–1085, 1998.

[4] L. A. Ambrosio and H. E. Hernández-Figueroa. Optical forces in lossless arbitrary refractive index optical trapping and micromanipulation. *Metamaterials*, 6(1):51–63, 2012.

[5] D. Appleyard, K. Vandermeulen, H. Lee, and M. Lang. Optical trapping for undergraduates. *American journal of physics*, 75(1):5–14, 2007.

[6] F. Arai, K. Onda, R. Iitsuka, and H. Maruyama. Multi-beam laser micromanipulation of microtool by integrated optical tweezers. In *Robotics and Automation, 2009. ICRA'09. IEEE International Conference on*, pages 1832–1837. IEEE, 2009.

[7] J. Arines, V. Durán, Z. Jaroszewicz, J. Ares, E. Tajahuerce, P. Prado, J. Lancis, S. Bará, and V. Climent. Measurement and compensation of optical aberrations using a single spatial light modulator. *Optics express*, 15(23):15287–15292, 2007.

[8] S. Asano and G. Yamamoto. Light scattering by a spheroidal particle. *Applied optics*, 14(1):29–49, 1975.

[9] A. Ashkin. Acceleration and trapping of particles by radiation pressure. *Physical review letters*, 24(4):156, 1970.

[10] A. Ashkin. Forces of a single-beam gradient laser trap on a dielectric sphere in the ray optics regime. *Biophysical journal*, 61(2):569, 1992.

[11] A. Ashkin. *Optical trapping and manipulation of neutral particles using lasers: a reprint volume with commentaries*. World Scientific, 2006.

[12] A. Ashkin and J. Dziedzic. Radiation pressure on a free liquid surface. *Physical Review Letters*, 30(4):139, 1973.

[13] A. Ashkin and J. Dziedzic. Optical trapping and manipulation of viruses and bacteria. *Science*, 235(4795):1517–1520, 1987.

[14] A. Ashkin, J. Dziedzic, J. Bjorkholm, and S. Chu. Observation of a single-beam gradient force optical trap for dielectric particles. *Optics letters*, 11(5):288–290, 1986.

[15] A. Ashkin, J. Dziedzic, and T. Yamane. Optical trapping and manipulation of single cells using infrared laser beams. *Nature*, 330(6150):769–771, 1987.

[16] N. G. Astrath, L. C. Malacarne, M. L. Baesso, G. V. Lukasievicz, and S. E. Bialkowski. Unravelling the effects of radiation forces in water. *Nature communications*, 5, 2014.

[17] M. Baba and K. Ohtani. A novel subpixel edge detection system for dimension measurement and object localization using an analogue-based approach. *Journal of Optics A: Pure and applied optics*, 3(4):276, 2001.

[18] T. C. Bakker Schut, G. Hesselink, B. G. Grooth, and J. Greve. Experimental and theoretical investigations on the validity of the geometrical optics model for calculating the stability of optical traps. *Cytometry Part A*, 12(6):479–485, 1991.

[19] S. M. Barnett. Resolution of the abraham-minkowski dilemma. *Physical review letters*, 104(7):070401, 2010.

[20] S. M. Barnett and R. Loudon. The enigma of optical momentum in a medium. *Philosophical Transactions of the Royal Society of London A: Mathematical, Physical and Engineering Sciences*, 368(1914):927–939, 2010.

[21] M. Bass, C. DeCusatis, J. Enoch, V. Lakshminarayanan, G. Li, C. Macdonald, V. Mahajan, and E. Van Stryland. *Handbook of optics, Volume II: Design, fabrication and testing, sources and detectors, radiometry and photometry.* McGraw-Hill, Inc., 2009.

[22] M. Bass and V. N. Mahajan. *Handbook of Optics, ; Volume I: Geometrical and Physical Optics, Polarized Light, Components and Instruments.* McGraw-Hill, 2010.

[23] W. Bates. A wavefront shearing interferometer. *Proceedings of the Physical Society*, 59(6):940, 1947.

[24] K. Berg-Sørensen and H. Flyvbjerg. Power spectrum analysis for optical tweezers. *Review of Scientific Instruments*, 75(3):594–612, 2004.

[25] M. Bertolotti. *The history of the laser.* CRC press, 2004.

[26] M. Bing-Huan, Z. Jin-Hua, Z. Min-Cheng, L. Yin-Mei, W. Jian-Guang, and R. Hong-Liang. Improvement of transverse trapping efficiency of optical tweezers. *Chinese Physics Letters*, 25(6):2300, 2008.

[27] F. Bloch. Nuclear induction. *Physical review*, 70(7-8):460, 1946.

[28] S. Block. *Constructing optical tweezers in Cell Biology: A Laboratory Manual.* PhD thesis, ed D Spector, R Goldman and L Leinward (Cold Spring Harbor, NY, Cold Spring Harbor Press), 1998.

[29] C. F. Bohren and D. R. Huffman. *Absorption and scattering of light by small particles.* John Wiley & Sons, 2008.

[30] F. Borghese, P. Denti, and R. Saija. *Scattering from model nonspherical particles: theory and applications to environmental physics.* Springer Science & Business Media, 2007.

[31] R. W. Bowman, A. Jesacher, G. Thalhammer, G. Gibson, M. Ritsch-Marte, and M. Padgett. Position clamping in a holographic counterpropagating optical trap. *Optics express*, 19(10):9908–9914, 2011.

[32] R. W. Bowman, A. J. Wright, and M. J. Padgett. An slm-based shack–hartmann wavefront sensor for aberration correction in optical tweezers. *Journal of Optics*, 12(12):124004, 2010.

[33] Bruker. Bruker corporation, 40 manning road, billerica, ma 01821, us, 2016.

[34] C. Butler, S. Fardad, A. Sincore, M. Vangheluwe, M. Baudelet, and M. Richardson. Multispectral optical tweezers for molecular diagnostics of single biological cells. In *SPIE BiOS*, pages 82250C–82250C. International Society for Optics and Photonics, 2012.

[35] A. Callegari, M. Mijalkov, A. B. Gököz, and G. Volpe. Computational toolbox for optical tweezers in geometrical optics. *JOSA B*, 32(5):B11–B19, 2015.

[36] M. Capitanio, R. Cicchi, and F. Pavone. Position control and optical manipulation for nanotechnology applications. *The European Physical Journal B-Condensed Matter and Complex Systems*, 46(1):1–8, 2005.

[37] M. Capitanio, G. Romano, R. Ballerini, M. Giuntini, F. Pavone, D. Dunlap, and L. Finzi. Calibration of optical tweezers with differential interference contrast signals. *Review of scientific instruments*, 73(4):1687–1696, 2002.

[38] A. Casner and J.-P. Delville. Giant deformations of a liquid-liquid interface induced by the optical radiation pressure. *Physical review letters*, 87(5):054503, 2001.

[39] L. W. Casperson, C. Yeh, and W. F. Yeung. Single particle scattering with focused laser beams. *Applied optics*, 16(4):1104–1107, 1977.

[40] Y.-R. Chang, L. Hsu, and S. Chi. Optical trapping of a spherically symmetric sphere in the ray-optics regime: a model for optical tweezers upon cells. *Applied optics*, 45(16):3885–3892, 2006.

[41] M. K. Cheezum, W. F. Walker, and W. H. Guilford. Quantitative comparison of algorithms for tracking single fluorescent particles. *Biophysical journal*, 81(4):2378–2388, 2001.

[42] T. Čižmár, H. Dalgarno, P. Ashok, F. Gunn-Moore, and K. Dholakia. Optical aberration compensation in a multiplexed optical trapping system. *Journal of Optics*, 13(4):044008, 2011.

[43] A. Clapp, A. Ruta, and R. Dickinson. Three-dimensional optical trapping and evanescent wave light scattering for direct measurement of long range forces between a colloidal particle and a surface. *Review of scientific instruments*, 70(6):2627–2636, 1999.

[44] A. Clebsch. über die reflexion an einer kugelfläche. *Journal für die reine und angewandte Mathematik*, 61:195–262, 1863.

[45] Coherent. Quantum energymax sensors, model-nr.: J-10si-he, coherent (deutschland) gmbh, dieselstrae 5 b, 64807, 2016.

[46] W. Collett, C. Ventrice, and S. Mahajan. Electromagnetic wave technique to determine radiation torque on micromachines driven by light. *Applied physics letters*, 82(16):2730–2732, 2003.

[47] S. D. Collins, R. J. Baskin, and D. G. Howitt. Microinstrument gradient-force optical trap. *Applied optics*, 38(28):6068–6074, 1999.

[48] A. Constable, J. Kim, J. Mervis, F. Zarinetchi, and M. Prentiss. Demonstration of a fiber-optical light-force trap. *Optics letters*, 18(21):1867–1869, 1993.

[49] A. Cox. A system of optical design. *A System of Optical Design by Arthur Cox London, GB: The Focal Press, 1964*, 1, 1964.

[50] A. Cox, A. J. DeWeerd, and J. Linden. An experiment to measure mie and rayleigh total scattering cross sections. *American Journal of Physics*, 70(6):620–625, 2002.

[51] A. J. Crick, M. Theron, T. Tiffert, V. L. Lew, P. Cicuta, and J. C. Rayner. Quantitation of malaria parasite-erythrocyte cell-cell interactions using optical tweezers. *Biophysical journal*, 107(4):846–853, 2014.

[52] J. C. Crocker and D. G. Grier. Methods of digital video microscopy for colloidal studies. *Journal of colloid and interface science*, 179(1):298–310, 1996.

[53] J. E. Curtis, B. A. Koss, and D. G. Grier. Dynamic holographic optical tweezers. *Optics Communications*, 207(1):169–175, 2002.

[54] R. Dasgupta, S. Ahlawat, P. K. Gupta, J. Xavier, and J. Joseph. Optical trapping with low numerical aperture objective lens. In *Photonics Global Conference (PGC), 2012*, pages 1–4. IEEE, 2012.

[55] E. J. Davis and G. Schweiger. *The airborne microparticle: its physics, chemistry, optics, and transport phenomena*. Springer Science & Business Media, 2012.

[56] J.-B. Decombe, S. K. Mondal, D. Kumbhakar, S. S. Pal, and J. Fick. Single and multiple microparticle trapping using non-gaussian beams from optical fiber nanoantennas. *Selected Topics in Quantum Electronics, IEEE Journal of*, 21(4):247–252, 2015.

[57] Y. N. Denisyuk. Photographic reconstruction of the optical properties of an object in its own scattered radiation field. In *Soviet Physics Doklady*, volume 7, page 543, 1962.

[58] W. Denk and W. W. Webb. Optical measurement of picometer displacements of transparent microscopic objects. *Applied optics*, 29(16):2382–2391, 1990.

[59] A. Dereux, C. Girard, O. Martin, and M. Devel. Optical binding in scanning probe microscopy. *EPL (Europhysics Letters)*, 26(1):37, 1994.

[60] G. A. Deschamps. Gaussian beam as a bundle of complex rays. *Electronics letters*, 7(23):684–685, 1971.

[61] DFG. Sonderforschungsbereich 622: Nanopositionier und nanomessmaschinen, 2002.

[62] J. Dharmadhikari, S. Roy, A. Dharmadhikari, S. Sharma, and D. Mathur. Torque-generating malaria-infected red blood cells in an optical trap. *Optics Express*, 12(6):1179–1184, 2004.

[63] K. Dholakia, M. MacDonald, and G. Spalding. Optical tweezers: the next generation. *Physics world*, 15(10):31, 2002.

[64] M. Dienerowitz, G. Gibson, R. Bowman, and M. Padgett. Holographic aberration correction: optimising the stiffness of an optical trap deep in the sample. *Optics express*, 19(24):24589–24595, 2011.

[65] E. R. Dufresne, G. C. Spalding, M. T. Dearing, S. A. Sheets, and D. G. Grier. Computer-generated holographic optical tweezer arrays. *Review of Scientific Instruments*, 72(3):1810–1816, 2001.

[66] J. Durnin. Exact solutions for nondiffracting beams. i. the scalar theory. *JOSA A*, 4(4):651–654, 1987.

[67] J. Durnin, J. Miceli Jr, and J. Eberly. Diffraction-free beams. *Physical Review Letters*, 58(15):1499, 1987.

[68] R. Dutra, N. Viana, P. Neto, and H. Nussenzveig. Optical tweezers absolute calibration. *arXiv preprint arXiv:1406.7176*, 2014.

[69] R. Dutra, N. Viana, P. M. Neto, and H. Nussenzveig. Absolute calibration of optical tweezers including aberrations. *Applied Physics Letters*, 100(13):131115, 2012.

[70] F. Ehrenhaft. On the physics of millionths of centimeters. *Phys. Z*, 18:352–368, 1917.

[71] R. L. Eriksen, P. C. Mogensen, and J. Glückstad. Multiple-beam optical tweezers generated by the generalized phase-contrast method. *Optics letters*, 27(4):267–269, 2002.

[72] E. Fällman and O. Axner. Influence of a glass-water interface on the on-axis trapping of micrometer-sized spherical objects by optical tweezers. *Applied optics*, 42(19):3915–3926, 2003.

[73] Q. Fang and D. A. Boas. Monte carlo simulation of photon migration in 3d turbid media accelerated by graphics processing units. *Optics express*, 17(22):20178–20190, 2009.

[74] F. M. Fazal and S. M. Block. Optical tweezers study life under tension. *Nature photonics*, 5(6):318–321, 2011.

[75] H. Felgner, O. Müller, and M. Schliwa. Calibration of light forces in optical tweezers. *Applied optics*, 34(6):977–982, 1995.

[76] J. T. Finer, R. M. Simmons, J. A. Spudich, et al. Single myosin molecule mechanics: piconewton forces and nanometre steps. *Nature*, 368(6467):113–119, 1994.

[77] E.-L. Florin, J. H. Hörber, and E. H. Stelzer. High-resolution axial and lateral position sensing using two-photon excitation of fluorophores by a continuous-wave nd: Yag laser. *Applied physics letters*, 69(4):446–448, 1996.

[78] E.-L. Florin, A. Pralle, E. Stelzer, and J. Hörber. Photonic force microscope calibration by thermal noise analysis. *Applied Physics A: Materials Science & Processing*, 66:S75–S78, 1998.

[79] M. Friese, H. Rubinsztein-Dunlop, N. Heckenberg, and E. Dearden. Determination of the force constant of a single-beam gradient trap by measurement of backscattered light. *Applied optics*, 35(36):7112–7116, 1996.

[80] D. Ganic, X. Gan, and M. Gu. Optical trapping force with annular and doughnut laser beams based on vectorial diffraction. *Optics express*, 13(4):1260–1265, 2005.

[81] R. Gauthier and S. Wallace. Optical levitation of spheres: analytical development and numerical computations of the force equations. *JOSA B*, 12(9):1680–1686, 1995.

[82] R. C. Gauthier. Computation of the optical trapping force using an fdtd based technique. *Optics Express*, 13(10):3707–3718, 2005.

[83] G. Gibson, R. Bowman, A. Linnenberger, M. Dienerowitz, D. Phillips, D. Carberry, M. Miles, and M. Padgett. A compact holographic optical tweezers instrument. *Review of Scientific Instruments*, 83(11):113107, 2012.

[84] F. Gittes and C. F. Schmidt. Interference model for back-focal-plane displacement detection in optical tweezers. *Optics letters*, 23(1):7–9, 1998.

[85] F. Gittes and C. F. Schmidt. Signals and noise in micromechanical measurements. *Methods in cell biology*, 55:129–156, 1998.

[86] J. W. Goodman and S. C. Gustafson. Introduction to fourier optics. *Optical Engineering*, 35(5):1513–1513, 1996.

[87] E. P. Goodwin and J. C. Wyant. *Field Guide to Interferometric Optical Testing.* SPIE, 2006.

[88] C. Gosse and V. Croquette. Magnetic tweezers: micromanipulation and force measurement at the molecular level. *Biophysical journal*, 82(6):3314–3329, 2002.

[89] G. Gouesbet and G. Gréhan. *Generalized Lorenz-Mie Theories.* Springer Science & Business Media, 2011.

[90] P. Gould, P. Lett, P. Julienne, W. Phillips, H. Thorsheim, and J. Weiner. Observation of associative ionization of ultracold laser-trapped sodium atoms. *Physical review letters*, 60(9):788, 1988.

[91] W. Grange, S. Husale, H.-J. Güntherodt, and M. Hegner. Optical tweezers system measuring the change in light momentum flux. *Review of scientific instruments*, 73(6):2308–2316, 2002.

[92] D. G. Grier. A revolution in optical manipulation. *Nature*, 424(6950):810–816, 2003.

[93] H. Gross, H. Zugge, M. Peschka, and F. Blechinger. *Handbook of Optical Systems: Aberration theory and correction of optical systems, vol. 3.* Wiley-VCH, 2007.

[94] M. Gu, D. Morrish, and P. C. Ke. Enhancement of transverse trapping efficiency for a metallic particle using an obstructed laser beam. *Applied Physics Letters*, 77(1):34–36, 2000.

[95] J. Guck, R. Ananthakrishnan, H. Mahmood, T. J. Moon, C. C. Cunningham, and J. Käs. The optical stretcher: a novel laser tool to micromanipulate cells. *Biophysical journal*, 81(2):767–784, 2001.

[96] H. Haferkorn. *Optik: Physikalisch-technische Grundlagen und Anwendungen: Weiterführende und aktuelle Ergänzungen.* Wiley Online Library, 2001.

[97] Y. Han, G. Gréhan, and G. Gouesbet. Generalized lorenz–mie theory for a spheroidal particle with off-axis gaussian-beam illumination. *Applied optics*, 42(33):6621–6629, 2003.

[98] Y. Harada and T. Asakura. Radiation forces on a dielectric sphere in the rayleigh scattering regime. *Optics communications*, 124(5):529–541, 1996.

[99] R. Harrington. *Feld computation by moment methods: Mc-Millan. and Co.* Mc-Millan. and Co, 1968.

[100] Y. Hayasaki, M. Itoh, T. Yatagai, and N. Nishida. Nonmechanical optical manipulation of microparticle using spatial light modulator. *Optical review*, 6(1):24–27, 1999.

[101] H. He, M. Friese, N. Heckenberg, and H. Rubinsztein-Dunlop. Direct observation of transfer of angular momentum to absorptive particles from a laser beam with a phase singularity. *Physical Review Letters*, 75(5):826, 1995.

[102] N. Heckenberg, R. McDuff, C. Smith, H. Rubinsztein-Dunlop, and M. Wegener. Laser beams with phase singularities. *Optical and Quantum Electronics*, 24(9):S951–S962, 1992.

[103] L.-O. Heim, J. Blum, M. Preuss, and H.-J. Butt. Adhesion and friction forces between spherical micrometer-sized particles. *Physical Review Letters*, 83(16):3328, 1999.

[104] T. R. Hillman, T. Yamauchi, W. Choi, R. R. Dasari, M. S. Feld, Y. Park, and Z. Yaqoob. Digital optical phase conjugation for delivering two-dimensional images through turbid media. *Scientific reports*, 3, 2013.

[105] P. J. Hore. *Nuclear magnetic resonance.* Oxford University Press, USA, 2015.

[106] T. Hoshino, H. Kuroda, T. Konno, K. Ishihara, R. Kometani, and K. Morishima. Muscle-powered nano mechanical system assembled by optical tweezers. In *Nanotechnology, 2009. IEEE-NANO 2009. 9th IEEE Conference on*, pages 636–639. IEEE, 2009.

[107] Z. Hu, J. Wang, and J. Liang. Manipulation and arrangement of biological and dielectric particles by a lensed fiber probe. *Optics express*, 12(17):4123–4128, 2004.

[108] J.-S. Huang and Y.-T. Yang. Origin and future of plasmonic optical tweezers. *Nanomaterials*, 5(2):1048–1065, 2015.

[109] H. C. Hulst and H. Van De Hulst. *Light scattering by small particles.* Courier Corporation, 1957.

[110] IDS. Ids imaging development systems gmbh,dimbacher strasse 6-8, 74182 obersulm, deutschland, 2016.

[111] Y. Igasaki, F. Li, N. Yoshida, H. Toyoda, T. Inoue, N. Mukohzaka, Y. Kobayashi, and T. Hara. High efficiency electrically-addressable phase-only spatial light modulator. *optical review*, 6(4):339–344, 1999.

[112] N. Ingle and S. K. Mohanty. Development of a two-photon polymerization and optical tweezers microscope for fabrication and manipulation of microstructures. In *SPIE OPTO*, pages 795006–795006. International Society for Optics and Photonics, 2011.

[113] IPG. Ipg photonics world headquarters, 50 old webster road, oxford, ma 01540, usa, 2016.

[114] ISO. Lasers and laser-related equipment-test methods for laser beam widths, divergence angles and beam propagation ratios. *ISO Standard*, pages 11146–2, 2005.

[115] L. Jia and E. L. Thomas. Optical forces and optical torques on various materials arising from optical lattices in the lorentz-mie regime. *Physical Review B*, 84(12):125128, 2011.

[116] P. Jones, O. Maragó, and G. Volpe. *Optical tweezers: Principles and applications.* Cambridge University Press, 2015.

[117] M. L. Juan, R. Gordon, Y. Pang, F. Eftekhari, and R. Quidant. Self-induced back-action optical trapping of dielectric nanoparticles. *Nature Physics*, 5(12):915–919, 2009.

[118] M. L. Juan, M. Righini, and R. Quidant. Plasmon nano-optical tweezers. *Nature Photonics*, 5(6):349–356, 2011.

[119] O. Kalthoff, R. Kampmann, S. Streicher, and S. Sinzinger. Fast and scalable algorithm for the simulation of multiple mie scattering in optical systems. *Applied Optics*, 55(15):3887–3896, 2016.

[120] R. Kampmann, A. Chall, R. Kleindienst, and S. Sinzinger. Optical system for trapping particles in air. *Applied optics*, 53(4):777–784, 2014.

[121] R. Kampmann, A. K. Chall, R. M. Kleindienst, and S. Sinzinger. Iterative design process for highly efficient optical trapping systems. In *International Optical Design Conference*, pages IM2B–1. Optical Society of America, 2014.

[122] R. Kampmann and S. Sinzinger. Analysis of the influence of manufacturing and alignment related errors on an optical tweezer system. In *International Optical Design Conference*, pages 92930D–92930D. International Society for Optics and Photonics, 2014.

[123] R. Kampmann and S. Sinzinger. Optical tweezers affected by monochromatic aberrations. *Appl. Opt.*, 56(5):1317–1326, Feb 2017.

[124] S. Kawata and T. Sugiura. Movement of micrometer-sized particles in the evanescent field of a laser beam. *Optics letters*, 17(11):772–774, 1992.

[125] S. Kawata and T. Tani. Optically driven mie particles in an evanescent field along a channeled waveguide. *Optics letters*, 21(21):1768–1770, 1996.

[126] P. C. Ke and M. Gu. Characterization of trapping force in the presence of spherical aberration. *journal of modern optics*, 45(10):2159–2168, 1998.

[127] J. B. Keller and W. Streifer. Complex rays with an application to gaussian beams. *JOSA*, 61(1):40–43, 1971.

[128] M. Keller, J. Schilling, and E. Sackmann. Oscillatory magnetic bead rheometer for complex fluid microrheometry. *Review of Scientific Instruments*, 72(9):3626–3634, 2001.

[129] M. Kerker. *The scattering of light.* Academic Press, New York, 1969.

[130] R. Kingslake. *Optical system design.* Academic Press, 1983.

[131] T. K. Kiong and H. Sunan. *Modeling and Control of Precision Actuators.* CRC Press, 2013.

[132] J. Köhler, R. Ghadiri, S. Ksouri, Q. Guo, E. Gurevich, and A. Ostendorf. Generation of microfluidic flow using an optically assembled and magnetically driven microrotor. *Journal of Physics D: Applied Physics*, 47(50):505501, 2014.

[133] Korvink. A modular micro nuclear magnetic resonance in vivo platform for the nematode caenorhabditis elegans, 2012.

[134] M. Krüger, R. Kampmann, R. Kleindienst, and S. Sinzinger. Time-resolved combination of the mueller–stokes and jones calculus for the optimization of a twisted-nematic spatial-light modulator. *Applied Optics*, 54(13):4239–4248, 2015.

[135] K. S. Kunz and R. J. Luebbers. *The finite difference time domain method for electromagnetics*. CRC press, 1993.

[136] S. C. Kuo and M. P. Sheetz. Force of single kinesin molecules measured with optical tweezers. *Science*, 260(5105):232–234, 1993.

[137] V. K. LaMer and D. Sinclair. Progress report on verification of mie theorycalculations and measurements of light scattering by dielectric spherical particles. *Mimeographed OSRD Rept*, 1857.

[138] M. J. Lang and S. M. Block. Resource letter: Lbot-1: Laser-based optical tweezers. *American Journal of Physics*, 71(3):201–215, 2003.

[139] M. R. LaPointe. Review of nondiffracting bessel beams. In *San Diego,'91, San Diego, CA*, pages 258–276. International Society for Optics and Photonics, 1991.

[140] J. Leach, K. Wulff, G. Sinclair, P. Jordan, J. Courtial, L. Thomson, G. Gibson, K. Karunwi, J. Cooper, Z. J. Laczik, et al. Interactive approach to optical tweezers control. *Applied optics*, 45(5):897–903, 2006.

[141] E. N. Leith and R. Hershey. Transfer functions and spatial filtering in grating interferometers. *Applied optics*, 24(2):237–239, 1985.

[142] M. H. Levitt. *Spin dynamics: basics of nuclear magnetic resonance*. John Wiley & Sons, 2001.

[143] T. Li. *Fundamental tests of physics with optically trapped microspheres*. Springer Science & Business Media, 2012.

[144] C. Liberale, P. Minzioni, F. Bragheri, F. De Angelis, E. Di Fabrizio, and I. Cristiani. Miniaturized all-fibre probe for three-dimensional optical trapping and manipulation. *Nature photonics*, 1(12):723–727, 2007.

[145] J. Liesener, M. Reicherter, T. Haist, and H. Tiziani. Multi-functional optical tweezers using computer-generated holograms. *Optics Communications*, 185(1):77–82, 2000.

[146] LightTrans. Virtuallab, international ug. kahlaische straße 4, 07745 jena germany, 2016.

[147] J. Lin and Y.-q. Li. Optical trapping and rotation of airborne absorbing particles with a single focused laser beam. *Applied Physics Letters*, 104(10):101909, 2014.

[148] P.-T. Lin, H.-Y. Chu, T.-W. Lu, and P.-T. Lee. Trapping particles using waveguide-coupled gold bowtie plasmonic tweezers. *Lab on a Chip*, 14(24):4647–4652, 2014.

[149] K.-n. Liou and J. E. Hansen. Intensity and polarization for single scattering by polydisperse spheres: a comparison of ray optics and mie theory. *Journal of the Atmospheric Sciences*, 28(6):995–1004, 1971.

[150] C. López-Quesada, J. Andilla, and E. Martín-Badosa. Correction of aberration in holographic optical tweezers using a shack-hartmann sensor. *Applied optics*, 48(6):1084–1090, 2009.

[151] L. Lorenz. *Lysbevægelsen i og uden for en af plane Lysbølger belyst Kugle.* na, 1890.

[152] A. Love. The scattering of electric waves by a dielectric sphere. *Proceedings of the London Mathematical Society*, 1(1):308–321, 1898.

[153] LTULTRA. Lt-ultra-precision technology gmbh, aftholderberg, wiesenstrasse 9, 88634 herdwangen-schnach, deutschland, 2016.

[154] W. Lubeigt, S. P. Poland, G. J. Valentine, A. J. Wright, J. M. Girkin, and D. Burns. Search-based active optic systems for aberration correction in time-independent applications. *Applied optics*, 49(3):307–314, 2010.

[155] Z.-P. Luo, Y.-L. Sun, and K.-N. An. An optical spin micromotor. *Applied Physics Letters*, 76(13):1779–1781, 2000.

[156] N. Magome, M. I. Kohira, E. Hayata, S. Mukai, and K. Yoshikawa. Optical trapping of a growing water droplet in air. *The Journal of Physical Chemistry B*, 107(16):3988–3990, 2003.

[157] B. Maheu, G. Gréhan, and G. Gouesbet. Diffusion de la lumiere par une sphere dans le cas d'un faisceau d'extension finie1. théorie de lorenz-mie generalisee: les coefficients gn et leur calcul numerique. *Journal of aerosol science*, 19(1):47–53, 1988.

[158] A. Mahmoudi and S. N. S. Reihani. The effect of immersion oil in optical tweezers. *Optics express*, 19(16):14794–14800, 2011.

[159] T. H. Maiman. Stimulated optical radiation in ruby. *Nature*, 1960.

[160] E. Manske, G. Jäger, T. Hausotte, and R. Füßl. Recent developments and challenges of nanopositioning and nanomeasuring technology. *Measurement Science and Technology*, 23(7):074001, 2012.

[161] O. J. Martin and C. Girard. Controlling and tuning strong optical field gradients at a local probe microscope tip apex. *Applied Physics Letters*, 70(6):705–707, 1997.

[162] H. Maruyama, R. Iitsuka, K. Onda, and F. Arai. Massive parallel assembly of microbeads for fabrication of microtools having spherical structure and powerful laser manipulation. In *Robotics and Automation (ICRA), 2010 IEEE International Conference on*, pages 482–487. IEEE, 2010.

[163] MathWorks. Matlab by the mathworks, inc, 1994-2016, 3 apple hill drive natick, ma 01760-2098, us, 2016.

[164] F. Mauch, M. Gronle, W. Lyda, and W. Osten. Open-source graphics processing unit–accelerated ray tracer for optical simulation. *Optical Engineering*, 52(5):053004–053004, 2013.

[165] J. C. Maxwell. *A Treatise on Electricity and Magnetism, vol. II. Clarendon.* Oxford, 1904.

[166] H. Melville, G. Milne, G. Spalding, W. Sibbett, K. Dholakia, and D. McGloin. Optical trapping of three-dimensional structures using dynamic holograms. *Optics Express*, 11(26):3562–3567, 2003.

[167] A. A. Michelson and E. W. Morley. On the relative motion of the earth and of the luminiferous ether. *Sidereal Messenger, vol. 6, pp. 306-310*, 6:306–310, 1887.

[168] M. Michihata, T. Hayashi, and Y. Takaya. Measurement of axial and transverse trapping stiffness of optical tweezers in air using a radially polarized beam. *Applied optics*, 48(32):6143–6151, 2009.

[169] M. Michihata, T. Yoshikane, T. Hayashi, and Y. Takaya. New technique of single-beam gradient-force laser trapping in air condition. In *Optomechatronic Technologies (ISOT), 2012 International Symposium on*, pages 1–6. IEEE, 2012.

[170] G. Mie. Beiträge zur optik trüber medien, speziell kolloidaler metallösungen. *Annalen der physik*, 330(3):377–445, 1908.

[171] G. Mie. Contributions to the optics of turbid media, particularly of colloidal metal solutions. *Contributions to the optics of turbid media, particularly of colloidal metal solutions Transl. into ENGLISH from Ann. Phys.(Leipzig), v. 25, no. 3, 1908 p 377-445*, 1:377–445, 1976.

[172] H. Minkowski. Die grundgleichungen für die elektromagnetischen vorgänge in bewegten körpern. *Mathematische Annalen*, 68(4):472–525, 1910.

[173] M. Mishchenko. Light scattering by randomly oriented axially symmetric particles. *JOSA A*, 8(6):871–882, 1991.

[174] M. I. Mishchenko, J. W. Hovenier, and L. D. Travis. *Light scattering by nonspherical particles: theory, measurements, and applications.* Academic press, 1999.

[175] J. E. Molloy, J. E. Burns, J. C. Sparrow, R. T. Tregear, J. Kendrick-Jones, and D. White. Single-molecule mechanics of heavy meromyosin and s1 interacting with rabbit or drosophila actins using optical tweezers. *Biophysical journal*, 68(4 Suppl):298S, 1995.

[176] J. E. Molloy and M. J. Padgett. Lights, action: optical tweezers. *Contemporary Physics*, 43(4):241–258, 2002.

[177] M. Morgan and K. Mei. Finite-element computation of scattering by inhomogeneous penetrable bodies of revolution. *IEEE Transactions on Antennas and Propagation*, 27(2):202–214, 1979.

[178] N. Morita, T. Tanaka, T. Yamasaki, and Y. Nakanishi. Scattering of a beam wave by a spherical object. *IEEE Transactions on Antennas and Propagation*, 16(6):724–727, 1968.

[179] J. Morrison and M.-J. Cross. Scattering of a plane electromagnetic wave by axisymmetric raindrops. *Bell System Technical Journal*, 53(6):955–1019, 1974.

[180] P. Mouroulis and J. Macdonald. *Geometrical optics and optical design.* Oxford University Press, USA, 1997.

[181] P. Mühlschlegel, H.-J. Eisler, O. Martin, B. Hecht, and D. Pohl. Resonant optical antennas. *science*, 308(5728):1607–1609, 2005.

[182] L. Murray, J. Dainty, J. Coignus, and F. Felberer. Wavefront-sensorless aberration correction of extended objects using a mems deformable mirror. In *MOEMS-MEMS 2006 Micro and Nanofabrication*, pages 61130G–61130G. International Society for Optics and Photonics, 2006.

[183] K. C. Neuman and S. M. Block. Optical trapping. *Review of scientific instruments*, 75(9):2787–2809, 2004.

[184] K. C. Neuman, G. F. Liou, S. M. Block, and K. Bergman. Characterization of photodamage induced by optical tweezers. In *Lasers and Electro-Optics, 1998. CLEO 98. Technical Digest. Summaries of papers presented at the Conference on*, pages 203–204. IEEE, 1998.

[185] Nieminen. Optical tweezers toolbox 1.3, 2004.

[186] T. Nieminen, H. Rubinsztein-Dunlop, and N. Heckenberg. Calculation of the t-matrix: general considerations and application of the point-matching method. *Journal of Quantitative Spectroscopy and Radiative Transfer*, 79:1019–1029, 2003.

[187] T. Nieminen, H. Rubinsztein-Dunlop, and N. Heckenberg. Multipole expansion of strongly focussed laser beams. *Journal of Quantitative Spectroscopy and Radiative Transfer*, 79:1005–1017, 2003.

[188] T. A. Nieminen, V. L. Loke, A. B. Stilgoe, N. R. Heckenberg, and H. Rubinsztein-Dunlop. T-matrix method for modelling optical tweezers. *Journal of modern optics*, 58(5-6):528–544, 2011.

[189] T. A. Nieminen, V. L. Loke, A. B. Stilgoe, G. Knöner, A. M. Brańczyk, N. R. Heckenberg, and H. Rubinsztein-Dunlop. Optical tweezers computational toolbox. *Journal of Optics A: Pure and Applied Optics*, 9(8):S196, 2007.

[190] Norland. Norland products inc., 2540 route 130, suite 100 cranbury, nj 08512, usanorland optical adhesive 72, 2016.

[191] L. Novotny, R. X. Bian, and X. S. Xie. Theory of nanometric optical tweezers. *Physical Review Letters*, 79(4):645, 1997.

[192] T. Numata, A. Takayanagi, Y. Otani, and N. Umeda. Manipulation of metal nanoparticles using fiber-optic laser tweezers with a microspherical focusing lens. *Japanese journal of applied physics*, 45(1R):359, 2006.

[193] A. Oeder. *System design of optical trapping setups*. PhD thesis, Ilmenau, Technische Universität Ilmenau, Diss., 2013, 2013.

[194] A. Oeder, S. Stoebenau, and S. Sinzinger. Optimized free-form optical trapping systems. *Optics letters*, 37(2):274–276, 2012.

[195] T. Oguchi. Scattering properties of oblate raindrops and cross polarization of radio waves due to rain- calculations at 19. 3 and 34. 8 ghz. *Radio Research Laboratories, Journal*, 20(102):79–118, 1973.

[196] T. Oguchi and Y. Hosoya. Scattering properties of oblate raindrops and cross polarization of radio waves due to rain. ii-calculations at microwave and millimeter wave regions. *Radio Research Laboratory, Journal*, 21:191–259, 1974.

[197] K. Okamoto and S. Kawata. Radiation force exerted on subwavelength particles near a nanoaperture. *Physical review letters*, 83(22):4534, 1999.

[198] R. Omori, T. Kobayashi, and A. Suzuki. Observation of a single-beam gradient-force optical trap for dielectric particles in air. *Optics letters*, 22(11):816–818, 1997.

[199] A. T. O'Neil and M. J. Padgett. Axial and lateral trapping efficiency of laguerre–gaussian modes in inverted optical tweezers. *Optics Communications*, 193(1):45–50, 2001.

[200] A. Ostendorf, R. Ghadiri, and S. Ksouri. Optical tweezers in microassembly. In *SPIE LASE*, pages 86070U–86070U. International Society for Optics and Photonics, 2013.

[201] T. Ota, S. Kawata, T. Sugiura, M. J. Booth, M. A. Neil, R. Juškaitis, and T. Wilson. Dynamic axial-position control of a laser-trapped particle by wave-front modification. *Optics letters*, 28(6):465–467, 2003.

[202] T. Ota, T. Sugiura, S. Kawata, M. J. Booth, M. A. Neil, R. Juškaitis, and T. Wilson. Enhancement of laser trapping force by spherical aberration correction using a deformable mirror. *Japanese journal of applied physics*, 42(6B):L701, 2003.

[203] M. Padgett. Optical tweezers: All-fibre design. *Nature Photonics*, 1(12):688–689, 2007.

[204] M. J. Padgett, J. Molloy, and D. McGloin. *Optical Tweezers: methods and applications.* CRC Press, 2010.

[205] Y.-L. Pan, S. C. Hill, and M. Coleman. Photophoretic trapping of absorbing particles in air and measurement of their single-particle raman spectra. *Optics express*, 20(5):5325–5334, 2012.

[206] L. Paterson, M. MacDonald, J. Arlt, W. Sibbett, P. Bryant, and K. Dholakia. Controlled rotation of optically trapped microscopic particles. *Science*, 292(5518):912–914, 2001.

[207] Á. B. Peña, B. Kemper, M. Woerdemann, A. Vollmer, S. Ketelhut, G. von Bally, and C. Denz. Optical tweezers induced photodamage in living cells quantified with digital holographic phase microscopy. In *SPIE Photonics Europe*, pages 84270A–84270A. International Society for Optics and Photonics, 2012.

[208] R. N. Pfeifer, T. A. Nieminen, N. R. Heckenberg, and H. Rubinsztein-Dunlop. Constraining validity of the minkowski energy-momentum tensor. *Physical Review A*, 79(2):023813, 2009.

[209] M. Pitzek, R. Steiger, G. Thalhammer, S. Bernet, and M. Ritsch-Marte. Optical mirror trap with a large field of view. *Optics express*, 17(22):19414–19423, 2009.

[210] B. C. Platt and R. Shack. History and principles of shack-hartmann wavefront sensing. *Journal of Refractive Surgery*, 17(5):S573–S577, 2001.

[211] J. Plewa, E. Tanner, D. Mueth, and D. Grier. Processing carbon nanotubes with holographic optical tweezers. *Optics Express*, 12(9):1978–1981, 2004.

[212] A. Pralle, M. Prummer, E.-L. Florin, E. Stelzer, J. Hörber, et al. Three-dimensional high-resolution particle tracking for optical tweezers by forward scattered light. *Microscopy research and technique*, 44(5):378–386, 1999.

[213] E. M. Purcell and C. R. Pennypacker. Scattering and absorption of light by nonspherical dielectric grains. *The Astrophysical Journal*, 186:705–714, 1973.

[214] E. M. Purcell, H. Torrey, and R. V. Pound. Resonance absorption by nuclear magnetic moments in a solid. *Physical review*, 69(1-2):37, 1946.

[215] X. Qi, T. A. Nieminen, A. B. Stilgoe, V. L. Loke, and H. Rubinsztein-Dunlop. Comparison of t-matrix calculation methods for scattering by cylinders in optical tweezers. *Optics letters*, 39(16):4827–4830, 2014.

[216] C.-W. Qiu, D. Palima, A. Novitsky, D. Gao, W. Ding, S. V. Zhukovsky, and J. Gluckstad. Engineering light-matter interaction for emerging optical manipulation applications. *Nanophotonics*, 3(3):181–201, 2014.

[217] B. Redding and Y.-L. Pan. Optical trap for both transparent and absorbing particles in air using a single shaped laser beam. *Optics letters*, 40(12):2798–2801, 2015.

[218] M. Reicherter, T. Haist, E. Wagemann, and H. Tiziani. Optical particle trapping with computer-generated holograms written on a liquid-crystal display. *Optics letters*, 24(9):608–610, 1999.

[219] S. N. S. Reihani and L. B. Oddershede. Optimizing immersion media refractive index improves optical trapping by compensating spherical aberrations. *Optics letters*, 32(14):1998–2000, 2007.

[220] M. Ribezzi-Crivellari, J. M. Huguet, and F. Ritort. Counter-propagating dual-trap optical tweezers based on linear momentum conservation. *Review of Scientific Instruments*, 84(4):043104, 2013.

[221] M. Rocha. Optical tweezers for undergraduates: theoretical analysis and experiments. *American Journal of Physics*, 77(8):704–712, 2009.

[222] P. J. Rodrigo, V. R. Daria, and J. Glückstad. Four-dimensional optical manipulation of colloidal particles. *Applied Physics Letters*, 86(7):074103, 2005.

[223] A. Rohrbach and E. H. Stelzer. Three-dimensional position detection of optically trapped dielectric particles. *Journal of Applied Physics*, 91(8):5474–5488, 2002.

[224] A. Rohrbach and E. H. Stelzer. Trapping forces, force constants, and potential depths for dielectric spheres in the presence of spherical aberrations. *Applied optics*, 41(13):2494–2507, 2002.

[225] Y. Roichman, A. Waldron, E. Gardel, and D. G. Grier. Optical traps with geometric aberrations. *Applied optics*, 45(15):3425–3429, 2006.

[226] T. Rother and M. Kahnert. *Electromagnetic wave scattering on nonspherical particles.* Springer, 2009.

[227] M. J. Saikia, R. Kanhirodan, and R. M. Vasu. High-speed gpu-based fully three-dimensional diffuse optical tomographic system. *Journal of Biomedical Imaging*, 2014:3, 2014.

[228] S. Sato, M. Ishigure, and H. Inaba. Optical trapping and rotational manipulation of microscopic particles and biological cells using higher-order mode nd: Yag laser beams. *Electronics letters*, 20(27):1831–1832, 1991.

[229] Schmidt. The interactive ftdt toolbox (iftdt), 2013.

[230] SCHOTT. Schott ag, hattenbergstrasse 10, 55122 mainz, deutschland, 2016.

[231] L. Seidel. Zur dioptrik. ueber die entwicklung der glieder 3ter ordnung, welche den weg eines ausserhalb der ebene der axe gelegenen lichtstrahles durch ein system brechender medien bestimmen, von herrn dr. l. seidel. *Astronomische Nachrichten*, 43(19):289–304, 1856.

[232] C. Shingyoji, H. Higuchi, M. Yoshimura, E. Katayama, and T. Yanagida. Dynein arms are oscillating force generators. *Nature*, 393(6686):711–714, 1998.

[233] T. Shoji and Y. Tsuboi. Plasmonic optical tweezers toward molecular manipulation: Tailoring plasmonic nanostructure, light source, and resonant trapping. *The journal of physical chemistry letters*, 5(17):2957–2967, 2014.

[234] V. Shvedov, A. S. Desyatnikov, A. V. Rode, Y. Izdebskaya, W. Krolikowski, and Y. S. Kivshar. Optical vortex beams for trapping and transport of particles in air. *Applied Physics A*, 100(2):327–331, 2010.

[235] V. G. Shvedov, A. V. Rode, Y. V. Izdebskaya, A. S. Desyatnikov, W. Krolikowski, and Y. S. Kivshar. Giant optical manipulation. *Physical review letters*, 105(11):118103, 2010.

[236] A. E. Siegmann. *Lasers.* University Science Books, 1986.

[237] R. M. Simmons, J. T. Finer, S. Chu, and J. A. Spudich. Quantitative measurements of force and displacement using an optical trap. *Biophysical Journal*, 70(4):1813, 1996.

[238] S. H. Simpson and S. Hanna. Application of the discrete dipole approximation to optical trapping calculations of inhomogeneous and anisotropic particles. *Optics express*, 19(17):16526–16541, 2011.

[239] D. Sinclair. Light scattering by spherical particles. *JOSA*, 37(6):475–480, 1947.

[240] W. Singer, M. Frick, S. Bernet, and M. Ritsch-Marte. Self-organized array of regularly spaced microbeads in a fiber-optical trap. *JOSA B*, 20(7):1568–1574, 2003.

[241] S. B. Smith, Y. Cui, and C. Bustamante. [7] optical-trap force transducer that operates by direct measurement of light momentum. *Methods in enzymology*, 361:134–162, 2003.

[242] S. P. Smith, S. R. Bhalotra, A. L. Brody, B. L. Brown, E. K. Boyda, and M. Prentiss. Inexpensive optical tweezers for undergraduate laboratories. *American Journal of Physics*, 67(1):26–35, 1999.

[243] W. J. Smith. *Modern optical engineering*. Tata McGraw-Hill Education, 4th edition, 2007.

[244] N. Spengler, J. Höfflin, A. Moazenzadeh, D. Mager, N. MacKinnon, V. Badilita, U. Wallrabe, and J. G. Korvink. Heteronuclear micro-helmholtz coil facilitates μm-range spatial and sub-hz spectral resolution nmr of nl-volume samples on customisable microfluidic chips. *PloS one*, 11(1):e0146384, 2016.

[245] S. Stallinga. Optical trapping at low numerical aperture. *Journal of the European Optical Society-Rapid publications*, 6, 2011.

[246] D. J. Stevenson, F. Gunn-Moore, and K. Dholakia. Light forces the pace: optical manipulation for biophotonics. *Journal of biomedical optics*, 15(4):041503–041503, 2010.

[247] S. Stoebenau, R. Kleindienst, R. Kampmann, and S. Sinzinger. Enhanced optical functionalities by integrated ultraprecision machining techniques (keynote paper). In *11th international conference of the European Society of Precision Engineering and Nanotechnology (EUSPEN), Lake Como, Italy*, volume 23, page 2011, 2011.

[248] J. Stratton. *Electromagnetic Theory, McGrow-Hill, New-York*. London, 1941.

[249] S. Streicher, R. Kampmann, S. Sinzinger, and O. Kalthoff. Efficient and precise simulation of multiple mie scattering events using gpgpus. In *SPIE OPTO*, pages 86190K–86190K. International Society for Optics and Photonics, 2013.

[250] J. W. Strutt. Lviii. on the scattering of light by small particles. *The London, Edinburgh, and Dublin Philosophical Magazine and Journal of Science*, 41(275):447–454, 1871.

[251] K. Svoboda and S. M. Block. Biological applications of optical forces. *Annual review of biophysics and biomolecular structure*, 23(1):247–285, 1994.

[252] K. Svoboda, C. F. Schmidt, B. J. Schnapp, S. M. Block, et al. Direct observation of kinesin stepping by optical trapping interferometry. *Nature*, 365(6448):721–727, 1993.

[253] A. Taflove, S. C. Hagness, et al. Computational electrodynamics: the finite-difference time-domain method. *Norwood, 2nd Edition, MA: Artech House, l995*, 1995.

[254] K. Taguchi, H. Ueno, T. Hiramatsu, and M. Ikeda. Optical trapping of dielectric particle and biological cell using optical fibre. *Electronics Letters*, 33(5):413–414, 1997.

[255] S. M.-R. Taheri, E. Madadi, M. Sadeghi, and S. N. S. Reihani. Optimized three-dimensional trapping of aerosols: the effect of immersion medium. *JOSA B*, 32(7):1494–1498, 2015.

[256] W. Tam. Off beam axis scattering by spherical particles. *Applied optics*, 16:2016–2018, 1977.

[257] R. Taylor and C. Hnatovsky. Particle trapping in 3-d using a single fiber probe with an annular light distribution. *Optics Express*, 11(21):2775–2782, 2003.

[258] G. Thalhammer, L. Obmascher, and M. Ritsch-Marte. Direct measurement of axial optical forces. *Optics express*, 23(5):6112–6129, 2015.

[259] Thorlabs. Thorlabs inc, newton, new jersey, usa, 2016.

[260] F. Träger. *Springer handbook of lasers and optics.* Springer Science & Business Media, 2012.

[261] W.-C. Tsai and R. J. Pogorzelski. Eigenfunction solution of the scattering of beam radiation fields by spherical objects. *JOSA*, 65(12):1457–1463, 1975.

[262] Y.-C. Tsai, R. Fardel, M. M. Panczyk, E. M. Furst, and C. B. Arnold. Non-spherical particles for optical trap assisted nanopatterning. *Nanotechnology*, 24(37):375303, 2013.

[263] C. W. Tyler. *Human symmetry perception and its computational analysis.* Psychology Press, 2003.

[264] J. Tyndall. On the blue colour of the sky, the polarization of skylight, and on the polarization of light by cloudy matter generally. *Proceedings of the Royal Society of London*, 17:223–233, 1868.

[265] USArmy. Military standard for photographic lenses, 1951.

[266] H. Van der Wulp. *Piezo-driven stages for nanopositioning with extreme stability: theoretical acpects and practical design considerations.* TU Delft, Delft University of Technology, 1997.

[267] I. Verdeny, A. Farré, J. Mas, C. López-Quesada, E. Martín-Badosa, and M. Montes-Usategui. Optical trapping: a review of essential concepts. *Opt. Pura Apl.*, 44:527–551, 2011.

[268] K. C. Vermeulen, G. J. Wuite, G. J. Stienen, and C. F. Schmidt. Optical trap stiffness in the presence and absence of spherical aberrations. *Applied optics*, 45(8):1812–1819, 2006.

[269] K. Visscher, S. P. Gross, and S. M. Block. Construction of multiple-beam optical traps with nanometer-resolution position sensing. *IEEE Journal of Selected Topics in Quantum Electronics*, 2(4):1066–1076, 1996.

[270] N. G. Walter. *Single Molecule Tools, Part A: Fluorescence Based Approaches*, volume 472. Academic Press, 2010.

[271] C. Wang, Y.-L. Pan, S. C. Hill, and B. Redding. Photophoretic trapping-raman spectroscopy for single pollens and fungal spores trapped in air. *Journal of Quantitative Spectroscopy and Radiative Transfer*, 153:4–12, 2015.

[272] M. D. Wang, H. Yin, R. Landick, J. Gelles, and S. M. Block. Stretching dna with optical tweezers. *Biophysical journal*, 72(3):1335, 1997.

[273] P. C. Waterman. Symmetry, unitarity, and geometry in electromagnetic scattering. *Physical review D*, 3(4):825, 1971.

[274] W. T. Welford. *Aberrations of optical systems.* CRC Press, 1986.

[275] D. A. White. Numerical modeling of optical gradient traps using the vector finite element method. *Journal of Computational Physics*, 159(1):13–37, 2000.

[276] D. A. White. Vector finite element modeling of optical tweezers. *Computer physics communications*, 128(3):558–564, 2000.

[277] Whitehouse. Whitehouse scientific ltd 2015, whitchurch rd, waverton, chester, ch3 7pb, uksilica microspheres 10m (mss010), 2016.

[278] J. B. Wills, K. J. Knox, and J. P. Reid. Optical control and characterisation of aerosol. *Chemical Physics Letters*, 481(4):153–165, 2009.

[279] M. Woerdemann, K. Berghoff, and C. Denz. Dynamic multiple-beam counter-propagating optical traps using optical phase-conjugation. *Optics express*, 18(21):22348–22357, 2010.

[280] K. D. Wulff, D. G. Cole, R. L. Clark, R. Di Leonardo, J. Leach, J. Cooper, G. Gibson, and M. J. Padgett. Holographic optical tweezers aberration correction using adaptive optics without a wavefront sensor. In *SPIE Optics+ Photonics*, pages 63262Y–63262Y. International Society for Optics and Photonics, 2006.

[281] K. D. Wulff, D. G. Cole, R. L. Clark, R. DiLeonardo, J. Leach, J. Cooper, G. Gibson, and M. J. Padgett. Aberration correction in holographic optical tweezers. *Optics express*, 14(9):4169–4174, 2006.

[282] J. C. Wyant. White light interferometry. In *AeroSense 2002*, pages 98–107. International Society for Optics and Photonics, 2002.

[283] J. C. Wyant and K. Creath. Basic wavefront aberration theory for optical metrology. *Applied optics and optical engineering*, 11(s 29):2, 1992.

[284] J. C. Wyant and K. Creath. Basic wavefront aberration theory for optical metrology. *Applied optics and optical engineering*, 11(s 29):2, 1992.

[285] C. Xie, D. Chen, and Y.-q. Li. Raman sorting and identification of single living micro-organisms with optical tweezers. *Optics letters*, 30(14):1800–1802, 2005.

[286] K. S. Yee et al. Numerical solution of initial boundary value problems involving maxwells equations in isotropic media. *IEEE Trans. Antennas Propag*, 14(3):302–307, 1966.

[287] Zemax. Zemax, llc; 10230 ne points dr. suite 540, kirkland, wa 98033 usa, 2016.

[288] D. Zhang and X.-C. Yuan. Optical doughnut for optical tweezers. *Optics letters*, 28(9):740–742, 2003.

[289] L. Zhang, W. She, N. Peng, and U. Leonhardt. Experimental evidence for abraham pressure of light. *New Journal of Physics*, 17(5):053035, 2015.

[290] W. Zhang, L. Huang, C. Santschi, and O. J. Martin. Trapping and sensing 10 nm metal nanoparticles using plasmonic dipole antennas. *Nano letters*, 10(3):1006–1011, 2010.

[291] Q. Zhao, C. Guclu, Y. Huang, F. Capolino, R. Ragan, and O. Boyraz. Plasmon optical trapping using silicon nitride trench waveguides. *JOSA B*, 33(6):1182–1189, 2016.

[292] S. Zwick, T. Haist, Y. Miyamoto, L. He, M. Warber, A. Hermerschmidt, and W. Osten. Holographic twin traps. *Journal of Optics A: Pure and Applied Optics*, 11(3):034011, 2009.

Awards, prices

- Nomination "AMA Innovationspreis 2013", "Infrarot-Detektor basierend auf einem neuartigem Mikro-Spiegel-Sensor", Nürnberg, 14.05. 2013.
- Förderpreis des Förder- und Freundeskreis (FFK) der TU Ilmenau e.V. für eine herausragende theoretische Master-Arbeit, 2011.
- Studienpreis der SEW-EURODRIVE-Stiftung für die Master-Arbeit "Kombinierte Simulation von Fresnelbeugung und Miestreuung zur Partikelcharakterisierung in fließenden Suspenisonen", 2010.

Journal articles

In preparation

- **R. Kampmann**, S. Sinzinger, J. G. Korvink, Topic: Optical system for trapping of particles in microfluidic channels.

2017

- **R. Kampmann**, S. Sinzinger, "Optical tweezers affected by monochromatic optical aberrations," Appl. Opt. 56, 1317-1326 (2017)

2016

- N. Schuergers, T. Lenn, **R. Kampmann**, M.V. Meissner, T. Esteves, M. Temerinac-Ott, J.G. Korvink, A.R. Lowe, C.W. Mullineaux, A. Wilde, "Cyanobacteria use micro optics to sense light directionm," eLife 5:e12620 (2016)
- O. Kalthoff, **R. Kampmann**, S. Streicher, S. Sinzinger, "A fast and scalable algorithm for multiple Mie-scattering in optical systems," Appl. Opt. 55, 3887-3896 (2016)

2015

- M. Krüger, **R. Kampmann**, R. Kleindienst, S. Sinzinger, "Time resolved combination of the Mueller-Stokes and Jones calculus for the optimization of a twisted-nematic spatial light modulator," Appl. Opt. 54, 4239-4248 (2015)

2014

- **R. Kampmann**, A. K. Chall, R. Kleindienst, and S. Sinzinger, "Optical system for trapping particles in air," Appl. Opt. 53, 777-784 (2014)

2012

- M. Hofmann, **R. Kampmann**, S. Sinzinger, "Perturbed Talbot patterns for the measurement of low particle concentrations in fluids," Appl. Opt. 51, 1605-1615 (2012)

2011

- R. Kleindienst, **R. Kampmann**, S. Stoebenau, S. Sinzinger, "Hybrid optical (freeform) componentsfunctionalization of nonplanar optical surfaces by direct picosecond laser ablation," Appl. Opt. 50, 3221-3228 (2011)

Conference and workshop talks

2017

- **R. Kampmann**, A. Asadollahbaik, V. Badilita, S. Sinzinger, J.G. Korvink, "Optical tweezers for trapping in a complex microfluidic environment," DGaO 2017

2016

- **R. Kampmann**, S. Sinzinger, "Optical tweezers affected by monochromatic aberrations," DGaO 2016

2015

- **R. Kampmann**, J.G. Korvink, S. Sinzinger, "Optical Forces," First annual IMT workshop on MEMS and NEMS simulation

2014

- **R. Kampmann**, A. K. Chall, R. M. Kleindienst, S. Sinzinger, "Iterative design process for highly efficient optical trapping systems," IODC 2014
- **R. Kampmann**, A. K. Chall, R. Kleindienst, S. Sinzinger, "Optische Manipulation sphärischer Partikel in Luft," DGaO 2014

2013

- **R. Kampmann**, R. Kleindienst, S. Sinzinger, "Optisches System für die Manipulation mikroskopischer Objekte in gasförmiger Umgebung," DGaO 2013
- **R. Kampmann**, R. Kleindienst, A. Grewe, E. Bürger, A. Oeder, S. Sinzinger, "Optimized systems for energy efficient optical tweezing," Photonics West 2013

2012

- **R. Kampmann**, R. Kleindienst, F. Rose, N. Hartung, M. Naglatzki, S. Sinzinger, "Laser Power Stabilization for Improved Ablation Depth Uniformity," DGaO 2012

Conference proceedings and book contributions

2017

- **R. Kampmann**, A. Asadollahbaik, V. Badilita, S. Sinzinger, J.G. Korvink, "Optical tweezers for trapping in a complex microfluidic environment," DGaO 2017 (in preparation)

2016

- **R. Kampmann**, S. Sinzinger, "Optical tweezers affected by monochromatic aberrations," in DGaO-Proceedings 2016, ISSN: 1614-8436 - urn:nbn:de:0287-2016-C006-7
- O. Kalthoff, **R. Kampmann**, S. Streicher, S.Sinzinger, "A fast scalable algorithm for the Monte Carlo simulation of elastic scattering in pertubed medium," in DGaO-Proceedings 2016, ISSN: 1614-8436 - urn:nbn:de:0287-2016-C002-0

2015

- J. Schuppich, **R. Kampmann**, S. Sinzinger, R. Mastylo, E. Manske, "High-precision optical step detection," in DGaO-Proceedings 2015, ISSN: 1614-8436, urn:nbn:de:0287-2015-A003-6

2014

- **R. Kampmann**, A. K. Chall, R. M. Kleindienst, S. Sinzinger, "Iterative design process for highly efficient optical trapping systems," in Classical Optics 2014 Hawaii, (Optical Society of America, 2014), paper IM2B.1.
- **R. Kampmann**, S. Sinzinger, "Analysis of the influence of manufacturing and alignment related errors on an optical tweezer system," in Proc. SPIE 9293, International Optical Design Conference, Hawaii, 2014
- M. Lawin, K. John, **R. Kampmann**, S. Sinzinger, P. Santi, "Implementation of Bessel Beam Illumination for sTSLIM," 1st LightSheet Fluorescence Microscopy International Conference and 6. LSFM International workshop, Barcelona 2014
- I. W. Rangelow, S. Sinzinger, M. Steffanson, M. Holz, T. Ivanov, R. Kleindienst, **R. Kampmann**, "Thermographischer Detektor basierend auf einem neuartigen Mikro-Spiegel Sensor," in Technisches Messen. Berlin: De Gruyter, ISSN 21967113, Bd. 81 (2014), 5, S. 219-227

- **R. Kampmann**, A. K. Chall, R. Kleindienst, S. Sinzinger, "Optische Manipulation sphärischer Partikel in Luft," in DGaOProceedings 2014, ISSN: 1614-8436, urn:nbn:de:0287-2014-A004-7
- M. Krüger, **R. Kampmann**, R. Kleindienst, S. Sinzinger, "Kombinierter Müller-Jones-Formalismus zur umfassenden Optimierung spatialer Flüssig-kristall Lichtmodulatoren," in DGaO Proceedings 2014, ISSN: 1614-8436, urn: nbn: de: 0287-2014-B032-5
- S. Streicher, **R. Kampmann**, S. Sinzinger, O. Kalthoff, "Hocheffiziente Simulation von Mehrfachstreuprozessen auf Basis der Mie-Theorie für die optische Sensorik," in DGaO-Proceedings 2014, ISSN: 1614-8436, urn:nbn:de:0287-2014-A037-3

2013

- R. Kleindienst, **R. Kampmann**, S. Stoebenau, S. Sinzinger, "Three dimensional laser ablation for functionalization of non-planar optical surfaces," in Congress proceedings / International Congress on Applications of Lasers & Electro-Optics ; 32 (Miami, Fla.) : 2013.10.06-10. - Orlando, Fla.: LIA (2013), S. 919-925
- M. Steffanson, K. Gorovoy, M. Holz, T. Ivanov, **R. Kampmann**, R. Kleindienst, S. Sinzinger,I. W. Rangelow, "Low-cost uncooled infrared detector using thermo-mechanical micro-mirror array with optical readout," in AMA conferences 2013 proceedings / AMA conferences ; 16 (Nürnberg) : 2013.05.14-16. - Wunstorf: AMA Service GmbH (2013), S. 85-88
- R. Kleindienst, **R. Kampmann**, S. Stoebenau, S. Sebastian, S. Sinzinger, "Integriertes Design und Fertigung optischer Bauelemente : Herstellung eines hybriden diffraktiv-reflektiven optischen Strahlformers," in Optik & Photonik. - Weinheim: Wiley-VCH, Bd. 8 (2013), 2, S. 48-51
- **R. Kampmann**, R. Kleindienst, S. Sinzinger, "Optisches System für die Manipulation mikroskopischer Objekte in gasförmiger Umgebung," in DGaO-Proceedings 2013, ISSN: 1614-8436, urn:nbn:de:0287-2013-B029-7
- S. Streicher, **R. Kampmann**, S. Sinzinger, O. Kalthoff, "3D Mie-Streuung in Simulation und Streulichtexperiment," in DGaO-Proceedings 2013, ISSN: 1614-8436, urn:nbn:de:0287-2013-P015-0
- S. Streicher, **R. Kampmann**, S. Sinzinger, O. Kalthoff, "Efficient and precise simulation of multiple Mie scattering events using GPGPUs," in Proc. SPIE 8619, Photonics West San Francisco, 2013
- **R. Kampmann**, R. Kleindienst, A. Grewe, E. Bürger, A. Oeder, S. Sinzinger, "Optimized systems for energy efficient optical tweezing," in Proc. SPIE 8637, Photonics West San Francisco, 2013

2012

- **R. Kampmann**, R. Kleindienst, F. Rose, N. Hartung, M. Naglatzki, S. Sinzinger, "Laser Power Stabilization for Improved Ablation Depth Uniformity," in DGaO Proceedings 2012, ISSN: 1614-8436, urn:nbn:de:0287-2012-B022-4
- R. Kleindienst, **R. Kampmann**, S. Stoebenau, S. Sinzinger, "Hybrid Beam Shapers - Compound Design and Integrated Fabrication Techniques," in DGaO Proceedings 2012, ISSN: 1614-8436, urn:nbn:de:0287-2012-B019-3
- M. Steffanson, K. Gorovoy, **R. Kampmann**, R. Kleindienst, S. Sinzinger, I. W. Rangelow, " Low-cost uncooled infrared detector using microcantilever arrays with optical readout," in 23rd Micromechanics and Microsystems Europe Workshop : MME 2012 Ilmenau, September 9 - 12, Ilmenau, Germany ; proceedings. - Ilmenau : Verl. ISLE. 2012
- S. Sinzinger, A. Oeder, S. Stoebenau, **R. Kampmann**, "Compact optical systems for micromanipulation : bringing optical tweezers into industrial applications," in Laser-Technik-Journal.- Berlin : Wiley-VCH, ISSN 18639119, Bd. 9 (2012), 4, S. 20-23

2011

- R. Kleindienst, **R. Kampmann**, S. Stoebenau, S. Sinzinger, "Synthetic design and integrated fabrication of multifunctional hybrid beam shapers," in Proc. SPIE 8130, Laser Beam Shaping XII, 81300E (September 07, 2011)
- R. Kleindienst, S. Stoebenau, **R. Kampmann**, S. Sinzinger, "Hybride freiformoptische Komponenten - Realisierung komplexer Strahlformungen mittels integrierter Fertigungsverfahren," in DGaO Proceedings 2011, ISSN: 1614-8436, urn:nbn:de:0287-2011-A033-1
- M. Hofmann, **R. Kampmann**, S. Sinzinger, "Mikrosystem zur Partikelkonzentrationsmessung auf Basis der Talbotinterferometrie," in DGaO Proceedings 2011, ISSN: 1614-8436, urn:nbn:de:0287-2011-B005-2
- M. Gruber, H. Winkelmann, M. Bohling, H. Knuppertz, R. Kleindienst, **R. Kampmann**, "Herstellung eines optischen Sensorkopfes zur Gasanalyse mittels spanender, ablativer und planarer Fertigungsverfahren," in DGaO Proceedings 2011, ISSN: 1614-8436, urn:nbn:de:0287-2011-P004-1
- S. Stoebenau, R. Kleindienst, **R. Kampmann**,S. Sinzinger, "Enhanced optical functionalities by integrated ultraprecision machining techniques," in International conference of the European Society for Precision Engineering and Nanotechnology ; 11 (Como) : 2011.05.23-26. - Bedford : Euspen (2011)
- **R. Kampmann**, "Kombinierte Simulation von Fresnel-Beugung und Mie-Streuung zur Partikelcharakterisierung in fließenden Suspensionen", VDM Verlag Dr. Müller, ISBN-10: 3639343786, (2011)

2010

- R. Kleindienst, **R. Kampmann**, S. Stoebenau, S. Sinzinger, "Reflective hybrid optical components - functionalization of nonplanar optical surfaces using direct ps-laser ablation," in EOS annual meeting 2010, (EOSAM 2010) / EOS annual meeting ; (Paris) : 2010.10.26-29. - Hannover : EOS, European Optical Society (2010)
- R. Kleindienst, S. Stoebenau, **R. Kampmann**, J. Pommer, N. Ebinger, S. Sinzinger, "Hybride, optische Bauteile - Funktionalisierung nicht planer, optischer Oberflächen mittels Laserablation," in DGaO Proceedings 2010, ISSN: 1614-8436, urn: nbn: de: 0287-2010-A006-3